# Optimal Control and Scheduling of an Experimental Laboratory-scale Hot-Rolling Mill using Intelligent Systems-based Paradigms

Miguel Angel Gama-Valdéz


The University Of Sheffield.

A thesis submitted in partial fulfillment
of the requirements for the degree of
Doctor of Philosophy

The University of Sheffield
2008

# Abstract

A novel mechanism for the optimal scheduling and the control of the hot-rolling of steel is presented in this work. Such a mechanism provides optimal rolling parameters to set-up an experimental laboratory-scale hot-rolling mill and thus produce metals with the desired microstructural and mechanical characteristics. The proposed methodology combines physically-based models and those associated with 'intelligence' such as Neural Networks, Fuzzy Systems, and Genetic Algorithms, to systematically calculate the optimal rolling schedule so as to achieve a *right-first-time* production of steel alloys, a challenge for academia in general. Unlike current design methods, the scheduling problem is here treated as an optimisation problem which aims at satisfying multiple process objectives and a set of user-defined requirements. Such objectives are expressed in terms of the quantitative elements of the steel microstructure and its mechanical properties such as strength and toughness. Three main aspects are considered to define and approach the optimisation problem: (1) THE PROCESS MODEL, which includes integrated knowledge of the stock microstructure, the mechanical properties, and the processing route; (2) THE PHYSICAL CONSTRAINTS associated with the metal due to its chemical composition, as well as the mill operating limitations; and (3) a set of OPTIMALITY CRITERIA which is used as a performance index to evaluate the quality and feasibility of each solution.

In order to show the efficacy of this methodology, extensive experimental studies, metallographic analyses, and laboratory mechanical tests, are presented using the commercial type C-Mn Steel alloy (Bright Mild Steel) grade 080A15. The results from such experimental studies showed that the final product was in good agreement with the desired design in terms of the microstructure and the mechanical properties. The experiment results also demonstrated the advantages of the proposed methodology over current methods which are generally *ad hoc* and lack adequate capabilities for finding the optimal process parameters. The software SISSCOR is also introduced as a friendly graphical user interface for a fast experiment design and analysis of the dynamic performance associated with the rolling mill.

This work will also review the application of a modified model-based approach in the form of the Generalised Predictive Control to reflect a Fuzzy Model of the mill. Such a hybrid strategy was implemented in order to provide robustness and flexibility to the overall control system, and to guarantee an optimal control performance during hot-rolling experiments.

# Acknowledgments

I thank Professor Mahdi Mahfouf for his encouragement and supervision during the course of this PhD, and also for his professionalism when giving advice not only during technical meetings but also in a personal level.

I am also grateful to my PhD examiners Professor Derek A. Linkens and Professor H. K. D. H. Bhadeshia for their invaluable feedback and suggestions.

Special thanks go to Dr. Mike Frolish who helped me perform the hot-rolling experiments reported in this thesis, as well as to Dr. Sabino Ayvar and Mr. Jorge Zuno for their assistance during the preparation of the laboratory tests and the metallographic analyses; without their help this work definitively would not have been possible.

I also wish to gratefully acknowledge Professor Andy Howe, Dr. George Panoutsos and Dr. Mouloud Denai for their help throughout this project.

I dedicate this work to my parents Tacho and Rosy, my brothers and sisters Julián, Liz, Dany and Mimi, as well as my best friends Álex and Jandia, for giving me their unconditional love, friendship and support.

This work was funded by CONACYT (Consejo Nacional de Ciencia y Tecnología) of Mexico.

# Contents

# List of Figures

# List of Tables

# List of Acronyms

**3MM** 3-Mass-Model

**ANFIS** Adaptive Network-based Fuzzy Inference System

**CARIMA** Control Autoregressive Integrated Moving Average

**FE** Finite Element

**FIS** Fuzzy Inference System

**FOC** Field-Oriented Control

**GA** Genetic Algorithms

**GPC** Generalised Predictive Control

**GUI** Graphical User Interface

**ITT** Impact Transition Temperature

**MPC** Model-based Predictive Control

**NN** Neural Networks

**PID** Proportional-Integral-Derivative

**PSC** Plane-Strain Compression

**PWM** Pulse Width Modulated

**RLS** Recursive Least Squares

**RMSE** Root Mean Square Error

**SISO** Single-Input Single-Output

**SISSCOR** Sheffield Integrated System for SCheduling and Optimisation in Rolling

**SLIMMER** Sheffield-Leicester Integrated Model for Microstructure Evolution in Rolling

**TMP** Thermomechanical Processing

**TS** Tensile Strength

**TSK** Takagi-Sugeno-Kang

**YS** Yield Strength

# Chapter 1

# Introduction

## 1.1 Motivation

Hot-rolling of steel alloys is one of the oldest metal-working processes used to produce metals with high strength, good ductility and toughness for innumerable applications. During decades, significant research has been undertaken by metallurgists and engineers to describe not only the underlying phenomena taking place in the metal during the rolling process, but also to establish the processing routes that lead to a faster and safer production. However, the steel industry is currently facing more challenges than ever before. Such challenges are mainly associated with environmental concerns, as well as the energy and raw materials availability. In the case of steel-making companies, very high standards of surface quality and tighter specifications on hot-rolled products are constantly being set, which result in stringent demands being imposed on the specified metallurgical properties. To cope with the increasing demand of advanced metals, steel companies are now being forced to promote a wider implementation of the latest technologies, as well as to invest in the development of new processing methods (see Figure 1.1). For instance, it is known that, only in the automotive industry, 60% of the steel grades used today were invented in the last 5 years.

In essence, the steel-making process represents a natural multi-disciplinary environment which renders its maintaining be very time-consuming and expensive. The continuous improvement of the production line requires understanding of the quantitative aspects of the process, the metal being processed, the rolling mills, the temperature profiles, and, of course, the way such aspects are all combined to satisfy the user requirements. This challenge may concern (not exclusively) metallurgists, mechanical engineers, as well as systems engineers whose inputs will contribute to the idea of the


Figure 1.1: Advanced metal designs for specific applications demand for new and more reliable processing strategies

'optimal' processing route. On the other hand, the need for improvement also implies that the control of the process should be enhanced as well. As a result, the main engineering aspects involved in the process can no longer be treated separately, but an integrated knowledge based on solid research should be considered.

Although significant achievements have been accomplished in this area, the development of optimal design and control methods for steel-making processes is still needed for improving metal designs, reducing production costs, and producing specified quality on a repeatable basis. Existing design methods usually respond to specific situations without including wider aspects in the metal design and process development. This scenario presents major challenges to control engineers who are faced with higher requirements and superior quality standards. Therefore, the new methodologies for process design and control should be based upon scientific principles, which sufficiently consider the workpiece behaviour and the mechanics of the manufacturing process.

**The motivation behind the research work described in this document is to redress the dichotomy between the approach of the metallurgist who**

**tries to understand and optimise the process, and the mill technologist who may only be interested in control problems.** This has shaped the idea of the *knowledge integration* where metallurgy principles, sophisticated control strategies, and evolutionary optimisation algorithms are used to achieve a *right-first-time* production of metal designs with specific microstructures and mechanical properties.

This research project seeks to improve the search performance toward the optimal rolling profile and scheduling to improve the designing process and production of steel alloys. It is worth noting that this objective includes two main parts: (1) it seeks improvement in the methodology to (2) find the optimal scheduling. This makes the main difference between the approach proposed here and the current methods used by industry, where the metallurgist decisions to optimise the process are judged by his/her own empirical experience (trial and error), and it is not clear what criteria he/she uses to decide on whether his/her decision is the best one. On the other hand, this work provides a set of optimality criteria which include the microstructural and control aspects of the process in order to meet the final product requirements. Such criteria are based on mathematical models with solid theoretical and experimental development.

In the same direction, this work attempts to improve the speed control system of the rolling mill to guarantee optimal performance under a wider range of operating conditions. Although conventional Proportional-Integral-Derivative (PID) controllers are still the most popular option to solve the majority of industrial control problems due to their simplicity, Model-based Predictive Control (MPC) has developed considerably both within the research control community and industry. MPC was found to be quite a robust type of control in most reported applications. This research work attempts to contribute to filling the gap between real-time industrial problems and the powerful but sometimes abstractly formulated techniques developed by control researchers. Part of this thesis focuses on the real-time implementation of the adaptive MPC in the speed loop of an experimental rolling mill.

This project aims at carrying-out extensive experimental research directed towards basic science and improved understanding to provide comprehensive frameworks for the development of simplified mechanisms when designing the rolling experiments.

## 1.2 IMMPETUS

This research work has been undertaken under the umbrella of the Institute for Microstructural and Mechanical Process Engineering: The University of Sheffield (IMMPETUS). IMMPETUS is a multi-disciplinary research centre established in May 1996 to study thermomechanical processing of metals by developing models describing their microstructural and nanostructural processes, and also by improving the control systems of the related industrial processes. IMMPETUS is based within three host departments at Sheffield University: the Department of Engineering Materials, the Department of Mechanical Engineering, and the Department of Automatic Control and Systems Engineering. During the last 10 years, the institute has proved to be an international leading research group with an excellent track record in technology transfer.

Among its "world-class" facilities, one can cite an experimental laboratory-scale hot-rolling mill, known as the "Hille-mill", which is located in the Department of Engineering Materials, at The University of Sheffield (UK). The mill has been the subject of a major refurbishment operation which allows for full investigation of the hot-rolling process on an experimental scale. As a result, the Hille-mill has provided improved knowledge about the microstructural changes taking place during processing, leading to the development of reliable thermomechanical models, new characterisation methodologies, and metal design.

## 1.3 About the Project

This project relates to the optimal scheduling and control of the hot-rolling process using an experimental laboratory-scale hot-rolling mill. The main aim is to design a new integrated mechanism to optimise the rolling schedule according to a set of user-defined requirements in terms of the desired mechanical properties of the metal. The proposed approach combines information of the steel microstructure and the Hille-mill working conditions to compute and synthesise the optimal rolling parameters. There are two main aspects considered in such an integrated system: (1) Optimisation – Genetic Algorithms (GA) are used to search for the appropriate deformation profiles and rolling schedules; and (2) Control – Fuzzy Inference System (FIS)-based modelling and Generalised Predictive Control (GPC) are used to improve the dynamic performance of the Hille-mill during the rolling experiments.

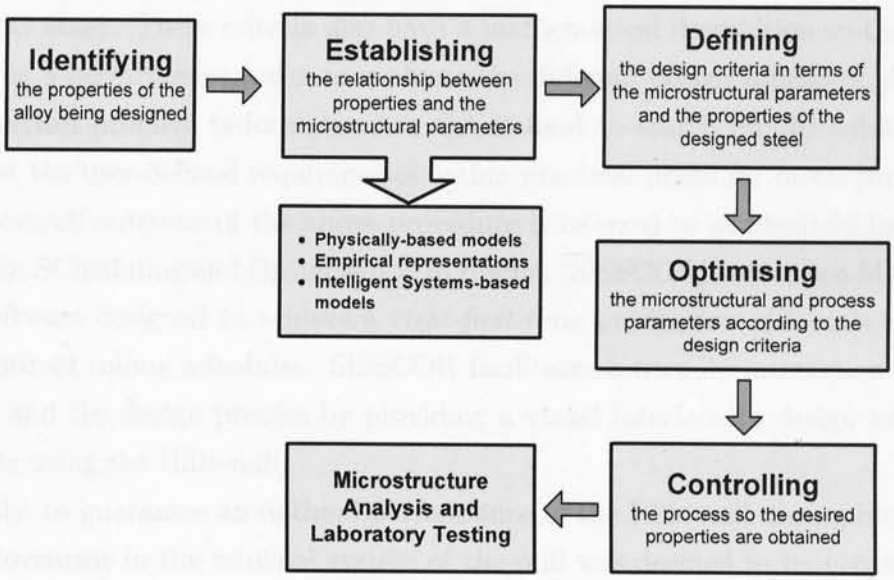


Figure 1.2: Block diagram of the main stages involved in the development of the proposed scheduling methodology

The *knowledge integration* and the *right-first-time* production of steel alloys entirely depend on the mathematical models of the metal behaviour during the rolling process. In metallurgical design, it is necessary not only to obtain the required final microstructure, but also to ensure that throughout the whole manufacturing process the structure at any given stage is optimal for processing at the next stage. Therefore, the role of the structure-property relationship is important to establish the correlation between the desired properties of the alloy, its microstructural parameters, and its processing.

The development of the scheduling strategy proposed in this work followed the steps shown in the block diagram of Figure 1.2. Usually, a set of user-defined requirements are used to specify the mechanical properties needed for a particular application; therefore, the fist step consists of **identifying** such properties, which are mainly related to the strength, toughness, and ductility of the steel alloy. The next step focuses on **establishing** the mathematical relationships that correlate the metal properties with its microstructure and processing. Such mathematical relationships are described by physically-based models, empirical representations, and intelligent systems-based models.

The **definition** of a set of optimality criteria to determine the design procedures

is the next stage. These criteria also have a mathematical description so that it can be used as a *performance index* to evaluate the different design solutions. After the **optimisation** problem is formulated, a GA is used to search for the solution that best meet the user-defined requirements within practical limits for metal processing.

The overall outcome of the above procedure is referred to as Sheffield Integrated System for SCheduling and Optimisation in Rolling (SISSCOR), which is a MATLAB®-based software designed to achieve a *right-first-time* production of metals by calculating optimal rolling schedules. SISSCOR facilitates a friendly interaction between the user and the design process by providing a visual interface to design rolling experiments using the Hille-mill.

Finally, to guarantee an optimal performance of the Hille-mill during hot-rolling, the improvement in the **control** system of the mill was deemed to be necessary. To accomplish this, sophisticated control strategies, including MPC, were implemented in order to provide the control system with adaptive capabilities and robustness.

Extensive experimental validation of the proposed scheduling mechanism was carried-out by performing real-time hot-rolling experiments using the Hille-mill, as well as **microstructural analysis and laboratory testing** of the rolled product. These experiments should prove useful in the assessment of the overall performance and the reliability of the scheduling mechanism.

### *1.3.1 Why are Optimisation and Adaptive Control needed in the Hille-mill?*

Currently, experimental data are used for finding relationships to correlate the microstructure and the mechanical properties of the steel alloy considering a wide range of processing scenarios. Such a correlation forms the basis for developing *metals by design*, which allows for tailoring the microstructure of an alloy to meet specific design criteria. However, understanding this correlation and optimising the microstructure is not a trivial exercise because of the complex nature of the variables involved in the process. Grain size, grain boundaries, grain morphology, alloying element properties, and parent-alloying element interactions are usually considered in studies dealing with the microstructure of alloys. The limitations of current practices are mostly felt while solving the design problems where multiple objectives need to be satisfied within the constraints of the metal derived from its chemical components.

Previously, no scheduling strategy had ever been implemented in the Hille-mill,

and no optimisation procedures for metal design and processing were the subject of research within the Department of Automatic Control and Systems Engineering. **Indeed, the novelty of this research work lies on the development of a new perspective in metal design and optimal scheduling of the hot-rolling process. This should provide new directions towards the use of Intelligent Systems to systematically define such optimal processing routes.**

With respect to the mill control, it is well-known that the rolling speed is one of the most important parameters within the rolling schedule. It has been observed that the use of conventional PID controllers in the Hille-mill produces a very active control signal and shaft chattering when working above the rated speed. This affects the deformation profile applied to the stock in terms of the amount of strain and the strain rate; as a result, a mismatch between the final product and the original design may be produced. Hence, to improve the overall control performance, the use of adaptive control algorithms is also investigated.

### *1.3.2 Research Objectives*

The following research objectives are pursued in this work:

1. The design of effective methodologies to set-up the optimal rolling schedule in the Hille-mill by integrating knowledge of the stock to be rolled using physically-based models and intelligent systems-based paradigms for the control of the metal microstructure and the mechanical properties.

2. The design of integrated strategies for knowledge elicitation of the microstructural behaviour and mill control supported by the development of a Graphical User Interface (GUI) for experiment design and computer simulation.

3. Conduct a series of real-time experiments on the Hille-mill using the C-Mn steel alloy and laboratory analyses of the microstructure and the mechanical properties for result validation and model refinement.

4. The study and analyses of the open- and closed-loop modelling aspects which relate to the Hille-mill by conducting a series of simulation and experimental studies of the mill operations.

5. The study of feedback and feedforward loops in order to develop model-based techniques for real-time control of the mill rolling speed.

## 1.4 Related Publications and Colloquia

The research work presented in this thesis has been published in the following papers:

1. M. A. Gama and M. Mahfouf. Optimal scheduling and control of an experimental laboratory-scale hot-rolling mill for 'right-first-time' production of steels. Colloquium of the Institute for Microstructural and Mechanical Process Engineering: The University of Sheffield (IMMPETUS). Sheffield, UK. May 2008.

2. M. Mahfouf, M. A. Gama and G. Panoutsos. Right-First-Time Production of Materials: A Reality or a Myth? Plenary presentation for the *International Conference on Neural Network and Genetic Algorithm in Materials Science and Engineering.* Shibpur, India. January 2008.

3. M. A. Gama and M. Mahfouf. Model-based optimisation and control of the hot-rolling process for the design of steel microstructure. *Symposium on Automation in Mining, Mineral and Metal Processing.* IFAC. Quebec city, Canada. August 2007.

4. M. A. Gama and M. Mahfouf. Rolling schedule optimisation for microstructure design and control using intelligent systems-based paradigms. Colloquium of the Institute for Microstructural and Mechanical Process Engineering: The University of Sheffield (IMMPETUS). Sheffield, UK. April 2007.

5. M. A. Gama and M. Mahfouf. Speed control of an experimental hot-rolling mill using generalised predictive control. *International Conference Control 2006.* Glasgow, Scotland. August - September 2006.

6. D. Theilliol, M. Mahfouf, D. Sauter and M. A. Gama. Actuator fault detection isolation method and state estimator design for hot-rolling mill monitoring. *Symposium on Fault Detection Supervision and Safety for Technical Processes.* SAFEPROCESS. IFAC. Beijing, China. August - September 2006.

7. M. A. Gama and M. Mahfouf. On the development of a model-based predictive speed control system for an experimental hot-rolling mill. Colloquium of the Institute for Microstructural and Mechanical Process Engineering: The University of Sheffield (IMMPETUS). Sheffield, UK. April 2006.

8. M. Mahfouf, Y. Yang, M. A. Gama and D. A. Linkens. Roll speed and roll gap control with neural network compensation. *Iron & Steel Institute of Japan (ISIJ) International*, Vol. 45, No. 6, pp. 841-850. 2005.

9. M. A. Gama and M. Mahfouf, D. A. Linkens, Y. Yang and M. F. Abbod. Modelling and simulation of an experimental ac induction motor drive and rolling mill system. Colloquium of the Institute for Microstructural and Mechanical Process Engineering: The University of Sheffield (IMMPETUS). Sheffield, UK. March 2005.

Additionally, two journal papers have been prepared to be submitted for review.

## 1.5 Thesis Outline

Figure 1.3 depicts a graphical outline of the thesis contents. As shown in this figure, all chapters are distributed within three main categories: (1) THEORY – sets the theoretical background and provides a brief description of the project; (2) DEVELOPMENT – shows detailed explanations of the design methodology proposed in this work as well as the associated simulation studies; and (3) EXPERIMENTATION AND RESULTS – presents the experimental procedures, the real-time implementations, and the metallographic/laboratory results.

**Chapter 2** introduces the important role of hot-rolling as a part of the thermo-mechanical processing of steel alloys. It provides a brief description of the processing route along with a quick overview of the theory behind hot-rolling and its general concepts.

**Chapter 3** presents the physically-based model of the C-Mn steel alloy which describes the evolution of its microstructure during hot-rolling. A special attention is paid to the role of the grain size in the characterisation of the microstructure and the final properties.

**Chapter 4** shows the development of the proposed GA-based optimisation of the steel microstructure. It presents the optimality criterion used to calculate optimal

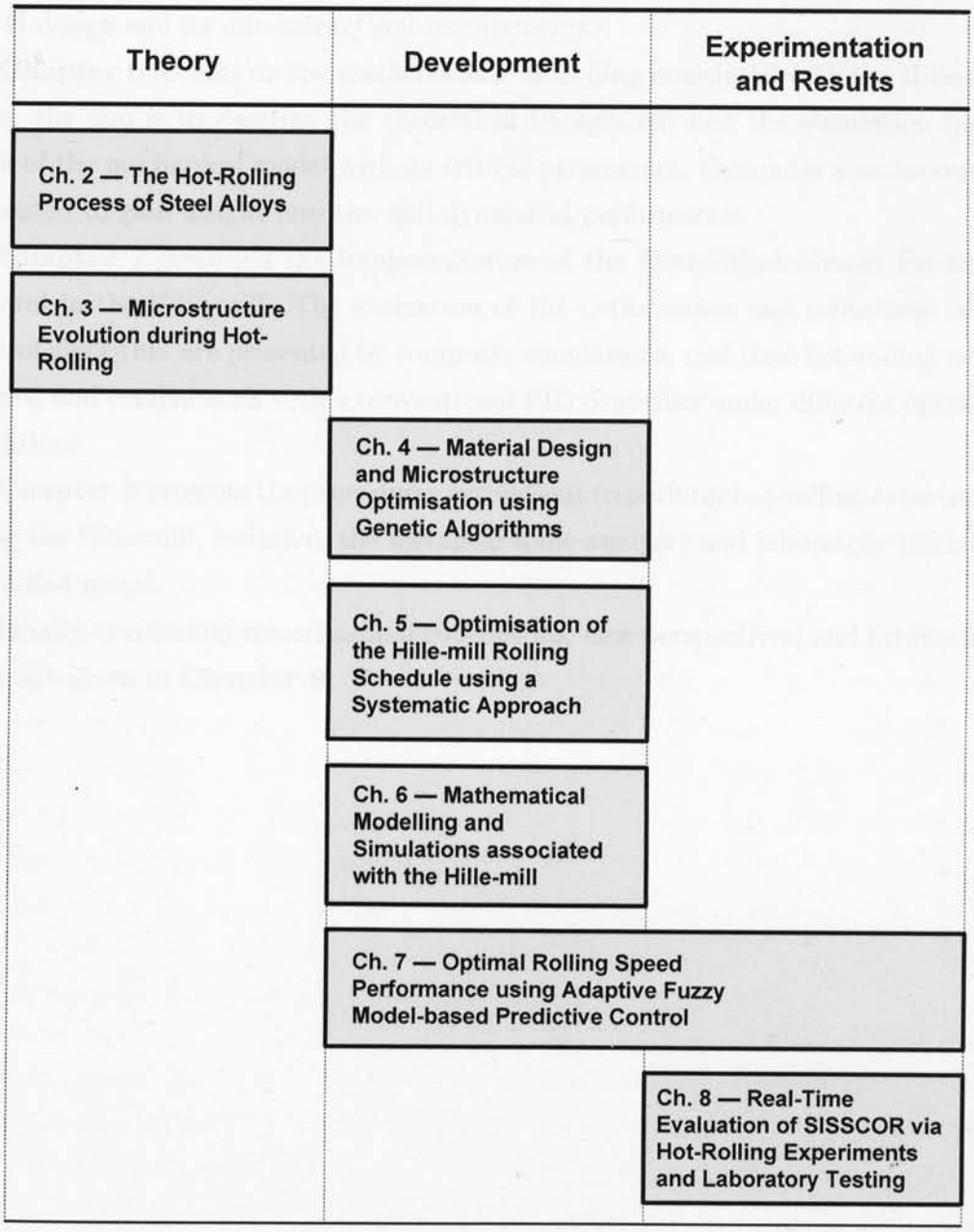


Figure 1.3: Graphic outline of contents

microstructural parameters in order to meet the user-defined requirements in terms of the mechanical properties of the metal.

**Chapter 5** provides the details which describe the second part of the proposed scheduling mechanism. It explains how to synthesise the rolling schedule by using the

metal design and its microstructural requirements.

**Chapter 6** focuses on the mathematical modelling associated with the Hille-mill. Here, the aim is to describe the theoretical background and the simulation framework of the mechanical model with its critical parameters. Computer simulations are presented to gain insight into the mill dynamical performance.

**Chapter 7** discusses the implementation of the Fuzzy Model-based Predictive Control in the Hille-mill. The evaluation of the performance and robustness of the control algorithm are presented by computer simulations, real-time hot-rolling experiments, and comparisons with a conventional PID controller under different operating conditions.

**Chapter 8** presents the procedures carried-out to perform hot-rolling experiments using the Hille-mill, including the metallographic analyses and laboratory testing on the rolled metal.

Finally, concluding remarks, final conclusions, new perspectives, and future directions are given in **Chapter 9**.

# Chapter 2

# The Hot-Rolling Process of Steel Alloys

## 2.1 Introduction

This chapter describes the hot-rolling process as a part of the thermomechanical processing route of steel alloys. First, a brief description of the processing route is given, in addition to a general overview of the hot-rolling process. Next, the physical concepts of the main variables involved in hot-rolling such as the stress, the strain, and the strain rate are presented. This chapter also establishes the importance of the predictive capabilities of the design methodology to estimate the metallurgical phenomena such as the rolling force and torque. The main aim of this chapter is to introduce some important aspects relating to the hot-rolling process in order to set the background for metal design and process optimisation.

## 2.2 Current Research on Rolling Mills Automation

Control systems have been applied to complex hot-rolling processes and currently control covers the whole production line. The ongoing research in the steel-making industry includes the design of control systems to improve the reheating process using furnace combustion, the scheduling of tandem mills [18], the development of new optimisation algorithms for dimensional control of steel bars [3], the design of on-line temperature control systems [48],[51], etc.

Further developments of advanced control strategies in this field have indeed been addressing the increasing demand for improving quality of the rolled products, such as the dimension accuracy, the mechanical and surface properties, as well as the rolling mill performance [29],[63],[65],[79]. For instance, Fuzzy Systems have been proposed for the control and the diagnosis of the roll eccentricity compensation [23],[45]. Fur-

thermore, innovations have been actively promoted by developing reliable mathematical models and implementing new control technologies such as Robust Multivariable Control [39], Nonlinear Control [46], Sequence and Supervisory Control [36],[87], Robust Control [16], Fuzzy Control [28], Neural Control [67], Iterative Learning Control [24], and Model-based Predictive Control [13],[21]. Hybrid Control Systems combining conventional controllers and Fuzzy Logic have also been proposed [19]; for instance a conventional linear controller was designed to use a Neural Network-based system to counteract the mill spring and to improve flatness control [56].

Process optimisation has also been an important aspect for metallurgists and control engineers. In this regard, Intelligent Systems-based paradigms have been proposed and applied to cope with the uncertainties involved in the process. Furthermore, the optimisation of the microstructure is crucial in obtaining the mechanical properties required by the customer. For example, Expert Systems have been proposed for the optimisation of the steel composition and the process route [58]. Also, Genetic Algorithms (GA) have been proposed to determine optimal microstructural parameters in aluminium alloys [47].

Current research is also focused on improving the model predictive capabilities when designing new metals. More reliable hybrid models are being developed to determine the main processing conditions in order to predict the mechanical properties and the microstructural events that affect the dynamic deformation of the metals. Different modelling methodologies have been proposed such as Neural Networks [50],[86],[74], Neural-Fuzzy Systems [11], Finite Element, and Fuzzy Logic [18].

For the purpose of quality control, physically-based and hybrid models that estimate the mechanical properties of hot-rolled strip, including the grain size, the yield strength, the tensile strength, and the elongation to fracture have been developed [68],[74]. These models are based on physical-metallurgical models describing the rolling process and the related microstructural changes. Some components of the model are based on an Adaptive Network-based Fuzzy Inference System (ANFIS) which predicts the metal properties for different deformation conditions, along with GA for parameter optimisation. Also, hybrid models have been developed to predict the evolution of state variables such as the dislocation density, sub-grain size, and misorientation between the sub-grains and subsequent recrystallisation behaviour [1].

## 2.3 Thermomechanical Processing of Steel Alloys

Thermomechanical Processing (TMP) is the exploitation of both the ease of shaping and the opportunity to modify the microstructure to the benefit of the final product properties. To do this in a control manner requires advanced control of the industrial operation as well as the understanding of the metallurgical events taking place during the processing. TMP does not start with a blank state, but works with the as-cast microstructure. However, the as-cast microstructure is normally undesired, hence TMP is used as a means to refine it in order to increase the strength of the product and improve the metal structure and texture. Also, TMP produces the starting microstructure for the remainder of the metal processing, such as cold-working and annealing. Because the aim of TMP is to achieve the desired product properties for a certain application, it is necessary to track the metal through the whole process and consider the relationships between the metal processing and its impact on the microstructure and on the final mechanical properties, the latter being what the customer usually requires. Figure 2.1 is a graphical representation of the three main aspects to be considered in the thermomechanical processing of steel products. As shown in this figure, TMP can be considered as a coupled system with different process operations which modify the microstructure and the mechanical properties of the steel alloy. The aim is to select an effective processing route in such a way that the final product reflects a good match when compared to the desired design, with an acceptable cost, performance, and feasibility.

The most important mechanical properties found in steel alloys are shown in Table 2.1; however, metal design involves more than meeting the minimum property requirements [9]. There are numerous options for product designs and metal selection that sometimes cannot be quantified. For instance, the design must be producible which means that a robust and safe process must be ensured. This precludes the use of mathematical optimisation routines that allow for specifying the criteria to equilibrate the quality of the product, costs, and process feasibility.

It is worth stressing the strong correlation between the metal properties, its microstructure, and processing. Evidently, the chemical composition and heat treatment also play a very important role in the final product [25]. As will be shown later, the performance of steels depends on the properties associated with their microstructures, that is, on the arrangements, volume fractions, sizes, and morphologies of the var-

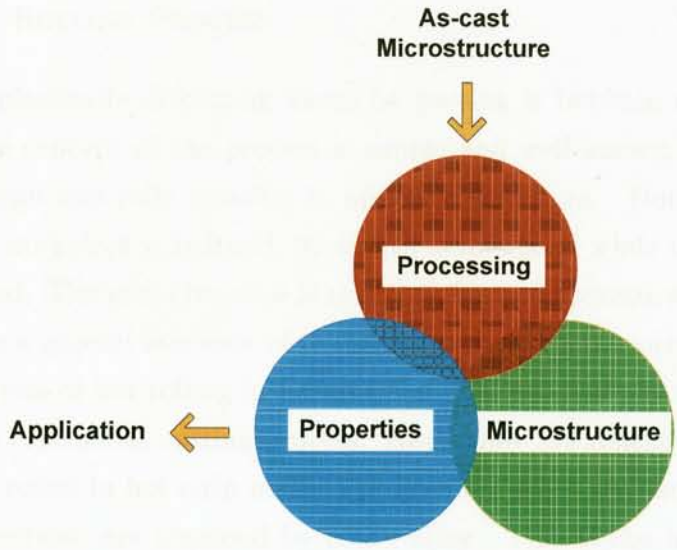


Figure 2.1: Relationships among the main stages of the thermomechanical processing and production of steel alloys

Table 2.1: Main mechanical properties of steel

| Mechanical Properties |
|---|
| **Strength**: Tensile Strength, Yield Strength, Compressive Strength |
| **Hardness** |
| **Toughness**: Notch Toughness, Fracture Toughness |
| **Ductility**: Total Elongation, Reduction in Area |
| **Fatigue resistance** |
| Other Properties or Characteristics |
| **Formability**: Drawability, Stretchability, Bendability |
| **Wear resistance**: Abrasion Resistance, Galling Resistance, Sliding Wear Resistance |
| **Machinability** |
| **Weldability** |

ious phases constituting a macroscopic section of steel with a given composition in a given processed condition. Each type of microstructure and product is developed to characterise the property ranges via specific processing routes that control and exploit microstructural changes. Thus, processing technologies not only depend on microstructure but are also used to tailor the final properties [44].

## 2.4 The Hot-Rolling Process

The process of plastically deforming metal by passing it between rolls is known as rolling [17]. The concept of the process is simple and well-known. Strips or plates are passed through two rolls rotating in opposite directions. During the pass the thickness of the workpiece is reduced, its length is increased while its width remains largely unchanged. The usual practice is to roll at high temperatures (800 - 1300°C). Figure 2.2 shows a general overview of the steel-making process including continuous casting and the role of hot-rolling in forming the final product. First, the billets are prepared by the continuous casting process. Next, they are reheated in the soaking pits and are hot-rolled in hot strip mills. The layers of scale are removed by pickling and further reductions are obtained by cold-rolling. This is the most widely used metalworking process because it lends itself to a high production and a close control of the final product.

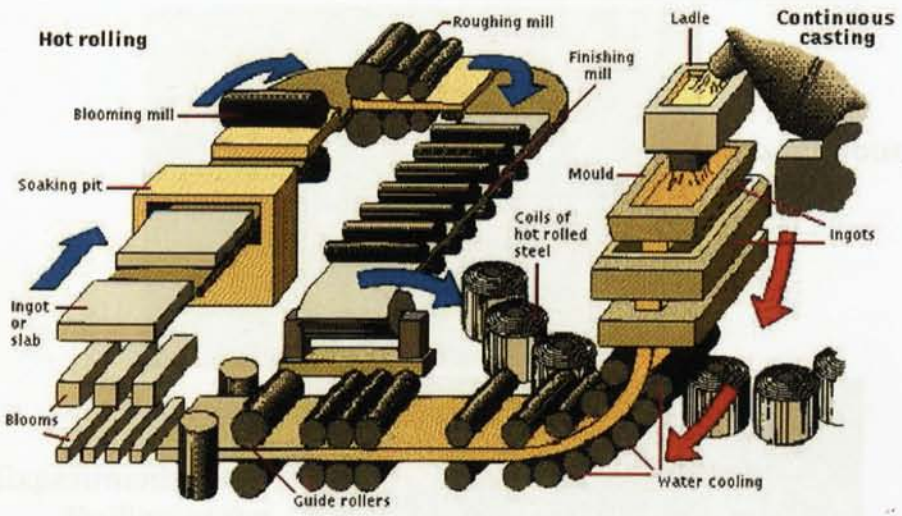


Figure 2.2: Hot-rolling of steel and continuous casting

A good perspective of industrial and experimental hot-rolling is shown in Figure 2.3. In deforming the metal between rolls, the workpiece is not only subjected to high compressive stresses from the squeezing action of the rolls, but also to surface shear stresses as a result of the friction between the rolls and the metal. The frictional forces are also responsible for drawing the metal into the rolls. Usually, the initial breakdown of ingots into blooms and billets is generally done by hot-rolling.

Industrial Hot-Rolling

Continuous Rolling

Experimental Hot-Rolling at the University of Sheffield

Figure 2.3: Industrial and experimental hot-rolling

Although primarily thought as a shaping process, hot-rolling has become more sophisticated because of the possibility of improving the mechanical properties of the final product by changing its microstructure. Thus, the hot-rolling process can be classified according to where the deformation occurs relative to the changes in the microstructure. Such a classification can be described as follows:

**Conventional hot-rolling:** during conventional hot-rolling, the rolling of steel is conducted continuously and is usually finished above the upper cooling transformation temperature. Therefore, the deformation occurs in the so-called austenite phase[1].

**Controlled rolling:** in controlled rolling, the rolling of steel is interrupted by one or two delays, which allows the steel to be deformed in the austenite phase in a wider range of temperatures, but always above the $A_3$ temperature, which marks the onset of the ferrite-austenite phase.

It is clear that knowledge of the microstructure evolution during rolling should be obtained with the objective of achieving the desired properties. Figure 2.4 represents the evolution of the microstructure as the metal is deformed. As shown in this figure, the granular structure changes in each pass going through different phases that eventually define the metal properties. The deformation profile applied per rolling pass is the determining aspect in the process optimisation, and from such a profile, the rolling schedule can be synthesised.

However, the setting-up of the rolling schedule is not an easy task due to the number of variables involved in it. Figure 2.5 schematically shows an example of the interactions of the process parameters to be considered when designing an adequate rolling schedule. As shown in this figure, the knowledge integration of all variables is a difficult challenge. For this reason, current methodologies tend to be *ad hoc*, and are usually ineffective for calculating optimal process parameters [84].

## 2.5 Configuration of an Experimental Laboratory-Scale Hot-Rolling Mill

This section briefly describes the configuration of a typical laboratory-scale hot-rolling mill. A mill for rolling of flat products includes one or a number of mill stands. A

[1]See Chapter 3 for a detailed description of the different phases of the steel microstructure.

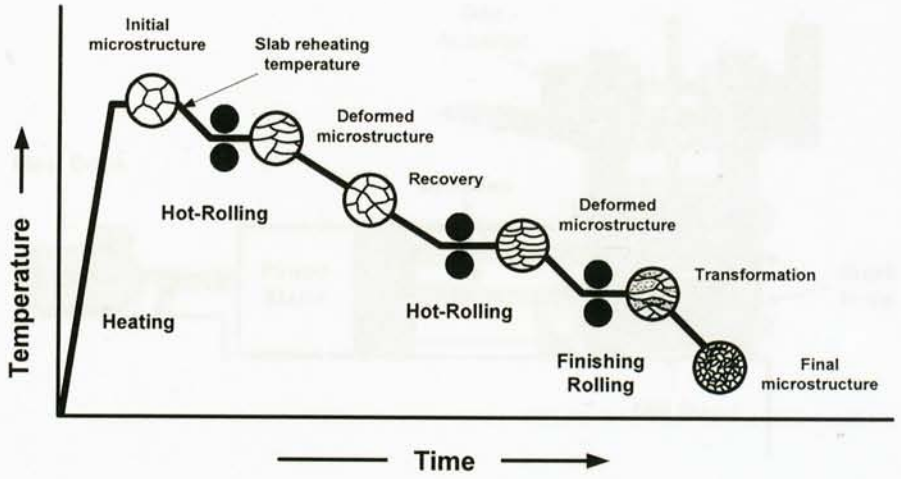


Figure 2.4: Evolution of the steel microstructure during a typical hot-rolling schedule

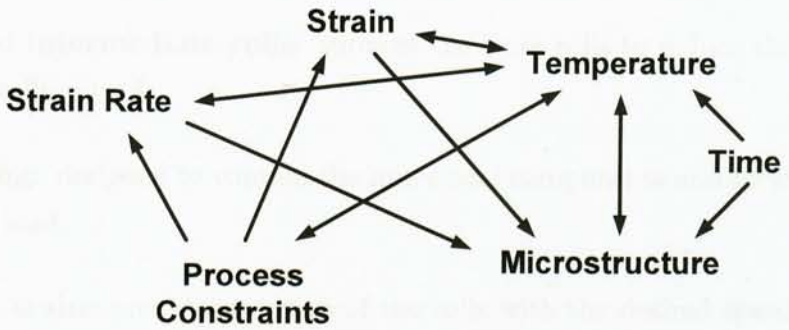


Figure 2.5: Interdependence of parameters during hot-rolling

stand consists basically of rolls, bearings, a housing for containing these parts, and a drive for applying power to the rolls and controlling their speed. Due to the forces involved in rolling, a very rigid construction is needed, and very large motors are required to provide the necessary power. The stands are usually arranged in line to produce a sequential reduction in thickness of the rolled product. Although a variety of the mill stand designs are known, it is possible to identify their common components from a functional viewpoint. Figure 2.6 illustrates schematically a laboratory-scale hot-rolling mill.

The main functional components of a hot-rolling mill are the following:

**Work Rolls:** work tools which directly contact the rolled product;

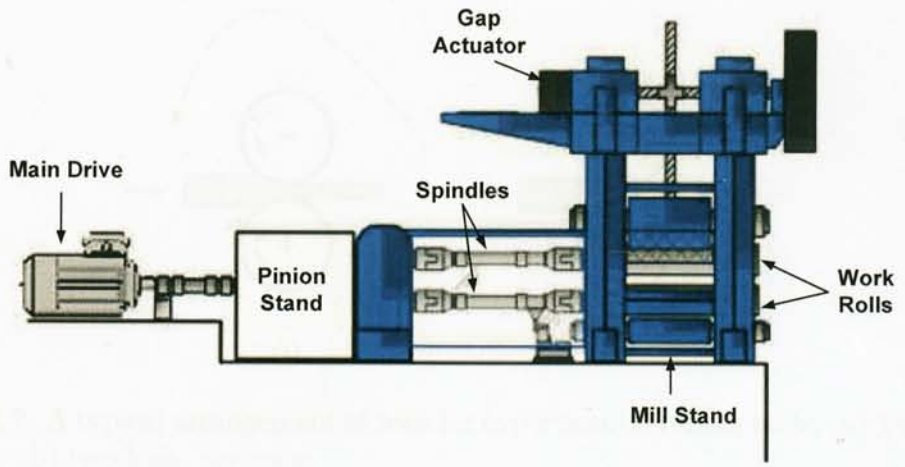


Figure 2.6: A schematic illustration of an experimental laboratory-scale rolling mill

**Backup and intermediate rolls:** support the work rolls to reduce their deflection under rolling load;

**Mill Housing:** designed to contain the mill stand components and to withstand the rolling load;

**Main drive train:** provides rotation of the rolls with the desired speed and rolling torque;

**Roll gap actuators:** provide the required gap between rolls;

**Pass line adjustment mechanism:** provides adjustment of elevation of the pass line;

**Strip profile and flatness actuators:** provide the displacement and/or deflection of the rolls to achieve the desired strip profile and flatness.

Rolling mills can be conveniently classified with respect to the number and arrangement of the rolls. The simplest and most common type of rolling mill is the two-high mill (Figure 2.7a). Rolls of equal size are rotated only in one direction. The stock is returned to the entrance, or rear, of the rolls for further reduction by hand carrying or by means of a platform which can be raised to pass the work above the rolls. An obvious improvement in speed results from the use of a two-high reversing

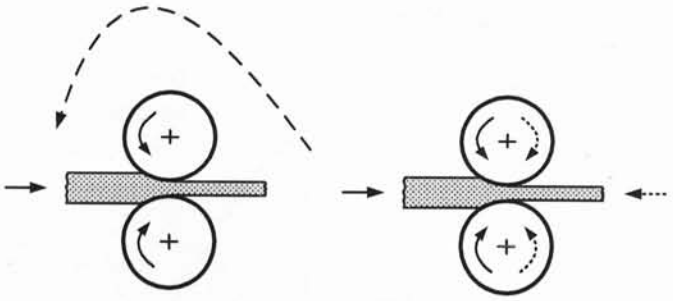

(a) (b)

Figure 2.7: A typical arrangement of rolls for experimental rolling mills; (a) Two-high, pullover; (b) two-high, reversing

mill, in which the stock can be passed back and forth through the rolls by reversing their direction of rotation (Figure 2.7b).

## 2.6 A Theoretical Description of Metal Rolling

The main purpose of the rolling theory is to determine the pressure distribution at the interfaces between the work roll and the rolled metal. Because hot-rolling is a process in which the workpiece is plastically deformed, before establishing the main concepts of the rolling theory, it is convenient at this point to look at some main element of the theory of plasticity. The theory of plasticity deals with the behaviour of metals at strains where Hooke's law is no longer valid because the shape and structure of the metals do not recover after deformation; in other words, plastic deformation by rolling is not a reversible process [17]. To describe the behaviour of a metal in terms of its elastic-plastic characteristics, the stress-strain curve is used, as shown in Figure 2.8.

The determination of the state of stress is necessary for the analysis of plastic deformation in metals. The state of the stress at a point may be determined by calculating the stresses acting on three mutually perpendicular oriented planes passing through the point. Consider the workpiece under a Plane-Strain Compression (PSC) test shown in Figure 2.9. The stress system at any point can be represented by three principal stresses which control the yielding behaviour of the metal and which give rise to the associated principal strains.

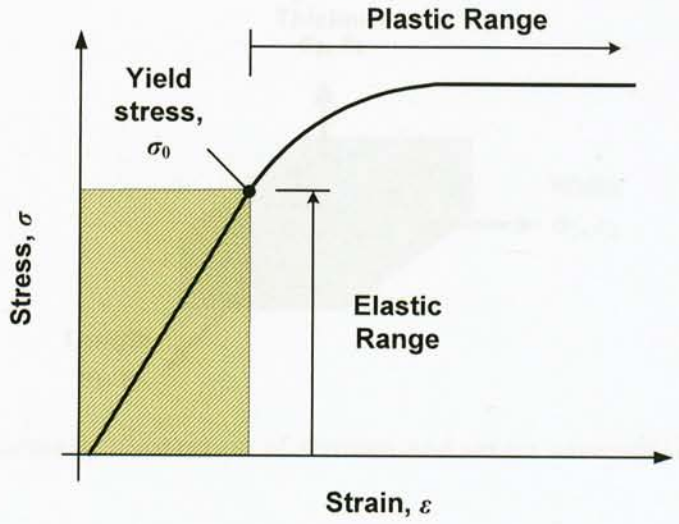


Figure 2.8: Typical elastic-plastic behaviour of metals

In the PSC test of Figure 2.9, $\sigma_3$ and $\varepsilon_3$ are the thickness stress and strain respectively, $\sigma_2$ and $\varepsilon_2$ are the width stress and strain respectively, $\sigma_1$ and $\varepsilon_1$ are the length stress and strain respectively. It is worth noting that in an ideal test (no spreading) $\varepsilon_2$ equals zero. Here the equivalent strain ($\bar{\varepsilon}$ ) is given by the following expression:

$$\bar{\varepsilon} = \frac{\sqrt{2}}{3}\left[(\varepsilon_1 - \varepsilon_2)^2 + (\varepsilon_2 - \varepsilon_3)^2 + (\varepsilon_3 - \varepsilon_1)^2\right]^{1/2}. \tag{2.1}$$

If the equivalent tensile strain in the workpiece deformation is calculated assuming ideal plane strain conditions, i.e. $\varepsilon_1 = -\varepsilon_3$ , and $\varepsilon_2 = 0$, then Equation (2.1) becomes:

$$\bar{\varepsilon} = \frac{\sqrt{2}}{3}\left[\varepsilon_3^2 + \varepsilon_3^2 + 4\varepsilon_3^2\right]^{1/2} = \frac{2}{\sqrt{3}}\varepsilon_3 = \frac{2}{\sqrt{3}}\ln\frac{h_0}{h_f}, \tag{2.2}$$

where $h_0$ and $h_f$ are the initial and final thickness of the workpiece respectively.

In hot-rolling, the flow stress is a function of both temperature and the rate of change of thickness or strain rate, which is related to the speed of the rolls. The mean strain rate ($\dot{\bar{\varepsilon}}$) for hot-rolling with sticking friction is given by the following equation:

$$\dot{\bar{\varepsilon}} = \frac{v_r}{\sqrt{R_r h_0}}\sqrt{r}\left(1 + \frac{r}{4}\right), \tag{2.3}$$

where $v_r$ is the peripheral speed of the rolls, $R_r$ is the roll radius, and $r$ represents the amount of reduction in thickness.

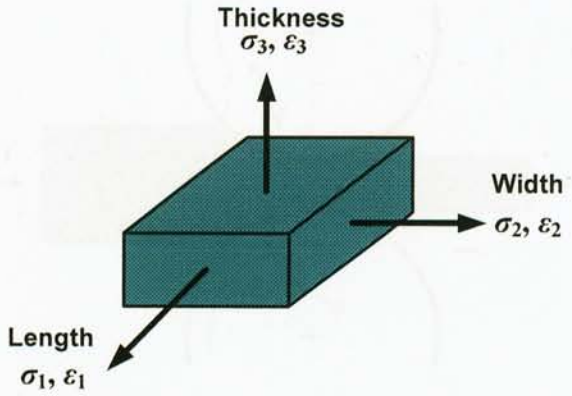


Figure 2.9: A schematic illustration of stresses and strain axes relative to PSC workpiece

**NOTE:** *From this point of the thesis onwards, unless otherwise specified, the equivalent strain will be referred to as strain, and the mean strain rate as strain rate. Also, the notations $\varepsilon$ and $\dot{\varepsilon}$ will refer to strain and strain rate respectively.*

As shown in Figure 2.10, when the work rolls are rotating with a peripheral speed $v_r$, at some point $N$ in the roll gap, the peripheral velocities of the rolls and the workpiece are equal. This point is known as the neutral point. To the left of this point, the surface velocity of the metal $v_1$ is lower than the roll peripheral velocity $v_r$, and this difference in speed produces a friction between the metal and the rolls which tend to draw the metal into the roll gap. To the right of $N$, the metal velocity $v_2$ is greater than the roll peripheral velocity $v_r$, so the friction tends to retain the metal in the roll gap. Because of this roll-metal velocity relationship, the pressure distribution at the interfaces between the work rolls and the roll metal will be uneven forming the so-called friction hill [25].

In Figure 2.10, $L$ is the roll contact length, $h_0$ and $h_f$ are the initial and final thickness respectively, and $\alpha$ is the roll bite angle. According to this figure, the following assumptions are made:

- The workpiece does not spread laterally;
- Roll flattening does not occur in the arc of contact;

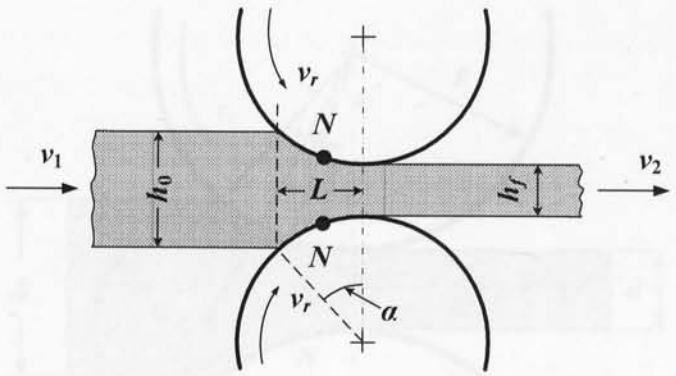


Figure 2.10: A schematic presentation of the deformation in hot-rolling

- The peripheral velocity of the rolls is constant;
- Compression rates from the point along the arc of contact does not have any effects on the magnitude of the compression strength; and
- The vertical component of the frictional force is negligible.

Figure 2.11 illustrates a number of important relationships between the geometry of the rolls and the forces involved in deforming a metal by rolling. At any point along the surface of contact, such as point $A$, two forces act on the metal. These are a radial force ($P$) and a tangential force ($F$). Between the entrance plane and the neutral point the metal is moving slower than the roll surface, and the frictional force acts in the direction shown in Figure 2.11 so as to draw the metal into the rolls. On the exit side of the neutral point the workpiece moves faster than the roll surface. The direction of the frictional force is then reversed so that it acts to oppose the delivery of the metal from the rolls.

The vertical component of $P$ is known as the *rolling load* or the *rolling force* because it is the force with which the rolls press against the metal and is also equal to the force exerted by the metal in trying to force the rolls apart. As mentioned before, the angle $\alpha$ between the entrance plane and the centreline of the rolls is called the angle of contact, or angle of bite. Referring to Figure 2.11, the horizontal component of the normal force is $P \sin \alpha$, and the horizontal component of the friction force is $F \cos \alpha$. For the workpiece to enter into the throat of the roll the horizontal component of the friction force, which acts toward the roll gap, must be equal to

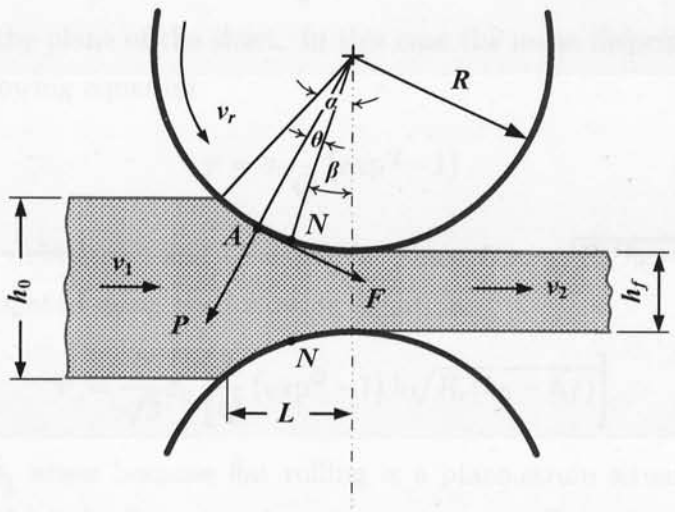


Figure 2.11: Acting forces during rolling

or greater than the horizontal component of the normal force, which acts away from the roll gap. The limiting condition for unaided entry of a slab into the rolls can be expressed mathematically via the following relationships:

$$\begin{cases} F\cos\alpha = P\sin\alpha \\ \frac{F}{P} = \frac{\sin\alpha}{\cos\alpha} = \tan\alpha \\ F = \mu P \\ \mu = \tan\alpha \end{cases} . \tag{2.4}$$

The workpiece cannot be drawn into the rolls if the tangent of the contact angle exceeds the coefficient of friction. If $\mu = 0$, rolling cannot occur, but as $\mu$ increases progressively larger slabs will be drawn in the roll throat. The high forces generated in rolling are transmitted to the workpiece through the rolls, under these loading conditions there are two major types of elastic distortion. First, the rolls tend to bend along their length because the workpiece tends to separate them while they are restrained at their ends. Second, the rolls flatten in the region where they contact the workpiece, so that the radius curvature is increased.

Over time, various metallurgists and researchers have proposed mathematical relationships to calculate the rolling force and torque developed by the workpiece [61],[72]. However, a simplified analysis proposed in [17] shows that the main parameters to calculate the rolling force are the roll diameter, the deformation resistance, the friction between the rolls and the workpiece, and the presence of front tension and/or

back tension in the plane of the sheet. In this case the mean deformation pressure is given by the following equation:

$$\bar{p} = \sigma_0 \frac{1}{Q} \left(\exp^Q - 1\right), \tag{2.5}$$

where $\sigma_0$ is the yield stress and $Q = \mu L/\bar{h}$. Since $L \approx \sqrt{R_r(h_0 - hf)}$, the rolling force can be calculated using the following equation:

$$P = \frac{2}{\sqrt{3}} \sigma_0 \left[\frac{1}{Q} \left(\exp^Q - 1\right) b\sqrt{R_r(h_0 - hf)}\right]. \tag{2.6}$$

The factor $\frac{2}{\sqrt{3}}$ arises because flat rolling is a plane-strain situation, so that the flow stress should be the flow stressing plane stress (see Equation (2.2)). Equation (2.6) shows that the rolling force and the length of contact are indirectly proportional to the roll diameter. Therefore, with small-diameter rolls, it is possible to produce a greater reduction before roll flattening becomes significant and no further reduction in thickness is possible. On the other hand, the rolling torque ($T_{LOAD}$) is equal to the total rolling force multiplied by the effective moment arm, and since there are two work rolls, the torque is given by the following equation:

$$T_{LOAD} = 2Pa_m, \tag{2.7}$$

where $a_m = m\sqrt{R(h_0 - h_f)}$ is the moment arm, $m$ being the moment arm coefficient.

The rolling force and torque prediction plays a critical role in modern rolling schedule control and optimisation. It is known that, for a given steel grade, the rolling force and torque can be determined by the stock temperature, mill reduction, rolling speed, friction, heat transfer, etc. They affect the mill schedule, the thickness of the rolled product, and the final product profile. Modern roll gap set-up and profile control demand accurate predictions of the rolling force and torque under various rolling conditions.

As shown above, there exist several methods which allow to predict rolling forces and torques, most of them being based on traditional models such as Equations (2.6) and (2.7). Nevertheless, the use of the Finite Element (FE) technique to predict the rolling forces and the torques has proved popular, and many commercial FE software packages have now become available [59],[10]. Also, Neural Networks (NN) have also become a popular modelling tool, thanks to their powerful modelling and flexible self-learning capability. The use of NN for intelligent data analysis has been

attracting a wider audience. Indeed, the main applications of NN in the steel-making industry includes the estimation of some adaptive parameters of a physically-based or empirical model with the help of available experimental data (see the work described in [50],[73]).

## 2.7 Concluding Remarks

The basic concepts of hot-rolling and its important role within the thermomechanical processing of steel alloys were introduced in this chapter. The understanding of such concepts, along with the phenomena taking place during hot-rolling, allows one to approach the problem by establishing a general view about the real hot-rolling conditions in the Hille-mill. This information is useful when developing optimisation strategies to make the process faster and safer, as well as being able to produce better rolled products.

It is clear that the mechanical properties of the alloy being design are directly related to the metal microstructure and its processing; therefore, special attention to establish the mathematical models that describe such relationships should be considered when establishing criteria for the mill scheduling. The next chapter will introduce some of the models used to describe the evolution of the steel microstructure during hot-rolling, and how such microstructural changes affect the final mechanical properties of a steel alloy.

# Chapter 3

# Microstructure Evolution during Hot-Rolling

## 3.1 Introduction

This chapter introduces the physically-based models associated with the C-Mn steel alloy, with a special focus on the role of grain size in the characterisation of the microstructure and the final properties. Such models should provide an understanding of the microstructure evolution during the rolling process, and provide an insight on how to exploit or reconfigure the thermomechanical processing of steels. They also provide an invaluable feedback in terms of a quantified guidance to design new methods of control and optimisation. A brief description of the main concepts is given, along with some theoretical bases relating to the steel microstructure and its composition, as well as the evolution of the microstructure through the various stages of the processing. The content of this chapter is of particular importance because the physically-based model of the stock is the base of the experiment design and the optimisation mechanism proposed in this research work.

## 3.2 The Steel Microstructures and Phases

The performance of steels depends on the properties associated with their microstructures, that is, on the arrangements, volume fractions, sizes, and morphologies of the various phases constituting a macroscopic section of steel with a given composition in a given processed condition. Steel microstructures are made up of various crystals, sometimes as many as three or four different types, which are physically blended by solidification, phase changes, hot-deformation, and heat treatment. Each type of

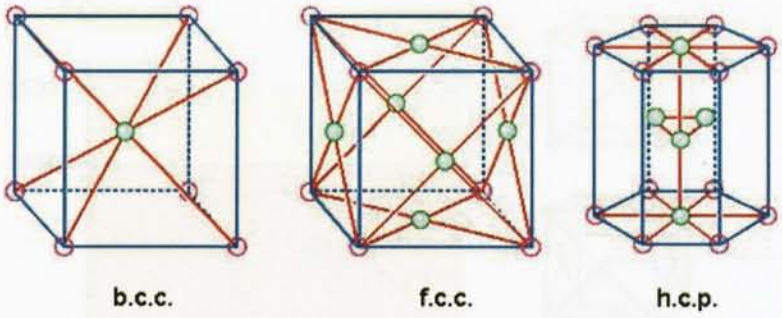


Figure 3.1: Principal types of crystal lattices

microstructure and product is developed to characteristic-property ranges by specific processing routes that control and exploit microstructural changes. Thus, processing technologies not only depend on microstructure but are also used to tailor the final properties [43].

The crystallisation of metals occurs during solidification, when the atoms of a liquid metal assemble themselves in an orderly arrangement and form a definite space pattern known as a space lattice. There are several types of lattices in which metallic atoms can arrange themselves upon solidification. The three most common crystal lattices are shown in Figure 3.1, and are known as:

- Body-centred cubic (b.c.c.);
- Face-centred cubic (f.c.c.); and
- Hexagonal closed-packed (h.c.p.).

A b.c.c. structure has an atom at each corner of an imaginary cube and an atom in the centre of this cube and generally produces strong metals which are reasonably ductile. An f.c.c. structure has an atom at each corner of a cube and an atom at the centre of each face of the cube. Metals with f.c.c. structures tend to be soft and ductile over a wide range of temperatures. Hexagonally closed-packed (h.c.p.) structures have an atom at the corners of an imaginary hexagonal prism and an atom at the centre of each hexagonal face and three atoms in the centre forming a prism. These metals are relatively brittle. When a metal undergoes a transformation from one crystal pattern to another, it is known as an allotropic change. The allotropic forms of iron, which is

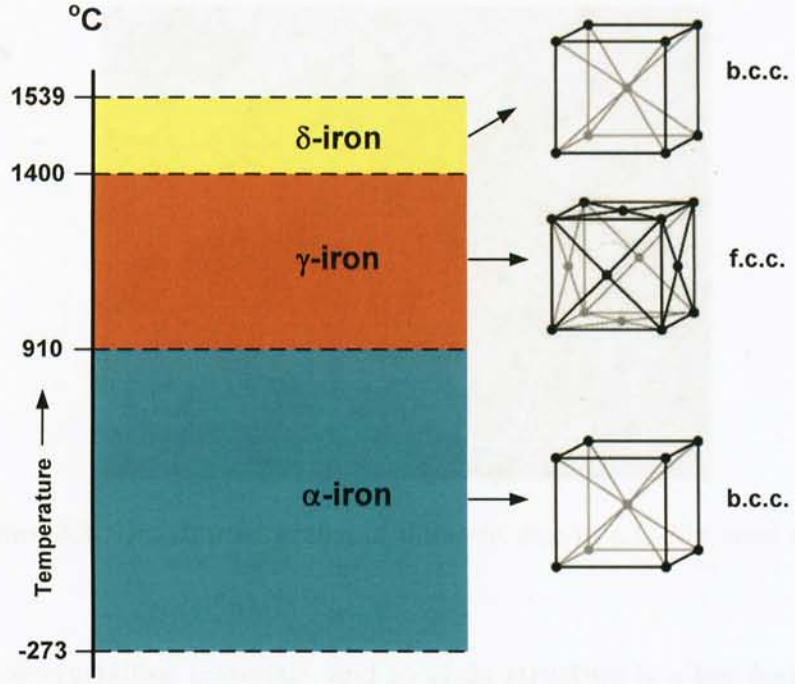


Figure 3.2: Allotropic changes of iron

the main component of steels, are temperature dependent as illustrated in Figure 3.2. When there is an allotropic change from a b.c.c. to an f.c.c. lattice, it is accompanied by a marked quantitative change in the characteristics and properties of the metal involved; therefore, the term microstructure in this context is used to describe a set of characteristic elements that can be identified in the arrangement of these crystals [49].

As shown in Figure 3.2, pure iron can exist in three separate crystalline forms which are designated by letters of the Greek alphabet: 'alpha' ($\alpha$), 'gamma' ($\gamma$), and 'delta' ($\delta$). $\alpha$-iron, which has a b.c.c. structure and exists at normal temperatures, changes to $\gamma$-iron, which is a f.c.c. structure, when heated to 910°C. At 1400°C the f.c.c. structure reverts to b.c.c., that is $\delta$-iron. The essential difference between $\alpha$-iron and $\delta$-iron, therefore, is only in the temperature range over which each exists [30].

Due to the crystalline structure of steel, it is clear that the objective of the metallurgical process is to manipulate the size, shape, and distribution of the crystalline grains and second-phase particles to create alloys with specific desired characteristics. Sometimes, even the orientations of the grains are controlled to provide texture. Most

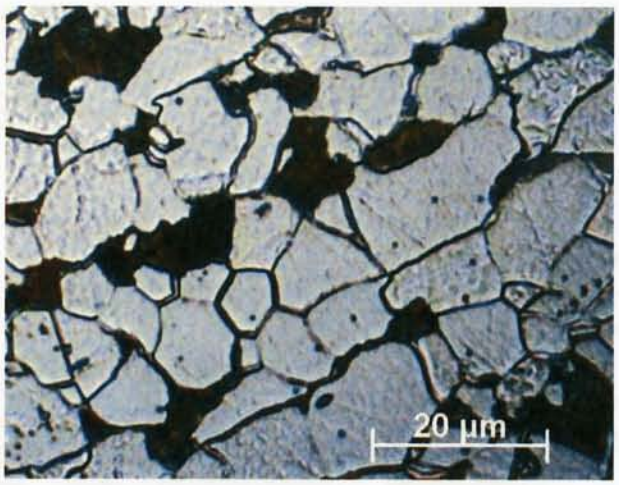


Figure 3.3: Distributed grains of different size in a C-Mn steel alloy

alloys are polycrystalline materials, and so grain structure is a key feature that can be examined and evaluated by metallographic analyses [2]. In metallurgy a grain is any of the small distributed crystals of varying sizes that compose a solid metal. The grains enter into contact with each other at surfaces called grain boundaries.

Figure 3.3 shows an example of the arrangements of grains and their boundaries of a C-Mn steel alloy. The structure and size of the grains determine the important physical properties of the solid metal. Fine grains and finely divided phase sections are typically the preferred microstructure (at least for good strength and ductility in room temperature structural applications), because the grain boundaries are stronger than individual grains in a properly processed metal [34]. The grain boundaries represent disruptions between the crystal lattice of individual grains, and such disruptions can provide a source of strengthening (at low creep temperatures) by pinning the movement of dislocations. Thus, a finer-grained alloy imparts more grain-boundary regions for improved strength [64],[2].

The size, distribution, and growth of grains and second-phase particles are affected by many factors which result in a particular microstructure. Due to the fact that steel is heat-treated to produce a great variety of microstructures and properties, desired results can be accomplished by heating within temperature ranges where a phase or a combination of phases are stable and also by producing changes in the microstructure (grain growth), and/or heating or cooling between temperature ranges in which

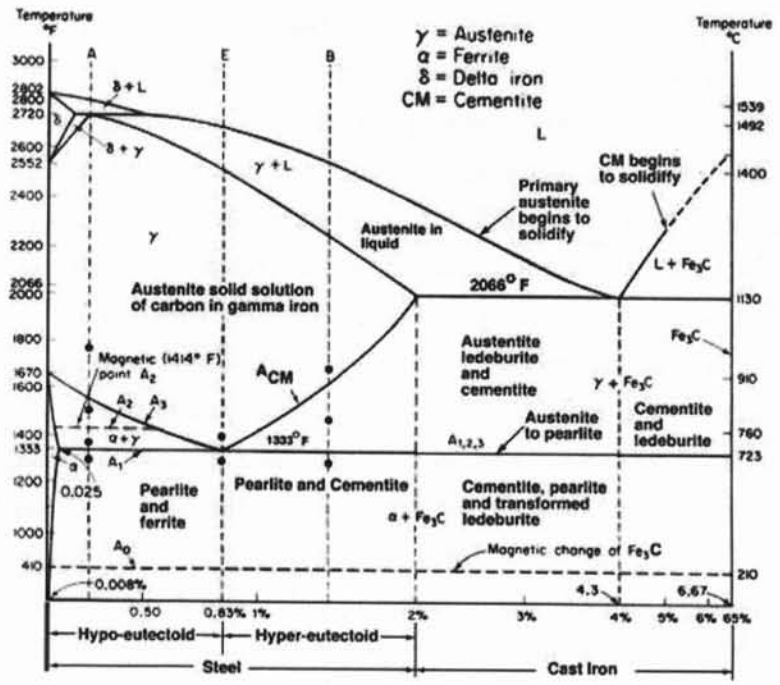


Figure 3.4: Iron-Carbon (Fe-C) phase diagram [34]

temperature phases are stable [43]. The changes in such phases and the resulting microstructures are described by a phase diagram which is a graphical representation of the temperature, pressure, and composition limits of the phase fields in an alloy system as they exist under conditions of complete equilibrium [25]. Figure 3.4 shows the iron-carbon (Fe-C) phase diagram, which defines the temperature-composition regions where the various phases in steel are stable, as well as the equilibrium boundaries between phase fields; temperature is plotted vertically while the composition (percentage of carbon content) is plotted horizontally. The upper curve on the phase diagram represents the liquidus temperature, above which the alloy is in the liquid phase. The liquid begins to solidify when the temperature cools to the liquidus temperature. On solidification, the amorphous liquid phase changes into a crystalline solid, and grains nucleate and grow. The solid phase just formed is called austenite ($\gamma$-phase). On further cooling to the $A_3$ temperature, the first ferrite ($\alpha$-phase) grains appear and the steel reaches the two-phase region. As the temperature drops again, the transformation stops and the steel becomes fully ferritic. This temperature is identified as the $A_1$. Depending on the carbon content and cooling rates, other

phases such as pearlite or bainite may appear as well [43],[52].

Another interesting feature of the Fe-C phase diagram is that it shows the influence of the carbon content on the different phases. Steels are alloys of iron, carbon, and other elements that contain less than 2% carbon - most frequently 1% or less. Therefore, the portion of the diagram below the 2% carbon is of primary interest for steel designs. On the other hand, alloys containing more than 2% carbon are classified as cast irons. The addition of carbon to iron produces several important changes in the phases and phase equilibrium of the alloy. Differences in the ability of ferrite and austenite to accommodate carbon result not only in important characteristics of the Fe-C diagram but also in the formation of $Fe_3C$. The crystal structures of the b.c.c. ferrite and f.c.c. austenite are modified by introducing carbon atoms into the interstices or interstitial sites between iron atoms.

Carbon is as well an element that stabilises austenite and thereby increases the range of austenite formation. Figure 3.4 also shows that, with the addition of carbon, the austenite field greatly expands from 912 to 1394°C - the range in pure iron - to a wide range of temperatures and compositions. The maximum solubility of carbon in austenite reaches 2.11% at 1130°C. Ferrite has a much lower ability to dissolve carbon than that of austenite: the solubility decreases continuously from a maximum of only 0.02% at 723°C. When the solubility limit for carbon in austenite is exceeded, a new phase - iron carbide or cementite - forms in iron-carbon alloys and steels. Cementite assumes many shapes, arrangements, and sizes that together with ferrite contribute to the great variety of microstructures found in steels [43].

Apart from iron and carbon, steels contain various alloying elements that are added to obtain specific properties. Such alloying elements and impurities are incorporated into austenite, ferrite, and cementite. Depending on their effect on the formation and stabilisation of phases in steel, the alloying elements are usually considered as the following [25]:

**Austenite formers:** Carbon (C), Cobalt (Co), Copper (Cu), Manganese (Mn), Nickel (Ni), and Nitrogen (Ni);

**Ferrite formers:** Aluminium (Al), Chromium (Cr), Niobium (Nb), Molybdenum (Mo), Phosphorus (P), Silicon (Si), Titanium (Ti), Tin (Sn), Tungsten (W), and Vanadium (V);

**Carbide formers:** Elements such as chromium, tungsten, vanadium, molybdenum, titanium, and niobium form very stable carbides. Other elements, such as manganese, are not strong carbide formers; however, they do contribute to the stability of the other carbides that are present.

Since the primary objective of this work is to design optimal rolling schedules, the knowledge and understanding of critical temperatures are essential, as these affect the hardening and softening processes that take place during and after rolling. These processes include precipitation, hardening, recrystallisation, and recovery, each of which may be static or dynamic, depending on whether loads are applied, and whether work hardening results from deformation below the recrystallisation stop temperature. The study of these processes leads to complex equations describing the overall microstructure evolution of the rolled product. The next section will describe this study.

## 3.3 Microstructural Changes of Steel during Hot-Rolling

The basis for the current understanding of the physical metallurgy of hot-working was developed in the 1960's and is still continuing. Models of various complexities and performance levels have been developed with the aim of achieving the accurate prediction of the metal flow stress and temperature fields. These models have demonstrated the high degree of sensitivity of microstructure to the operating conditions. The determining variables are normally characterised by the temperature ($T$), the strain ($\varepsilon$), and the strain rate ($\dot{\varepsilon}$), with flow stress ($\sigma$) being the measurable response of the microstructure to these conditions [7]. In this regard, the correlation between the parameters of hot-deformation and the development of the resulting microstructure has been extensively investigated and a number of papers have been published in the literature. Among them, the works presented in [69], [66], [32], and [85] should be mentioned. In these, various closed form of equations are presented, describing the processes of recrystallisation and grain growth. The focus of this section is to review particularly the equations proposed by Sellars in [68] for the prediction of the microstructure evolution for C-Mn steels.

Figure 3.5 shows that, prior to the start of hot-rolling, the steel microstructure consists of coarse grains of austenite type. When passed through the rolls, the austenite grains are flattened and elongated on average, while each austenite grain undergoes

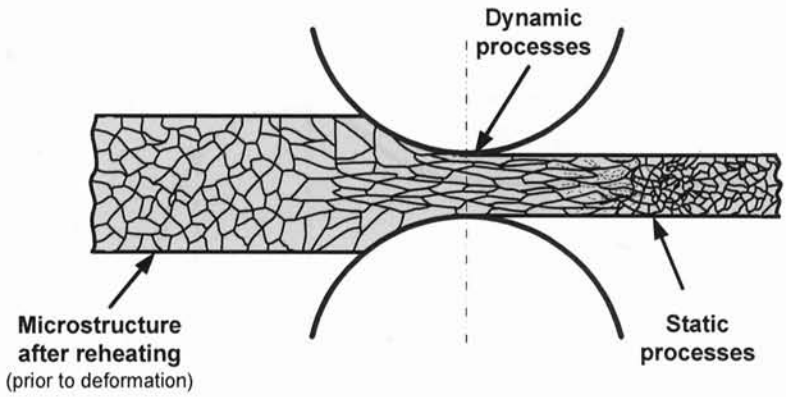


Figure 3.5: Microstructural changes during hot-rolling

a dimensional change that corresponds to that of the workpiece as a whole. The following three types of restoration processes are associated with hot-rolling:

1. **Dynamic restoration processes** which start and are complete during deformation;

2. **Metadynamic restoration processes** which start during deformation and are complete after deformation; and

3. **Static restoration processes** which start and are complete after deformation.

When steel is deformed in the austenitic state at high temperatures, the flow stress rises due to work hardening because the metal accumulates dislocations during the deformation, making further deformation more difficult. After an initial rapid work hardening, the stress goes through a maximum associated with the occurrence of dynamic recrystallisation. Figure 3.6 shows the dynamic characteristics represented by the stress-strain curve. The appearance of initially unworked crystals produces a drop in the stress-strain curve, but it soon levels off as repeated cycles of work hardening and dynamic recrystallisation become established.

The level of the stress-strain curve is sensitive to both strain rate and temperature because dynamic recovery is a thermally-activated process and hence it leads to a more effective softening at low strains and/or high temperatures. The effects of the strain rate and the temperature on the stress and the microstructure can be

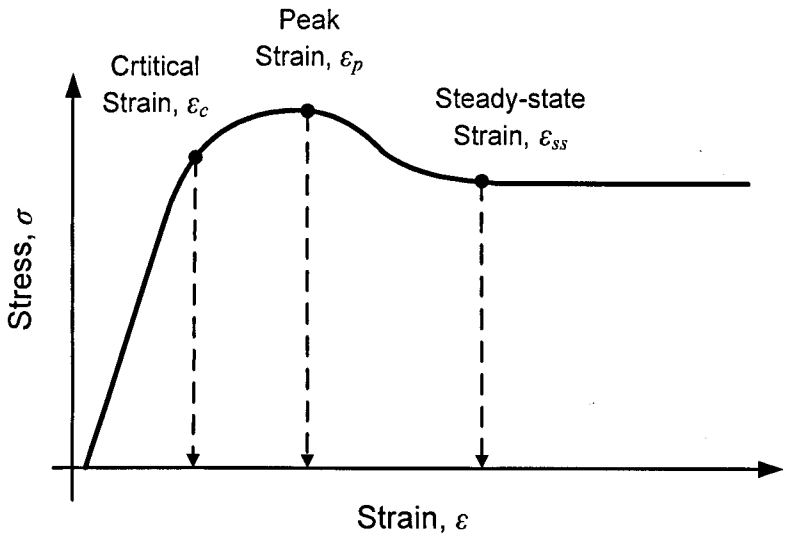


Figure 3.6: Stress-strain curve of the C-Mn steel alloy

conveniently combined in terms of the Zener-Hollomon parameter ($Z$) by using the following relationship:

$$Z = \dot{\varepsilon} \exp\left(\frac{Q_{def}}{RT}\right), \tag{3.1}$$

where $Q_{def}$ is the activation energy for deformation ($312\times10^3$ J/mol for C-Mn steel alloys), $R$ is the gas constant (8.31 J/Kmol), and $T$ is the absolute deformation temperature.

The stress-strain behaviour of the C-Mn steel alloy shown in Figure 3.6 can be represented by the following system of equations [7]:

$$\begin{cases} \sigma = \sigma' = 1.155\left\{\sigma_0 + (\sigma_e - \sigma_0)\left[1 - \exp\left(-C'\varepsilon\right)\right]^{0.5}\right\} & (\varepsilon < 0.7\varepsilon_p) \\ \sigma = \sigma' - 1.155\left(\sigma_e - \sigma_{ss}\right)\left\{1 - \exp\left[-0.49\left(\frac{\varepsilon - 0.7\varepsilon_p}{\varepsilon_p}\right)^{1.4}\right]\right\} & (\varepsilon \geq 0.7\varepsilon_p) \end{cases}, \tag{3.2}$$

where

$$\begin{cases} \sigma_0 = 103.84 \sinh^{-1}\left[\left(\frac{Z}{4.92\times10^{13}}\right)^{0.13}\right] \\ \sigma_e = 103.41 \sinh^{-1}\left[\left(\frac{Z}{1.77\times10^{11}}\right)^{0.217}\right] \\ \sigma_{ss} = 106.72 \sinh^{-1}\left[\left(\frac{Z}{3.88\times10^{12}}\right)^{0.146}\right] \end{cases}. \tag{3.3}$$

In the above formulations, $\sigma$ represents the flow stress in N/mm$^2$ at strain $\varepsilon$, $\sigma_0$ is the stress at a plastic strain of zero, $\sigma_e$ and $\sigma_{ss}$ are the steady-state flow stress and

actual steady-state flow stress respectively achieved at larger strains; $C'$ is a variable dependant on the deformation conditions, and $\varepsilon_p$ is the strain for the peak in the flow stress which can be calculated by the following equation:

$$\varepsilon_p = 4.9 \times 10^{-4} d_0^{0.5} Z^{0.15}, \tag{3.4}$$

where $d_0$ is the grain size in micrometers ($\mu m$) prior to deformation. The role of dynamic recrystallisation of austenite in the actual rolling of C-Mn steels is small, due to the fact that the critical strain required for achieving the steady-state of the flow stress is very large even at high temperatures. The grain refinement of these steels is usually achieved by static recrystallisation.

### *3.3.1 The Dynamic Restoration Process*

Dynamic microstructural changes take place during deformation, but for thermomechanical processing the most important phenomena are work hardening, dynamic recovery, and dynamic recrystallisation [7]. Dynamic recovery is a reduction of the work hardening effects without the motion of large grain boundaries and occurs in a range of strain that is less than that for the peak stress. It involves the rearrangement of dislocations, but it has only an indirect influence on modelling the microstructure evolution by controlling the onset of dynamic recrystallisation.

Dynamic recrystallisation takes place in the range of strain that corresponds to the steady-state of flow stress. When modelling thermomechanical processing, it is assumed that, when the dislocation density reaches its critical value, dynamic recrystallisation starts and becomes the dominant softening phenomenon. This critical value of the density corresponds to the critical strain ($\varepsilon_c$), which is a function of the strain rate, the temperature, and the austenite grain size prior to deformation, and can be expressed as follows:

$$\varepsilon_c = 3.92 \times 10^{-4} d_0^{0.5} Z^{0.15}. \tag{3.5}$$

### *3.3.2 The Static Restoration Process*

Microstructures developed by dynamic restoration are not stable and, at elevated temperatures, are modified by the metadynamic and static restoration processes. The latter processes can include static recovery, static recrystallisation, and metadynamic recrystallisation. In hot-rolling, static recrystallisation can start spontaneously. The

nuclei of recrystallisation occurs preferentially at the elongated grain boundaries and the interfaces of the deformation bands. Softening by static recrystallisation occurs at rates that depend on prior deformation conditions and holding temperatures. In C-Mn steels, the recystallisation curves generally follow an Avrami equation of the following form:

$$\begin{cases} X = 1 - \exp\left[-0.639\left(\frac{t}{t_{50}}\right)^2\right] & (\varepsilon < \varepsilon_c) \\ X = 1 - \exp\left[-0.639\left(\frac{t}{t_{50}}\right)\right] & (\varepsilon \geq \varepsilon_c) \end{cases}, \tag{3.6}$$

where $X$ is the volume fraction recrystallised after time $t$, whereas $t_{50}$ is the time in seconds for half fraction recrystallised, and changes by orders of magnitude over the range of conditions encountered during rolling. The recrystallisation rate and size of the recrystallised grains are controlled by three major factors: the austenite grain size prior to deformation, the temperature of recrystallisation, and the amount of deformation prior to any recrystallisation [71].

Since the nucleation sites for recrystallisation are located predominantly at the grain boundaries, both recrystallisation time and recrystallised grain size are affected by the initial grain size. In [68], it was found that 50% of the recrystallisation time for C-Mn steels depends on the strain and can be described by the following system of equations:

$$\begin{cases} t_{50} = 2.5 \times 10^{-19} d_0^2 \varepsilon^{-4} \exp\left(\frac{300\times10^3}{RT}\right) & (\varepsilon < \varepsilon_c) \\ t_{50} = 1.06 \times 10^{-5} Z^{-6} \exp\left(\frac{300\times10^3}{RT}\right) & (\varepsilon \geq \varepsilon_c) \end{cases}, \tag{3.7}$$

where $Z$ is the Zener-Hollomon parameter, $R$ is the gas constant, and $T$ is the recrystallisation temperature. The conditional range implies that dynamic recrystallisation had not occurred in the previous deformation [7]. The grain size produced by complete recrystallisation without previous dynamic recrystallisation ($d_{rex}$) is described by the following system of equations:

$$\begin{cases} d_{rex} = 0.5 d_0^{0.67} \varepsilon^{-1.0} & (\varepsilon < \varepsilon^*) \\ d_{rex} = 1.8 \times 10^3 Z^{-0.15} & (\varepsilon \geq \varepsilon^*) \end{cases}, \tag{3.8}$$

where $\varepsilon^* = 2.8 \times 10^{-4} d_0^{0.67} Z^{0.15}$. As recrystallisation takes place, the original, unrecrystallised grains are consumed by new grains. The resulting mean grain size is given by the following equation:

$$\bar{d} = X^{4/3} d_{rex} + (1 - X)^2 d_0. \tag{3.9}$$

It is worth noting that depending on the amount of deformation, the static restoration process can proceed in the following three forms:

1. **Recovery** occurs when the metal is rolled with a reduction that is less than the critical value for partial recrystallisation. In this case, grain coalescence instead of grain refinement occurs due to the strain-induced grain boundary migration, and produces much larger grains than the initial ones;

2. **Partial recrystallisation** occurs when the rolling reduction is sufficient to initiate partial recrystallisation, therefore a mixed microstructure of recrystallised grains and recovery grains is produced; and

3. **Complete recrystallisation** occurs when a uniformly distributed recrystallised microstructure is produced.

When recrystallisation is complete, further grain growth may take place even in the relatively short time available between passes. The time dependence of grain growth ($d_{gg}$) may be represented by the following equation:

$$d_{gg}^{10} = d_{rex}^{10} + 1.19 \times 10^{39} t \exp\left(\frac{-567 \times 10^3}{RT}\right). \tag{3.10}$$

In the case of calculations of microstructure for further rolling passes being needed, the final microstructure provided by the above models can be used as the initial microstructure for the next pass.

Figure 3.7 illustrates the evolution of microstructural parameters between passes. In this figure, $d_{01}$ represents the initial austenite grain given by either reheating or a previous rolling pass. As mentioned earlier, during and after deformation, several dynamic and static microstructural changes take place which are functions of the temperature ($T$), and the deformation profile of the pass, i.e. the strain ($\varepsilon$) and the strain rate ($\dot{\varepsilon}$). The amount of deformation applied to the stock affects the static restoration process occurring during the inter-pass time, whether it is recovery, partial recrystallisation, or complete recrystallisation ($X = 1$). When recrystallisation is complete, the recystallised grain size ($d_{rex}$) grows at a rate depending on the temperature and the holding-time prior to the next rolling pass. The final grain size ($d_{02}$) is taken as the initial microstructure for the next rolling pass.

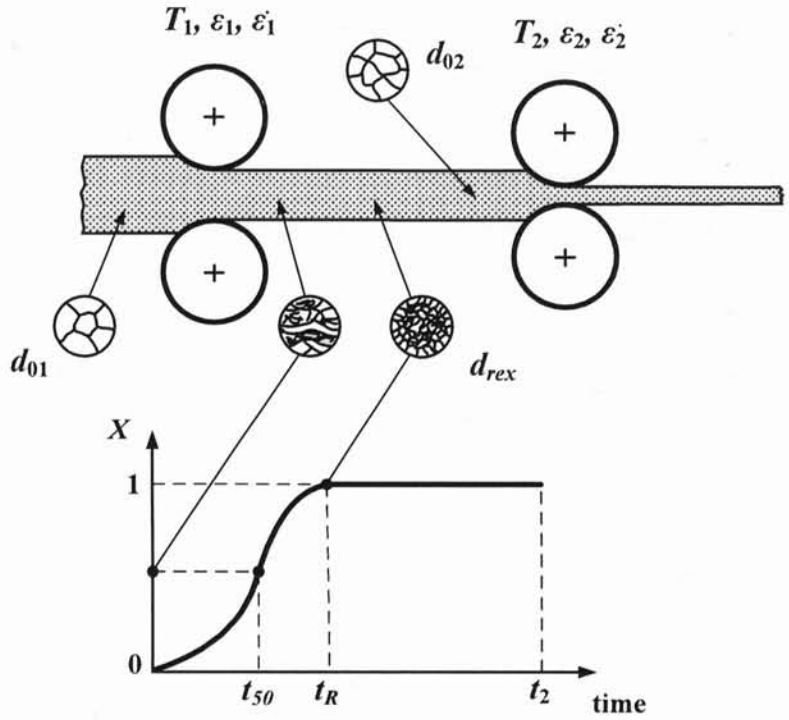


Figure 3.7: Evolution of microstructural parameters between passes

## 3.4 Mechanical Properties of Steel at Room Temperature

The objective of modern steel-making industry is to produce high strength products. Modelling the correlation between the thermomechanical history and the mechanical properties of the final product, especially after experimental substantiation of the predictions, is very useful during the development process. Although modelling thermomechanical processing in hot-rolling is reasonably advanced, progress in the prediction of transformed microstructures, and the resulting mechanical properties, taking into account the transformation, is still limited [52]. The next sections will show some of the models published in recent literature which are used to describe the phase transformation process and the mechanical properties at room temperature.

### *3.4.1 Structural Changes during Cooling*

As steel continues to cool after hot-rolling, its microstructure transforms from austenite to lower temperature phases. In the predominantly ferritic microstructures, the transformation to ferrite and pearlite takes place. Here **the main parameter of**

**interest is the ferrite grain size**, since it is considered to be the underlying factor when defining mechanical properties such as the yield strength and the ultimate tensile strength.

The factors that mainly affect the ferrite grain size are the final austenite grain size and the retained strain, both of which relate to the deformation history, the composition and the cooling rate, which are external influences. The final austenite grain size is the last fully recrystallised grain size, increased by grain growth between the last pass and the beginning of the transformation. The transformation from austenite to ferrite can be expressed by the following formula [64]:

$$d_\alpha = \left\{ a + b\left(\frac{dT}{dt}\right)^{-0.5} + c\left[1 - \exp\left(-0.015 d_\gamma\right)\right] \right\} \left(1 - 0.45\sqrt{\varepsilon}\right), \tag{3.11}$$

where $d_\alpha$ and $d_\gamma$ are the grain size in the ferrite and austenite phase respectively, $dT/dt$ is the cooling rate during the phase transformation, $\varepsilon$ is the accumulated strain in the austenite; furthermore $a$, $b$, and $c$ are metal constants for the C-Mn steel alloy calculated as follows:

$$\begin{cases} a = -0.4 + 6.4\ \mathrm{C}_{eq} \\ b = 24.2 - 59\ \mathrm{C}_{eq} \\ c = 22 \end{cases}, \tag{3.12}$$

where $\mathrm{C}_{eq} = \mathrm{C} + \mathrm{Mn}/6$, and represents the equivalent carbon content. Although the model of Equation (3.11) was determined on the basis of very few data, it has proven to be robust and forms the basis of many such models that have since been developed.

### *3.4.2 Yield Strength*

The mechanical properties of a steel alloy are usually associated with the Yield Strength (YS), indicating the beginning of plastic deformation or the end of pure elastic behaviour of the loaded metal. The yield strength and the lower yield stress definitions are taken to be identical [52].

The effects of the various microstructural and composition parameters on the mechanical properties of steels with ferrite-pearlite microstructures have been statistically analysed by multiple linear regression analysis [64],[35]. **The resulting empirical equations are limited to steels with less than 0.25% carbon and therefore to microstructures that are largely ferritic.** The model used in [32]

for the prediction of YS can be expressed by the following formula:

$$\text{YS} = K + 26\ \text{Mn} + 60\ \text{Si} + 759\ \text{P} + 3286\ \text{N} + 19.7\ d^{-1/2}, \tag{3.13}$$

where $K$ is 88 MPa for air-cooled steel and 62 MPa for furnace-cooled steel [26],[43]; N is the free nitrogen dissolved in the ferrite lattice and $d$ is the mean linear intercept ferrite grain size in millimeters. The beneficial effect of the ferrite grain size on YS is apparent from the above equation. The effect of both manganese and silicon is to increase YS by the solid solution strengthening of the ferrite.

### *3.4.3 Ultimate Tensile Strength*

The ultimate Tensile Strength (TS) is the maximum resistance to fracture. It is equivalent to the maximum load that can be carried by one square inch of cross-sectional area when the load is applied as a simple tension. In a stress-strain curve, TS appears as the stress coordinate value of the highest point on the curve. The model used in [32] for the prediction of TS is expressed by the following formula:

$$\begin{aligned}\text{TS} = \ & 165 + 54\ \text{Mn} + 100\ \text{Si} + 652\ \text{P} + 476\ \text{Ni} + \\ & 635\ \text{C} + 3339\ \text{N} + 11\ d^{-1/2}.\end{aligned} \tag{3.14}$$

The above equation has been used for plate, rod, bar, and structural mills for low carbon steels and some microalloyed grades. It is worth noting that such relationships seem to be adequately explained by a linear function of their arguments. Additionally, the linear nature of the mechanical properties as a function of the ferrite grain size is very well understood by the Hall-Petch relationship where the yield stress may be related linearly to the reciprocal of the square root of the grain size, [26]. The Hall-Petch relationship describes the effect of the ferrite grain size in the yield stress ($\sigma_y$) as follows:

$$\sigma_y = \sigma_0 + k_y d^{-1/2}, \tag{3.15}$$

where $\sigma_0$ and $k_y$ are constants. This type of relationship holds for a wide variety of steels [64].

### *3.4.4 Toughness*

In addition to the mechanical properties that characterise the strength and ductility of steels, toughness, or the energy absorbed during fracture, is also of considerable

engineering importance. Ferritic steels are unique in that they show a transition from ductile to brittle fracture when broken at successively lower temperatures. Generally, the transition for a given steel and microstructure is determined by breaking a series of V-notched bars by impact loading at temperatures above and below room temperature. The Impact Transition Temperature (ITT) is a measure of the metal toughness and marks the transition between the ductile and the brittle fracture. Low-carbon steels have sub-zero ITT and as a result, they are quite tough at room temperature [34]. To predict ITT in degrees Celcius (°C) using the composition and the ferrite grain size, the following model can be used [43]:

$$\text{ITT} = -19 + 44\ \text{Si} + 700\ \text{N} - 11.5\ d^{-1/2} + 2.2\ V_p. \tag{3.16}$$

As shown in the above expression, ITT is also favourably affected by the ferrite grain size ($d$) and the volume fraction of pearlite ($V_p$). The above models show that, in practical terms, the finer the grain size, the better the resulting YS, TS, and ITT; as a result, in modern steel-working much attention is paid to the final ferrite grain size [34]. For instance, while a coarse grain size of 250 $\mu$m leads to a YS in mild steels of around 100 MPa, the grain refinement to 2.5 $\mu$m raises the yield stress to over 500 MPa. Also, the unique feature of the grain size strengthening is that it is the only strengthening mechanism which also increases toughness. Refining the grain size of steel alloys which show a ductile-brittle transition results in a decrease in ITT. Furthermore, refining the ferrite grain size also increases the flow stress at any given strain during plastic deformation and also the work-hardening rate of the ferrite-pearlite structures. In addition, the fracture stress is raised and the total strain at fracture is increased by refining the ferrite grain size [64].

The grain size of the steel can also affect many other properties; for example, the austenite grain size affects the transformation characteristics and thereby the hardenability, whilst increasing the grain size improves the creep strength but decreases the creep of rupture ductility [44]. Because of the importance of the ferrite grain size as a strengthening mechanism, but more especially because a fine grain size is so beneficial to toughness and ductility, this research work is focused on the development of a mechanism to promote the refinement of the ferrite grain and thus improving the ensuing mechanical properties too.

## 3.5 Concluding Remarks

This survey of the effects of the process variables on the microstructural changes that take place during hot-rolling of C-Mn steels showed that there is good quantitative knowledge and consistency of observations that have led to the formulation of physically-based models to predict the metal behaviour. The combination of such models enables the microstructure prediction during complex rolling operations. This allows for designing reliable mechanisms which can integrate metallurgical knowledge and process optimisation methods.

The equations described in this chapter can be divided into two groups:

1. The property models which predict the metal strength and toughness; and

2. The microstructural models whose determining variables are normally characterised by the temperature, the strain, and the strain rate.

It is apparent that the key factor which enables to improve the mechanical properties is the ferrite grain size, which can be refined by a series of recrystallisation cycles during the austenite phase. It was observed that, by selecting effective deformation profiles, one can control the microstructural changes of the metal so as to achieve the desired mechanical properties. How to choose the optimal values for such deformation profiles is directly related to the mill scheduling. This is the main topic of the next chapter.

# Chapter 4

# Metal Design and Microstructure Optimisation using Genetic Algorithms (GA)

## 4.1 Introduction

This chapter outlines the methodology which will allow one to tailor the microstructure of steel alloys for developing *metals by design* and achieving a *right-first-time* production. The property models already described in Chapter 3 are combined with Neural-Fuzzy models to map the final mechanical properties of the steel with its microstructure and chemical composition. An optimality criterion is also defined in order to minimise the error between a user-defined metal design and the one described by its property-structure characteristics after processing. A GA is used to carry-out an optimal search for the best microstructural parameters such as the ferrite grain size and the volume fraction of pearlite that satisfy the mechanical property requirements. The efficacy of this approach is evaluated by analysing a series of proposed metal designs using the C-Mn steel alloy.

## 4.2 Definition of the Multi-Objective Optimisation Problem

The scheduling problem of the Hille-mill requires the definition of different optimality criteria which may include multiple objectives. Such criteria can be represented by 'objective' functions to be minimised. The problem also has a number of constraints which any feasible solution (including the optimal solution) must satisfy. In a general

form, the multi-objective optimisation problem can be defined as follows:

$$\begin{cases} \text{Minimise:} & F_m(x), & m = 1, 2, \ldots, M. \\ \text{Subject to:} & G_j(x) \geq 0, & j = 1, 2, \ldots, J; \\ & H_k(x) = 0, & k = 1, 2, \ldots, K; \\ & x_i^L \leq x_i \leq x_i^U, & i = 1, 2, \ldots, n. \end{cases} \tag{4.1}$$

A solution $x$ is a vector of $n$ decision variables where $x = [x_1, x_2, \ldots, x_n]^T$. The last set of constraints in Equation (4.1) are called variable bounds, restricting each decision variable ($x_i$) to take a value within a lower ($x_i^L$) and an upper ($x_i^U$) bound; these bounds constitute the *decision variable space.* Associated with the problem, are the $J$ inequality and $K$ equality constraints. In the above formulation, the terms $G_j(x)$ and $H_k(x)$ are called constraints' functions. A solution $x$ that does not satisfy all of the $(J + K)$ constraints and all the $2n$ variable bounds stated above is called an *infeasible solution.* On the other hand, if any solution $x$ satisfies all constraints and variable bounds, it is known as a *feasible solution.* Therefore, in the presence of constraints, the entire decision variable space need not be feasible. The set of all feasible solutions is called the *feasible region.* Also, there are $M$ objectives that have to be minimised. In multi-objective optimisation the objective functions constitute a multi-dimensional space called the *objective space.* In the application described in this chapter, the optimality criteria are defined in order to meet the metal design requirements by means of finding feasible solutions in terms of the microstructure and the processing conditions. Such criteria include the physical-related constraints of the metal as well as the mill processing limitations.

Figure 4.1 represents a graphical interpretation of the multi-objective optimisation problem associated with the Hille-mill. As shown in this figure, the aim is to find correlating points or solutions among the different spaces. For instance, the coordinates of the solution $p$, represent the user-defined values for the desired mechanical properties $P_1$, $P_2$,...,$P_{np}$. As already explained in Chapter 3, for certain deformation conditions, there exists a solution $m$ within the microstructure space that represents the critical microstructural parameters $M_1$, $M_2$,...,$M_{nm}$, which define those properties. Similarly, for each solution $m$ in the microstructure space, there exists a solution $r$ in the processing space, whose components may be described by a set of rolling parameters $R_1$, $R_2$,...,$R_{nr}$. It is worth noting that the optimal solution for the microstructure and the processing should be within the feasible regions of each space in

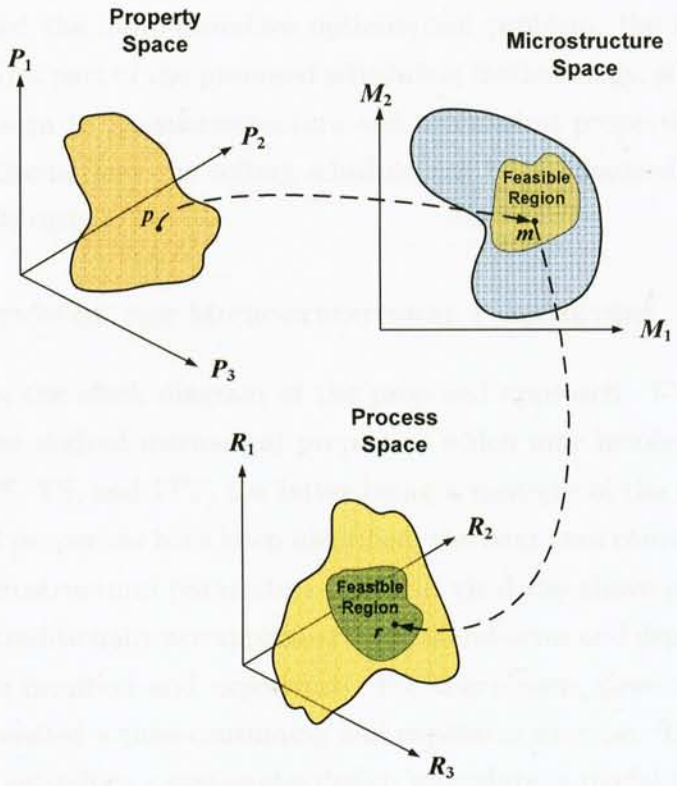


Figure 4.1: A graphical representation of the optimisation problem of the Hille-mill

order to guarantee repeatability of the rolling process.

The graphical representation of Figure 4.1 can also be expressed using the following equation which relates (1) the metal mechanical properties with its microstructure, and (2) the microstructure via a set of rolling parameters:

$$\begin{cases} f(p) = m = [M_1, M_2, \ldots, M_{nm}]^T \\ g(m) = r = [R_1, R_2, \ldots, R_{nr}]^T \end{cases}, \tag{4.2}$$

where $f(\cdot)$ is a function that defines the metal properties and whose arguments are the quantitative elements of the metal microstructure, such as the ferrite grain size and the volume fraction, whereas $g(\cdot)$ is a function representing the microstructure described in terms of the deformation parameters, such as the temperature, the strain, and the strain rate applied to the stock. In other words, given the desired mechanical properties ($p$), one can optimise $f(p)$ to find the best microstructural parameters, which are also the components of $m$; then, the rolling parameters can be found by using $m$ and $g(m)$ along with an optimality criterion.

Having defined the multi-objective optimisation problem, the following section will discuss the first part of the proposed scheduling methodology, which will link the desired metal design to its microstructure and mechanical properties (MODULE 1). Chapter 5 will discuss how the rolling schedule can be synthesised using the metal microstructure (MODULE 2).

## 4.3 OPTIMISATION OF THE MICROSTRUCTURAL PARAMETERS

Figure 4.2 shows the block diagram of the proposed approach. First, the designer has to specify the desired mechanical properties which may involve one or more of the following: TS, YS, and ITT, the latter being a measure of the metal toughness. Once the critical properties have been identified, the next task consists of finding the quantitative microstructural parameters that will yield the above properties. These steps have been traditionally accomplished by trial-and-error and depend considerably on the designer's intuition and experience. For this reason, developing new metals has always represented a time-consuming and expensive exercise. To overcome these problems and to introduce a systematic design procedure, a model-based mechanism was developed which is included in MODULE 1.

Three basic elements for defining and approaching the problem are considered in MODULE 1:

1. The **Stock Model** which relates the mechanical properties with the critical microstructural parameters;

2. The **Optimality Criterion** which is related to achieving the desired mechanical properties of the steel alloy in terms of the quantitative elements of its microstructure; and

3. The **Physical Constraints** which include the limitations of the forming process and the hot-workability of the metal.

The characteristics of these three components for the optimisation will be discussed in the following sections.

Figure 4.2 also shows that further information on the metal characteristics should be provided to carry-out the optimisation. For instance, the content of each chemical element, as well as the phase diagram profile of the alloy, are important to set the

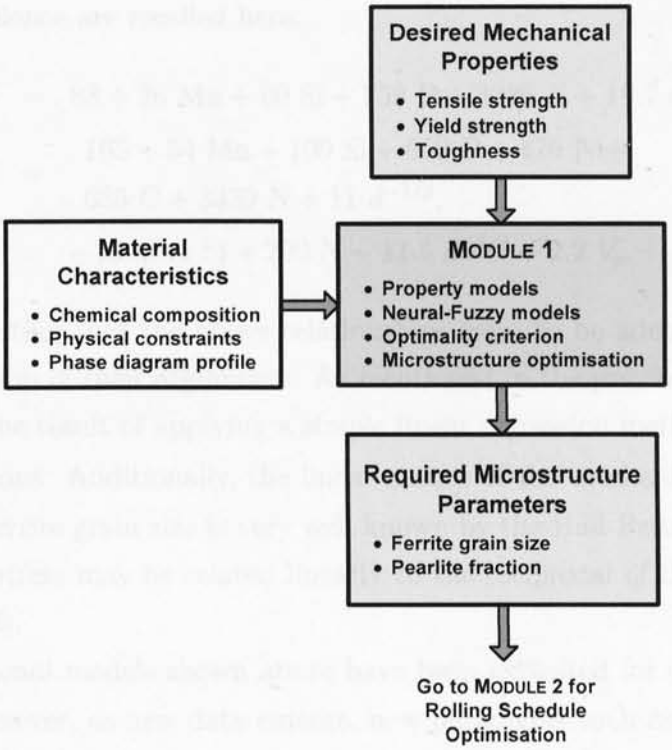


Figure 4.2: Block diagram of the proposed mechanism for microstructure optimisation

physical constraints that will form the boundaries of the feasible region within the solution space. Furthermore, these metal characteristics will prove useful in determining the expected microstructures and the dynamics of the phase transformations.

## 4.4 MODULE 1 - FROM THE DESIRED PROPERTIES TO THE REQUIRED MICROSTRUCTURE

This section describes the components of MODULE 1 of Figure 4.2. In this case the optimal search is focused on finding the best microstructural parameters required to achieve the desired mechanical properties. As mentioned in Chapter 3, the ferrite grain size affects many properties, including those considered in this study, i.e. YS, TS, and ITT. Equations (3.13) to (3.16) in Chapter 3 described the corresponding relationships of the above properties as functions of the ferrite grain size in millimeters ($d = d_\alpha/1000$)), the volume fraction of pearlite ($V_p$), and the chemical composition,

which for convenience are recalled here:

$$\text{YS} = 88 + 26\ \text{Mn} + 60\ \text{Si} + 759\ \text{P} + 3286\ \text{N} + 19.7\ d^{1/2}, \tag{4.3}$$

$$\text{TS} = \begin{array}{l} 165 + 54\ \text{Mn} + 100\ \text{Si} + 652\ \text{P} + 476\ \text{Ni} + \\ 635\ \text{C} + 3339\ \text{N} + 11\ d^{-1/2}, \end{array} \tag{4.4}$$

$$\text{ITT} = -19 + 44\ \text{Si} + 700\ \text{N} - 11.5\ d^{-1/2} + 2.2\ V_p. \tag{4.5}$$

It is worth noting that the above relationships seem to be adequately explained by a linear function of their arguments. As mentioned in the previous chapter, these equations were the result of applying a simple linear regression method to fit experimental observations. Additionally, the linear nature of the mechanical properties as function of the ferrite grain size is very well known by the Hall-Petch relationship by which the yield stress may be related linearly to the reciprocal of the square root of the grain size [26].

The conventional models shown above have been exploited for off-line designs of steel grades. However, as new data emerge, new paradigms such as those associated with 'intelligence' (flexible, self-learning and self-organising) can be used to complement the current knowledge and trends. In this case, Intelligent Systems-based paradigms are proposed to improve the predictive capabilities of the overall optimisation approach.

### *4.4.1 Neural-Fuzzy Modelling of the Tensile Strength*

Because this is a model-based strategy, a model should be at the centre of the optimisation process, from analysis and design to implementation and testing. Therefore, the more accurate the model is, the more reliable the solutions will be. Although the models linking properties and microstructures presented above are widely used both in academia and industry, a new model is proposed in this work to enhance the user's predictive capabilities when dealing with TS. For this purpose, a set of industrial data was used in order to capture the relationship between the chemical composition, the ferrite grain size, and TS of the C-Mn steel alloy. To extract knowledge from such data, Intelligent Systems-based paradigms are used because they provide a flexible methodology to create models that combine the human-like reasoning and interpretability of Fuzzy Inference System (FIS) with the learning and generalising abilities of Neural Networks (NN).

Consider the Adaptive Network-based Fuzzy Inference System (ANFIS) proposed in [37]. Such a Neural-Fuzzy paradigm allows for developing a data-driven nonlinear model. Five-hundred and sixty-three data points were used from which 60% was taken for training and 40% for testing. The model inputs included the content of four chemical elements such as carbon (C), silicon (Si), manganese (Mn), and nitrogen (N), and the ferrite grain size (expressed as $d = d_\alpha/1000$); the metal TS was considered as the model output.

The Neural-Fuzzy model development was carried-out as follows. First, the number of rules and the antecedent membership functions were obtained by using the subtracting clustering method proposed in [12]; the least squares algorithm was then used to find each rule's consequent function. The resulting fuzzy rules corresponded to a Takagi-Sugeno-Kang (TSK)-type model whose fuzzy rules can be expressed as follows:

$$\text{IF } x_1 \text{ is } B_1^1 \text{ and } \cdots \text{ and } x_n \text{ is } B_n^i, \text{ THEN } \begin{array}{l} y_i = c_0^i + c_1^i x_1 + \cdots + c_n^i x_n, \\ i = 1, \ldots, p, \end{array} \tag{4.6}$$

where $x = (x_1, \ldots, x_n)^T$ and $y$ are the input and output linguistic variables respectively, $B_n^i$ are the linguistic values characterised by membership functions, and $c_i$ are real-valued parameters, $p$ being the number of clusters or partitions. Figure 4.3 shows the graphical interpretation of the Neural-Fuzzy model. Observe that, after the training process, the model captured the linear relationship of the grain size and the carbon content with the strength of the metal in good agreement with the Hall-Petch relationship. It is worth noting that, the model describes the nonlinear nature of the effect that other chemical elements have over TS. Figure 4.4 shows the obtained input membership functions after training using a centre range of influence of 0.55 for the data clustering method. The model is comprised of 5 inputs with 4 Gaussian membership functions per input, 4 fuzzy rules, and 1 output. The resulting fuzzy rules are the following:

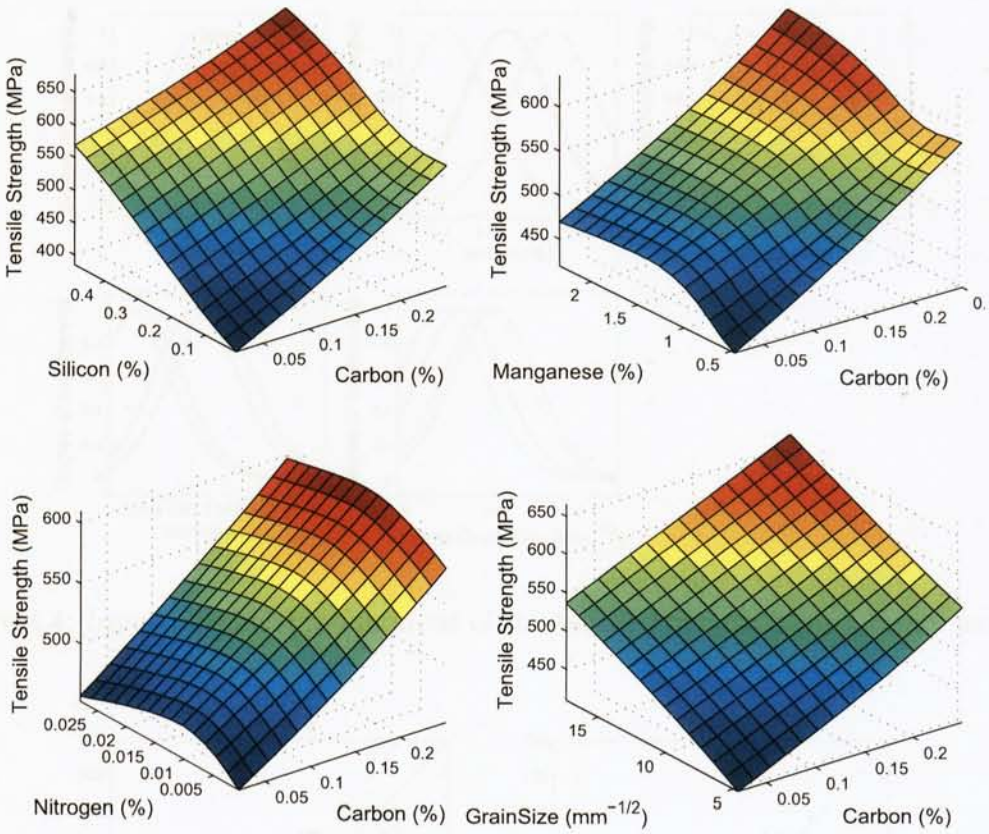


Figure 4.3: Neural-Fuzzy model for predicting the tensile strength of C-Mn steels

$R_1$ : IF C is *Low* and Si is *High* and Mn is *Very High* and N is *High* and $d^{-1/2}$ is *Very High*, THEN TS = 302.32 + 577.66 C + 446.94 Si − 13.35 Mn − 1838.50 N + 9.00 $d^{-1/2}$;

$R_2$ : IF C is *High* and Si is *Medium* and Mn is *Medium* and N is *Medium* and $d^{-1/2}$ is *Medium*, THEN TS = 139.89 + 915.79 C + 218.69 Si + 125.54 Mn − 10341 N + 7.06 $d^{-1/2}$;

$R_3$ : IF C is *Very High* and Si is *Very High* and Mn is *High* and N is *Low* and $d^{-1/2}$ is *High*, THEN TS = −55.37 + 713.68 C + 202.34 Si + 4758.5 Mn + 4758.5 N + 5.61 $d^{-1/2}$;

$R_4$ : IF C is *Medium* and Si is *Low* and Mn is Low and N is *Very High* and $d^{-1/2}$ is *Low*, THEN TS = 78.898 + 647.44 C + 652.58 Si + 151.05 Mn + 2149.7 N + 19.48 $d^{-1/2}$.

Figure 4.5 presents a comparison between the measured and the predicted TS using the above Neural-Fuzzy model. As shown in this figure, all predictions were reasonably accurate as marked by the ±10% confidence band represented by the

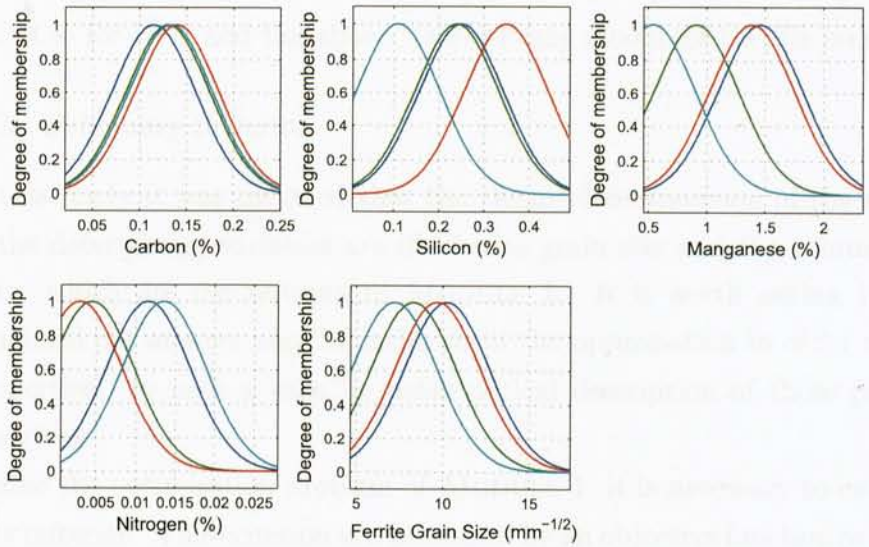


Figure 4.4: Input membership functions of the tensile strength Neural-Fuzzy model

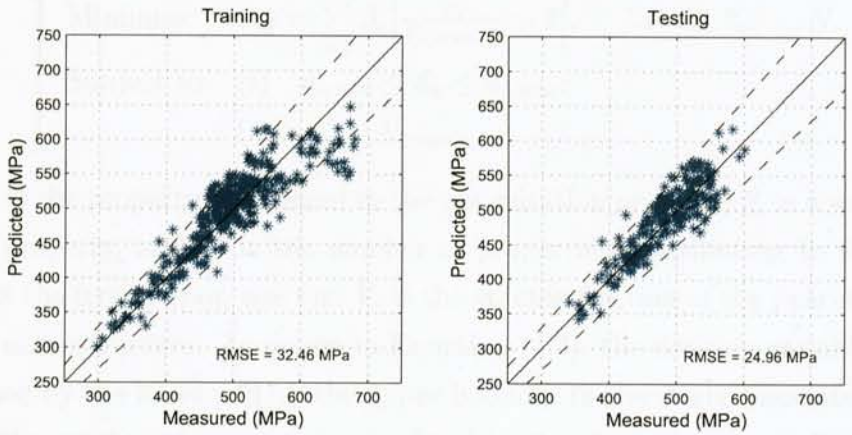


Figure 4.5: Measured and predicted tensile strength using the Neural-Fuzzy model

discontinuous lines. A quantitative analysis between the Neural-Fuzzy model and the linear model of Equation (4.4) revealed a reduction of the Root Mean Square Error (RMSE) in the predictions given by the intelligent model which was 32.46 MPa for the training data and 24.96 MPa for the testing data; whereas using the linear model, the RMSE for the training data was 47.98 MPa and 38.17 MPa for the testing data.

In summary, the model used by MODULE 1 is comprised of Equation (4.3) for YS, Equation (4.5) for ITT, and the above Neural-Fuzzy model for the TS prediction.

### *4.4.2 The Optimality Criterion*

Since in this study it was assumed that the chemical composition of the steel alloy is fixed, the determining variables are the ferrite grain size and the volume fraction of pearlite, which are the outputs of MODULE 1. It is worth noting that other microstructural parameters may be included in the optimisation in order to achieve other properties. In such a case, a mathematical description of these parameters should be given.

To define the optimisation problem of MODULE 1, it is necessary to establish an optimality criterion. This criterion is represented by an objective function as described in Equation (4.1). The cost ($J_M$) of the objective function can be calculated using the following equation:

$$\begin{cases} \text{Minimise:} & J_M = \sum_{i=1}^{N} \beta_i \left| \frac{P_i}{P_{i(desired)}} - 1 \right|, \qquad i = 1, 2, \ldots, N. \\ \text{Subject to:} & (i) \quad d_{\alpha\,\min} \leq d_\alpha \leq d_{\alpha\,\max}; \\ & (ii) \quad V_p \leq V_{p\,\max}; \end{cases} \tag{4.7}$$

where $P_i$ is the property considered in the optimisation problem, $\beta_i$ is a weight factor for each property, and $N$ is the number of properties contributing to the cost; $d_\alpha$ represents the ferrite grain size and $V_p$ is the volume fraction of the pearlite colony in the final microstructure. As shown in Equation (4.7), the decision variables are only constrained by the lower and/or the upper bounds. In the study associated with this chapter, the number of properties considered is $N = 3$, so that expanding the above formulation yields the following objective function:

$$J_M = \beta_{\mathrm{TS}} \left| \frac{\mathrm{TS}}{\mathrm{TS}_{(desired)}} - 1 \right| + \beta_{\mathrm{YS}} \left| \frac{\mathrm{YS}}{\mathrm{YS}_{(desired)}} - 1 \right| + \beta_{\mathrm{ITT}} \left| \frac{\mathrm{ITT}}{\mathrm{ITT}_{(desired)}} - 1 \right|. \tag{4.8}$$

Each term in Equation (4.8) represents an objective in the optimisation and accounts for deviations in the mechanical properties from their desired value. Therefore, the strategy in Equation (4.8) scales a set of objectives into a single one by pre-multiplying each objective with a user-supplied weight vector $\beta = \begin{bmatrix} \beta_{\mathrm{TS}} & \beta_{\mathrm{YS}} & \beta_{\mathrm{ITT}} \end{bmatrix}$, which is also used to express priorities among the selected properties of the overall criterion. These weights are called the **priority factors**. Thus, the weighted sum

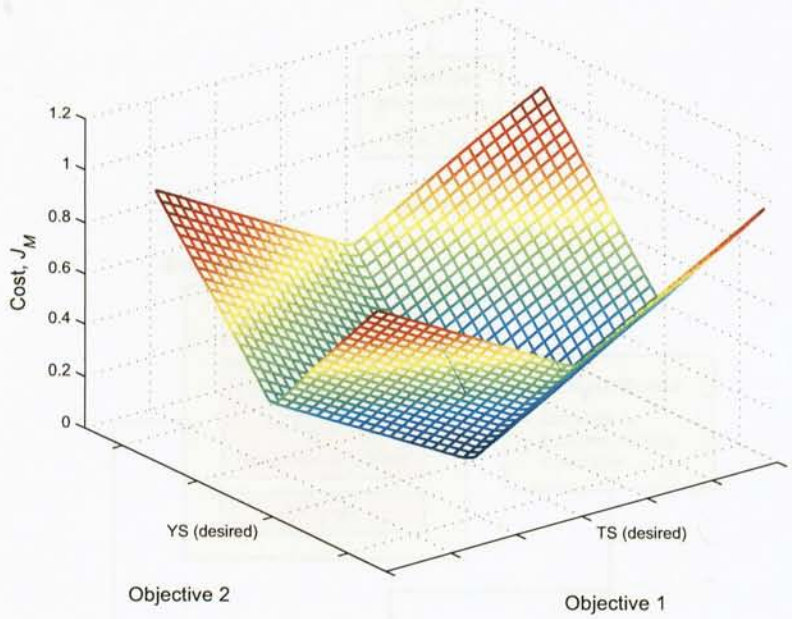


Figure 4.6: Objective space of MODULE 1

converts the multi-objective optimisation problem of minimising each designed objective into a scalar one. This simple strategy is considered here as the optimality criterion of MODULE 1. Figure 4.6 shows the objective space considering only two objectives. Note that the optimal (minimum) value of $J_M$ is only reached when the mechanical properties of the proposed design are equal to the desired values. Therefore, the optimal solution is found when the cost of the optimality criterion equals zero (i.e. $J_M = 0$).

Here, the GA-based optimisation procedure involves working with a population of microstructures represented by a two-dimensional vector in binary code known as chromosome or individual. Each individual is a possible solution to the optimisation problem. In this case, an individual consists of one value for the ferrite grain size, and another value for the volume fraction of pearlite. Using genetic operators involving reproduction, crossover, and mutation, generations of new individuals are created from the initial population. This generational cycle continues until a desired termination criterion is reached. Figure 4.7 shows the searching procedure of MODULE 1 using the principle of GA with its main elements and operations.

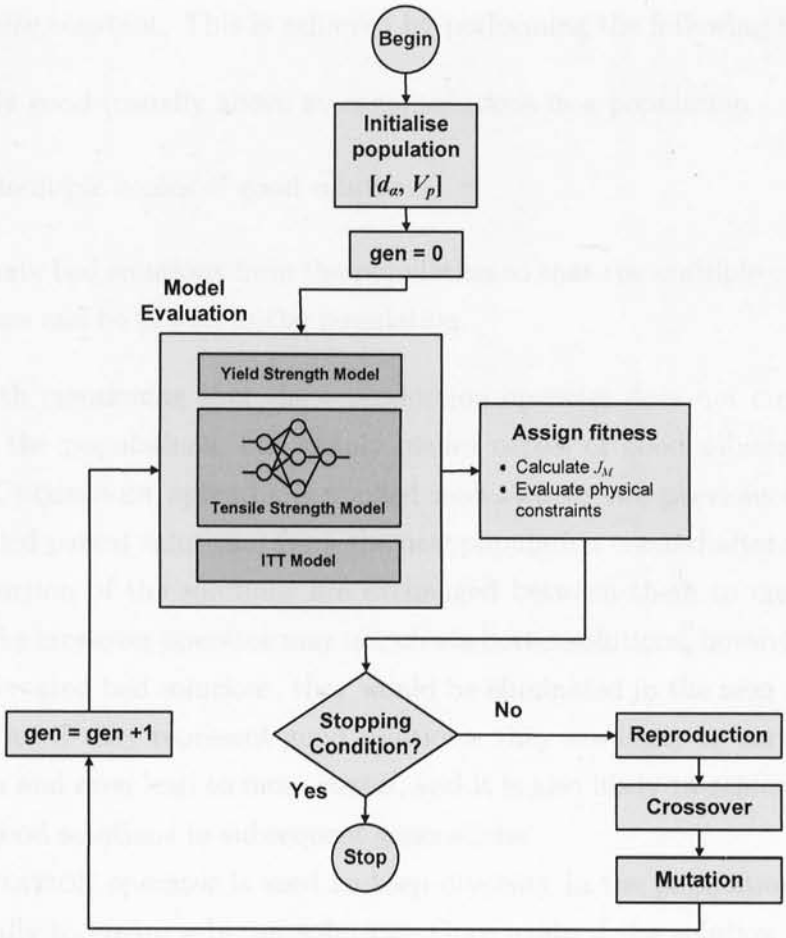


Figure 4.7: Microstructure optimisation development

GA begins its search with a random set of solutions containing the values for the ferrite grain size ($d_\alpha$) and the volume fraction of pearlite ($V_p$). When a population of solutions is created, each solution is evaluated in the context of the optimality criteria and a fitness value is assigned to each solution according to Equation (4.8). The evaluation of a solution is equivalent to calculating the objective function value and constraints violations. A termination condition is then checked. If the termination criterion is not satisfied, the population of the solutions is modified by the 3 operators and a new (and better) population is created. The generation counter (gen) is then incremented to indicate the number of generations used [27].

The primary objective of the REPRODUCTION operator is to make duplicates of good solutions and eliminate bad solutions in a population, while keeping the

population size constant. This is achieved by performing the following tasks:

1. Identify good (usually above average) solutions in a population.

2. Make multiple copies of good solutions.

3. Eliminate bad solutions from the population so that the multiple copies of good solutions can be placed in the population.

It is worth mentioning that the reproduction operator does not create any new solutions in the populations, but simply makes copies of good solutions. For this reason the CROSSOVER operator is applied next, where two previous solutions are selected (called parent solutions) from the new population created after reproduction and some portion of the solutions are exchanged between them to create two new solutions. The crossover operator may not create better solutions, however even in the case that it created bad solutions, they would be eliminated in the next reproduction operation. But if they represent good solutions, they are likely to survive the next reproduction and even lead to more copies, and it is also likely to achieve a crossover with other good solutions in subsequent generations.

The MUTATION operator is used to keep diversity in the population. It alters a solution locally to create a better solution. Once again if the solution created were a bad solution, then it would not survive reproduction, but if it is a good solution, then it will survive and contribute to create new good solutions.

Because there is more than one solution being processed simultaneously and used to update every solution in the population, it is likely that the expected GA solution may have been a global solution. Another advantage is that GA does not require any auxiliary information of the problem (e.g. gradient information) except the objective function values [40].

To evaluate the efficacy of the above approach, the next sections will present a series of proposed metal designs using the C-Mn steel alloy.

## 4.5 SISSCOR – An Integrated Graphical User Interface for Metal Design

A MATLAB®-based software was developed to work as a friendly Graphical User Interface (GUI) to facilitate the implementation of the microstructure optimisation

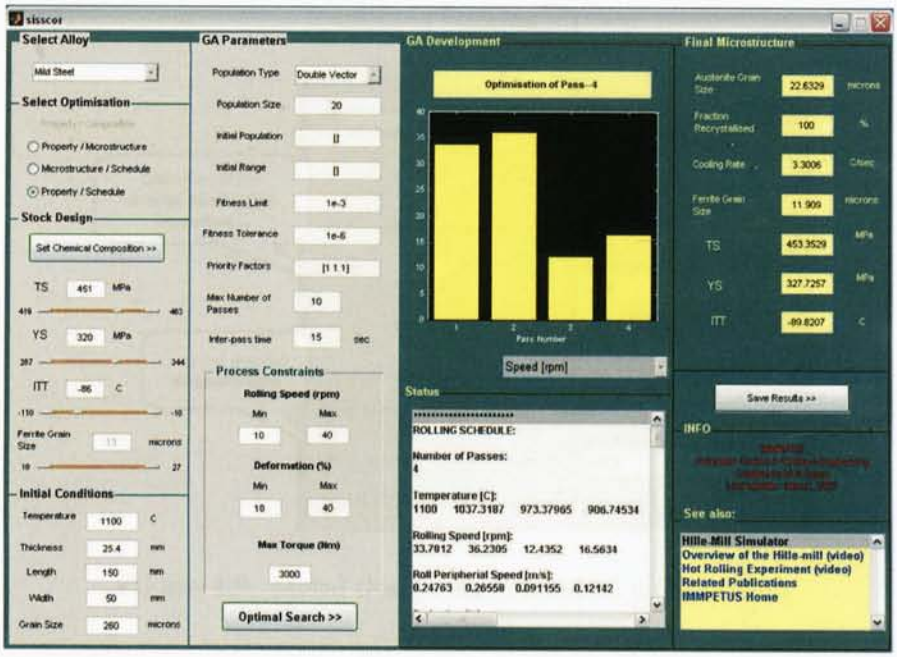


Figure 4.8: SISSCOR — Sheffield Integrated System for SCheduling and Optimisation in Rolling

mechanism discussed in the previous section, as well as the computation of the rolling schedule[1]. This GUI has been named SISSCOR, which stands for Sheffield Integrated System for SCheduling and Optimisation in Rolling. It provides a computing platform to handle information, plot graphics, and log data which can be easily used in the laboratory. As shown in Figure 4.8, SISSCOR includes different sections that guide the user to develop his/her own metal design and obtain the optimal microstructural and rolling parameters.

The first step consists of selecting the steel alloy to be designed. SISSCOR supports three different steel alloys: (1) the C-Mn steel alloy, which is also known as Mild Steel; (2) the 316L Stainless Steel; and (3) the 304 Stainless Steel. It is worth mentioning though that only the C-Mn steel alloy was considered in this thesis and was also the only material used experimentally.

The next step relates to the design of the steel in terms of the desired mechanical properties. Figure 4.9 shows a simple design in which one has to set the chemical composition of the metal and enter the value for the desired mechanical properties.

[1]The systematic computation of the rolling schedule will be discussed in Chapter 5.

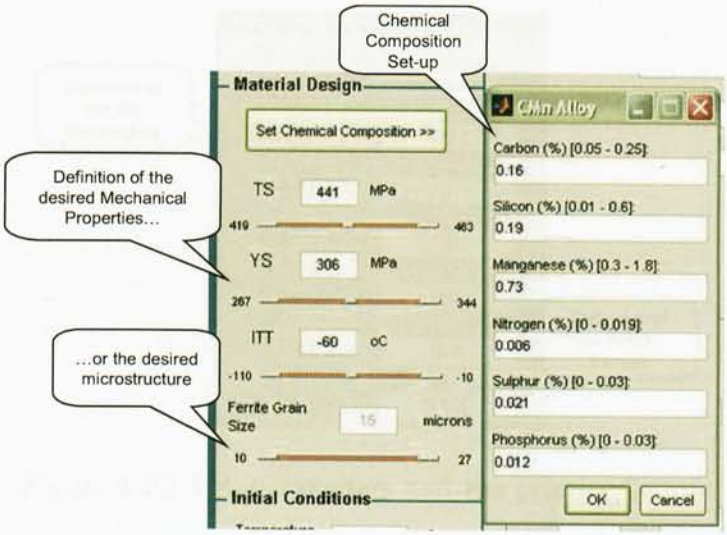


Figure 4.9: Metal design and chemical composition

The chemical elements considered for the C-Mn steel alloy are: carbon, silicon, manganese, nitrogen, sulphur, and phosphorus. The ranges of the element contents shown in Figure 4.9 are based on typical chemical compositions for this alloy in particular. The default specification corresponds to the composition found in the alloy used experimentally in this research work; this information was provided by the material's manufacturer. Every time the user sets the chemical composition or amends it, an internal subroutine is called to estimate the property ranges based on the metal physical constraints.

Once the chemical composition has been defined, the desired values for the mechanical properties should be specified by either entering numeric characters to the text windows or by moving the sliders forward or backward. Depending on the type of optimisation selected, one may set the desired microstructure instead of the mechanical properties, but not both.

The next step relates to the set-up of the GA parameters. These may include the type of population (i.e. double vector or bit string), the probability of crossover and mutation, the stopping criteria, etc. Figure 4.10 shows the GA parameters that can be varied to add flexibility to the optimisation mechanism. Observe that the user has to set-up the priority factors (i.e. weighting factors; the $\beta$'s in Equation (4.8)) to establish the design priorities among the mechanical properties when searching

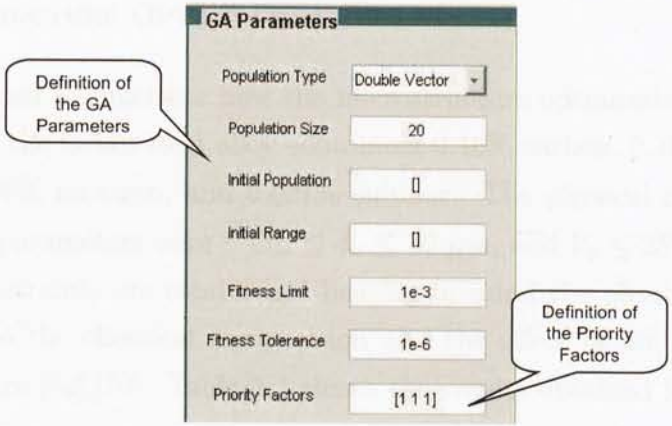


Figure 4.10: GA parameters and the priority factors

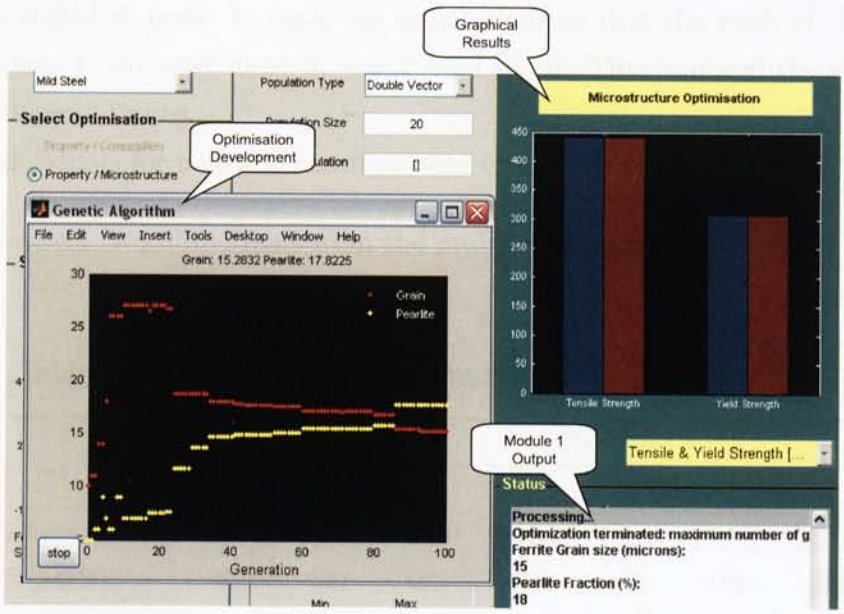


Figure 4.11: GA development for MODULE 1

for the best microstructure. With this information, the microstructure optimisation procedure can be initiated. As shown in Figure 4.11, the GA development is visualised before delivering the best suitable microstructure for the proposed design.

## 4.6 Microstructure Optimisation Results

SISSCOR was used to illustrate how the microstructure optimisation in Module 1 works. Consider the C-Mn steel alloy containing 0.16% carbon, 0.19% silicon, 0.73% manganese, 0.006% nitrogen, and 0.021% sulphur. The physical constraints of the microstructural parameters were 8 $\mu$m $\leq d_\alpha \leq$ 30 $\mu$m, and $V_p \leq 25\%$. As mentioned earlier, such constraints are established bearing in mind the physical limitations of the metal due to the chemical composition and the effect of air cooling in the final microstructure [52],[70]. Table 4.1 shows the results obtained for various design criteria.

The GA parameters were set as follows: a random initial population with uniform distribution was used with 20 individuals; each individual received a fitness score which was scaled in order to rank the population, so that the rank of the most fit individual was 1, the next most fit was 2, and so on. This removed the effect of the spread of the raw scores.

The individuals for a new generation were created as follows:

- 1 - 2 : best two individuals from the previous generation;

Table 4.1: Optimal microstructure for different design criteria

| | Case | | | | | | | |
|---|---|---|---|---|---|---|---|---|
| | 1 | 2 | 3 | 4 | 5 | 6 | 7 | 8 |
| Priority Factors | 1,0,0 | 1,1,0 | 10,1,0 | 1,10,0 | 1,1,1 | 10,1,1 | 1,10,1 | 1,1,10 |
| Desired TS (MPa) | 450 | 450 | 450 | 450 | 450 | 450 | 450 | 450 |
| Calculated TS (MPa) | 450 | 443 | 450 | 443 | 444 | 450 | 443 | 442 |
| Desired YS (MPa) | — | 310 | 310 | 310 | 310 | 310 | 310 | 310 |
| Calculated YS (MPa) | — | 309 | 322 | 309 | 312 | 321 | 310 | 307 |
| Desired ITT (°C) | — | — | — | — | -70 | -70 | -70 | -70 |
| Calculated ITT (°C) | — | — | — | — | -73 | -69 | -69 | -70 |
| | Optimal Microstructure | | | | | | | |
| Ferrite Grain Size ($\mu$m) | 12.7 | 14.6 | 12.7 | 14.7 | 14.3 | 12.7 | 14.6 | 15 |
| Pearlite Fraction (%) | 7.01 | 6.20 | 9.90 | 7.57 | 14.9 | 17.4 | 4.3 | 13.7 |
| Cost value, $J_M$ | 0 | 0.015 | 0.037 | 0.014 | 0.022 | 0.038 | 0.0152 | 0.023 |

- 3 - 17: generated by crossover;
- 18 - 20: generated by mutation.

The stochastic universal sampling method was used to select individuals for mating. The mutation operator randomly generated directions that were adaptive with respect to the last successful or unsuccessful generation. Because the feasible region was bounded by the upper and lower constraints, a step length was chosen along each direction so that the bounds were satisfied. Finally, the stopping criteria were defined in such a way that the process completed 50 generations or the cost function value was below $10^{-6}$.

In Case 1, the user-defined requirement specified a TS of 450 MPa. The requirement was met with $d_\alpha = 12.7$ $\mu$m, and $V_p = 7.01\%$. Figure 4.12(a), which was obtained by calculating TS using the best microstructure of each generation, shows the change in TS as the solution evolved with successive generations. The values of the microstructural parameters corresponding to the best solutions per generation are shown in Figure 4.12(b). This figure shows the real evolution of GA as the decision space was explored for the best solution starting from the 1st generation to the 50th generation. As GA evolved, the fitness value was decreasing until the optimal microstructure was found, that is when the desired value for TS was achieved. Clearly, the final solution was not intuitively obvious. The final microstructure was inside the search space specified by the limits on the decision variables rather than on the boundary.

In addition to a TS of 450 MPa, Cases 2-4 required a YS of 310 MPa. The optimal microstructure was sought by considering different priority factors for the two properties. In Case 2, both properties were equally weighted. Conversely, a higher factor was placed on meeting TS and YS in Cases 3 and 4 respectively. Figure 4.13 shows the changes in both properties, as well as the exploration of the decision space with successive generations for Case 2. Similar microstructures were found for Cases 1 and 3, and for Cases 2 and 4. This occurred as a result of the selected priority factors which gave more importance to TS and YS respectively.

The optimisation problems considered in Cases 5-10 were more challenging since the design criteria involved meeting the requirements of 3 properties: TS, YS, and ITT. For this reason the stopping criterion regarding the number of generations was extended to 100 generations using a population of 30 individuals. Figure 4.14 shows

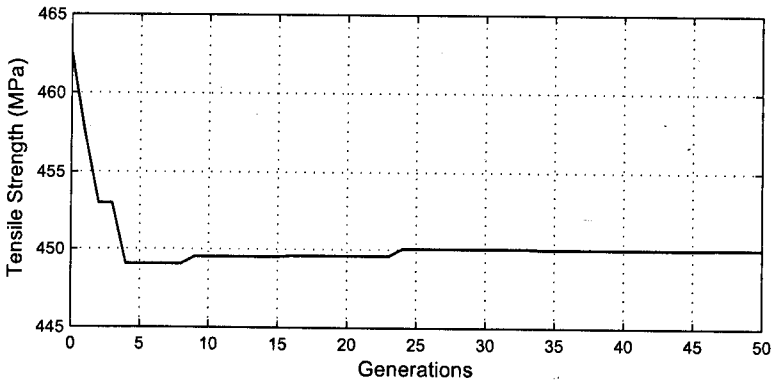


(a)

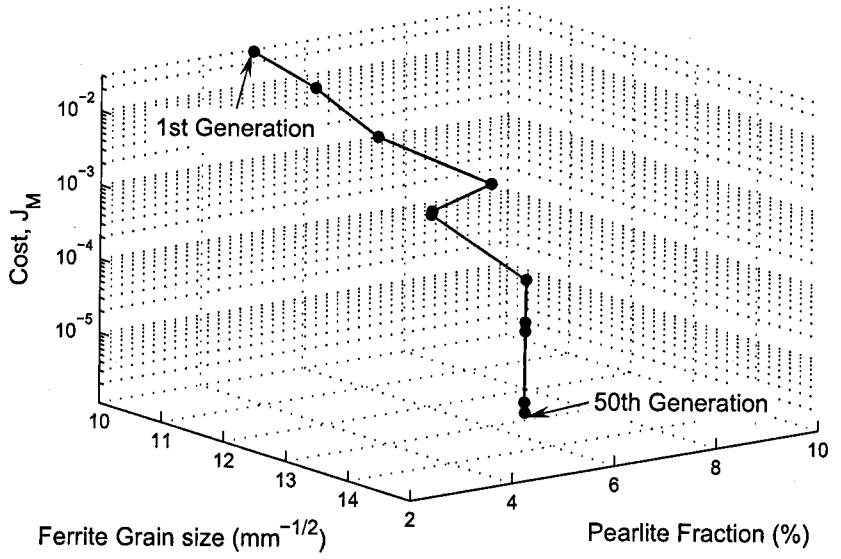


(b)

Figure 4.12: GA development for Case 1; (a) evolution of the tensile strength; (b) decision space exploration

the results for Case 5. The parameter exploration of the decision space is also depicted in this figure, which shows the conflicting requirements in meeting the desired criteria. This is reflected in the wider search space used by the GA to find the optimal solution. Interestingly, the objective concerning ITT was first met and very quickly, just in 5 generations, whereas the strength-related objectives were met after the 90th generation. This occurred due to the fact that the optimisation of ITT

used two degrees of freedom, so that any small change in microstructure resulted in a faster evolution. On the other hand, both TS and YS were only affected by the grain size and consequently less sensitive to the microstructure changes. The obtained microstructures for Cases 6 - 8 were similar to the ones already presented and the results were in good agreement with the priority factors selected.

The general trend of the results presented in Table 4.1 suggests that the property with the highest priority factor was better achieved. It can be seen that the ferrite grain size was the most important factor affecting the three properties by increasing the strength and improving the toughness. Also, it was observed that the role of the pearlite fraction was not that important since the presence of pearlite was small assuming that the rolled metal would be air-cooled after deformation.

The results shown in Table 4.1 for each case are typical ones. Since GA relies on random operations, dispersion of the results were expected when the algorithm worked with a different initial population. However, a careful study revealed that a similar grain size was found despite using different initial populations; but for the pearlite fraction a different value was obtained in some cases indicating the existence of local minima. Having said this, GA was still effective to find the microstructure that was close to the optimal solution. Table 4.2 shows the results of this study.

## 4.7 Concluding Remarks

This chapter described the development and the application of Neural-Fuzzy modelling and GA in the design procedure to find optimal microstructural parameters. The correlation between the mechanical properties of a steel alloy and its microstructure was used to optimise the microstructure within practical limits in order to satisfy the user-specified design criteria. Although a specific alloy and only 3 mechanical properties were considered in this chapter, no special assumptions are made to preclude the use of this methodology for other alloys or properties. However, in such a case, additional objectives have to be included in the cost function, which will strongly depend on the mathematical models.

The next chapter will discuss the second part of the proposed scheduling mechanism associated with the Hille-mill, which includes the description of the systematic approach used to compute the optimal rolling schedule(s).

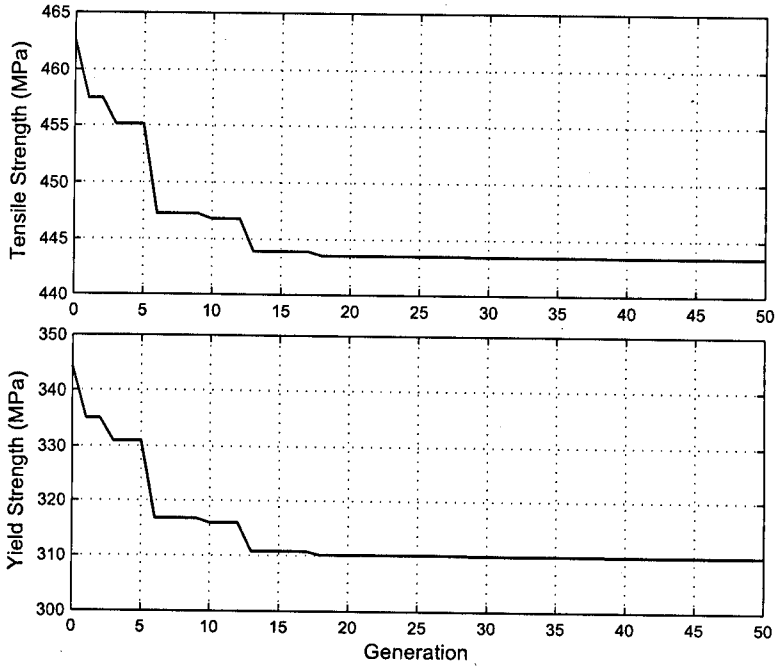


(a)

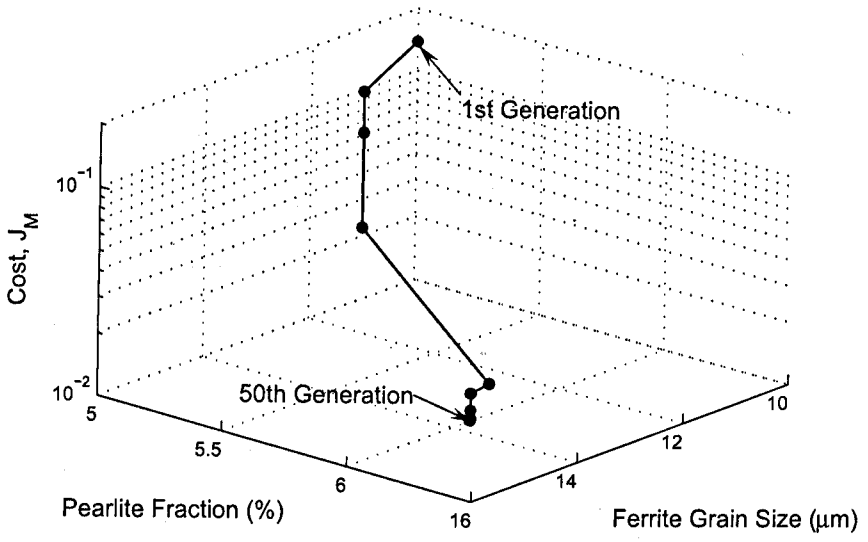


(b)

Figure 4.13: GA development for Case 2; (a) evolution of the tensile and yield strength; (b) decision space exploration

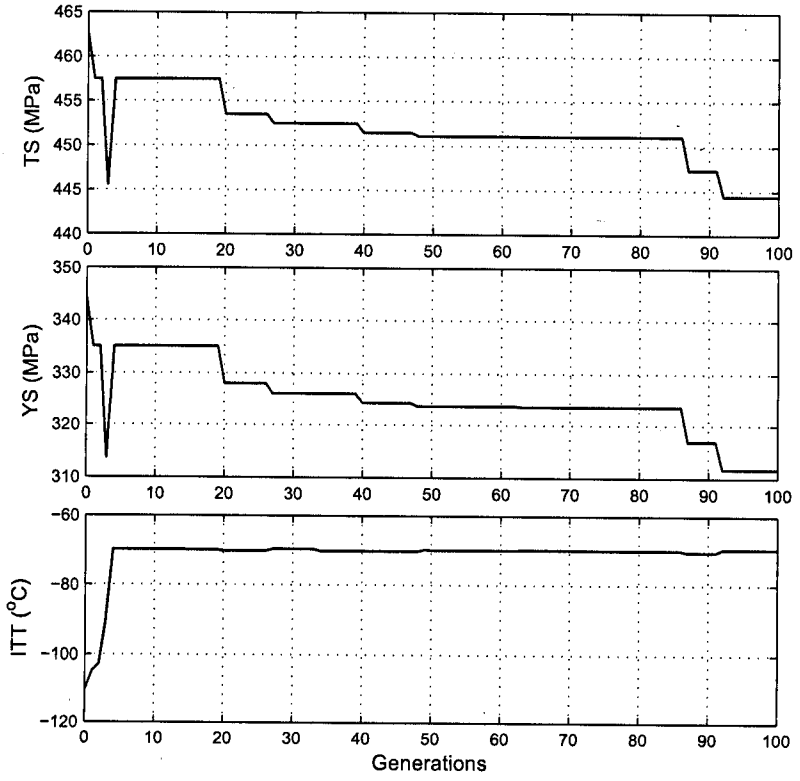


(a)

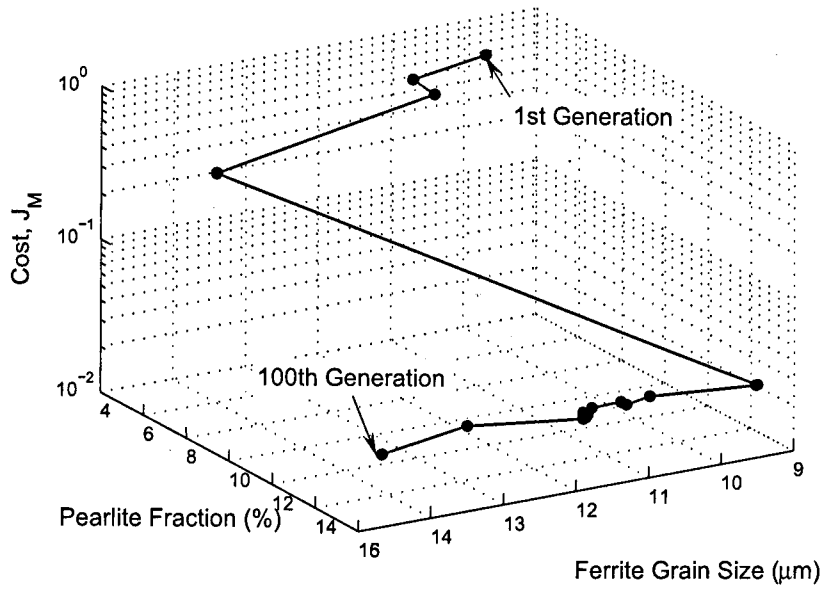


(b)

Figure 4.14: GA development for Case 5; (a) evolution of tensile strength, yield strength, and transition temperature; (b) decision space exploration

Table 4.2: Dispersion of microstructural parameters for different initial populations

| Case | Trial number | Ferrite size ($\mu$m) | Pearlite fraction (%) | Cost value $J_M$ |
|---|---|---|---|---|
| 1 | 1 | 12.74 | 5.13 | $2.80\times10^{-7}$ |
| | 2 | 12.74 | 13.84 | $2.26\times10^{-6}$ |
| | 3 | 12.74 | 9.51 | $7.92\times10^{-5}$ |
| | 4 | 12.74 | 5.92 | $2.44\times10^{-6}$ |
| | 5 | 12.74 | 14.13 | $3.97\times10^{-7}$ |
| 2 | 1 | 14.64 | 8.62 | 0.01455 |
| | 2 | 14.64 | 5.63 | 0.01456 |
| | 3 | 14.64 | 12.39 | 0.01454 |
| | 4 | 14.64 | 7.06 | 0.01455 |
| | 5 | 14.64 | 8.53 | 0.01454 |
| 5 | 1 | 14.67 | 14.21 | 0.0167 |
| | 2 | 14.7 | 14.23 | 0.0215 |
| | 3 | 13.83 | 15.55 | 0.0239 |
| | 4 | 14.11 | 15.11 | 0.2072 |
| | 5 | 14.5 | 14.5 | 0.0160 |

# Chapter 5

# Optimisation of the Hille-Mill Rolling Schedule using a Systematic Approach

## 5.1 Introduction

This chapter describes the model-based approach designed to find the optimal processing parameters that synthesise the rolling schedule. The main aim is to use the knowledge about the desired metal characteristics, including its microstructural features, to systematically calculate rolling parameters per pass such as the rolling speed, the percentage of reduction, the deformation temperature, etc. The physically-based models introduced in Chapter 3, combined with an optimality criterion, are used to calculate the effective process parameters that lead to the control of the microstructure events taking place in the stock during rolling; hence a *right-first-time* production of the desired properties can be achieved. To evaluate the efficacy of the developed mechanism, a few experimental scenarios are presented, which complement the microstructure optimisation results presented in Chapter 4.

## 5.2 Knowledge Integration of the Steel Alloy and the Hille-mill

The selection of the mill set-up is a demanding task that requires not only the understanding of the behaviour of the rolled material, but also information from the performance of the mill during the rolling process. As already discussed in Chapter 4, one can achieve the desired mechanical properties by correlating different microstructure profiles that satisfy an optimality criterion. The same principle can be applied when finding optimal process parameters; the scheduling problem can also be solved by using the quantitative information included in the microstructure to search for the

optimal deformation profiles.

Although the microstructure optimisation mechanism described in Chapter 4 was relatively simple, the search for the optimal rolling schedule requires further information on the process, such as the initial deformation conditions (i.e. heat treatment, microstructure prior to deformation), the cooling rates after processing, the influence of the mill spring on the material thickness, etc. [36].

In this work, the setting-up of the rolling schedule is also treated as an optimisation problem which includes the integration of two main aspects: (1) the microstructural changes taking place before, during, and after rolling; and (2) the Hille-mill working conditions. Figure 5.1 shows the block diagram of the proposed scheduling mechanism associated with the Hille-mill. In fact, this diagram complements the one shown in Figure 4.2. As shown in this figure, once MODULE 1 has provided the required microstructure to accomplish the metal design, MODULE 2 should be able to process this information in order to compute the most suitable rolling schedule and to synthesise the optimal route for processing. The overarching aim is to integrate knowledge of both the stock and the rolling mill to create a systematic mechanism that allows one to control the microstructural events taking place during hot-deformation. According to the definition of the optimisation problem in Section 4.2, it is assumed that, a *right-first-time* production of metals is achieved by performing the rolling schedule calculated in this manner.

In Chapter 3, it was shown that by applying effective rolling parameters, one can control the refinement of the austenite grain size by recrystallisation cycles so as to produce small ferrite grains, hence improving the metal strength and toughness. However, in order to find realistic solutions, the integration of other important aspects has to be carefully considered. For instance, consider the following:

**Before rolling:** Heat treatment and the initial microstructure;

**During Rolling:** Rolling force and torque, the mill processing limitations; temperature gradients, and the inter-pass times;

**After rolling:** Phase transformation temperature, and the cooling rate.

Figure 5.1 shows how this important information is integrated and processed in MODULE 2. The design approach requires three basic components: (1) the stock

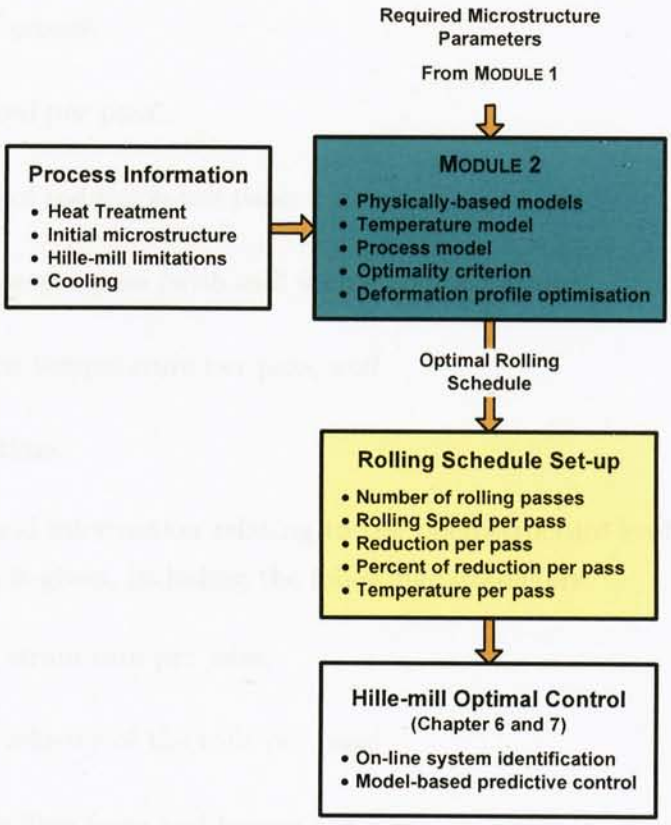


Figure 5.1: Block diagram of the proposed optimisation mechanism for the Hille-mill scheduling

model, (2) the process constraints present in the mill, and (3) an optimality criterion for scheduling. The stock model describes the microstructure evolution of the material during hot-rolling. Constraints include the limitations of the mill to carry-out the deformation process. The optimality criterion is related to achieving the required microstructure given by MODULE 1, while ensuring that the material is rolled within feasible and safe processing conditions.

The overall outcome of the proposed approach is given in the form of the rolling schedule, which can be set-up in the Hille-mill either manually or automatically by means of a user interface implemented on a PC. It is therefore assumed that, by performing the obtained schedule, the final product will have the specified properties so as to achieve correctly the desired product at the first attempt. The rolling parameters considered here are the following:

- Number of passes;
- Rolling speed per pass;
- Percentage of reduction per pass;
- Gap position per pass (with mill spring compensation);
- Deformation temperature per pass; and
- Inter-pass time.

Also, additional information relating to the microstructure evolution during and after the process is given, including the following parameters:

- Strain and strain rate per pass;
- Peripheral velocity of the rolls per pass;
- Predicted rolling force and torque per pass;
- Exit thickness per pass;
- State of the recrystallisation after the holding-time (i.e. partial or full recrystallisation) per pass;
- Recrystallised grain size per pass;
- Austenite grain size after the holding-time per pass;
- Cooling rate during austenite-ferrite transformation (considering air cooling);
- Final ferrite grain size and volume fraction of pearlite; and
- Predicted properties at room temperature.

A detailed description of the optimisation procedure of MODULE 2 will be discussed in the next section.

## 5.3 MODULE 2 - FROM THE REQUIRED MICROSTRUCTURE TO THE OPTIMAL ROLLING SCHEDULE

In the thermomechanical processing of steel alloys, the determining variables normally include the temperature ($T$), the strain ($\varepsilon$), and the strain rate ($\dot{\varepsilon}$), with the flow stress ($\sigma$) being the measurable response of the microstructure to these conditions [7]. In metal design, the aim is to achieve fine ferrite grains to add strength and toughness to the material. This is accomplished by passing the stock through the rolls so that each austenite grain undergoes a dimensional change following dynamic and static restoration processes. Such microstructural processes are well described by the physically-based equations introduced in Chapter 3, which for convenience are summarised in Table 5.1.

To predict the rolling force and torque of the stock, two Neural Networks (NN)-based models are used; such models are based on a previous Finite Element (FE) model of the rolling process which was used to generate the training data. The resulting models were simple in structure and gave good predictions across the whole

Table 5.1: Equations of the microstructure model for C-Mn steels [71],[32]

| DESCRIPTION | EQUATION |
|---|---|
| Zener-Hollomon Parameter | $Z = \dot{\varepsilon} \exp\left(\frac{Q_{def}}{RT}\right)$ |
| Fraction Recrystallised | $\begin{cases} X = 1 - \exp\left[-0.639\left(\frac{t}{t_{50}}\right)^2\right] & (\varepsilon < \varepsilon_c) \\ X = 1 - \exp\left[-0.639\left(\frac{t}{t_{50}}\right)\right] & (\varepsilon \geq \varepsilon_c) \end{cases}$ |
| Time to 50% Recrystallisation | $\begin{cases} t_{50} = 2.5 \times 10^{-19} d_0^2 \varepsilon^{-4} \exp\left(\frac{300\times10^3}{RT}\right) & (\varepsilon < \varepsilon_c) \\ t_{50} = 1.06 \times 10^{-5} Z^{-6} \exp\left(\frac{300\times10^3}{RT}\right) & (\varepsilon \geq \varepsilon_c) \end{cases}$ |
| Recrystallised Grain Size | $\begin{cases} d_{rex} = 0.5 d_0^{0.67} \varepsilon^{-1.0} & (\varepsilon < \varepsilon^*) \\ d_{rex} = 1.8 \times 10^3 Z^{-0.15} & (\varepsilon \geq \varepsilon^*) \end{cases}$ |
| Grain Growth | $d_{gg}^{10} = d_{rex}^{10} + 1.19 \times 10^{39} t \exp\left(\frac{-567\times10^3}{RT}\right)$ |
| Ferrite Grain Size | $d_\alpha = \left\{a + b\left(\frac{dT}{dt}\right)^{-0.5} + c[1 - \exp(-0.015 d_\gamma)]\right\}(1 - 0.45\sqrt{\varepsilon})$ |

rolling range as verified by experiments conducted under various processing conditions. Further details about such models can be found in [86]. The rolling force ($P$) and torque ($T_{LOAD}$) estimations can be expressed as follows:

$$P = f(T, \varepsilon, \dot{\varepsilon}, k_H, k_F), \tag{5.1}$$

$$T_{LOAD} = g(T, \varepsilon, \dot{\varepsilon}, k_H, k_F), \tag{5.2}$$

where $f(\cdot)$ and $g(\cdot)$ are nonlinear functions described by the NN's, and $k_H$ and $k_F$ are the heat coefficient and the friction coefficient of the work rolls respectively.

MODULE 2 uses an empirical temperature model to determine the temperature gradients during the whole process. Such a model is accurate enough to predict the stock temperatures up to 5 rolling passes. It can be expressed as a function of the stock thickness, the material heat transfer coefficients, and the ambient temperature, using the following differential equation:

$$\frac{dT}{dt} = (T - T_{air}) \left( \frac{-2 \times H_{air}}{h \times \sigma \times \rho} \right), \tag{5.3}$$

where $T$ is the average stock temperature and $T_{air}$ is the ambient temperature; the heat loss in air cooling ($H_{air}$), the specific heat ($\sigma_H$), and density ($\rho$) are given by the following equations respectively:

$$H_{air} = \text{BHTC} \times (T - T_{air}) + \text{EHTC} \times 5.67\text{e}^{-11} \times (T + 273)^4, \tag{5.4}$$

$$\sigma = 622 + 0.0677 \times (T - 500), \tag{5.5}$$

$$\rho = 7800 - 0.5 \times (T - 500), \tag{5.6}$$

where, in the case of the C-Mn steel alloy, BHTC = 0.0125 is the convection coefficient, whereas EHTC = 0.84 represents the material emissivity.

The rolling parameters per pass can be calculated using the strain and the strain rate applied to the material along with the mill characteristics. Therefore, the process model is comprised of the following equations:

- Rolling Speed:

$$\omega_r = \frac{60}{2\pi R_r} v_r = \frac{60}{2\pi R_r} \times \frac{\dot{\varepsilon}\sqrt{R_r(h_f - h_0)}}{\varepsilon}; \tag{5.7}$$

- Percentage of Reduction:

$$\%r = \left[ 1 - \exp\left( \frac{\varepsilon\sqrt{3}}{2} \right) \right] \times 100; \tag{5.8}$$

- Exit Thickness:

$$h_f = h_0 \times [1 - 0.01(\%r)]\,; \tag{5.9}$$

- Gap Position:

$$\theta = h_f - \frac{P}{K_{MILL}}; \tag{5.10}$$

where $v_r$ is the peripheral roll speed, $R_r$ represents the roll radius, $h_0$ is the initial thickness, $P$ is the rolling force[1], and $K_{MILL}$ is the mill structural stiffness [36].

In summary, the assembly of the physically-based models, the NN-based rolling force and torque models, the temperature model, and the process model, represents the overall model used by MODULE 2.

### *5.3.1 The Optimality Criterion for Scheduling*

To find the most appropriate design solution, the optimality criterion of MODULE 2 was formulated as a series of objective functions to be minimised in order to accomplish the required microstructure [84]. A set of $N$ objective functions can be lumped together into a single scalar optimality criterion ($J_S$) in the following form:

$$J_S = J_1^F + J_2^F + \cdots + J_N^F, \tag{5.11}$$

where

$$J_i^F = (x - x_{target})^2 \qquad i = 1, 2, \ldots N, \tag{5.12}$$

where the superscript $F$ refers to the requirements on the desired final states of the microstructure. In this case, a quadratic cost-function is used when it is desirable that a microstructure feature $x$ achieves a value $x_{target}$ at the termination of the deformation process. Using this criterion, the optimisation problem was defined as follows:

$$\begin{cases} \text{Minimise:} & J_S = \left[\frac{d_\gamma(i) - d_{target}(i)}{d_{\gamma\,\max}}\right]^2 + [1 - X(i)]^2 \qquad i = 1, 2, \ldots, n. \\ \text{Subject to:} & (i) \quad \omega_{\min} \leq \omega(i) \leq \omega_{\max}, \\ & (ii) \quad \%r_{\min} \leq \%r(i) \leq \%r_{\max}, \\ & (iii) \quad T_{LOAD}(i) \leq T_{LOAD\,\max}, \end{cases} \tag{5.13}$$

where $d_\gamma$ is the austenite grain size, $d_{target}$ represents the austenite grain size target of the rolling pass, $\omega$ is the rolling speed, $\%r$ represents the percentage of reduction,

[1]See Section 2.6 for a description of the physical meaning of the rolling force.

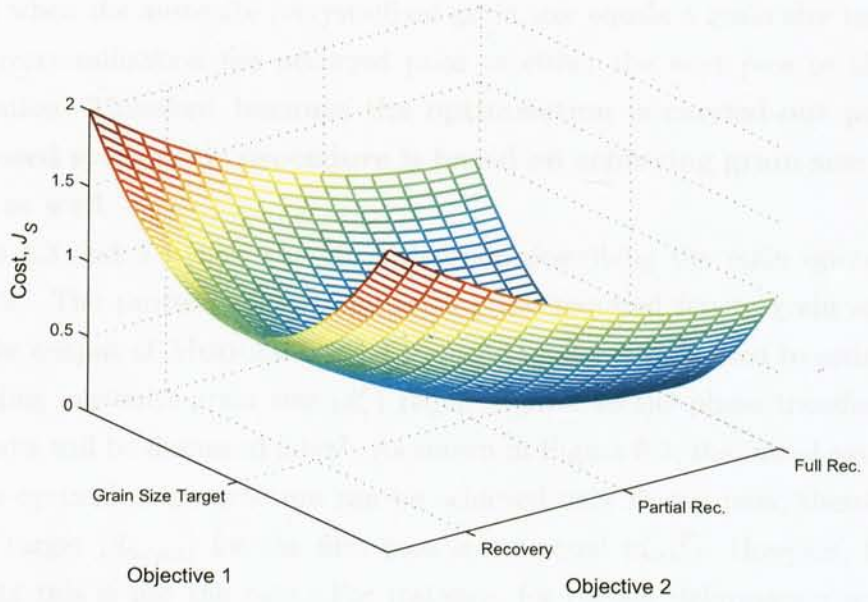


Figure 5.2: Objective space of MODULE 2

and $T_{LOAD}$ is the rolling torque, $n$ being the total number of rolling passes. The first term of Equation (5.13) minimises the variance between the desired austenite recrystallised grain size and the one required after each rolling pass. The second objective establishes that full recrystallisation has to be achieved before the next pass begins. Also, the above formulation defines the Hille-mill limitations in the form of constraints in order to create the feasible region for the optimal search. Figure 5.2 shows the objective space of MODULE 2.

Note that the decision variables of Equation (5.13) do not include either the ferrite grain size or the volume fraction of pearlite. This is due to the fact that hot-rolling takes place when the stock microstructure is in its austenite phase, and it is until the temperature drops down when the ferrite grains start to form. It is also worth noting that the microstructure optimisation of MODULE 1 restricts the pearlite content of the C-Mn alloy to less than 25%, so that it does not contribute to the strength of the material.

The optimisation can be now focused on the controlled refinement of the austenite grain size so as to lead the material microstructure to the required state at the end

of the processing. As shown in Figure 5.2, there is only one global minimum which is reached when the austenite recrystallised grain size equals a grain size target and complete recrystallisation has occurred prior to either the next pass or the phase transformation. Therefore, **because the optimisation is carried-out per pass, the proposed systematic procedure is based on achieving grain size targets per pass as well.**

Figures 5.3 and 5.4 show the block diagram describing the main operations of MODULE 2. The procedure starts by setting the required ferrite grain size ($d_\alpha^F$), which is the output of MODULE 1[2]. A FIS-based model is then used to estimate the corresponding austenite grain size ($d_\gamma^F$) required prior to the phase transformation. Such a model will be discussed later[3]. As shown in Figure 5.3, the initial assumption is that the optimal microstructure can be achieved only in one pass; therefore, the grain size target ($d_{target}$) for the first pass is set equal to $d_\gamma^F$. However, for most experiments this is not the case. For instance, for certain deformation conditions the smallest grain size achievable in one pass may be much larger than the final requirement. In this case, although GA has minimised $J_S$, the resulting deformation profile will not lead to the required microstructure, so that a new pass target must be provided by multiplying the previous target by a scaling factor ($\lambda$).

The scaling operation automatically leads to the search and optimisation of the subsequent passes, whose parameters are optimised until the final requirement is achieved (i.e. $d_\gamma$ is approximately $d_\gamma^F$). The pass counter will indicate the number of passes needed to achieve the requirement. Next, the austenite-ferrite transformation is considered by calculating the cooling rate and the transformation temperature of the material. It is assumed that no accumulated strain prior to transformation is present. Using the phase diagram shown in Chapter 3, the transformation temperature ($T_{\gamma-\alpha}$) of steels with carbon content up to 0.8% can be calculated as follows:

$$T_{\gamma-\alpha} = -231.25\ \mathrm{C} + 912. \tag{5.14}$$

The ferrite grain size ($d_\alpha$) is calculated using Equation (3.11) and is compared to its required value ($d_\alpha^F$). As the proposed mechanism uses only feedforward information of the state of the microstructure at each rolling pass, it is expected that the final microstructure will lead to a small discrepancy (off-set) between the calculated

[2]See Chapter 4.

[3]See Section 5.5.2.

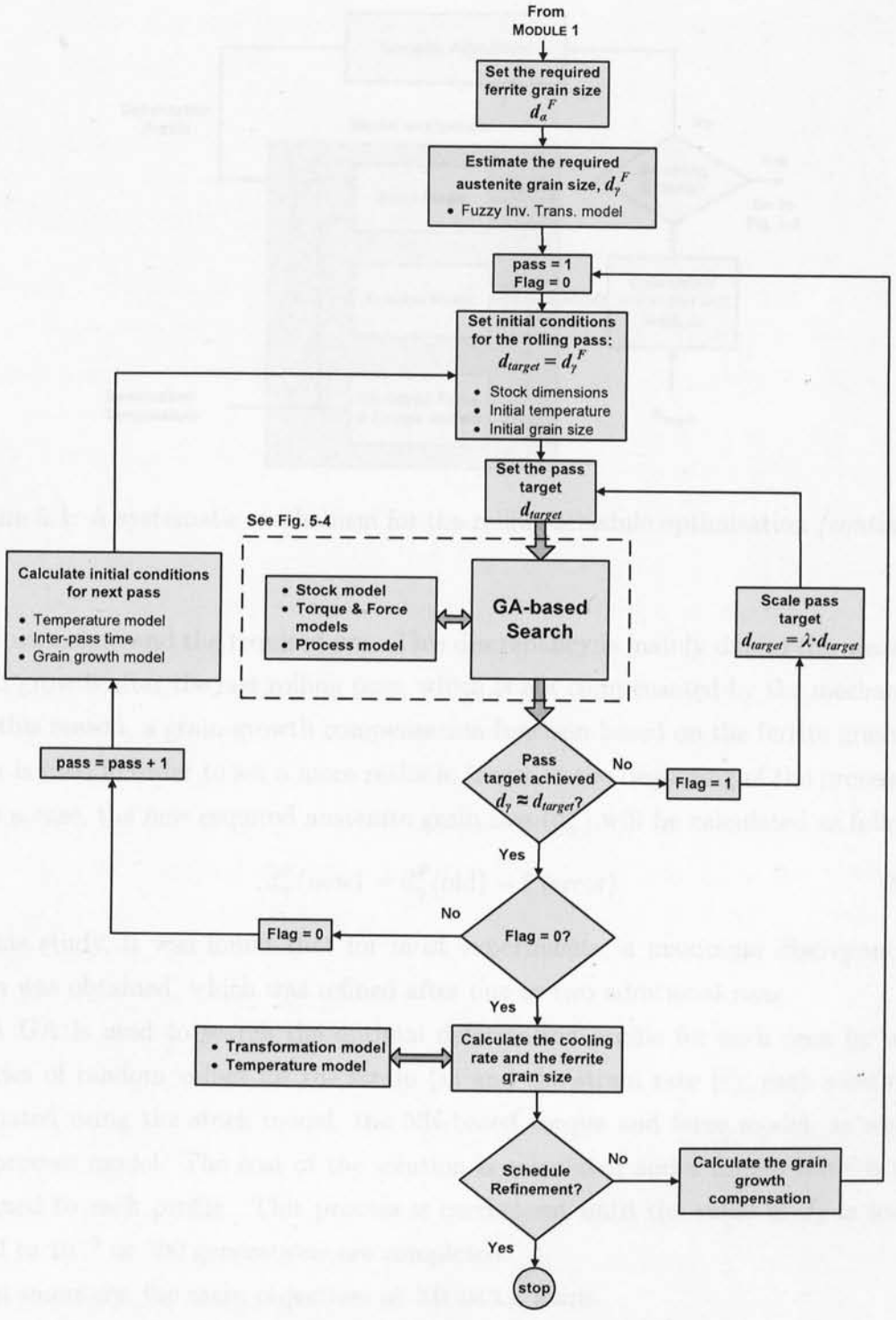


Figure 5.3: A systematic mechanism for the rolling schedule optimisation

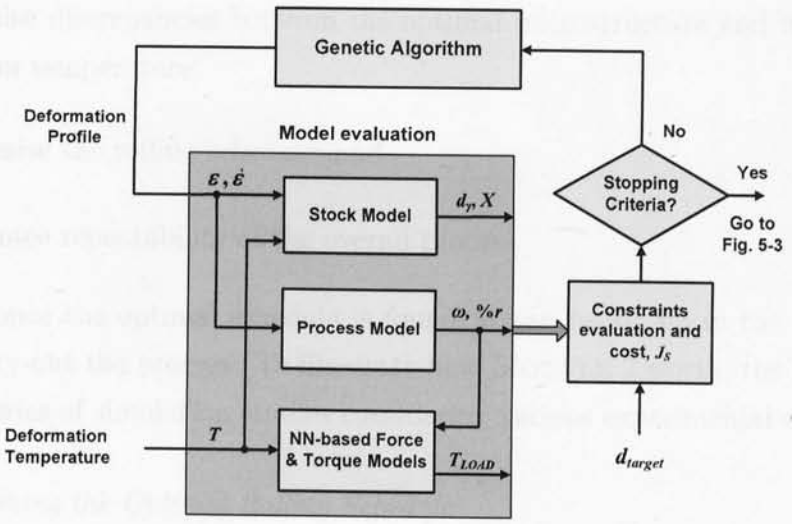


Figure 5.4: A systematic mechanism for the rolling schedule optimisation *(continued)*

microstructure and the required one. This discrepancy is mainly due to the austenite grain growth after the last rolling pass, which is not compensated by the mechanism. For this reason, a grain-growth compensation function based on the ferrite grain size error is used in order to set a more realistic target at the beginning of the process. In such a case, the new required austenite grain size ($d_\gamma^F$) will be calculated as follows:

$$d_\gamma^F(\text{new}) = d_\gamma^F(\text{old}) - \xi\,(\text{error})\,. \tag{5.15}$$

In this study, it was found that for most experiments, a maximum discrepancy of 3 $\mu$m was obtained, which was refined after one or two additional runs.

A GA is used to search the optimal deformation profile for each pass by using a series of random values for the strain ($\varepsilon$) and the strain rate ($\dot{\varepsilon}$); each solution is evaluated using the stock model, the NN-based torque and force model, as well as the process model. The cost of the solution is calculated and a fitness value is then assigned to each profile. This process is carried-out until the value of $J_S$ is less or equal to $10^{-3}$ or 300 generations are completed.

In summary, the main objectives of MODULE 2 are:

1. Find feasible rolling parameters per pass;

2. Ensure that the deformation profile leads to full recrystallisation for the grain size refinement;

3. Minimise discrepancies between the optimal microstructure and its final state at room temperature;

4. Synthesise the rolling schedule; and

5. Guarantee repeatability of the overall process.

Finally, once the optimal schedule is found, it can be set-up in the Hille-mill in order to carry-out the process. To illustrate how MODULE 2 works, the next section presents a series of simulation studies considering various experimental scenarios.

### *5.3.2 Obtaining the Optimal Rolling Schedule*

As described in Chapter 4, SISSCOR allows for a friendly interaction between the designer and the scheduling mechanism. Once the material design has been specified, the microstructure optimisation of MODULE 1 will take place as described in Chapter 4. The required microstructure is then set-up to enable MODULE 2 to compute the rolling schedule. Figures 5.5 and 5.6 show the development of the scheduling optimisation as well as its final state using SISSCOR. The "GA Development" section allows the user to graphically interpret the results of the optimisation, and by using the pop-up menu provided, it is possible to visualise up to 13 different variables, including the strain and the strain rate per pass, the rolling force and torque per pass, the chemical composition used, etc. Also, in the "Status" section, one can scan through the optimisation history to review the different targets used and see which deformation profiles were unsuccessful.

The "Final Microstructure" section provides the predicted values of important variables, such as the final austenite grain size, the percentage of recrystallised material, the estimated cooling rate during transformation, and the final ferrite grain size. Also, the calculated values for the mechanical properties are shown. Finally, the headline called "See also" in the bottom right hand corner of Figure 5.6 provides further information about rolling experiments, related publications, the IMMPETUS web-site, and other related material.

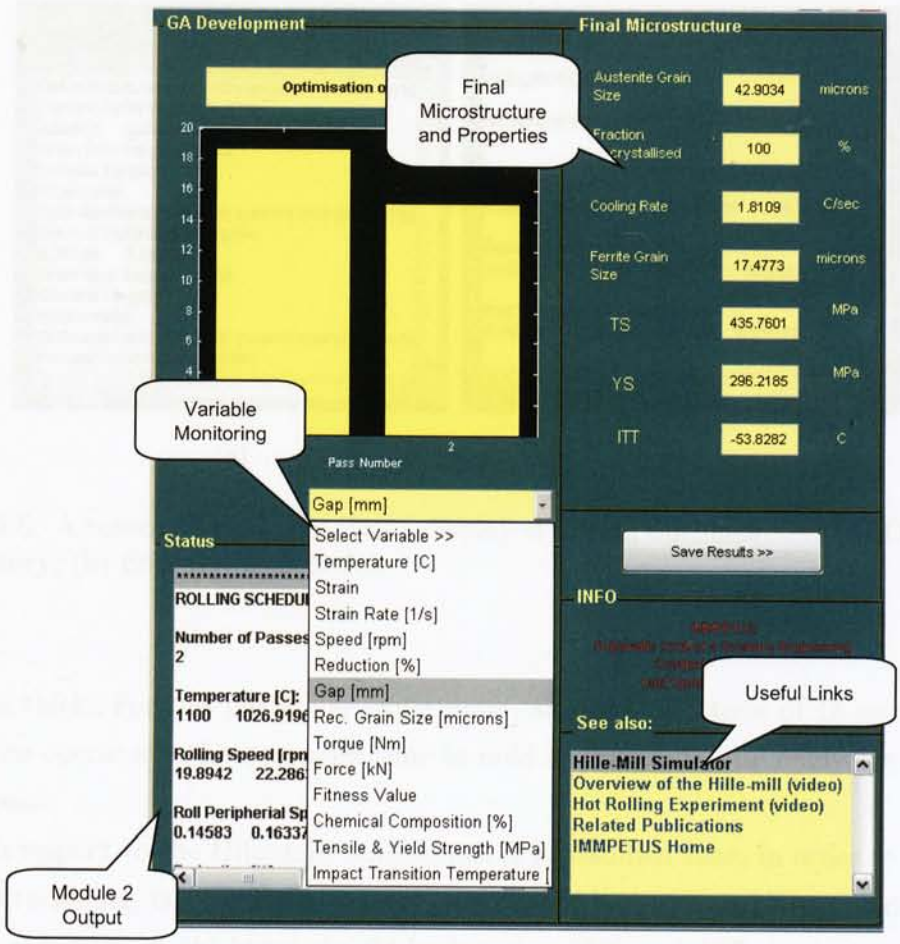


Figure 5.5: The GA development for MODULE 2 and the final microstructures and properties

## 5.4 Rolling Schedule Optimisation Results

SISSCOR was used to evaluate MODULE 2 for different study cases. The aim of the optimisation is to find the best rolling schedule that will yield the required microstructure. Let us first take the output of MODULE 1 for Case 1 of Table 4.1, in which a ferrite grain size of 13 $\mu$m[4] was required in order to achieve a TS of 450 MPa. To begin the scheduling process, let us assume that after heating, the austenite grain size was 260 $\mu$m, and that the initial temperature for rolling was 1100°C. Additionally, the initial dimensions of the stock were the following: 150 mm long, 50 mm wide, and

[4]The target values were rounded-off.

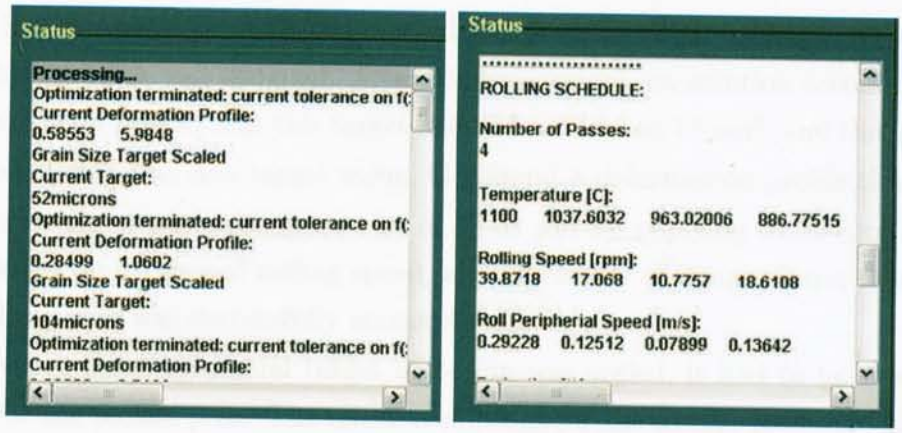


(a) (b)

Figure 5.6: A screen shot of Test/Data displayed during optimisation. (a) Optimisation history; (b) final rolling schedule

25.4 mm thick. For this particular experiment, an inter-pass time of 15 seconds was set for the operator to have enough time to hold the stock and be ready for the next rolling pass.

With respect to the Hille-mill limitations, it is assumed that, in order to perform a 'safe' processing, the rolling speed per pass should be between 10 rpm and 40 rpm, and the reduction in thickness should be between 15% and 40%, hence producing a rolling torque no higher that 3000 kNmm per pass. The GA parameters were set as follows: a random initial population with a uniform distribution was used with 20 individuals. Each individual received a fitness score which was scaled in order to rank the population, leading to the rank of the most fit individual to be 1, the next most fit being 2, and so on. This is done in order to remove the effect of the spread of the raw scores. GA would stop its search when either the value of Equation (5.13) was less or equal to $10^{-3}$ or 300 generations were complete.

Referring to the block diagram of Figure 5.3, the scheduling mechanism started with a required ferrite grain size of 13 $\mu$m. This value was transformed into a required austenite grain size, which for this example was estimated at 24 $\mu$m[5]. This value represented the initial target of the process (i.e. $d_{target}$). Next, assuming that the target could be achieved in only one pass, GA started its search considering the

[5]This value was estimated using the fuzzy inverse transformation model of Section 5.5.2.

above initial conditions and the selected constraints. Each solution was evaluated and a fitness value was assigned. After 300 generations, no solution accomplished the grain size of 24 $\mu$m, so that this target had to be scaled to 73 $\mu$m[6], and the GA search resumed. Using this new target value, GA found a deformation profile that led to a full recrystallised austenite grain size of 73.03 $\mu$m by applying 21.80% of reduction in thickness, at 10 rpm of rolling speed, and at 1100°C of temperature; therefore the first rolling pass was successfully accomplished.

However, since the initial target of 24 $\mu$m was scaled, it had to be re-set as the target for the second pass. The initial conditions for the second pass were calculated, which included the grain growth during the holding time, initial stock thickness, and the temperature gradients. With this new information, GA performed the same procedure as in the first pass, until the initial target was eventually achieved. Table 5.2 shows the resulting rolling schedule for this example. It is worth noting that 4 rolling passes were needed to achieve the desired microstructure with a final ferrite grain size of 12.46 $\mu$m, which is very close to the requirement.

The results shown in Table 5.2 reveal that no constraints violation was encountered in any of the rolling passes in terms of the rolling speed, the percentage of reduction, or the rolling torque. Furthermore, full recrystallisation was achieved after each rolling pass leading to a homogenous austenite microstructure prior to transformation.

Figure 5.7 shows a computer simulation of the microstructure evolution using the above rolling parameters. The simulation was carried-out using the Sheffield-Leicester Integrated Model for Microstructure Evolution in Rolling (SLIMMER), which is a computing platform based on a finite difference temperature model that allows for calculating the microstructural changes at different sections of the stock, including the centre and the surface [7].

As shown in Figure 5.7, the amount of deformation applied to the stock affected the static restoration process that occurred during the inter-pass time, leading to a complete recrystallisation after each pass. Notice that, when recrystallisation was completed, the recrystallised grains grew at a rate depending on the temperature and the holding-time prior to the next rolling pass. The effective deformation profile obtained by the scheduling mechanism was accurate enough to control the microstructure events during the whole process.

[6]See Section 5.5.1 The Scaling Factor ($\lambda$).

Table 5.2: Rolling schedule and microstructure parameters for Case 1

| | Rolling Pass No. | | | |
|---|---|---|---|---|
| | 1 | 2 | 3 | 4 |
| Temperature (°C) | 1100 | 1045 | 983 | 920 |
| Strain | 0.284 | 0.422 | 0.294 | 0.400 |
| Strain Rate ($s^{-1}$) | 1.05 | 4.62 | 5.84 | 2.51 |
| Rolling Speed (rpm) | 10.00 | 30.84 | 40.00 | 12.67 |
| Reduction (%) | 21.80 | 30.61 | 22.48 | 29.30 |
| Gap Position (mm) | 19.61 | 13.44 | 10.39 | 7.10 |
| Exit Thickness (mm) | 19.86 | 13.77 | 10.68 | 7.55 |
| Torque (kNmm) | 1122 | 1716 | 1445 | 2750 |
| Force (kN) | 129 | 169 | 147 | 230 |
| Grain Target ($\mu$m) | 73 | 21 | 22 | 14 |
| Recrystallised Grain ($\mu$m) | 73.03 | 21.17 | 22.12 | 13.99 |
| Austenite Grain ($\mu$m) | 73.93 | 46.05 | 34.63 | 24.56 |
| Fraction Recrystallised (%) | 100 | 100 | 100 | 100 |
| Predicted Microstructure and Properties at Room Temperature | | | | |
| Ferrite Grain Size ($\mu$m) | | | | 12.46 |
| Pearlite Fraction (%) | | | | 5 |
| Tensile Strength (MPa) | | | | 451.07 |

As the final austenite grain size of 24.56 $\mu$m started to transform into ferrite grains, the air cooling rate was estimated using the temperature model. The estimated air cooling rate was 3.10°K/s and led to a ferrite grain size of 12.46 $\mu$m. Using this value to calculate TS yields 451.07 MPa[7], which is in good agreement with the desired design.

As discussed in Chapter 3, when the deformation is finished in the austenite region (as in this case), the dislocation density in the ferrite structure is relatively low. When the deformation is extended to the austenite-ferrite or the ferrite region, the dislocation strengthening becomes much more significant. The dislocation contribution to strengthening is very complex, and usually is an effect of the interactions among forest, mobile dislocations, and the substructure. When the last rolling pass

[7]This value was calculated using the Neural-Fuzzy model developed in Chapter 4.

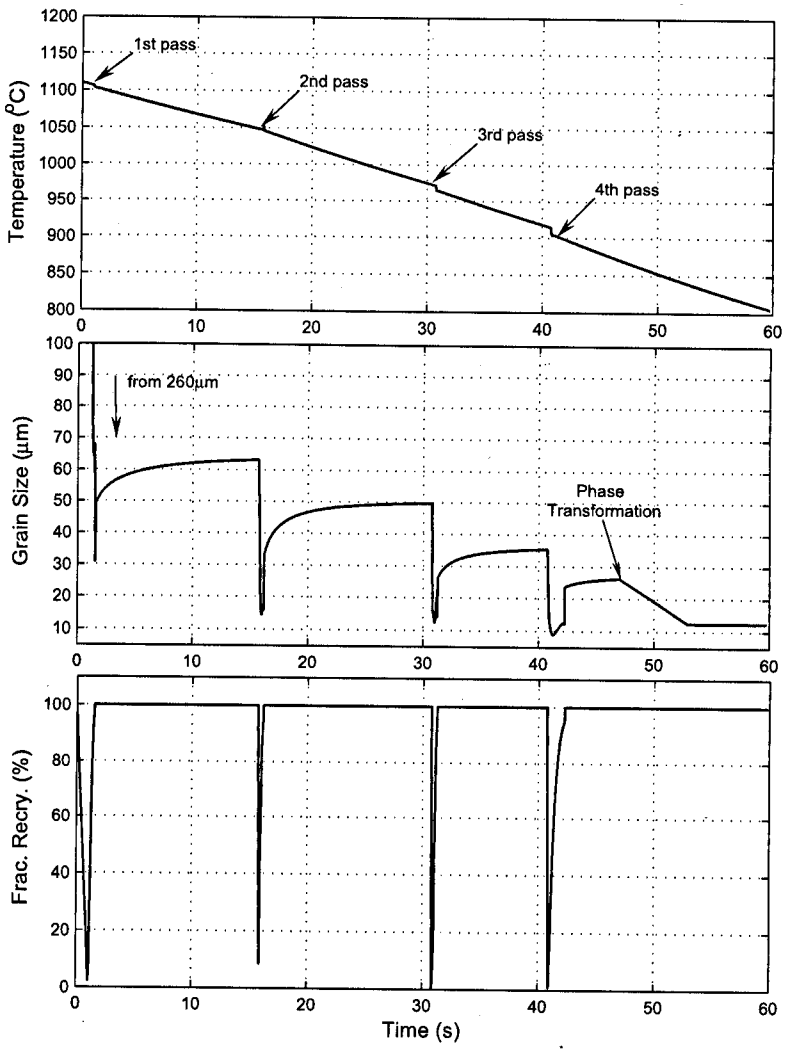


Figure 5.7: Computer simulation of the microstructure evolution for Case 1 using SLIMMER

is in the ferrite region, it is difficult to distinguish between the contributions due to precipitation and dislocation hardening leading to inaccurate predictions of TS and YS. Therefore, it is necessary to have full recrystallisation of the austenite grains with no accumulated strain, and ensure that the last rolling pass is carried-out before the stock temperature reaches its transformation temperature. In this case, the austenite-ferrite transformation temperature was 870°C.

To observe the sensitivity of the optimisation process when small changes in the material microstructure are required, the next simulation study focused on Case 5

and 8 of Table 4.1, where a ferrite grain size of 14 $\mu$m and 15 $\mu$m were required respectively. Both microstructures were optimised to produce a C-Mn steel alloy with the following characteristics: 450 MPa of TS, 310 MPa of YS, and -70°C for ITT. In this study, the same initial conditions used in Case 1 were assumed. Tables 5.3 and 5.4 show the resulting rolling schedules. It is worth noting that only 3 rolling passes were needed to achieve the requirements.

Figure 5.8 shows the microstructure evolution of the rolled material using the obtained rolling schedules. It can be seen that the static recovery after the first pass was almost identical for both cases due to similar first-pass reductions (Case 5: 32.92%; Case 8: 31.22%). However, the differences in the temperature gradients led to different deformation profiles for the subsequent passes. Prior to phase transformation,

Table 5.3: Rolling schedule and microstructure parameters for Case 5

| | Rolling Pass No. | | |
|---|---|---|---|
| | 1 | 2 | 3 |
| Temperature (°C) | 1100 | 1037 | 959 |
| Strain | 0.461 | 0.588 | 0.410 |
| Strain Rate ($s^{-1}$) | 5.48 | 3.88 | 4.26 |
| Rolling Speed (rpm) | 39.27 | 19.62 | 20.72 |
| Reduction (%) | 32.92 | 39.94 | 29.90 |
| Gap Position (mm) | 16.77 | 9.80 | 6.74 |
| Exit Thickness (mm) | 17.03 | 10.23 | 7.17 |
| Torque (kNmm) | 1270 | 2915 | 2478 |
| Force (kN) | 133 | 221 | 219 |
| Grain Target ($\mu$m) | 45 | 20 | 15 |
| Recrystallised Grain ($\mu$m) | 44.9 | 20.0 | 14.9 |
| Austenite Grain ($\mu$m) | 58.18 | 41.36 | 27.97 |
| Fraction Recrystallised (%) | 100 | 100 | 100 |
| Predicted Microstructure and Properties at Room Temperature | | | |
| Ferrite Grain Size ($\mu$m) | | | 14.02 |
| Tensile Strength (MPa) | | | 448.94 |
| Yield Strength (MPa) | | | 319.82 |
| Imp. Trans. Temp. (°C) | | | -63.20 |

Table 5.4: Rolling schedule and microstructure parameters for Case 8

| | Rolling Pass No. | | |
|---|---|---|---|
| | 1 | 2 | 3 |
| Temperature (°C) | 1100 | 1040 | 975 |
| Strain | 0.432 | 0.319 | 0.335 |
| Strain Rate ($s^{-1}$) | 1.34 | 5.44 | 1.61 |
| Rolling Speed (rpm) | 10.00 | 40.00 | 10.03 |
| Reduction (%) | 31.22 | 24.17 | 25.22 |
| Gap Position (mm) | 17.18 | 12.99 | 9.55 |
| Exit Thickness (mm) | 17.46 | 13.24 | 9.90 |
| Torque (kNmm) | 1733 | 1294 | 2007 |
| Force (kN) | 147 | 126 | 180 |
| Grain Target ($\mu$m) | 48 | 24 | 19 |
| Recrystallised Grain ($\mu$m) | 47.99 | 24.00 | 18.9 |
| Austenite Grain ($\mu$m) | 59 | 44.60 | 32.98 |
| Fraction Recrystallised (%) | 100 | 100 | 100 |
| Predicted Microstructure and Properties at Room Temperature | | | |
| Ferrite Grain Size ($\mu$m) | | | 14.7 |
| Tensile Strength (MPa) | | | 443.29 |
| Yield Strength (MPa) | | | 309.71 |
| Imp. Trans. Temp. (°C) | | | -57.30 |

each rolling schedule led to a successful refinement of the austenite gain size to finally accomplish the requirements.

As shown in Figure 5.8, the different temperature gradients and deformation profile led to a different final austenite grain size, which was 27.97 $\mu$m for Case 5, whereas for Case 8 it was 32.98 $\mu$m. As the temperature dropped, the final ferrite grain size was 14.02 $\mu$m and 14.7 $\mu$m for Case 5 and 8 respectively, which in terms of the mechanical properties, the final material deemed to be very close to the desired design. Furthermore, the predictions of temperature and microstructural development provided by the proposed mechanism were in good agreement with the simulation results observed using SLIMMER.

Clearly, the task of setting-up the rolling schedule was not intuitively obvious, considering that small differences in the processing led to different microstructures and

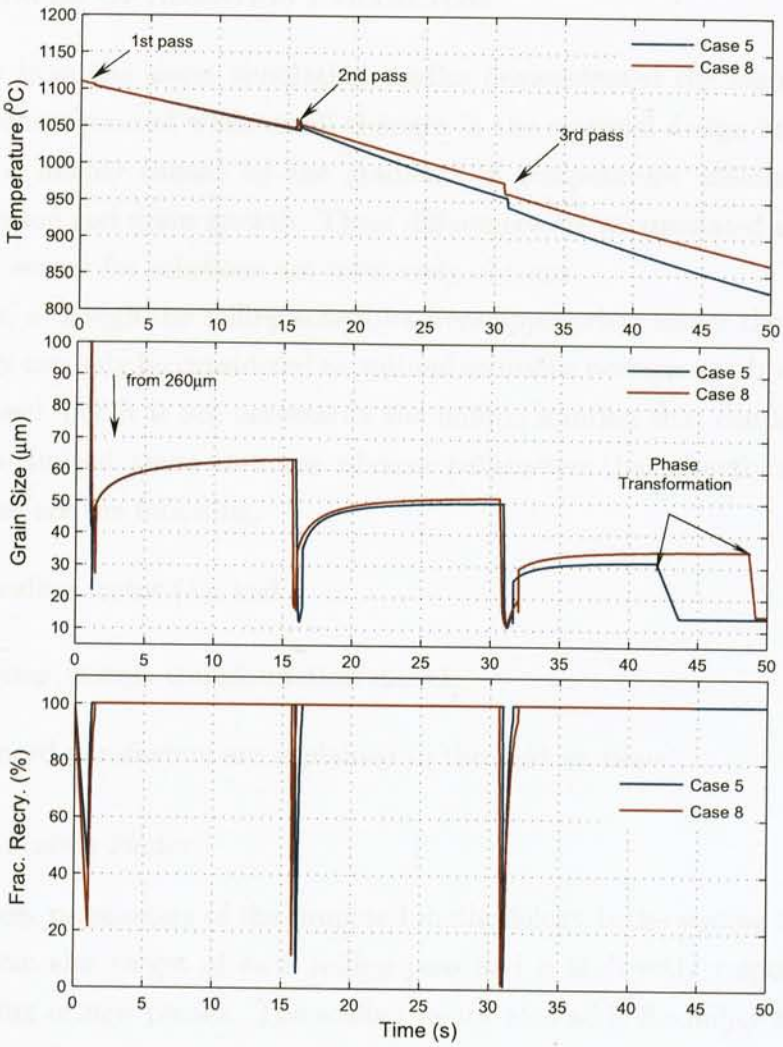


Figure 5.8: Computer simulation of the microstructure evolution for Case 5 and Case 8 using SLIMMER

mechanical properties. Although the rolling schedules shown in this section worked well under the given deformation conditions, the proposed approach uses other advanced parameters that add flexibility to the mechanism and may lead to a different rolling route. This is discussed in the next section.

## 5.5 Advanced Optimisation Parameters

The results from the above simulation studies demonstrated the high sensitivity of the optimisation process when small changes in the material design are made. Such sensitivity is mainly caused by the gradients of temperature affecting the rate of recrystallisation and grain growth. These differences are accumulated after each pass making the search for solutions not intuitively obvious.

However, although the rolling schedules were appropriate under the specified conditions, they can only be considered as optimal solutions because an objective function was minimised, but it is not necessarily the unique solution that can lead to the desired design. Indeed, there are some advance parameters that directly affect the final result. These are the following:

1. The scaling factor ($\lambda$); and

2. The fuzzy inverse transformation model.

These advanced parameters are explained in the next sections.

### *5.5.1 The Scaling Factor*

One of the key parameters of the proposed methodology is the scaling factor. It controls the grain size target of each rolling pass and it is directly responsible for the recommending of new passes. The scaling factor also adds flexibility to the optimisation by providing a systematic target adaptation mechanism. As shown in Figure 5.3, when a pass target cannot be achieved by any solution, it means that it is not physically possible to refine the austenite grain size down to the selected target value under the current operating conditions. Therefore, a new pass target is set by scaling the unsuccessful target. Depending on the deformation conditions, the pass target may be scaled several times until GA is able to find a feasible solution. However, the pass will be declared infeasible should the pass target value not be accomplished after several unsuccessful trials.

The scaling factor ($\lambda$) is a varying parameter defined as the ratio between the new pass target and the unsuccessful one. It can be expressed by the following equation:

$$\lambda(i) = \frac{d_{target}(i+1)}{d_{target}(i)} \qquad i = 1, 2, \ldots, n_t, \tag{5.16}$$

where

$$d_{target}(i+1) = d_{\gamma}^{F} + \eta(n_t \times \Delta d), \tag{5.17}$$

and $\Delta d = d_0 - d_{\gamma}^{F}$, $d_0$ being the initial grain size for the pass; $n_t$ is the number of trials and $\eta$ is a weighting factor used to *modulate* the scaling. This study showed that values of $\eta$ between 0.1 and 0.5 led to satisfactory and consistent results. It is clear that the new grain size target cannot be bigger than or equal to the initial grain size of the pass.

To illustrate the influence of the scaling factor, let us consider a rolling schedule in which the initial grain size for the first pass is 260 $\mu$m and the initial pass target is set to 24 $\mu$m. It is expected that the GA will not find a deformation profile with the sufficient strain to refine the grain size to this target and, at the same time, satisfy the selected constraints for the rolling torque and the percentage of reduction. Therefore, using Equation (5.17) with $\eta = 0.12$, a new target of 52 $\mu$m will be set, and GA resumed. For this new target, the GA may find a solution which will refine the grain size down to approximately 52 $\mu$m. This will automatically create the need for new rolling passes. However, let us assume that even with this new pass target, GA is not able to find a solution; in such a case 52 $\mu$m will be scaled to 80 $\mu$m, and then 109 $\mu$m, and so on until 222 $\mu$m before declaring the pass infeasible.

The dynamics of the scaling factor is shown in Figure 5.9 for different modulating values. As shown in this figure, by varying $\eta$ one can provide the GA with different targets values so that the search becomes more flexible when finding a solution. This was demonstrated by the rolling schedules obtained for Case 1, which required a final ferrite grain size of 13 $\mu$m. Tables 5.5 and 5.6 show the rolling schedules obtained for $\eta = 0.05$ and $\eta = 0.3$ respectively (see Table 5.2 for $\eta = 0.12$). It is worth noting that both rolling schedules led to the desired microstructure even though the rolling parameters were significantly different. This emphasises the fact that the optimal solution is by no means intuitively obvious but rather an exhaustive search process that needs accurate knowledge of both the material and the mill.

Figure 5.10 shows the microstructure development of the rolled material during the process using different $\eta$'s for Case 1. Note that the main differences in the refinement of the austenite grain size are due to the amount of strain applied to the stock per pass and the resulting cooling rates (5.5°K/s with $\eta = 0.05$; 4.3°K/s with $\eta = 0.3$). While the four-pass rolling schedule used a light deformation per pass, the three-pass schedule required more strain to achieve the targets. However, care

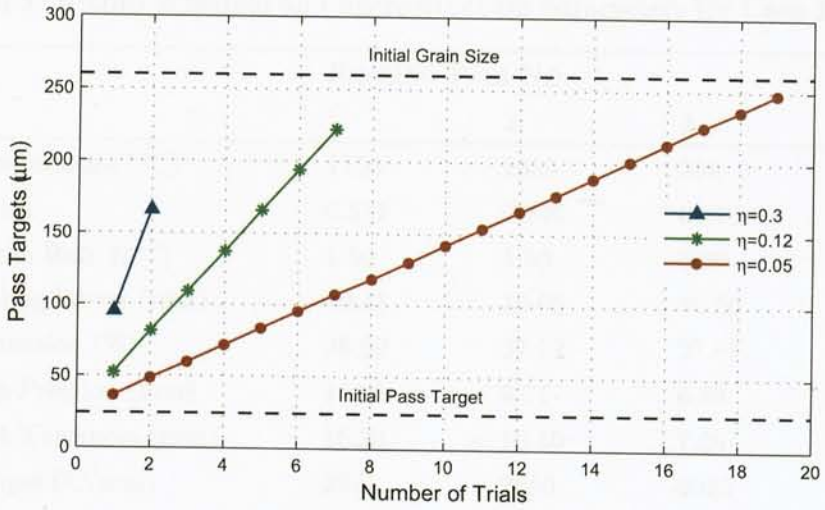


Figure 5.9: New grain targets (and scaling factors) for different $\eta$'s

should be taken when using a high modulating factor (e.g. $\eta > 0.5$) because of the fact that the optimality criterion will be limited to find small amounts of reductions per pass (i.e. less than 15%), which may result in grain coalescence instead of grain refinement. At the end of the process, both schedules delivered similar results in terms of the ferrite grain size (13.03 $\mu$m with $\eta = 0.05$; 13.68 $\mu$m with $\eta = 0.3$), and mechanical properties (448.89 MPa with $\eta = 0.05$; 446.58 MPa with $\eta = 0.3$), which are very close to the desired design (13 $\mu$m and 450 MPa).

### *5.5.2 Fuzzy Inverse Transformation Model*

Another important aspect of the proposed mechanism is the estimation of the initial austenite grain size target, which is calculated using the required ferrite grain size. As shown in Figure 5.3, a FIS-based model is used to make a static mapping between the grain size before and after the austenite-ferrite transformation.

As already mentioned, although the ferrite grain size is one of the major structural parameters affecting the properties of most steels, there is still little quantitative information to accurately represent the ferrite grain size as a function of the austenite grain size. Experimental results published in the literature show that the ferrite grain size increases with the austenite grain size [68],[52],[32]. Such results also emphasise the importance of the retained strain in the austenite grains at the time of transfor-

Table 5.5: Rolling schedule and microstructure parameters for Case 1, $\eta = 0.05$

| | Rolling Pass No. | | |
|---|---|---|---|
| | 1 | 2 | 3 |
| Temperature (°C) | 1100 | 1035 | 956 |
| Strain | 0.517 | 0.546 | 0.376 |
| Strain Rate ($s^{-1}$) | 1.50 | 1.93 | 5.99 |
| Rolling Speed (rpm) | 10.41 | 10.00 | 30.50 |
| Reduction (%) | 36.09 | 37.72 | 27.81 |
| Gap Position (mm) | 15.91 | 9.71 | 6.88 |
| Exit Thickness (mm) | 16.23 | 10.10 | 7.29 |
| Torque (kNmm) | 2071 | 2650 | 2025 |
| Force (kN) | 164 | 203 | 209 |
| Grain Target ($\mu$m) | 40 | 22 | 16 |
| Recrystallised Grain ($\mu$m) | 40.13 | 22.00 | 15.94 |
| Austenite Grain ($\mu$m) | 57.26 | 40.84 | 30.86 |
| Fraction Recrystallised (%) | 100 | 100 | 100 |
| Predicted Microstructure and Properties at Room Temperature | | | |
| Ferrite Grain Size ($\mu$m) | | | 13.03 |
| Tensile Strength (MPa) | | | 448.89 |

mation. In addition to these variables, the cooling rate through the transformation is important in determining accurately the ferrite grain size. At this stage it is worth noting that Equation (3.11) is an empirical description of how the phase transformation takes place, but more research has to be done to include other phenomena such as the differences in residual element contents or the appearance of the Widmanstätten ferrite at large austenite grain sizes [52].

A FIS-based model is used here to invert the phase transformation and estimate the austenite grain size from the ferrite grain size given the conditions present in the Hille-mill. To develop such a model, it was necessary to state some important assumptions. Firstly, because of the fact that no temperature control is available in the Hille-mill, only air-cooling can be considered for all experiments; furthermore, it is known that for slabs of 20-60 mm in thickness, the cooling rate has little influence on the ferrite grain size [71]. Secondly, if full static recrystallisation of the austenitic

Table 5.6: Rolling Schedule and Microstructure development for Case 1, $\eta = 0.3$

| | Rolling Pass No. | | | |
|---|---|---|---|---|
| | 1 | 2 | 3 | 4 |
| Temperature (°C) | 1100 | 1047 | 994 | 939 |
| Strain | 0.233 | 0.273 | 0.269 | 0.390 |
| Strain Rate ($s^{-1}$) | 3.78 | 1.14 | 5.04 | 5.98 |
| Rolling Speed (rpm) | 39.87 | 10.00 | 39.49 | 34.26 |
| Reduction (%) | 18.28 | 21.10 | 20.78 | 28.05 |
| Gap Position (mm) | 20.58 | 16.10 | 12.71 | 8.89 |
| Exit Thickness (mm) | 20.75 | 16.37 | 12.96 | 9.33 |
| Torque (kNmm) | 861 | 1333 | 1310 | 2072 |
| Force (kN) | 88 | 137 | 133 | 223 |
| Grain Target ($\mu$m) | 89 | 37 | 25 | 15 |
| Recrystallised Grain ($\mu$m) | 88.96 | 36.99 | 25.04 | 14.93 |
| Austenite Grain ($\mu$m) | 89.13 | 48.53 | 37.82 | 26.14 |
| Fraction Recrystallised (%) | 100 | 100 | 100 | 100 |
| Predicted Microstructure and Properties at Room Temperature | | | | |
| Ferrite Grain Size ($\mu$m) | | | | 13.68 |
| Tensile Strength (MPa) | | | | 446.58 |

microstructure has taken place before transformation, then it can be assumed that there is no accumulated strain that can affect the ferrite grain size. This leads to the estimation of the ferrite grain size on the basis of the austenite grain size solely.

Data generated using Equation (3.11) and experimental observations found in the current literature were used to generate a Mamdami-type fuzzy model, which contains fuzzy sets both in the *premise* and the *consequent* part of the fuzzy rules. The fuzzy model was developed following the guidelines proposed in [88], which led to the following fuzzy rules:

$R_1$ : If Ferrite Grain Size is *Very Small*, Then Austenite Grain Size is *Very Small*;
$R_2$ : If Ferrite Grain Size is *Small*, Then Austenite Grain Size is *Small*;
$R_3$ : If Ferrite Grain Size is *Medium*, Then Austenite Grain Size is *Medium*;
$R_4$ : If Ferrite Grain Size is *Large*, Then Austenite Grain Size is *Large*;
$R_5$ : If Ferrite Grain Size is *Very Large*, Then Austenite Grain Size is *Very Large*.

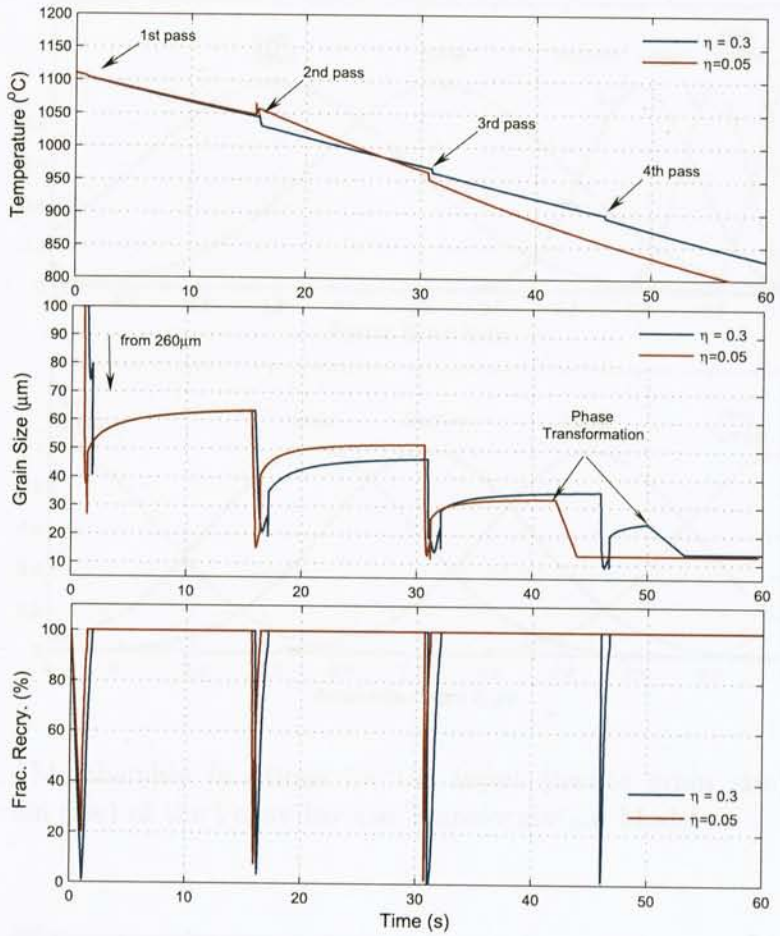


Figure 5.10: Microstructure development for Case 1 under different $\eta$'s

It is important to mention that the definition of the fuzzy labels are not the same from the austenite to ferrite grain size as shown in Figure 5.11, which is a plot of the membership functions. Note that the universes of discourse are all normalised. Figure 5.12 presents the input-output correlation described by the developed FIS, as well as the data used. As will be demonstrated by hot-rolling experiments and metallographic analysis, the developed fuzzy model has an acceptable accuracy.

## 5.6 Concluding Remarks

This chapter proposed a systematic approach for solving the scheduling problem of the Hille-mill. This mechanism provided effective rolling schedules based on the mi-

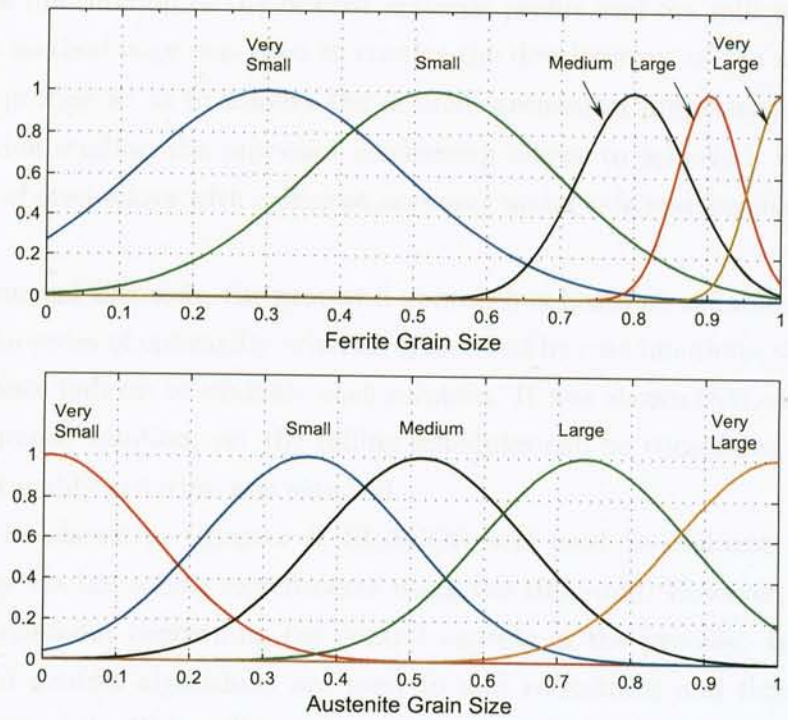


Figure 5.11: Membership functions for the input (ferrite grain size) and output (austenite grain size) of the Fuzzy Inverse Transformation Model

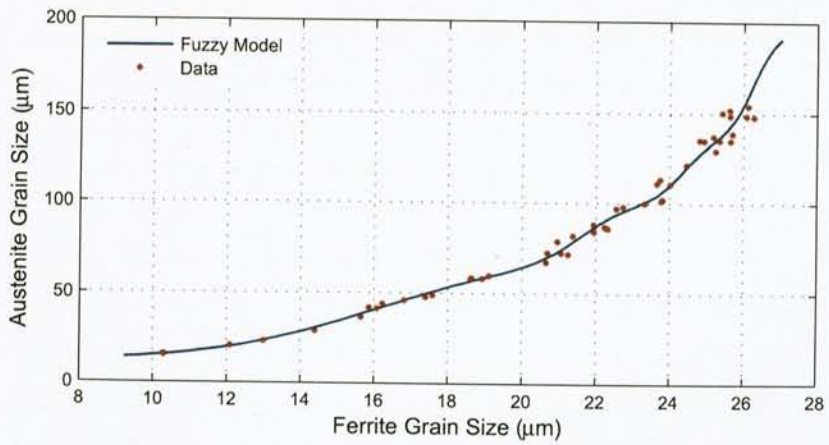


Figure 5.12: Fuzzy Inverse Transformation Model considering air-cooling rate and no accumulated strain prior to phase transformation

crostructure information of the desired material profile and the mill working conditions. This methodology was used to control the development of the microstructure during the process so as to achieve the desired mechanical properties. As shown by the simulation studies, the proposed mechanism allows to achieve a *right-first-time* production of steel alloys with sufficient accuracy under safe and feasible deformation conditions.

Unlike current methods, the proposed approach is based on reliable models of the process and a series of optimality criteria represented by cost functions, which are used as performance indexes to evaluate each solution. It was shown that, although there exists not unique solution, yet the rolling schedules can be considered as "optimal" since an optimality criterion was satisfied.

As will be shown in Chapter 8, SISSCOR was used to evaluate the proposed methodology via hot-rolling experiments using the Hille-mill. However, further work was first carried-out concerning the control aspects of the process. In this regard, sophisticated control algorithms are used to add robustness and flexibility to the control system of the Hille-mill in order to guarantee optimal performance during the rolling experiments. This will be discussed in the next two chapters.

# Chapter 6

# Mathematical Modelling and Simulations Associated with the Hille-mill

## 6.1 Introduction

This chapter focuses on the mathematical modelling of the hot-rolling Hille-mill. The aim is to describe the theoretical background and the main framework of the mechanical model with its critical system parameters such as the inertia of the different rotational parts, friction coefficients, and stiffness. Additionally, computer simulations are presented in order to gain a *real* insight into the mill dynamical performance and define the important aspects to consider when solving the rolling speed control problem. Hence, the main objective of such a model development is to analyse the system dynamics so that advanced control strategies and decision-making procedures for the mill operation can be investigated and implemented.

## 6.2 A General Overview of the Hille-mill

Figure 6.1 shows the hot-rolling Hille-mill located in the Laboratory of the Sheffield Department of Engineering Materials. The mill is currently used by IMMPETUS for research on steel and aluminium microstructures through rolling experiments. Because of the importance of the steel-making processes in modern industry, this experimental laboratory-scale mill has been the object of several investigations in different engineering areas at The University of Sheffield, including the Department of Automatic Control and Systems Engineering.

During the last three years the mill has been modernised and fully instrumented to conduct complex rolling schedules which may include up to 10 rolling passes at various

Figure 6.1: The hot-rolling Hille-mill located at the Engineering Materials Laboratory

speeds, deformation profiles, and temperatures. The main aim is to investigate the evolution of steel and aluminium microstructures during hot-rolling and thus provide knowledge for the development of physically-based models, structure characterisation, and metal design. This "world-class" IMMPETUS facility has materialised because of the integration of the three main disciplines of Mechanical Engineering, Engineering Materials, and Automatic Control and Systems Engineering, whose research on the Hille-mill can be seen in the large number of publications produced during the last few years.

The Hille-mill is a one-stand 50-tons hot-rolling mill with a maximum torque of 3467 Nm available in two main work rolls which have direct contact with the rolled product, hence producing a sequential reduction in thickness. Figure 6.2 illustrates schematically the main configuration of the Hille-mill. The rolls, whose individual diameter measures 139 mm, are within the mill housing which is designed to contain

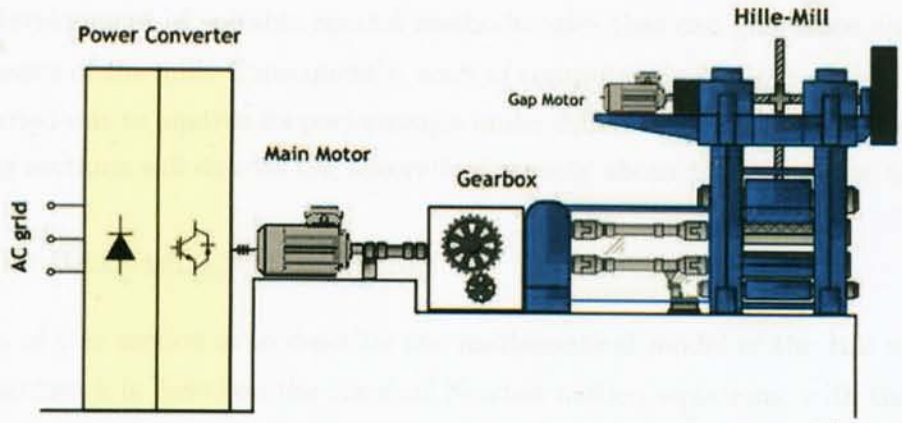


Figure 6.2: A schematic illustration of the Hille-mill

the mill stand components and to withstand the rolling load. As shown in Figure 6.2, the main electric drive (i.e. power converter and main motor) provides rolling in both directions with adjustable speed (from 1 to 60 rpm) and rolling torque. The drive also includes a roll gap actuator to adjust the required gap between the work rolls. The gearbox is as well used both as a means of coupling the motor shaft with the Hille-mill, and to reduce the speed and increment the available torque in the work rolls.

As already mentioned, the purpose of the Hille-mill is to produce a plate from a preheated slab with a specific thickness and with the required microstructure. This is very important in thermomechanical processing because, as discussed in the previous chapters, one can define a correlation between the material properties and its microstructure with the deformation profile applied during rolling. It has also been discussed that the design of microstructure is related not only to the alloy composition and the heat treatment, but also to the hot-deformation process which leads to improved strength, ductility, and toughness of the worked product [6]. Therefore, precise knowledge of the process critical variables such as the rolling speed, the amount of deformation, the rolling force and torque, among others, is needed for the optimal development of the microstructure and eventually the desired characteristics of the final product.

The accurate understanding of the dynamics involved in Hille-mill can be only obtained by means of mathematical analysis and study of the different working conditions that take place during rolling experiments. Acquiring such a knowledge leads

to the development of suitable control methodologies that can guarantee an optimal performance of the mill. Consequently, a set of computer simulations of the Hille-mill were carried-out to analyse its performance under different operating conditions. The following sections will discuss the theoretical aspects about this particular topic.

## 6.3 The Hille-mill 3-Mass-Model

The aim of this section is to describe the mathematical model of the Hill-mill. The main framework is based on the classical Newton motion equations, with the critical model parameters, such as the inertia of different rotational parts, the friction coefficients, and the stiffness. For modelling purposes, the mechanical elements (shafts and gears) were treated as flexible links to obtain a more detailed representation, so that the effects of torsional spring rates are present in the shafts and affect the rolling speed.

Figure 6.3 shows an equivalent diagram of the Hille-mill rotating system based on the real configuration. As shown in this figure, the main critical parameters considered for modelling are: the inertia ($J$) of the shafts, the friction ($B$) in the couplings, and the stiffness ($K$); $\omega$ represents the shaft speed. The subscripts $r$, $g$, and $m$ represent the variables associated to the roll shaft, gear shaft, and motor shaft respectively; $R_g$ is the gearbox ratio. It is also assumed that in the roll shaft, the dry friction ($B_{DRY}$) is also present and it is much bigger that the viscous friction, hence, a nonlinear effect is present in the system which produces torque in the same direction of the rolling speed. The electromagnetic torque ($T_{EM}$) is considered to be the system input, whereas the rolling speed ($\omega_r$) represents the system output. Disturbances are present in the form of load torque applied to the roll shaft, that is when a stock is being rolled producing the rolling torque[1] ($T_{LOAD}$) which can be estimated using different approaches [17],[25].

Using Figure 6.3 a set of differential equations was obtained to describe the dynamical behaviour of the rotating system through time [57]. Based on the classical

[1]See Chapter 2 for a description of the rolling torque developed by the stock during rolling.

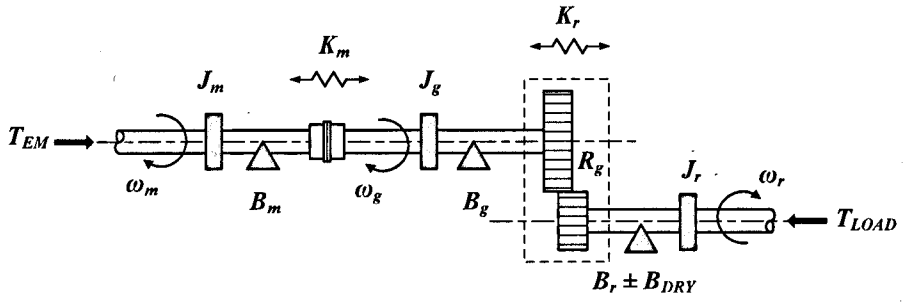


Figure 6.3: Equivalent diagram of the Hille-mill rotating system

Newton motion laws, such equations can be expressed as follows:

$$\dot{\omega_m} = \frac{1}{J_m}\left(T_{EM} - T_m - B_m\omega_m\right), \tag{6.1}$$

$$\dot{\omega_g} = \frac{1}{J_g}\left[T_m - \left(\frac{T_r}{R_g}\right) - B_g\omega_g\right], \tag{6.2}$$

$$\dot{\omega_r} = \frac{1}{J_r}\left[T_r - T_{LOAD} - (B_r \pm B_{DRY})\cdot\omega_r\right], \tag{6.3}$$

$$\dot{T_m} = K_m\left(\omega_m - \omega_g\right), \tag{6.4}$$

$$\dot{T_r} = K_r\left(\frac{\omega_g}{R_g} - \omega_r\right). \tag{6.5}$$

Equations (6.1) to (6.5) represent the 3-Mass-Model (3MM) that describe the dynamics of the Hille-mill. When the mill operates in the steady-state (i.e. constant speed), speed in each shaft is basically affected by their friction, which in the case of the roll shaft, it is a combination of both viscous and dry. Under these conditions there is no torsional spring rate in any shaft, so that the torques produced at the couplings are constant. However, in the transient state (i. e. when a slab is being rolled or during a sudden change of speed), all shafts are subjected to fluctuating loads and torsion with various degrees of stress concentration. This effect produces torque changes across the shafts and, as a consequence, speed is affected not only by friction but also by their inertia. The physical meaning of the time-constant of each shaft can be understood as the ratio between the shaft inertia and the friction coefficient, so that the more inertia is in the shaft, the slower its dynamic response will be [22]. Table 6.1 shows all system parameters which have been determined by different approaches ranging from analytical to experimental estimations as well as *know-how* [57].

Table 6.1: Critical parameters of the Hille-mill

| PARAMETER | VALUE | UNITS |
|---|---|---|
| $B_r$ | 2 | Nm |
| $B_g$ | 0.03 | Nm |
| $B_m$ | 0.04 | Nm |
| $B_{DRY}$ | 50 | Nm |
| $J_r$ | 0.5 | Kg-m$^2$ |
| $J_g$ | 0.077 | Kg-m$^2$ |
| $J_m$ | 0.147 | Kg-m$^2$ |
| $K_r$ | $6.43 \times 10^5$ | Nm/rad |
| $K_m$ | $1.96 \times 10^5$ | Nm/rad |

As mentioned earlier, a nonlinear component in the form of dry friction is assumed to be present only in the rolls; its effect produces torque in the same direction of the rolling speed. Therefore, in Equation (6.3) the sign of $B_{DRY}$ depends on whether the rolling speed is positive (forward direction) or negative (backward direction). The rolling torque is considered as a transient disturbance to the system because of the fact that it is present only when a slab is being rolled.

## 6.4 The Electric Drive Model

The main upgrading operation carried-out on the Hille-mill consisted of providing an electric drive which offers an easy way to regulate both the frequency and the magnitude of the voltage applied to the motor. This was necessary in order to control the electromagnetic torque applied to the mill, and consequently its speed. As a result, a much higher efficiency and a better performance are achieved and various types of hot-rolling experiments can now be carried-out including those associated with complex multi-pass schedules.

The main electric drive is comprised of a balanced 3-phase ac voltage source, a power converter, and an 18.5 kW, 400 V, 1500 rpm, 50 Hz induction motor. The drive has the capability of reaching twice the motor rated speed by means of applying a Pulse Width Modulated (PWM) voltage to the stator terminals. In the Hille-mill, the electric drive uses the well known Field-Oriented Control (FOC) technique to

control the electromagnetic torque and magnetic flux, so that the drive can act as a torque transducer wherein the electromagnetic torque can nearly instantaneously be made equal to a torque command [83]. Under this scheme the speed control is dramatically simplified because all the electrical dynamics of the motor drive have now become irrelevant to the speed control problem [42],[81]. Appendix A shows a computer simulation of the electric drive associated with the Hille-mill.

However, the electric dynamics of the power inverter can often cause undesirable effects mainly on the electromagnetic torque (the input variable of the Hille-mill), that is a high-frequency noise due to the switching of the electronic elements of the power converter. To observe to what extent this phenomenon can affect the mill's performance, a detailed study of the motor dynamics was carried-out. This study included the analysis of the induction motor model in terms of its voltage equations given by the well known arbitrary reference frame [60]. From this analysis, it was concluded that, although such noise should not pose a significant effect on the rolling speed, it has an undesirable effect in the control effort, especially if the controller has no low-pass filters.

Because of the complexity of the electric dynamics included in the drive, the complete motor model was not suitable for computer simulations of the Hille-mill and hence a simplified model was used, which includes only the motor torque response [20],[57]. Such a model is described by the following relationships:

$$T_0 = \frac{1}{\tau_{mo}s + 1} T_{REF}, \tag{6.6}$$

$$T_{EM} = \begin{cases} T_0, & \text{if } T_0 \leqslant T_{\max}(\omega_m) \\ T_{\max}(\omega_m), & \text{if } T_0 > T_{\max}(\omega_m) \end{cases}, \tag{6.7}$$

where $T_{EM}$ is the electromagnetic torque produced by the motor, $T_{REF}$ is the torque command, $\tau_{mo}$ is the motor time constant, $T_{\max}(\omega_m)$ is the maximal torque available at the speed $\omega_m$, with $s$ being the Laplace operator. The effect of the power inverter is considered by adding a zero-mean white noise sequence to the electromagnetic torque signal.

## 6.5 The Rolling Gap Mechanism Model

In rolling practice, one is more concerned with the thickness of the rolled product rather than the roll gap. The difference between the roll gap (free load) and the exit

thickness is caused by the spring effect of the mill structure. Indeed, the principal causes of gauge variation in flat rolling may be analysed from the following well-known expression which is often referred to as the *gaugometer equation* [25]:

$$h_f = C_0 + \frac{P}{K_{MILL}}, \tag{6.8}$$

where $h_f$ is the exit thickness of the rolled product, $C_0$ is the no-load gap position, $P$ is the rolling force developed by the stock during deformation[2], and $K_{MILL}$ represents the mill structural stiffness.

The ratio $P/K_{MILL}$ is known as the *mill spring*. Thus, to obtain the desired exit rolled product thickness, the no-load roll gap must be less than the exit rolled product thickness by the amount that is equal to the mill spring. In [36], the author determined experimentally the value of the spring effect in the Hille-mill by performing a series of experiments using different rolling parameters. He found that a value between 475 and 539 kN/mm for $K_{MILL}$ can be considered when calculating the correct set-point for the gap position control system in order to counteract the mill spring effect and obtain the desired exit thickness of the rolled product.

In this case, the Hille-mill uses a worm-wheel screw-down mechanism to adjust the roll gap. For simulation purposes only, a mathematical model was developed considering the dynamics of the gap motor shaft. A PID controller was designed to control the position of the gap. Figure 6.4 depicts the block diagram of the gap control system where $\theta_{REF}$ and $\theta_{GAP}$ are the desired and current gap position respectively, $T_{GAP}$ is the gap motor torque, and $\omega_{GAP}$ is the shaft speed; $K_p$, $T_i$, and $T_d$ are the controller parameters, whereas $\tau_1$ and $\tau_2$ are the time constants of the actuator and the shaft respectively.

From the mathematical models shown above, it is clear that accurate prediction of the rolling force and torque should be carried-out to perform realistic computer simulation of the hot-rolling experiments. As shown previously in Chapter 2, there exist different approaches to calculate these variables such as empirical models, FE models, and intelligent systems-based models. In this work, the NN-based models developed in [86] are used because they have proved to be more accurate than conventional models.

[2]See Chapter 2 for a detailed description of the rolling force.

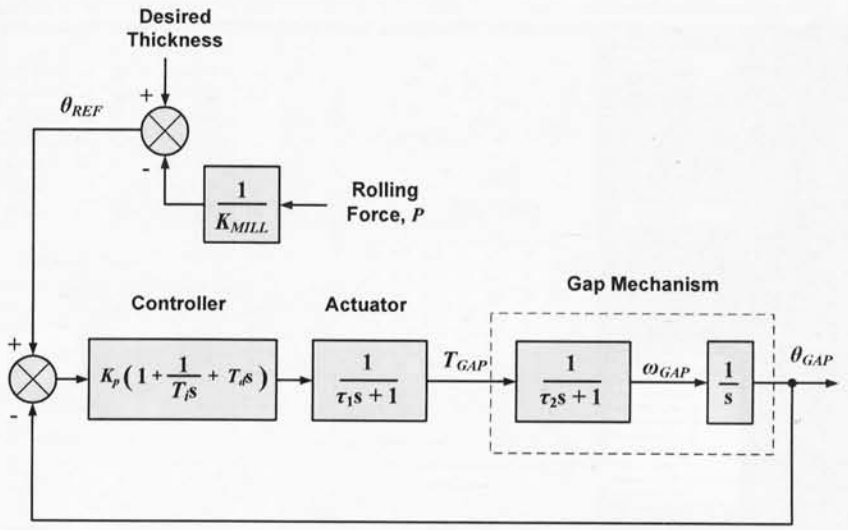


Figure 6.4: Block diagram of the gap control system in the Hille-mill

## 6.6 Computer Simulations using the Hille-Mill Model

Using the Hille-mill 3MM, the electric drive model, and the above gap mechanism control system, along with the NN-based rolling force and torque models, a simulation platform was developed in MATLAB®/SIMULINK®, which is a high-level language and interactive environment that enables one to perform computationally intensive tasks with the aid of graphical interfaces. The Hille-mill simulation platform can be used together with SISSCOR in order to have a comprehensive analysis of both the metal design and the Hille-mill control performance. Figures 6.5 and 6.6 show the SISSCOR – Hille-mill GUI and the SIMULINK® model respectively with the different blocks containing the mathematical description of the system.

A closer look at the SIMULINK® "Hille-mill 3MM" block reveals a detailed view of the simulation process and provides a good understanding about the energy transfers taking place in the real system. Figure 6.7 illustrates the block diagram for dynamic simulation of the rotating system represented by Equations (6.1) to (6.5). Observe that the block diagram consists of ideal summations or subtractors, constant multipliers, and integrators. Any $n$-th order constant-coefficient differential equation can be simulated by means of these components. Each integration block represents a state variable and its output is the integral of its input at the current time step. It is worth

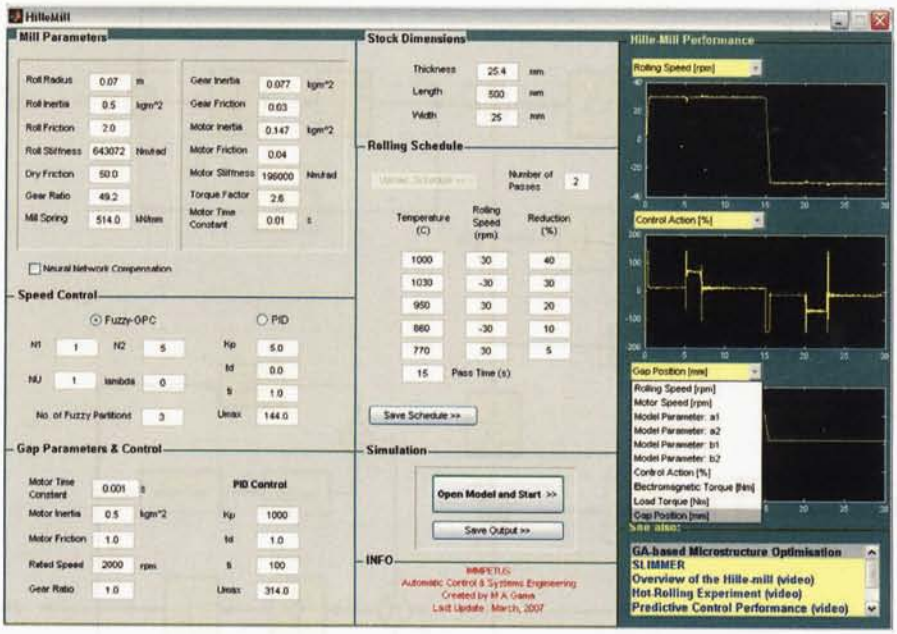


Figure 6.5: SISSCOR – The Hille-mill Graphical User Interface

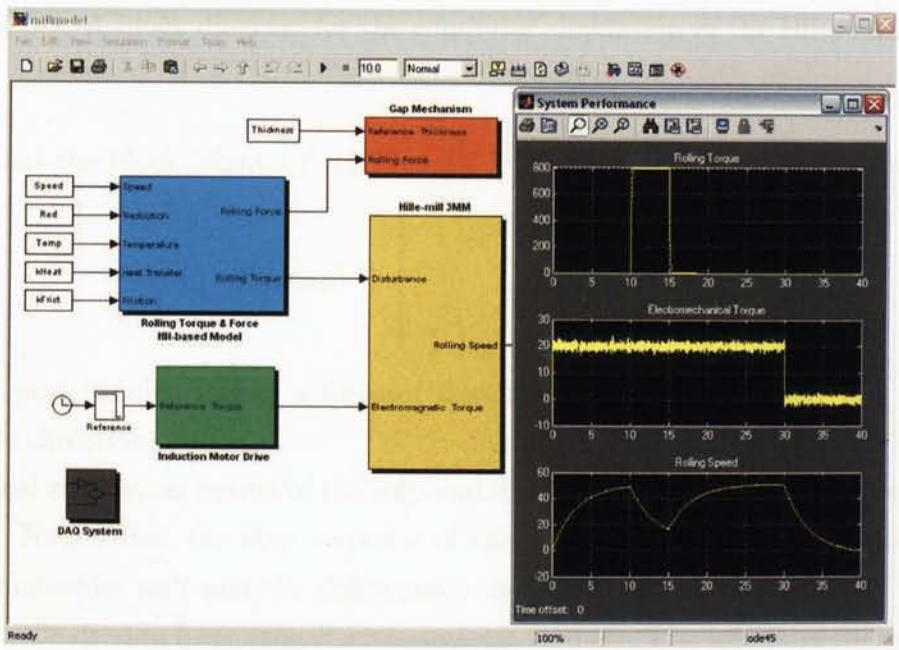


Figure 6.6: A SIMULINK®-based model of the Hille-mill

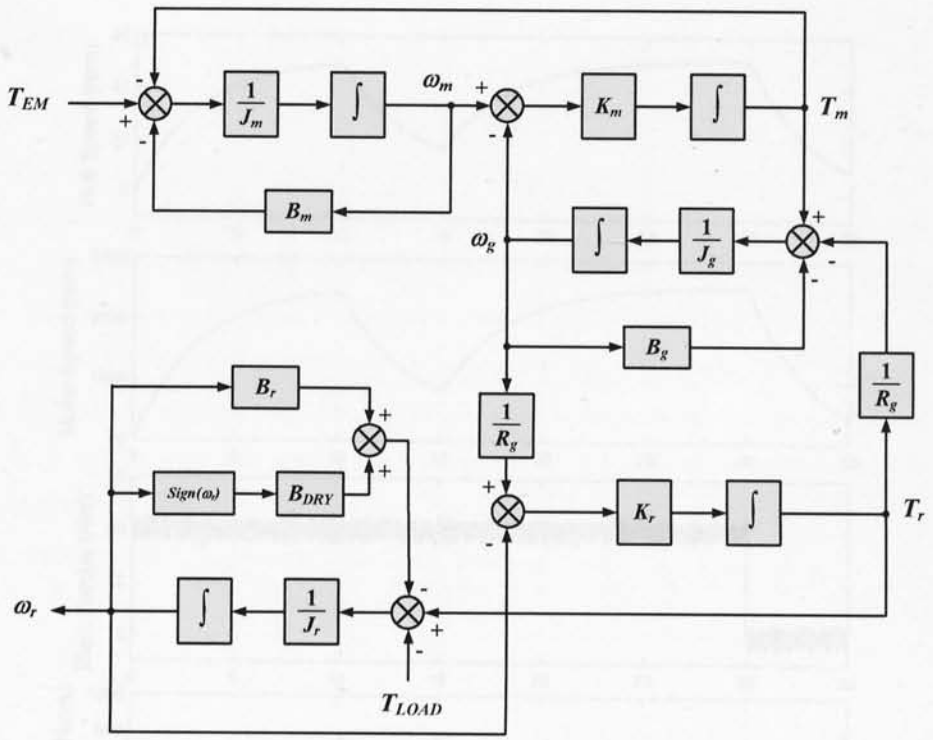


Figure 6.7: A block diagram for the computer simulation of the Hille-mill 3MM

noting that the block "sign($\omega_r$)" in Figure 6.7 performs the following function:

$$\text{sign}\,(\omega_r) = \begin{cases} +1, & \text{if}\,\omega_r > 0 \\ 0, & \text{if}\,\omega_r = 0 \\ -1, & \text{if}\,\omega_r < 0 \end{cases}, \tag{6.9}$$

where a positive sign means a forward direction whereas a negative sign means a backward direction.

Typical simulation results of the step and disturbance responses are shown in Figure 6.8. Notice that the step response of the rolling speed behaved similarly to a typical first-order unit and the disturbance dynamics also showed a scaled counteraction to the driving force (the electromagnetic torque). The effects of the electronic elements of the power converter are clearly seen in the electromagnetic torque signal in the form of high-frequency zero-mean-noise; the amplitude of the oscillation increased with the voltage applied to the motor terminals, and the PWM technique used. However, as already mentioned, such noise should not pose a significant effect on the rolling speed control.

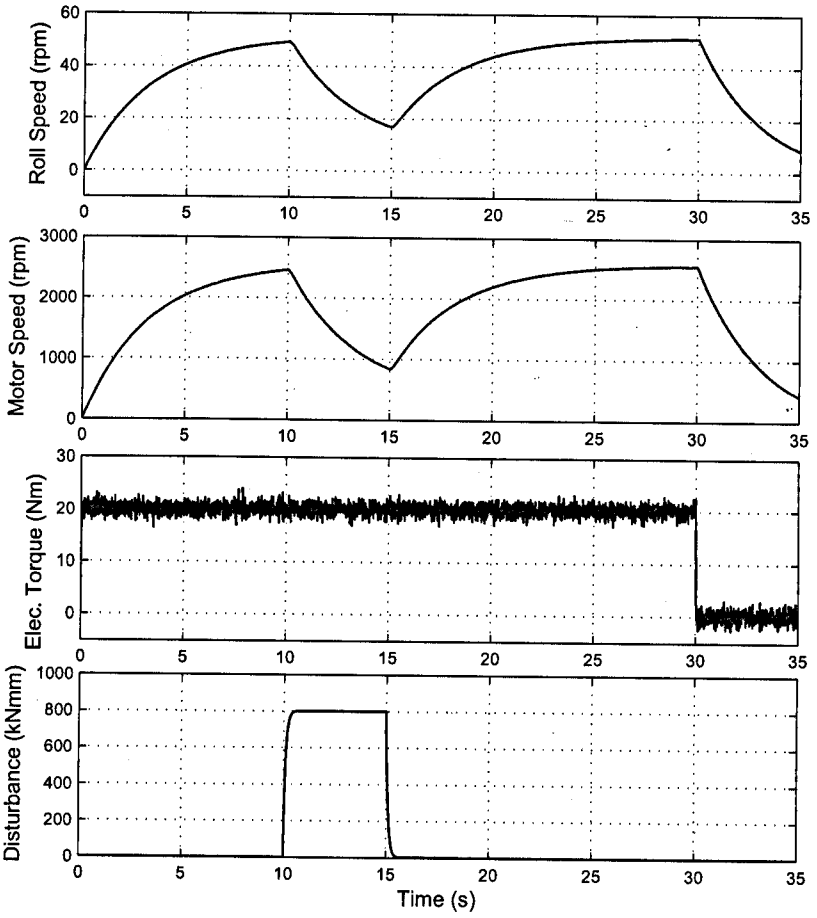


Figure 6.8: Open-loop response of the Hille-mill during a step input and a transient disturbance

The increasing demand on the accuracy of the rolling speed leads to consider other important aspects relating the dynamic performance and the control system of the Hille-mill. Additionally, such a control system should be flexible and robust enough to cope with the plant nonlinearities, time-varying parameters, uncontrolled disturbances, noise, etc. The application of model-based control algorithms has become popular in recent years because of their simplicity and capability of controlling complex systems. Next chapter will review the application of the Generalised Predictive Control in the Hille-mill.

## 6.7 Concluding Remarks

In this chapter the mathematical model of the Hille-mill was presented. The model was based on basic physical principles governing the rotational movement of the shafts and their energy transactions using real system parameters. For the analysis and study of the Hille-mill dynamics, a typical computer simulation was carried-out showing the mill response under a step input and disturbance. The developed simulation platform for the 3MM is useful not only for mathematical analysis, but also for the fact that it can become a significant tool for the design of advanced control strategies for the mill operation. Even more importantly, it will help to determine the feasibility of implementing such control designs for real-time operations. The next chapter will discuss such control implementations in detail.

# Chapter 7

# Optimal Rolling Speed Performance using Adaptive Fuzzy Model-based Predictive Control

## 7.1 Introduction

In Chapter 5, the proposed optimisation mechanism aimed at setting-up the rolling schedule was presented, and it was shown how the mill constraints can be included to ensure safe and feasible processing conditions for hot-deformation. However, although the optimal rolling schedule is found in this manner, one needs to ensure that the mill will apply this schedule in an optimal way. In fact, the rolling speed regulation is paramount when deforming the stock, for this reason one also needs to identify further improvements on the control system of the Hille-mill. This chapter will review the development and application of a modified model-based approach in the form of Generalised Predictive Control (GPC) to reflect a Takagi-Sugeno-Kang (TSK) Fuzzy model of the Hille-mill. Such an hybrid strategy provides robustness and flexibility against model uncertainties and disturbances to the overall control system, and also provides the possibility of obtaining a more accurate control performance without the need for a complex model of the process.

The main framework is based on the real-time implementation of the adaptive GPC to calculate the optimal control actions so as to cope with the nonlinear phenomena and the time-varying process parameters involved. A simulation platform will first be developed to set the controller design parameters and study the control system under different operating regimes. Finally, the performance and robustness of the control algorithm will be evaluated by real-time hot-rolling experiments.

## 7.2 The TSK Fuzzy System-based Process Model

An alternative to classical system identification is to use a Fuzzy Inference System (FIS) to provide a computing paradigm for modelling the nonlinear process dynamics when a sufficiently accurate model of the process is unavailable [54]. A method for expressing fuzzy rules was proposed in [76], and it is usually referred as the TSK Fuzzy inference system, which includes fuzzy sets only in the *premise* part of the fuzzy rules and a regression model (which can be either linear or nonlinear) as the *consequence*, i.e.

$$\text{IF } x_1 \text{ is } B^1 \text{ and } \cdots \text{ and } x_n \text{ is } B^i, \text{ THEN } y = c_0 + c_1 x_1 + \cdots + c_n x_n, \tag{7.1}$$

where $x = (x_1, \ldots, x_n)^T$ and $y$ are the input and output linguistic variables respectively, $B^i$ are linguistic values characterised using membership functions, and $c_i$ are real-valued parameters. Using the above formulation, a complex high-dimensional nonlinear modelling problem can be decomposed into a set of simpler linear models valid within certain operating regions defined by fuzzy boundaries. Fuzzy inference is then used to interpolate the output of the local models in a smooth fashion to lead to an overall process model. This modelling approach has shown good accuracy and is free of the problems arising from model incompleteness [75],[53].

Consider a Single-Input Single-Output (SISO) system to be modelled using a TSK Fuzzy system. Assuming that the input space is partitioned using $p$ fuzzy partitions and that the system can be represented by fuzzy implications (one in each sub-space), each sub-model can be written as follows:

$$\begin{aligned} L_i : \text{IF } y(t) \text{ is } B^i, \text{ THEN } \; & \Delta y_m^i(t+1) = -a_1^i \Delta y(t) - \cdots - a_j^i \Delta y(t-j+1) + \\ & b_1^i \Delta u(t) + \cdots + b_k^i \Delta u(t-k+1), \\ & i = 1, \ldots, p;\ j = 1, \ldots, na;\ k = 1, \ldots, nb, \end{aligned} \tag{7.2}$$

where $y(t)$ and $u(t)$ are the process and controller output respectively at time $t$; $y_m(t+1)$ is the one-step ahead model prediction; $B^i$ is the fuzzy set representing the fuzzy sub-space in which implication $L_i$ can be applied for reasoning; and $\Delta = 1 - z^{-1}$, with $z^{-1}$ being the backward shift operator.

In the consequent part of such a model representation is a Control Autoregressive Integrated Moving Average (CARIMA) structure which is known for being effective against offsets that can be present in the data [82]. Figure 7.1 presents a block diagram of the main components of the TSK Fuzzy model used in this work. In this figure,

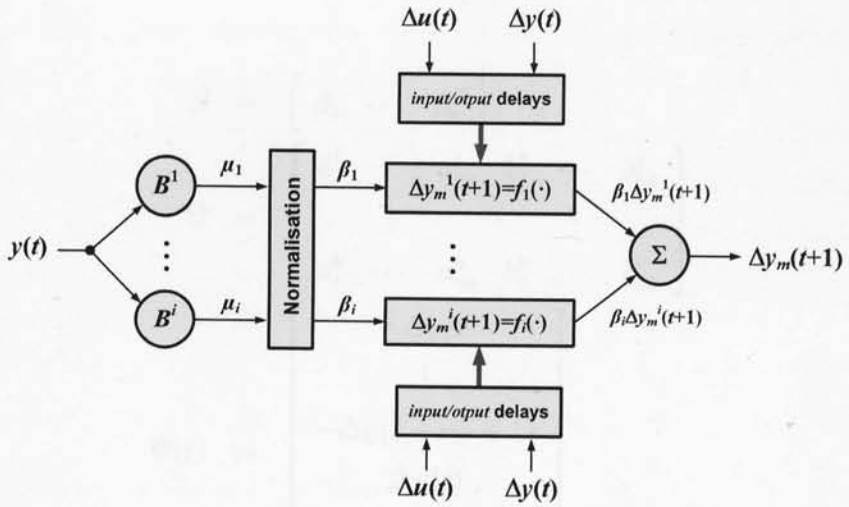


Figure 7.1: The TSK Fuzzy System-based process model

$\mu_i$ represents the grade of membership of $y(t)$ in $B^i$, as described by the Gaussian membership function expressed by the following equation:

$$\mu_i = \exp\left\{-\frac{1}{2}\left[\frac{y(t) - c_i}{r_i}\right]^2\right\} \qquad i = 1, \ldots, p, \tag{7.3}$$

where $c_i$ and $r_i$ are the centre and width of the Gaussian function. In addition, $\beta_i$ is the ratio of the $i$-th implication's firing strength to the sum of all implications' firing strengths, which can be calculated according to the following formula:

$$\beta_i = \frac{\mu_i}{\sum_{i=1}^{p} \mu_i} \qquad i = 1, \ldots, p. \tag{7.4}$$

The implications' firing strengths are now normalised, such that $\sum_{i=1}^{p} \beta_i = 1$. Additionally, $\beta_i$ may be referred as the weight assigned to each of the $p$ implications at each sampling instant in the following form:

$$\begin{aligned} \beta_i \Delta y_m^i(t+1) = \; & \beta_i[-a_1^i \Delta y(t) - \cdots - a_j^i \Delta y(t-j+1) + \\ & b_1^i \Delta u(t) + \cdots + b_k^i \Delta u(t-k+1)], \\ & i = 1, \ldots, p;\ j = 1, \ldots, na;\ k = 1, \ldots, nb. \end{aligned} \tag{7.5}$$

The overall fuzzy model output (in incremental form) can be written as follows:

$$\Delta y_m(t+1) = \sum_{i=1}^{p} \beta_i \Delta y_m^i(t+1) = \beta \cdot \Theta \cdot \Phi(t), \tag{7.6}$$

where

$$\beta = \begin{bmatrix} \beta_1 & \cdots & \beta_p \end{bmatrix}, \tag{7.7}$$

$$\Theta = \begin{bmatrix} a_1^1 & \cdots & a_{na}^1 & b_1^1 & \cdots & b_{nb}^1 \\ \vdots & & & \vdots & & \\ a_1^p & \cdots & a_{na}^p & b_1^p & \cdots & b_{nb}^p \end{bmatrix}, \tag{7.8}$$

$$\Phi(t) = \begin{bmatrix} -\Delta y(t) \\ \vdots \\ -\Delta y(t-na+1) \\ \Delta u(t) \\ \vdots \\ \Delta u(t-nb+1) \end{bmatrix}. \tag{7.9}$$

The above modelling technique forms the basis for the development of the long-range predictive control strategy which is discussed in the next section.

## 7.3 The Generalised Predictive Control Algorithm

GPC is a model-based algorithm which predicts the output of the plant over a time horizon based on the assumption about future controller output sequences. An appropriate sequence of the control signals is then calculated to reduce the tracking error by minimising a quadratic cost function, after which only the first element of the control signals is applied to the system. This process is repeated for every sample interval while new information is also updated. It is widely accepted that, GPC leads to good rejection properties against modelling errors and disturbances [14]. Furthermore, it can be extended to include system constraints to add consistency to the concept of the "optimal" control solution [55]. The algorithm formulation is briefly described next. Consider the following input-output linear discrete-time system:

$$A(z^{-1})\Delta y(t) = B(z^{-1})\Delta u(t) + C(z^{-1})\zeta(t), \tag{7.10}$$

where

$$A(z^{-1}) = 1 + a_1 z^{-1} + a_2 z^{-2} + \cdots + a_{na} z^{-na}, \tag{7.11}$$

$$B(z^{-1}) = z^{-k}(b_1 + b_2 z^{-1} + b_3 z^{-2} + \cdots + b_{nb} z^{-nb+1}), \tag{7.12}$$

$$C(z^{-1}) = c_0 + c_1 z^{-1} + c_2 z^{-2} + \cdots + c_{nc} z^{-nc}, \tag{7.13}$$

$$\Delta = 1 - z^{-1}. \tag{7.14}$$

$y(t)$ and $u(t)$ are the measurable output and input of the plant respectively, and $\zeta(t)$ denotes a vector of uncorrelated sequences of random variables with zero-mean and covariance $\sigma$. Any time-delay $(k)$ can be absorbed in the structure of the $B(z^{-1})$ polynomial. The controller computes the control action using optimisation of the following cost function:

$$J_{GPC} = \sum_{j=N_1}^{N_2} \left[P(z^{-1})y(t+j) - w(t+j)\right]^2 + \sum_{j=1}^{N_U} \left[\lambda(j)\Delta u(t+j-1)\right]^2, \qquad (7.15)$$

where

$N_1$ minimum costing (output) horizon;

$N_2$ maximum costing horizon;

$N_U$ control horizon;

$w$ future set-point;

$\lambda(j)$ control weighting sequence; and

$P(z^{-1})$ inverse model in the model-following context with $P(1) = 1$.

Usually, the polynomial $C(z^{-1})$ is not estimated but replaced by a fixed polynomial $T(z^{-1})$, also known as the *observer polynomial.* Its parameters are chosen so that the whole system has better disturbance rejection properties, and it can compensate for any unmodelled dynamics for the predictions $P(z^{-1})y(t+j)$ [15]. The minimisation of the cost function described in Equation (7.15) leads to the following projected control increment:

$$\Delta u(t) = \bar{g}^T(w - \Lambda), \qquad \Lambda = [\Lambda(t+N_1), \ldots, \Lambda(t+N_2)], \qquad (7.16)$$

where $\bar{g}^T$ is the first row of the matrix $(G_d^T G_d + \lambda I)^{-1} G_d$, and $G_d$ is the dynamic (step-response) matrix of the form:

$$G_d^T = \begin{bmatrix} g_0 & g_1 & \cdots & g(N_2-1) \\ 0 & g_0 & \cdots & g(N_2-2) \\ \vdots & \vdots & & \\ 0 & 0 & \cdots & g(N_2-N_U) \end{bmatrix}, \qquad (7.17)$$

where $g_i$ are the step-response coefficients, and $\Lambda$ is a vector of future output responses weighted by $P(z^{-1})$.

The synergy between the GPC algorithm and Fuzzy Logic takes place when the TSK Fuzzy model is used by the predictive controller to calculate the control sequence of Equation (7.16). Even though the fuzzy model shown in Figure 7.1 consists of a number of linear sub-models, the overall model output is nonlinear. However, to facilitate the implementation of the fuzzy model into the GPC algorithm, a simple method of linearising the fuzzy model about the current operating point by weighting the fuzzy model parameters at each sampling instant was used. In such a case, the overall fuzzy model output becomes:

$$\Delta y_m(t+1) = \Theta' \cdot \Phi(t), \tag{7.18}$$

where $\Theta'$ represents a vector of $\beta_i$-weighted parameters of $\Theta$ such that:

$$\Theta' = \left[ \begin{array}{cccccc} a'_1 & \cdots & a'_{na} & b'_1 & \cdots & b'_{nb} \end{array} \right], \tag{7.19}$$

$$a'_j = \sum_{i=1}^{p} \beta_i \cdot a_j^{(i)} \qquad j = 1, \ldots, na, \tag{7.20}$$

$$b'_k = \sum_{i=1}^{p} \beta_i \cdot b_k^{(i)} \qquad k = 1, \ldots, nb. \tag{7.21}$$

A comparison of the effectiveness of this method of linearisation with the traditional method of linearisation of nonlinear models based on determining the gradient is provided in [41]. Better linearised modelling accuracy by weighting the fuzzy model parameters can be achieved by increasing the number of fuzzy partitions. Therefore, the improvement in model accuracy achieved by using more fuzzy partitions should be reflected in better performance by the controller using the linearised model. In practice, it was found that the controller performance tends to converge as the number of partitions was increased, and there was a little benefit to be gained by using too many fuzzy partitions. In this research work it was generally not necessary to go beyond 5 fuzzy partitions.

Figure 7.2 depicts the block diagram representing the main components of the Fuzzy Model-based GPC implemented in the Hille-mill. System identification is carried-out on-line using a TSK Fuzzy model where only the consequent part of the fuzzy rules is updated at every sampling instant. Once that inference takes place, an

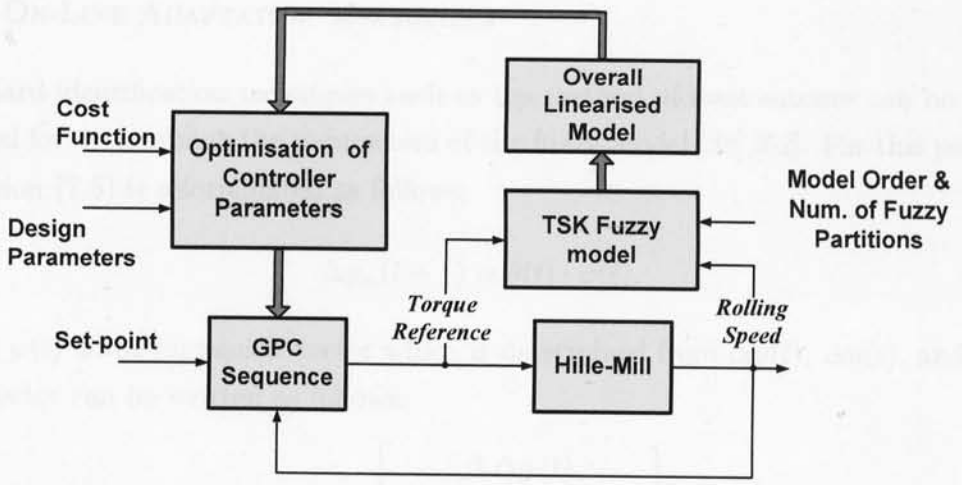


Figure 7.2: Block diagram of the Fuzzy model-based GPC

overall linearised model is computed for GPC to predict the output of the plant over a time horizon. Note that before control is applied, the model order, number of fuzzy partitions, and other design parameters such as the minimum and maximum horizons, as well as the control horizon and the control weighting sequence should be defined by the user. As stated earlier, the speed set-point is provided by the GA-based rolling schedule optimisation mechanism presented in Chapter 5.

In summary, the following advantages can be obtained by implementing GPC within the Hille-mill real-time operation:

- The process model is built upon a TSK Fuzzy model with a CARIMA structure which not only solves the offset problem inherently, but also provides a qualitative dimension to the control problem;

- Its ease of implementation and great flexibility by allowing for various tuning factors to tailor it to a particular application; and

- Its inclusion of key control objectives by means of a cost function that encompasses the variance of the output as well as the control effort.

## 7.4 On-Line Adaptation Mechanism

Standard identification techniques such as the method of least squares can be easily applied for determining the parameters of the fuzzy model [38],[62]. For this purpose Equation (7.6) is reformulated as follows:

$$\Delta y_m(t+1) = \theta(t) \cdot \varphi(t), \tag{7.22}$$

where $\varphi(t)$ is the regression vector which is determined from $\Delta y(t)$, $\Delta u(t)$, and $\beta(t)$; this vector can be written as follows:

$$\varphi(t) = \begin{bmatrix} \beta_1 \Delta y\,(t) \\ \vdots \\ \beta_1 \Delta u\,(t-nb+1) \\ \vdots \\ \beta_p \Delta y\,(t) \\ \vdots \\ \beta_p \Delta u\,(t-nb+1) \end{bmatrix}. \tag{7.23}$$

On the other hand, $\theta(t)$ is the parameter vector determined from $\Theta$, and is given by the following equation:

$$\theta(t) = \begin{bmatrix} a_1^1 & \cdots & a_{na}^1, & b_1^1 & \cdots & b_{nb}^1, & \cdots, & a_1^p & \cdots & a_{na}^p, & b_1^p & \cdots & b_{nb}^p \end{bmatrix}. \tag{7.24}$$

In most circumstances, the standard Recursive Least Squares (RLS) algorithm in its UD-factorisation form was used in this work to estimate the values of the model parameters [8]. As mentioned before, once the fuzzy model parameters are estimated, an overall linearised model is calculated.

Finally, it is worth observing another interesting aspect of GPC as follows; reformulating Equation (7.10) yields the following equation:

$$A(z^{-1})\frac{\Delta y(t)}{T(z^{-1})} = B(z^{-1})\frac{\Delta u(t)}{T(z^{-1})} + \zeta(t). \tag{7.25}$$

From the above expression it is clear that the input-output data is "band-pass" filtered by the $T$-polynomial, which affects only the disturbance rejection properties of the system [15].

## 7.5 The Rolling Speed Control System

The adaptive control algorithm presented in the previous sections was used to control the rolling speed of the Hille-mill. From Chapter 6, it is clear that all electric dynamics can be neglected when there is an inner loop controlling the electromechanical torque ($T_{EM}$) of the induction motor. Therefore, by providing a torque command, the motor will drive the Hille-mill to the desired speed; hence, for this particular application, the controller output represents the torque reference[1] ($T_{REF}$), whereas the controller inputs are the current rolling speed (feedback signal) and the set-point.

In order to analyse the feasibility of the real-time implementation, as well as to set-up the design parameters for the controller, a series of computer simulations were carried-out under different working conditions. To this effect, the following sections present 5 different study-cases:

1. Reference tracking;
2. Speed regulation;
3. Control under time-varying process parameters;
4. Control within a noise-contaminated environment; and finally
5. Control with pre-specified set-points.

Furthermore, in order to carry-out the dynamic analysis of the system, a comprehensive simulation platform using MATLAB®/SIMULINK® was developed. Figure 7.3 shows the simulation model which includes the dynamic model of the Hille-mill, the roll gap control system, and the electric drive model as discussed in Chapter 6. The simulation model also uses blocks for the rolling force and torque prediction, as well as the load force compensation [86],[56]. The block "Speed Control" includes the developed C++ code of the model identification mechanism and the GPC algorithm. The C++ code was embedded into an S-function block to make it suitable for simulation within the SIMULINK® environment.

The rolling parameters such as the number of passes, the rolling speed, the gap position, the stock dimension, the deformation temperature, the holding time, etc.,

[1] See Equation(6.6).

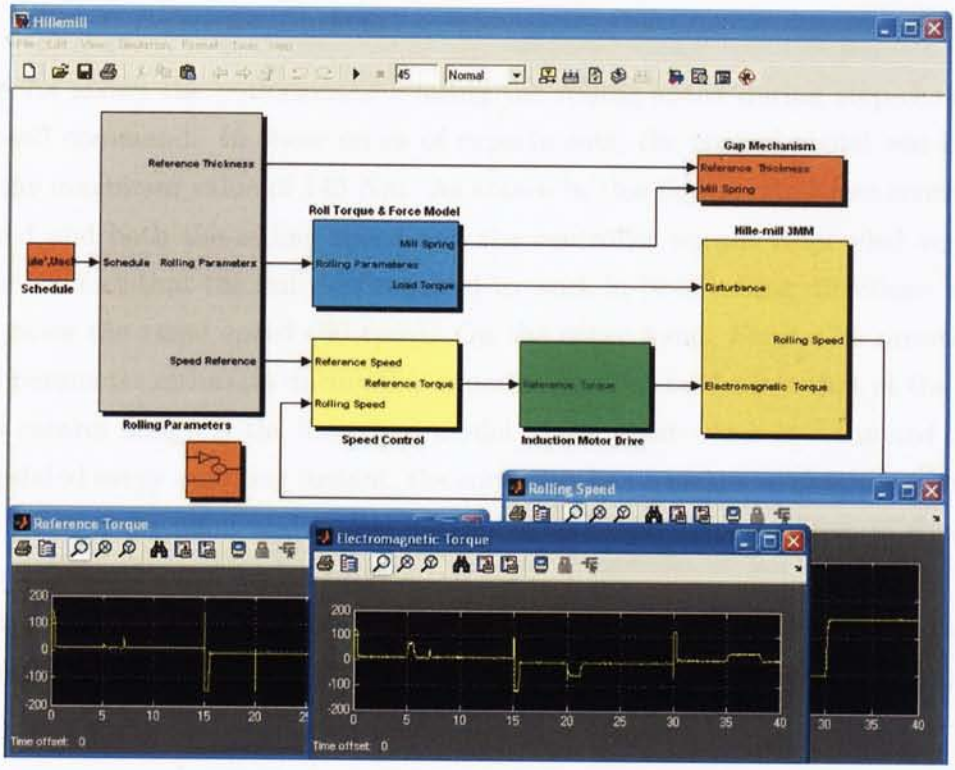


Figure 7.3: Hille-mill simulation model with speed and gap control systems

are set-up in the block "Rolling Parameters". For the plant model identification, a TSK Fuzzy model with 5 partitions was used to create 5 second-order CARIMA sub-models with 2 $a$'s and 2 $b$'s per fuzzy partition with a sampling time of 8 ms.

On the other hand, the selection of the GPC tuning factors such as $N_1$, $N_2$ and $N_U$ was conducted under the following criteria: $N_1$ is directly related to the process time-delay, but it was usually set to 1 with no loss of generality; $N_2$ was chosen to exceed the degree of the polynomial $A(z^{-1})$ , so that the value of this factor can be formulated as $N_2 \approx 2n - 1$ ($n$ = order of $A(z^{-1}) + 1$). It is known that when $N_U$ equals 1, it usually leads to satisfactory results, while greater values lead to a more activated control signal [14]. Further, $\lambda$ was set to 0, and for the polynomials $T(z^{-1})$ and $P(z^{-1})$, they were selected to be of the following form: $T(z^{-1}) = (1 - 0.9z^{-1})^2$ (for both control and identification) and $P(z^{-1}) = (1 - 0.8z^{-1})/0.2$. For parameter estimation the UD-factorisation method was used on incremental data with initial covariance of $10^{+3} \cdot I$ ($I$ being the identity matrix) and a forgetting factor of 0.99. The initial conditions for the fuzzy model were set to 0 for all $a$'s and 1 for all $b$'s.

### *7.5.1 Case 1: Reference Tracking*

Figure 7.4 shows the performance relating the rolling speed during step-changes of the speed command. In these series of experiments, the control signal was clipped to at the maximum value of 145 Nm. As shown in this figure, offset-free control was achieved and both the rolling speed and the controller output responded very well despite the fact that the mill was required to work in both rolling directions, and at up to twice the rated speed (60 rpm). On the other hand, Figure 7.5 presents the model parameter estimates during this experiment. Due to the fact that at the centre of this control design is the linearised model of the plant which is estimated on-line and updated every sampling instant, the controller has a means to obtain information of the state of the plant and makes it capable to adapt its parameters to cope with complex dynamics and nonlinearities.

A typical multi-pass schedule is shown in Figure 7.6, in which the speed command remained constant but the rolling direction was changed continuously forward and

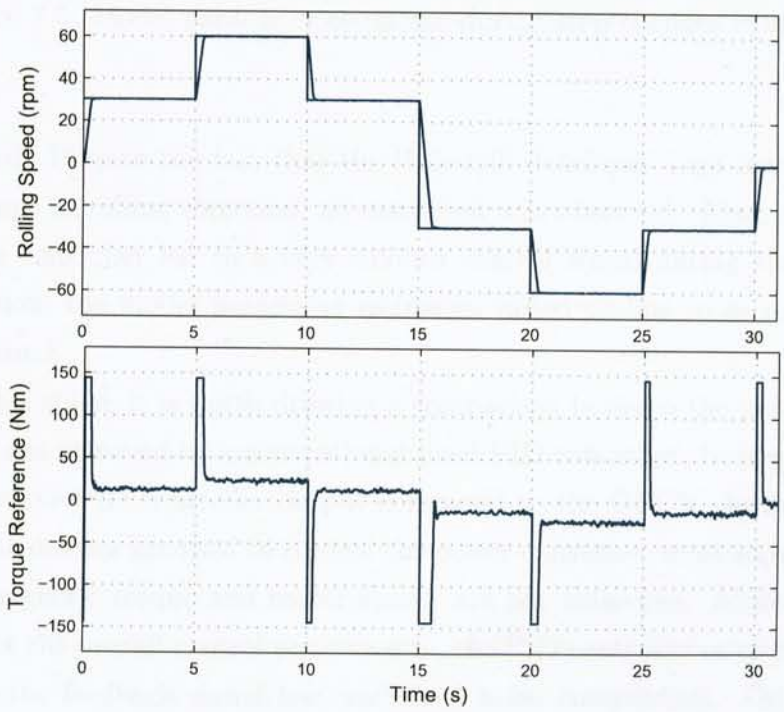


Figure 7.4: Control performance during step-changes in the speed command

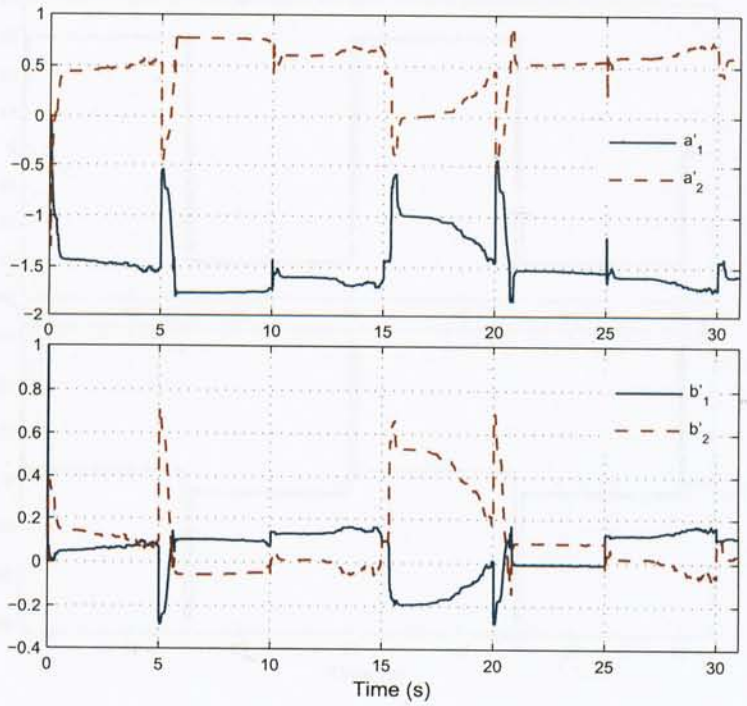


Figure 7.5: Model parameter estimates during step-changes in speed command

backward. Despite the fact that the Hille-mill developed high inertial forces during the change of rolling direction, no overshoot was observed. Also, it is worth noting that the controller led to a very smooth control signal during the transient state. In addition, the model parameter estimates varied on-line so as to provide optimal performance.

At this stage, it is worth drawing a comparison between the performance of GPC and the one achieved by a conventional fixed PID controller. Notice in Figure 7.7 the highly-active PID controller output compared to the GPC's. In this system, where electronic devices are used to control the power converter, most signals, including the electromagnetic torque and motor speed, are not noise-free. Although this fact did not affect the overall control performance, the PID controller output was more active because the feedback signal had unfiltered noise components. On the other hand, one advantage of GPC is the use of the $T$-polynomial which first filters the feedback signal, and then uses it to compute the optimal control action.

For this simulation study, the PID controller was first tuned using the Ziegler-

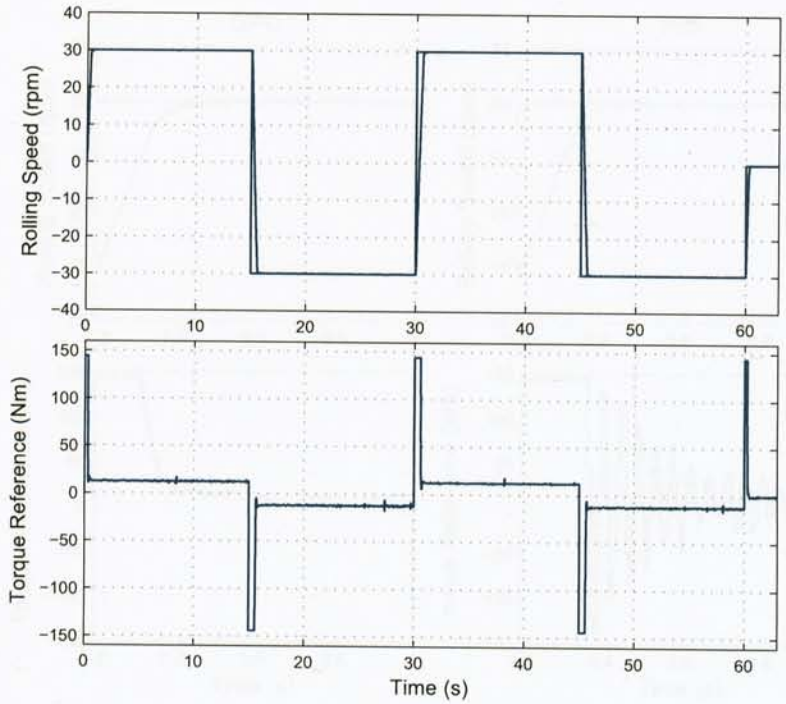


Figure 7.6: Forward and backward control at rated rolling speed

Nichols method with a step-reference at the rated speed. Then, its control performance was refined by trial and error. A quantitative comparison between both control performances can be obtained in terms of the RMSE, which resulted in 10.803 rpm for GPC and 11.143 rpm for the PID controller.

### *7.5.2 Case 2: Speed Regulation*

Figure 7.8 presents the results of a single-pass hot-rolling. As shown in this figure, good speed regulation was achieved during this test where the controller compensated for the transitory disturbance by requiring the motor to generate the electromagnetic torque to counteract the rolling torque ($T_{LOAD}$). By maintaining such a good speed regulation, the controller allowed the Hille-mill to apply a constant strain rate when deforming the material. With respect to the model parameter estimates during the test, Figure 7.9 shows how the model parameters were detuned as the stock was dragged into the rolls, but they quickly converged towards new values.

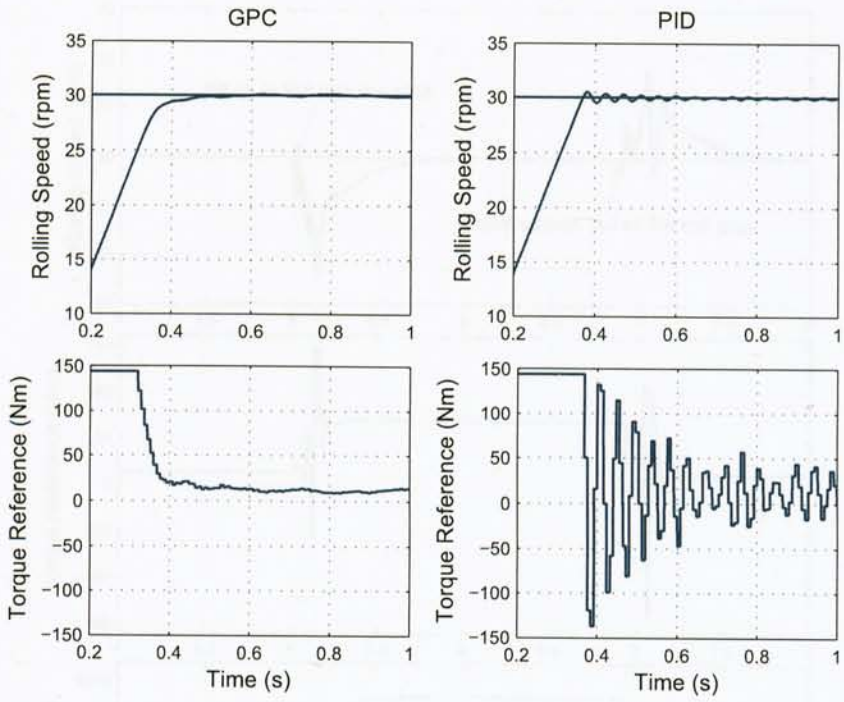


Figure 7.7: GPC vs. PID during a step-change in the speed command

### *7.5.3 Case 3: Time-Varying Process Parameters*

Figure 7.10 shows the performance of the system under time-varying process parameters. Initially, the Hille-mill was operating in steady-state at 30 rpm. After 3 seconds, the friction coefficient of the work rolls was increased to up to 600% its rated value. As expected, the controller identified this new operating condition and adapted its parameters in such a way that the rolling speed was maintained constant. Then, after 7 seconds, the motor inertia was also incremented to up to 800%. The effect of this change was only seen in the transient state when at 10 seconds the speed reference was decreased to 30 rpm. Despite the fact that the plant rising time was increased, no overshoot in the rolling speed was observed. Figure 7.11 shows the dynamics of the model parameter estimates during this test.

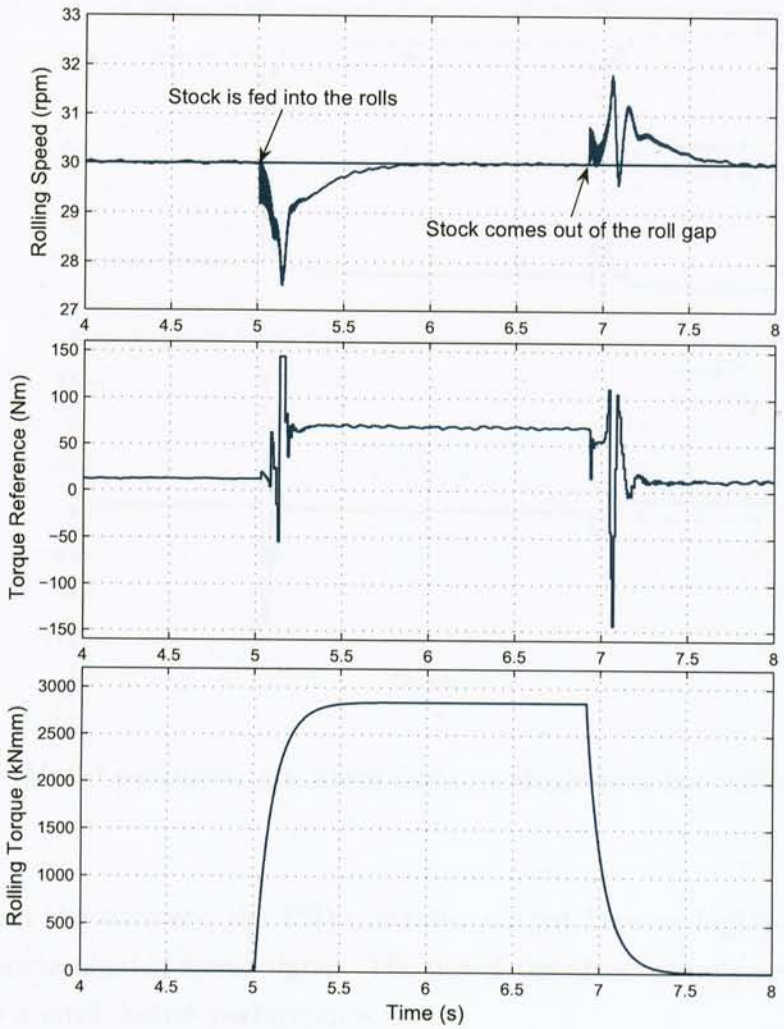


Figure 7.8: Speed regulation during a single-pass hot-rolling experiment

### *7.5.4 Case 4: Noise-Contaminated Environments*

The next case focused on the system when it operated within a noise-contaminated environment. Figure 7.12 shows the rolling speed and the controller output using both GPC and PID control. For this simulation, zero-mean white-noise was added to the feedback signal to simulate extra noise which may be produced either by external signal disturbances or bad calibration of the speed sensors. As seen in this figure, the overall performance remained acceptable showing a good degree of robustness and adequate noise rejection properties both in the control signal and the rolling speed

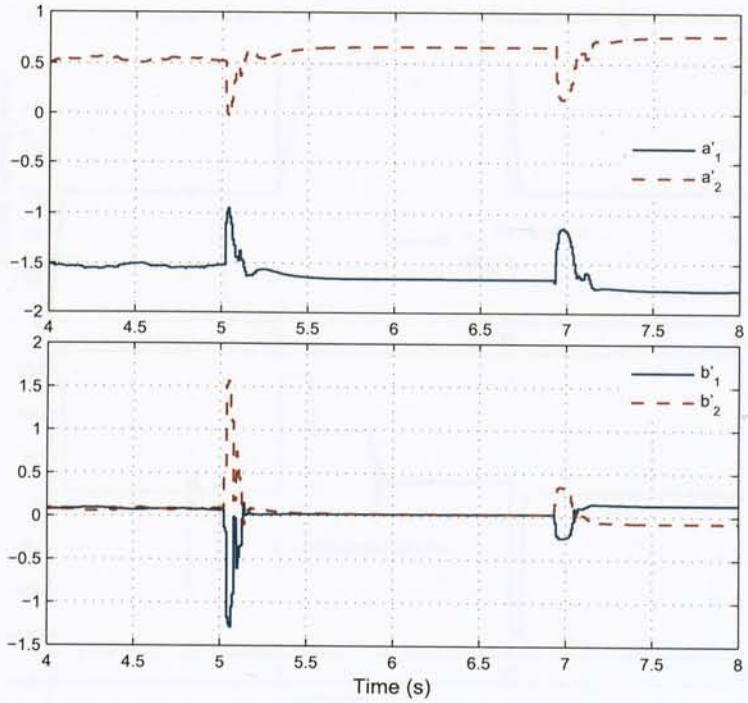


Figure 7.9: Model parameter estimates during a single-pass hot-rolling experiment

response. On the contrary, the PID controller output became highly-active leading to a more contaminated speed signal. The use of the observer polynomial $T(z^{-1})$ in GPC led to a much better performance.

The RMSE values for the speed performance resulted in 5.64 rpm for GPC and 5.47 rpm for the PID controller. Because the system worked in a highly noisy environment, another performance index can be used to quantitatively compare the control effort of both controllers. Such an index is related to the average power the controller demands to the motor in order to carry-out the test. The average mechanical power ($P_{avg}$) is defined by the following formula:

$$P_{avg} = \frac{1}{N} \sum_{k=1}^{N} \tau(k) \cdot \omega(k), \tag{7.26}$$

where $\tau$ is the torque and $\omega$ represents the angular speed; $N$ being the total number of $k$ samples. In this experiment, the average power demanded by GPC was 1.20 kW, whereas for the PID controller it was 1.22 kW.

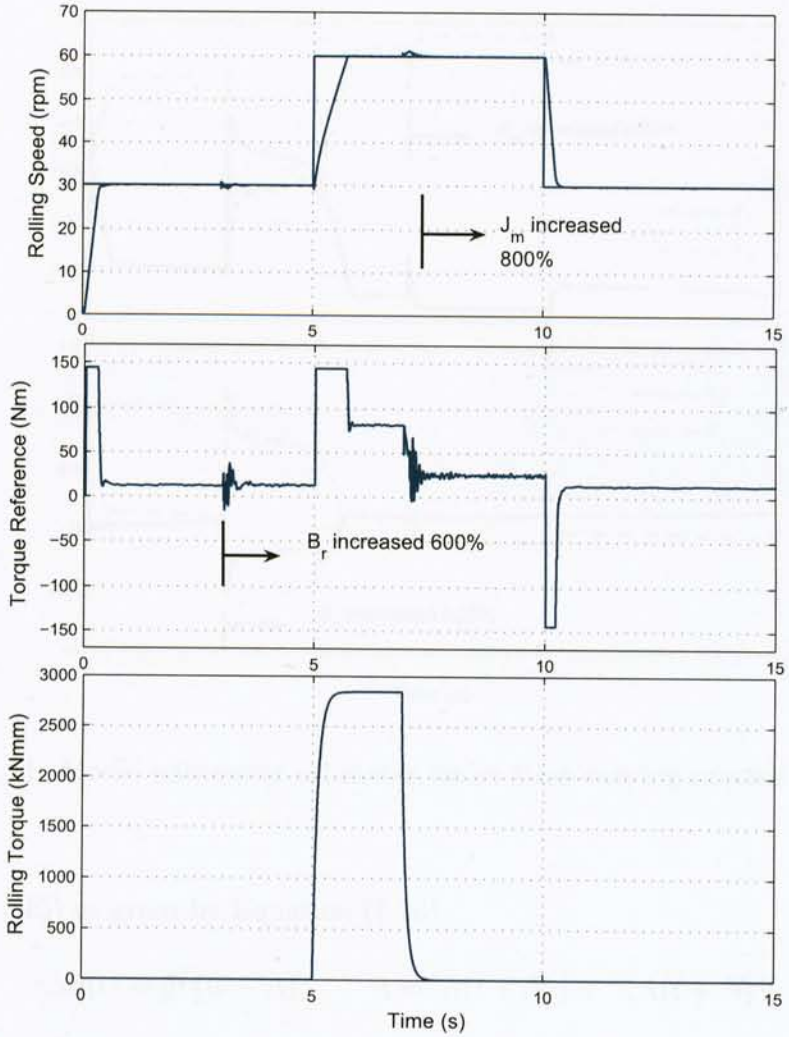


Figure 7.10: Performance under varying system parameters

### *7.5.5 Case 5: Pre-Specified Set-Points*

Another advantage of predictive controllers in general, and GPC in particular, is the exploitation of the idea of pre-programmed set-points [55]. Unlike other linear controllers, GPC allows for changes in the set-point profile, if known, to be communicated to the algorithm some samples ahead, thus giving the opportunity to the controller to adjust itself before the changes take place. This interesting feature has proven very popular in areas of industry where the knowledge of these changes is possible.

Let us recall the result of the minimisation of the cost function described by

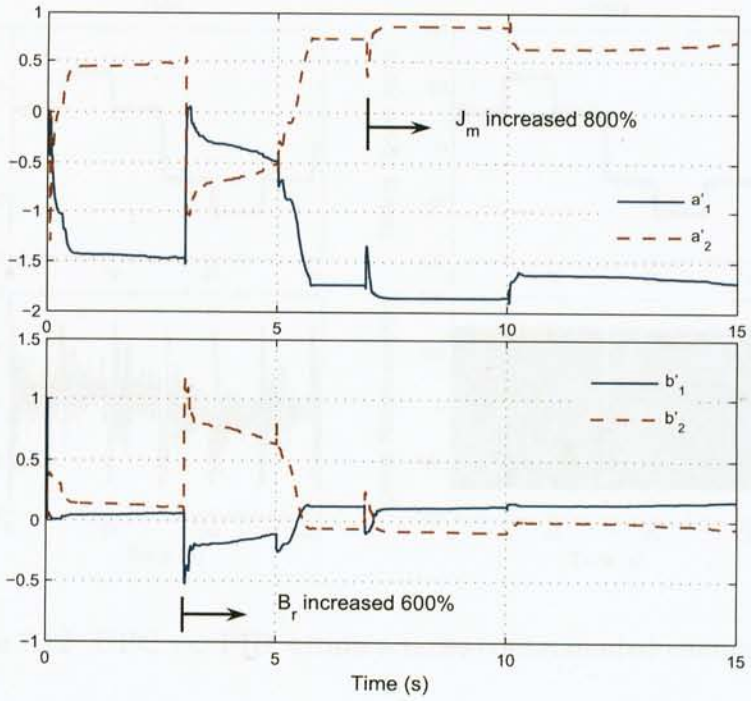


Figure 7.11: Model parameter estimates under time-varying process parameters

Equation (7.15) as given by Equation (7.16):

$$\Delta u(t) = \bar{g}^T(w - \Lambda), \qquad \Lambda = [\Lambda(t + N_1), \ldots, \Lambda(t + N_2)],$$

where $g^{-T}$ is the first row of the matrix $(G_d^T G_d + \lambda I)^{-1} G_d$, and $G_d$ is the dynamic (step-response) matrix of the form shown in Equation (7.17) [14].

In order to introduce the pre-specified set-points into the calculation of GPC, the future set-point trajectory ($w$) is used to calculate the future set-point errors. This feature consists of minimising the difference between the range of future predictions and the trajectory of future set-points instead of a constant set-point $w(t) = w$ for $t = 1, 2, \ldots, N_2$. Thus, at time $t$ the control calculation procedure may be forced to take into account set-point changes occurring $N_2$ samples in the future. One can take advantage of this feature when controlling the rolling mill due to the fact that the speed set-point (i.e. the rolling schedule) is known well in advance.

For this simulation study, let us consider the following speed profile:

- Pass 1: Start the mill with a forward pass at 50 rpm for 15 seconds;

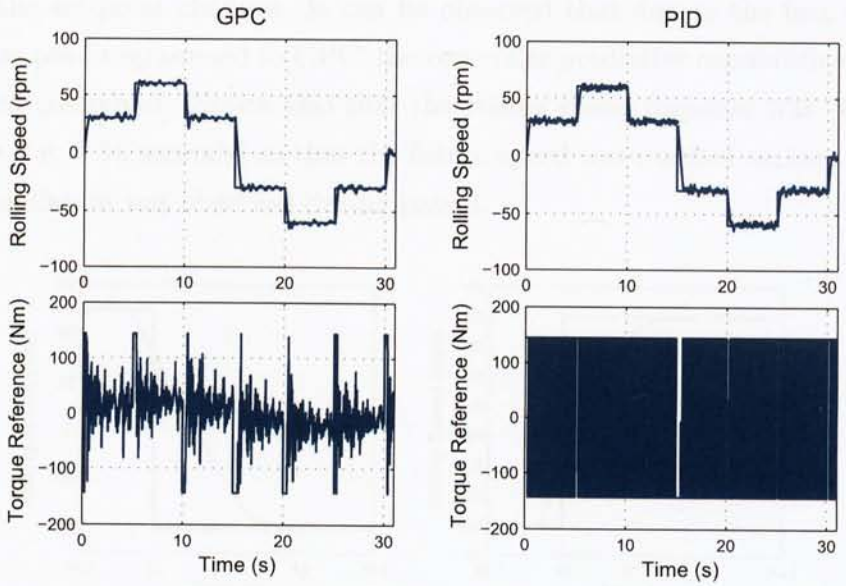


Figure 7.12: GPC vs. PID within a noise-contaminated environment

- Pass 2: Backward pass at 40 rpm for 15 seconds;
- Pass 3: Forward pass at 30 rpm for 15 seconds;
- Pass 4: Backward pass at 20 rpm for 15 seconds, and then stop.

Also, a disturbance in the rolling speed of 5 seconds was applied during pass 3. For this experiment, the maximum costing horizon was chosen to be large to observe even better the pre-specified set-point feature. The GPC parameters used were $N_1 = 1$, $N_2 = 20$, $N_U = 1$, $\lambda = 0$, $T(z^{-1}) = 1$, and $P(z^{-1}) = 1$.

The set-points were known to the algorithm $N_2$ samples in advance. It is worth noting that only for this experiment noise due to the electric dynamics was neglected. For the plant model identification, a TSK Fuzzy model with 3 partitions was used to create 3 second-order CARIMA sub-models with 2 $a$'s and 2 $b$'s per fuzzy partition with a sampling time of 8 ms. The UD-factorisation method was used on incremental data with initial covariance of $10^{-3} \cdot I$ and a forgetting factor of 0.99. The output tracked the set-point adequately without any overshoot and a reasonable control activity. The overall performance of the system was very smooth both during speed changes and disturbances. Figure 7.13 shows the speed response of the rolling speed

during the set-point changes. It can be observed that due to the fact that the set-point was pre-programmed to GPC, the controller predictive capabilities acted before the speed command. Notice also that the rolling speed response was $N_2$ samples in advance (i.e. 0.16 seconds) so that the future speed was reached earlier. Also, a good speed regulation was observed during pass 3.

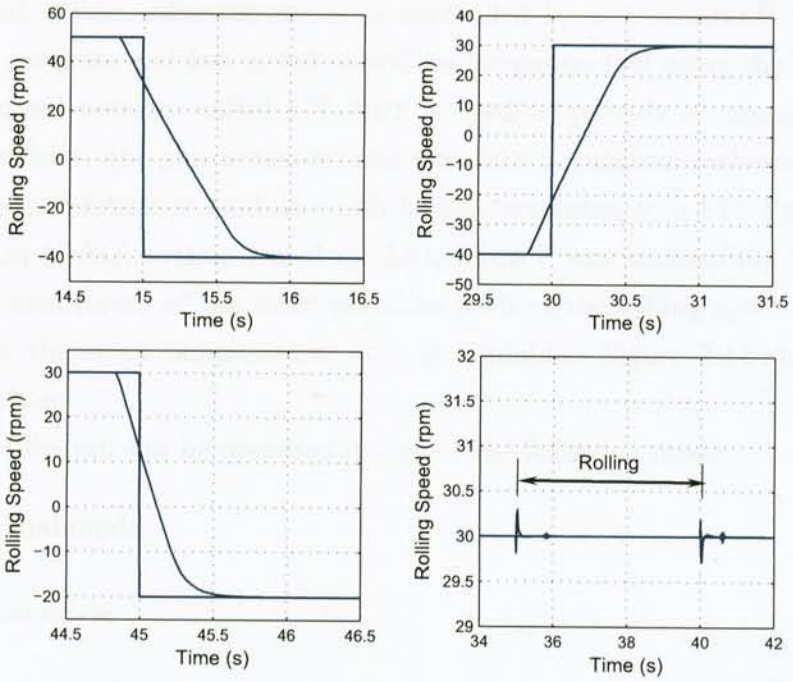


Figure 7.13: Performance using GPC with the pre-specified set-points feature

It is worth mentioning that when the prediction horizon has to be chosen to be large, smoother control actions are to be expected and if tighter control is required, the control horizon $N_U$ should be chosen larger than 1, which may compromise the control effort; this is due to the fact that the controller needs more degrees of freedom to choose the appropriate control sequence [55].

So far, a comprehensive study of the Fuzzy model-based GPC applied to the Hille-mill has been discussed through computer simulations. Five different study cases were presented showing the robustness and versatility of the control strategy and the modelling technique, as well as the useful features it offers to applications where the set-point profile is known in advance. The next section will describe further aspects

of GPC and the control performance during real-time hot-rolling experiments.

## 7.6 Real-Time Implementation

The inclusion of a powerful ac induction motor drive in the Hille-mill made it capable of performing more complex and sophisticated multi-pass hot-rolling experiments. The speed of the induction motor is controlled by a UNIDRIVE® SP drive which provides accurate and fast speed as well as torque control using the FOC technique. A high-speed network called CT-NET is used to provide communication between the main drive, the gap actuator, and the data acquisition instruments, as well as the main user interface module which is also connected to a PC. Previously, a data acquisition (DAQ) system based on LAB-VIEW® was successfully implemented so that full monitoring of the main variables such as the rolling speed, the roll torque and load, the stock temperature, etc., is available. Figure 7.14 shows the system configuration.

The Hille-mill can be operated in any of the following modes:

- Manual mode
- Local mode

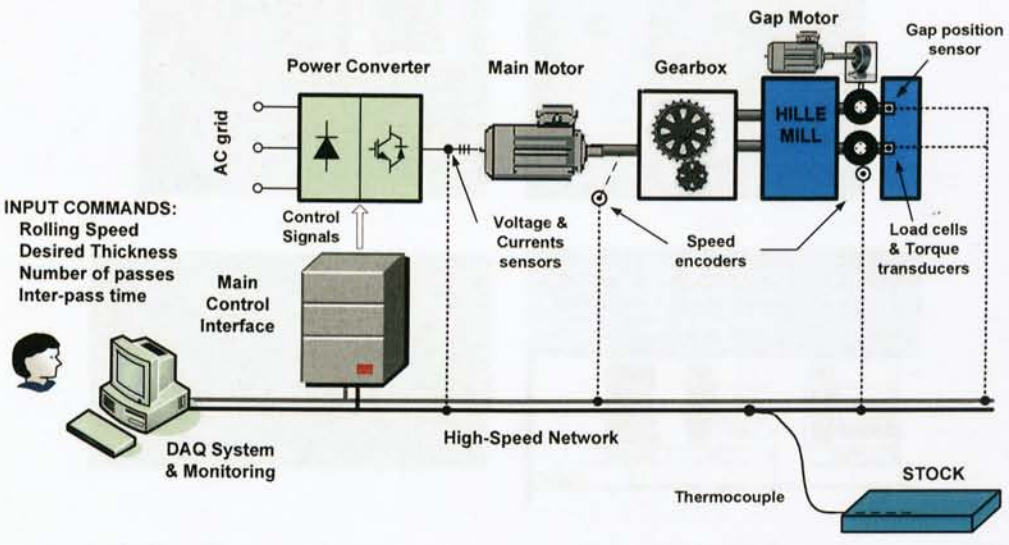


Figure 7.14: Hille-mill instrumentation and communication environment

- Remote mode

In the manual mode, the mill is started and stopped using push buttons and the speed is increased or decreased with up and down buttons on the operator panel. The current speed is displayed on the main screen of the user interface module called CTIU operator screen. Likewise, the rolls gap can also be changed by using the gap up and down buttons. In the local mode, the user operates the mill from the CTIU by means of programming up to 10 rolling passes which are automatically processed. Finally, in the remote mode, the system is operated from a remote PC where the user can schedule the rolling experiment and monitor the main variables on the PC screen. Figure 7.15 shows some pictures from the main features of the system.

The UNIDRIVE® SP offers a multitude of in-built features for the motor speed and torque control. However, for the task of implementing the GPC algorithm, it was necessary to use an additional module called *SM-Applications* module (see Figure 7.15(b)). This module includes an additional processor for the drive and allows one to utilise existing, or write new application software. It also offers more powerful

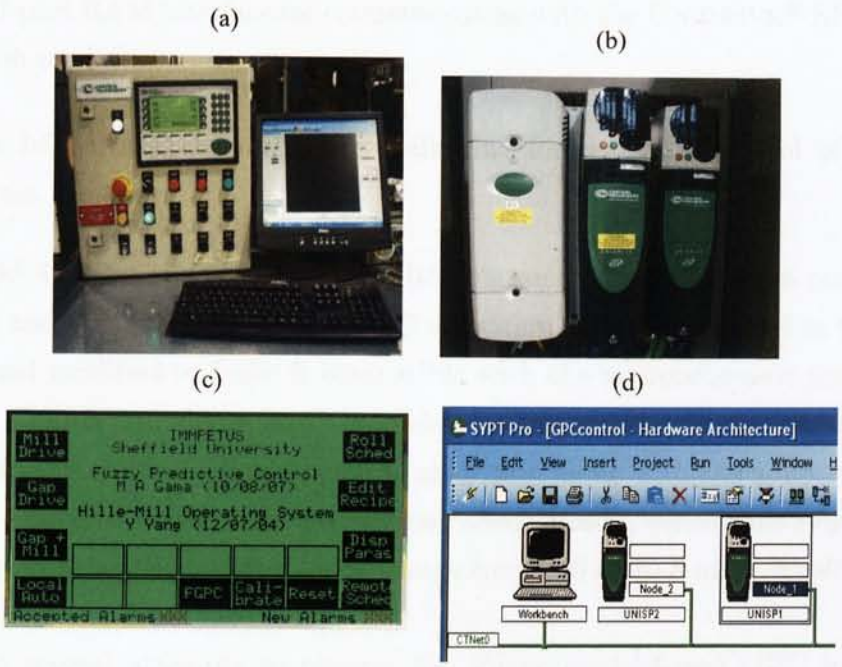


Figure 7.15: Hill-mill control and monitoring system; (a) CTIU and remote PC; (b) UNIDRIVE® SP and *SM-Application* module; (c) hardware communication; (d) main user screen

networking capabilities to enable the gap drive (and other equipment) to be connected together in order to communicate process-wide information of the hot-rolling process. The main characteristics of the *SM-Application* module can be listed as follows:

- High-speed dedicated microprocessor;
- 384 kb Flash memory for user program;
- 80 kb user program memory;
- EIA-RS485 port offering ANSI, Modbus-RTU slave and master and Modbus-ASCII slave and master protocols;
- CT-NET high-speed network connection offering up to 5 Mbit/s data rate;
- Two 24 V digital inputs;
- Two 24 V digital outputs
- Dual-port RAM interface for communicating with the UNIDRIVE® SP and other option modules;
- Task based programming system allowing for real-time control of drive and process.

The *SM-Applications* module should be programmed using its own programming structures and syntax, therefore the GPC algorithm, previously coded in C++ , was re-coded and modified to make it compatible with the microprocessor programming language. Figure 7.16 shows how the code was embedded into the *SM-Application* module software. In this figure, the GPC algorithm along with the adaptation mechanism are embedded within the sub-routine called "Pos0", which runs synchronously to a multiple of the drive control loops (range from 250 $\mu$s to 8 ms). "Pos0" was used here to control the drive speed loop.

Despite several attempts to observe the Fuzzy model-based GPC in real-time operation, it was clear that the computational effort required by the model estimation mechanism and the control algorithm was too large for the microprocessor to complete all the mathematical operations within the selected sampling time (8 ms). A careful

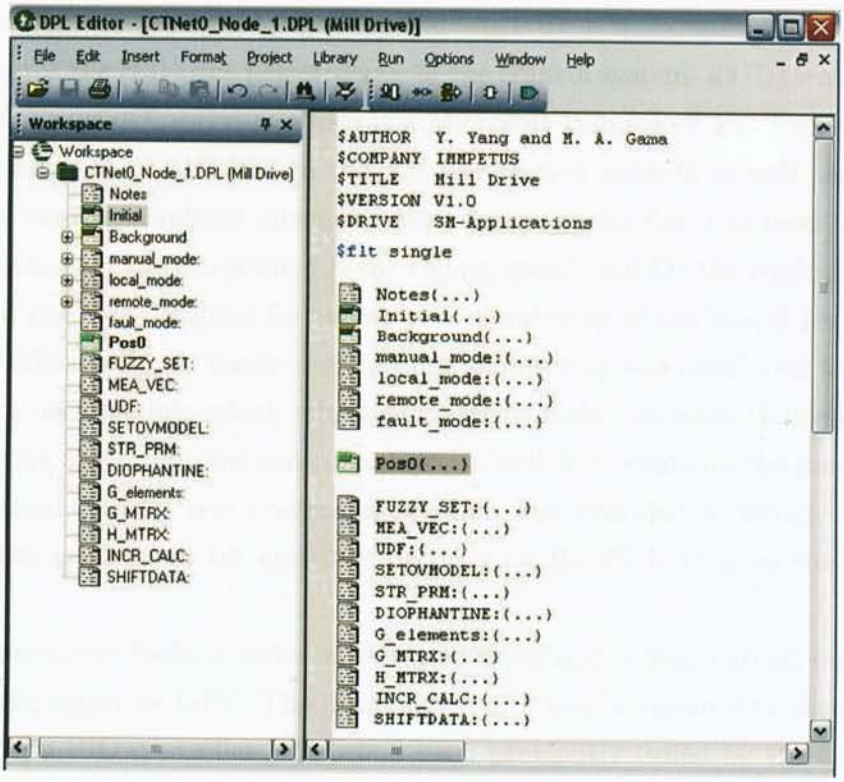


Figure 7.16: Workspace of the *SM-Application* module. The GPC algorithm and the adaptation mechanism were embedded within the "Pos0" routine. The number of fuzzy partitions was set to 1 (linear model case)

examination of GPC from a computational viewpoint revealed that, for the operating conditions concerning the Hille-mill, the time required for the derivation of the fuzzy rules and the control law was excessive for the sampling time required by the process and the number of loops implemented. It was then decided to operate the controller using two fuzzy partitions with fixed parameters. Furthermore, even when using a fuzzy model with two partitions and no adaptation mechanism, it was difficult to test GPC using large output horizons or higher model orders than those used in simulations. On the other hand, a slower sampling rate would affect the stability of the system and, as a result, a complete failure of the communication network. Therefore, it was decided not to do further modifications to the GPC algorithm but using only a linear model with adaptive parameters instead. Bearing in mind the computational limitations of the microprocessor, it was clear through the computer simulations that an acceptable performance should be expected even by using a linear

process model.

To monitor the real-time performance of the control system, a GUI was developed using the CTSCOPE® software which is a Microsoft Windows® PC Tool designed to trace the values of parameters on the *SM-Application* module as well as the motor drive. Two similar graphical interfaces were designed; the first one used three channels to monitor (1) the set-point, (2) the rolling speed, and (3) the controller output. The second one was designed for the on-line monitoring of the model parameter estimates. Additionally, a "quick-look" on-line monitoring was developed to be shown in the main user module which allows him/her to make set-point changes, read the current rolling speed, current control action, as well as to evaluate the model parameter estimates. Also, a user-controlled function was provided to switch the system identification mechanism ON and OFF by pressing the F5 button on the main user panel.

Using the above tools, a series of real-time experiments were carried-out to evaluate the performance of GPC. The obtained results were compared to those given by a conventional PID controller which had been previously tuned by the drive manufacturer [78]. The real-time tests conducted in the Hille-mill were:

1. Speed control during changes in the set-point; and

2. Speed regulation during the hot-rolling of steel alloys.

Bearing in mind the computational limitations of the Hille-mill, the GPC design parameters were selected to be as follows: $N_1 = 1$, $N_2 = 5$, $N_U = 1$, $\lambda = 0$, $T(z^{-1}) = (1 - 0.9z^{-1})^2$ and $P(z^{-1}) = (1 - 0.8z^{-1})/0.2$. Further, an adaptive linear discrete-time CARIMA model was used with 2 $a$'s and 2 $b$'s with a sampling time of 8 ms. The resulting linear model can be expressed as follows:

$$\Delta y_m(t+1) = -a_1'\Delta y(t) - a_2'\Delta y(t-1) + b_1'\Delta u(t) + b_2'\Delta u(t-1). \tag{7.27}$$

Unlike the simulation studies, for these real-time experiments GPC was allowed to run with some initial parameter estimates, which were obtained at the end of a trial run at the rated rolling speed of 30 rpm. Also, it is worth noting that the adaptation mechanism was made to be operational. The next sections will present and discuss the results obtained from such real-time experiments.

### *7.6.1 Experiment 1: Speed Control*

Figure 7.17 shows the first test when the rolling speed was required to follow a reference signal both in forward and backward direction, and at up to twice the rated speed. As shown in this figure, the speed response was offset-free and the dynamic response did not show either an overshoot or oscillations. For comparison purposes, the same figure shows the real-time performance for the same test conditions using a PID controller.

GPC provided a less active control signal leading to a smoother torque reference for the electric drive. Notice that when the system changed from 30 rpm to 60 rpm, the maximum torque required in the transient state was 94% of the motor rated torque; on the other hand, the PID controller demanded 135%. It can be also observed that when using a PID controller at 60 rpm, the roll shaft presented torsional oscillations commonly known as chattering; however, when using GPC this effect was eliminated. Figure 7.18 shows the system identification process during this real-time experiment. The RMSE performance index for this experiment resulted in 7.26 rpm for GPC and 9.70 rpm for the PID controller. On the other hand, the average power used by the motor when using GPC was 1.268 kW, whereas for the PID controller it was 2.831 kW.

The next experiment consisted on switching ON and OFF the model estimates during a multi-pass schedule. Initially, GPC started with a fixed model previously set, which was obtained as a result of a 20 second test at rated speed. After 26 seconds the identification mechanism was allowed to be operational for 20 seconds only. Figure 7.19 shows the results of this test. As shown in this figure, there is a clear difference of performance observed in the controller output before and after the system identification mechanism started up. Note that the initial fixed model led to a more active control signal in transient state, but when there was on-line identification the signal ripples disappeared even when the mechanism was switch OFF again. The model parameter estimates during this test are shown in Figure 7.20.

### *7.6.2 Experiment 2: Speed Regulation during Hot-Rolling Experiments*

A series of real-time hot-rolling experiment were carried-out to evaluate the GPC performance in terms of the rolling speed regulation. In this experiment, a stock of the aluminium AA5182 alloy with an initial thickness of the of 25.5 mm was used.

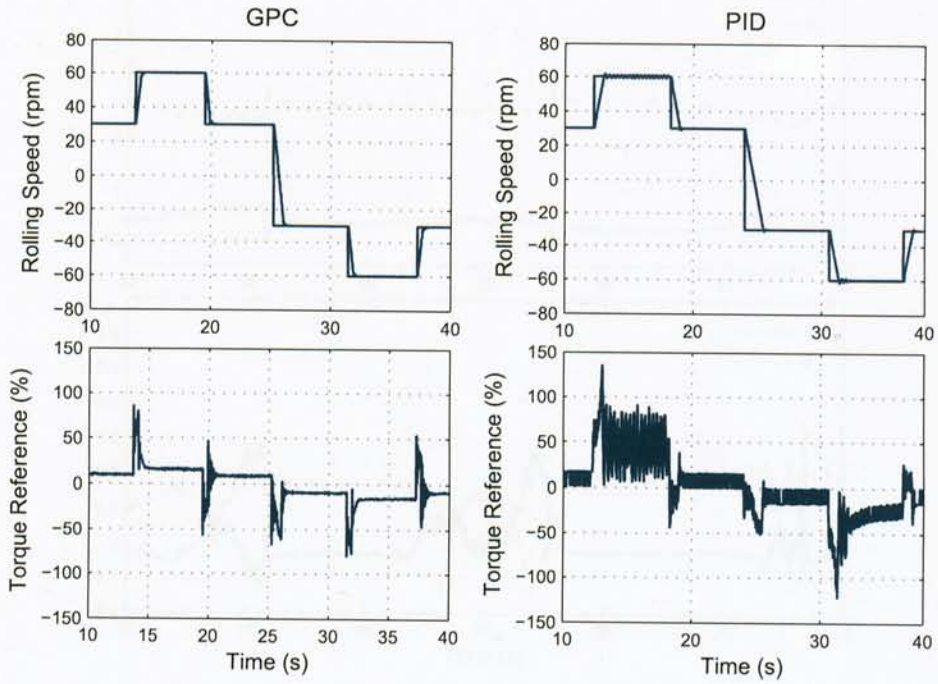


Figure 7.17: GPC vs. PID real-time speed control

The stock was heated and prepared for rolling at 300°C. The experiment was designed to be a 4 rpm single-pass and 60% reduction in thickness. As shown in Figure 7.21 the speed regulation was acceptable for this test, showing good disturbance rejection properties when the stock was fed into and came out of the rolls. This figure also shows the GPC performance compared to the one given by the PID controller under the same rolling conditions. It can be seen that although the time-response of GPC was slower, it was much smoother both in the rolling speed and torque, leading to a more effective energy-consumption during the stock deformation. The RMSE values for this experiment resulted in 0.139 rpm for GPC and 0.123 rpm for the PID controller. Finally, the average power used by the motor was 0.312 kW for GPC and 0.322 kW for the PID controller.

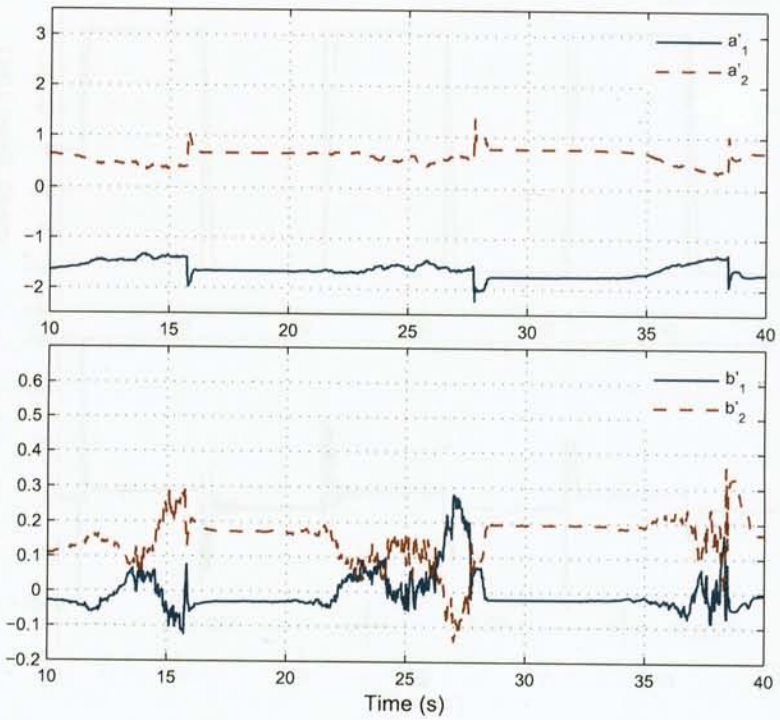


Figure 7.18: Model parameter estimates in real-time control under step-changes in the speed command

## 7.7 Results from Typical Rolling Schedules Performed in the Hille-Mill

Finally, this section shows experimental results from typical rolling schedules designed by IMMPETUS members to be performed in the Hille-mill under real conditions of deformation and temperature. GPC was used both in its adaptive and fixed forms. However, only selected (typical) experiments are presented here to show that the development and real-time implementation of GPC in the Hille-mill is one of the major contributions of this research work. The first experiment was designed to be a two-pass hot-rolling of a stainless steel stock with initial thickness of 50 mm. The operating mode of the Hille-mill was set to "manual". The sample was pre-heated at 1100°C and was subjected to 20% reduction per pass. The rolling schedule for this experiment is shown in Table 7.1.

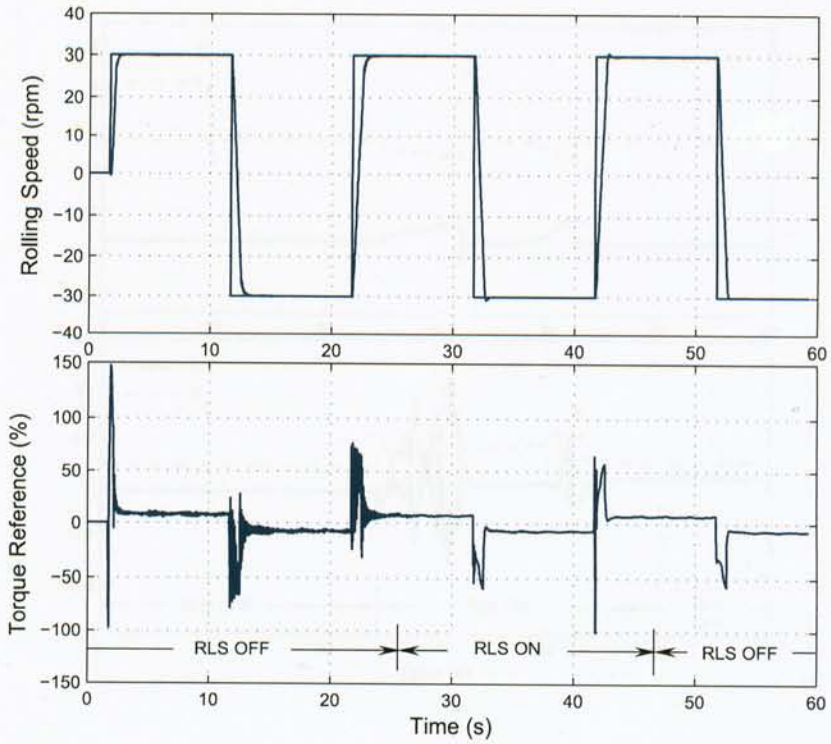


Figure 7.19: Real-time performance of GPC with ON/OFF-line system identification

Figure 7.22 shows the results of this test. GPC was allowed to run with some initial parameter estimates, which were obtained at the end of a trial run at the rated rolling speed. The identification system was also allowed to be on-line during the whole test. Initially the system followed a speed command of 20 rpm in forward direction followed by the first rolling pass with a reduction in thickness of 20%, typical of this kind of experiment. As soon as the stock came out of the rolls, the motor was stopped to allow the operator to adjust the gap position down to 32 mm. The second pass was then

Table 7.1: Rolling schedule for experiment 1

| Pass No. | Rolling Speed (rpm) | Reduction (%) | Gap (mm) |
|---|---|---|---|
| 1 | 20 | 20 | 40 |
| 2 | 20 | 20 | 32 |

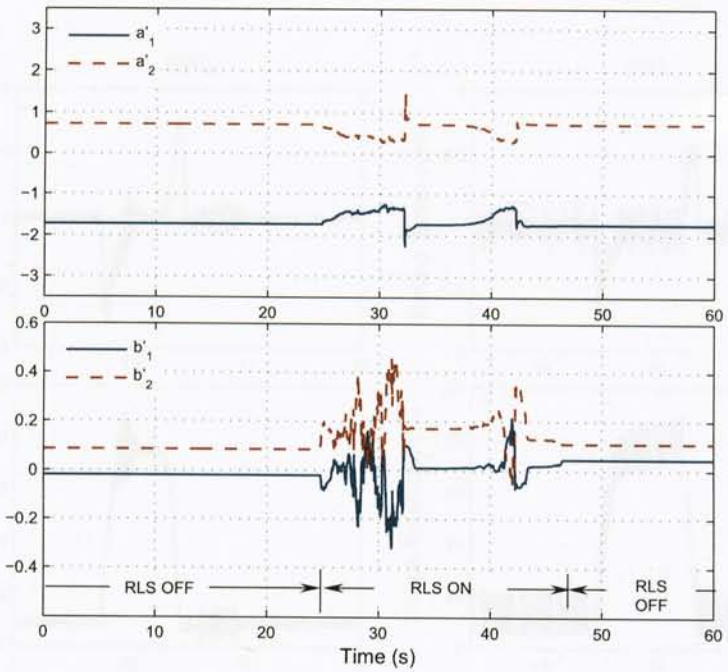


Figure 7.20: Model parameter estimates when RLS was switched ON/OFF

carried-out at 20 rpm in backward direction. As shown in Figure 7.22, GPC did not demonstrate any unstable modes but there were large control excursions especially during the disturbance phases. Notice that when the system was stopped and re-started for the second pass, the response seems to be slow at tracking the set-point change resulting in large control effort, this being due to the fact that the parameter estimates were detuned. However, once enough excitation had been provided, the parameter estimates led to a better set-point tracking with a good speed regulation.

The rolling schedule for the second rolling experiment is shown in Table 7.2. In this case, a four-pass forward-reverse hot-rolling experiment was performed using the C-Mn steel alloy which had been heated at 1100°C. The initial thickness was 25.4 mm. After 8 seconds, the parameter estimation mechanism was switched-off. Figure 7.23 shows the results of this experiment, where an acceptable set-point tracking was observed with a good speed regulation despite the fact that the systems was required to operate at twice the rated speed. Although there was no system identification from $t = 8$ s onwards, the control effort was kept low even at the finishing rolling pass when

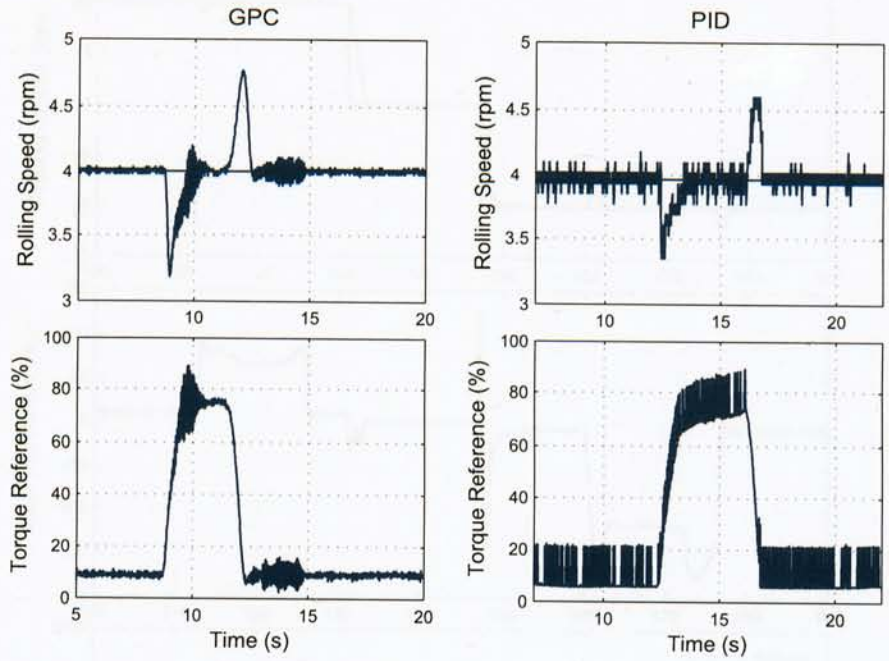


Figure 7.21: GPC vs. PID real-time performance during a speed regulation test

the system worked in a different operating point.

Table 7.2: Rolling schedule for experiment 2

| Pass No. | Rolling Speed (rpm) | Reduction (%) | Gap (mm) |
|---|---|---|---|
| 1 | 60 | 20 | 20.32 |
| 2 | 60 | 20 | 16.25 |
| 3 | 60 | 20 | 13.00 |
| 4 | 30 | 20 | 10.4 |

## 7.8 Concluding Remarks

The control performance shown by GPC in the Hille-mill represents an important achievement for the accurate control and regulation of the rolling speed and it is

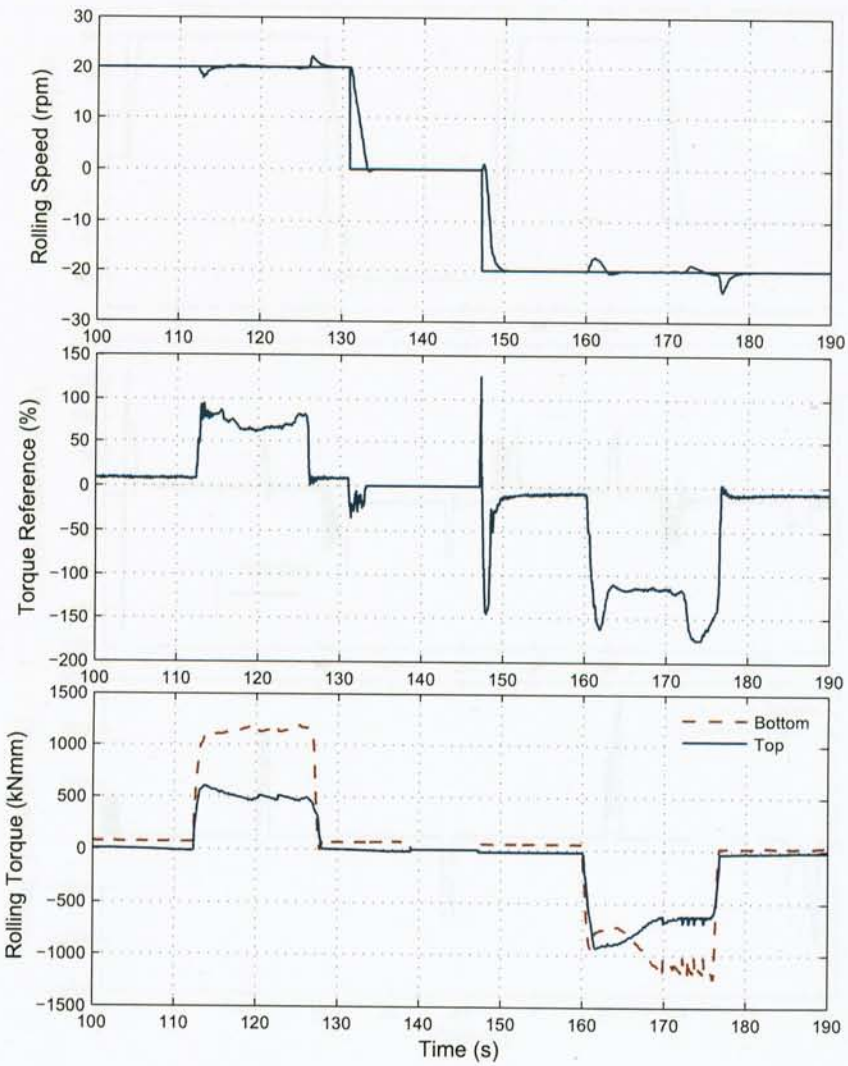


Figure 7.22: Real-time performance of GPC during the hot-rolling of steel

one of the major contributions of this research work. The use of conventional PID controllers in this particular application produced a very active control signal and shaft chattering when working above the rated speed. This varies the amount of strain or strain rate applied to the stock when rolled and, as a result, a possible mismatch between the final product and the original design may be produced.

Examining GPC from a computational viewpoint revealed that the computational burden of the control algorithm was big compared to the one in conventional controllers. This was inevitably due to the series of calculations that take place at ev-

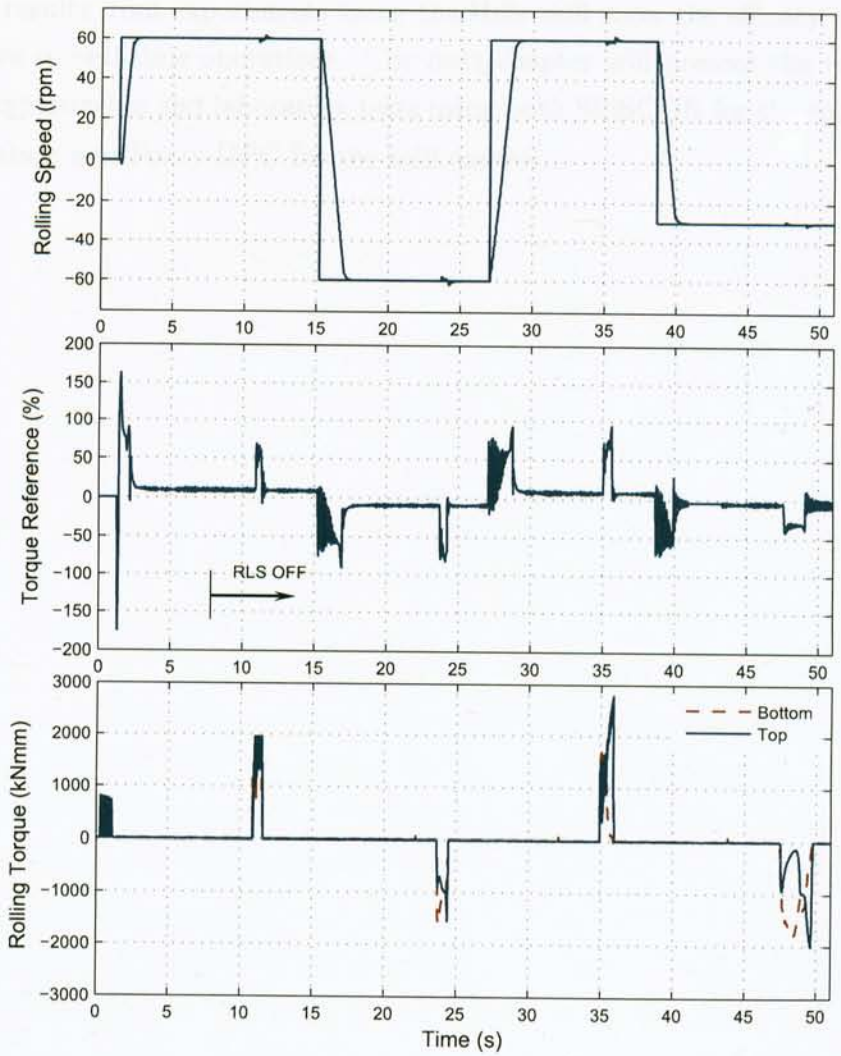


Figure 7.23: Real-time performance of GPC during the hot-rolling of steel at the maximum speed

ery sampling instant such as parameter estimation, output prediction, optimisation, etc. This became more evident during the real-time operations. Due to the time-consuming nature of this strategy, it was decided to use an adaptive linear model which led to acceptable results and yet optimal performances when rolling experiments in the Hille-mill were performed. The real-time implementation of GPC in the Hille-mill allowed for obtaining optimal control of the rolling speed, so that effective application of deformation profiles could be expected.

The results from experiments using the Hille-mill show the efficacy of the control algorithm in real-time operations. The next chapter will present the results of hot-rolling experiments and laboratory tests using both SISSCOR for the rolling schedule optimisation and Fuzzy-GPC for the mill control.

# Chapter 8

# Real-Time Evaluation of SISSCOR via Hot-Rolling Experiments and Laboratory Testing

## 8.1 Introduction

This chapter presents the experimental and laboratory procedures to carry-out hot-rolling experiments using the Hille-mill, from stock preparation to microstructure analyses and mechanical testing. SISSCOR is used to calculate the optimal rolling schedule according to a set of pre-defined requirements so as to achieve a *right-first-time* production. The optimisation procedures already described in Chapters 4 and 5 are implemented within the SISSCOR computing platform to facilitate the metal design and the process development. Up to 23 hot-rolling experiments were carried-out under different working conditions and design criteria. After each rolling experiment, the samples were cut, polished, and etched to reveal the quantitative features of the microstructure; then, selected specimens were machined to be subjected to mechanical testing. The results from such laboratory tests were then compared to the desired metal design in order to evaluate the accuracy and reliability of the proposed optimisation mechanism. Further details relating to the methodology which enables to carry-out these laboratory tests can be found in Appendix B.

The adaptive Generalised Predictive Control developed in Chapter 7 was also used during the rolling experiments in order to guarantee the optimal control performance of the Hille-mill.

## 8.2 Stock Preparation

The experimental material was the commercial type C-Mn Steel alloy (Bright Mild Steel) grade 080A15, of composition 0.16% carbon, 0.19% silicon, 0.73% manganese, 0.021% sulphur, and 0.012% phosphorus according to the manufacturer specifications. The material was received in the form of hot-rolled bars with a 50×25.4 mm cross section and were all 3 m long. For hot-rolling experiments using the Hille-mill, small slabs of 150 mm long were cut to facilitate reheating using a laboratory furnace.

A 20 mm long hole was drilled at the centre of each sample to insert a K-type thermocouple, which is made of a nickel-chromium/nickel-aluminium junction. This thermocouple is widely used in these types of applications since it is suitable for temperatures within the range of 95°C to 1260°C with a reasonable accuracy, having a sensitivity of 41 $\mu$V/°C approximately. The fact that the thermocouple was embedded in the metal allowed for good temperature readings during the whole process, including reheating, rolling, and cooling, as well as allowing for real-time recording of the temperature gradients. Figure 8.1 shows such an arrangement. As shown in this figure, a metallic hook was also embedded into the metal to hold the thermocouple wire and prevent a possible rupture or crack, as a result of the high temperature on the metal surface and excessive strain or twist in the wire when the stock was being deformed or handled by the operator. The thermocouple was connected to the high-speed network and interfaced to the PC, so that the stock temperature was continuously monitored and recorded automatically using the LabView-based DAQ system.

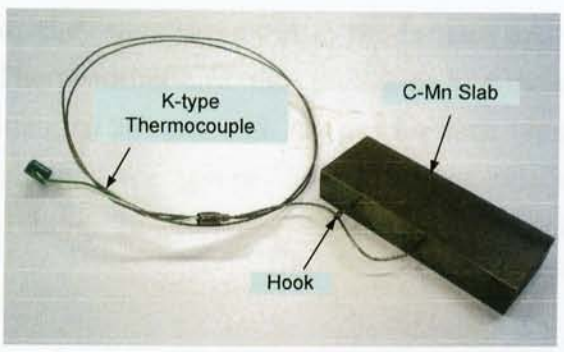


Figure 8.1: Arrangement of the stock to be rolled with an embedded K-type thermocouple

## 8.3 The Hot-Rolling Procedure using the Hille-mill

The procedure associated with the hot-rolling experiment using the Hille-mill can be divided in three main stages:

1. Reheating;
2. Hot-rolling; and
3. Cooling.

It is worth noting that important microstructural events take place during each stage. As already described in Chapter 3, during reheating grains grow and the microstructure itself consists of coarse grains of austenite. When passed through the rolls, the austenite grains are flattened and elongated on average, while each austenite grain undergoes a dimensional change that corresponds to that of the workpiece as a whole. Finally, after deformation and when the metal temperature is sufficiently low, phase transformation takes place leading to a predominantly ferrite-pearlite microstructure. As already discussed in Chapter 5, the above metallurgical phenomena are considered in SISSCOR; however, important information has to be first obtained in order to calculate the rolling parameters, such as the initial microstructure prior to hot-rolling (after reheating).

### *8.3.1 Reheating and the Initial Microstructure before Rolling*

In order to obtain the initial microstructure for hot-rolling, two samples were placed in the interior of an electric furnace for reheating either at 1180°C or 1100°C during 45 minutes; after that, they were taken out of the furnace and quenched in water at room temperature. The resulting austenite grain size was measured using the mean intercept method leading to 260 $\mu$m and 220 $\mu$m for each temperature respectively. Figure 8.2 shows a photomicrograph of the coarse austenite microstructure of the stock just before hot-rolling. To guarantee repeatability, all samples were reheated in the same manner.

### *8.3.2 The Hot-Rolling Experiment*

To illustrate the procedure of a typical hot-rolling experiment using the Hille-mill, consider Figure 8.3, which illustrates the sequence of a two-pass hot-rolling schedule.

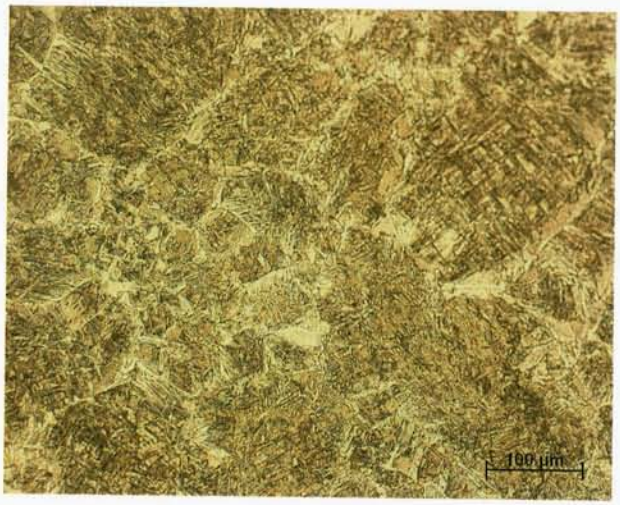


Figure 8.2: Austenite microstructure prior to hot-rolling

The sequence shown in this figure can be described as follows:

1. After heat treatment, the operator takes the stock out of the furnace.

2. The Hille-mill is started-up and the DAQ system is made to be operational. The stock temperature, the rolling speed, and the gap position are verified in order to initiate the experiment. The operator waits for the green light which will mark the beginning of the first pass.

3. The first pass takes place using the pre-defined rolling parameters. The rolling force and torque are measured along with the stock temperature. During this time, the metal microstructure goes through dynamic changes such as work hardening and the dynamic restoration processes.

4. The stock comes out of the rolls; its thickness has been reduced, its length increased, while its width remains largely unchanged. The steel microstructure begins its static changes such as recrystallisation and grain growth.

5. The operator holds the stock during the inter-pass time. During this time, the mill rolling direction and speed are changed, and the gap position adjusted according to the rolling schedule for the second pass.

6. After the holding-time, the operator introduces the stock back to the rolls to begin the second pass. Careful monitoring of the stock temperature is essential to accomplish the rolling schedule appropriately.

7. The second pass is carried-out. Further microstructural changes take place as a result of the additional strain applied to the metal leading to a refinement of the austenite grain size.

8. The operator holds the rolled metal. The mill is stopped, and the DAQ system remains operational until the stock temperature drops down to the transformation temperature. The stock is labelled, and put away for microstructural and mechanical analyses.

Although the sequence presented in Figure 8.3 represents a two-pass rolling experiment, further passes may be carried-out exactly in the same manner. As will be shown later, the experiments conducted in this work consist of up to 5 rolling passes.

### *8.3.3 Cooling*

Due to the fact that there was no available automatic mechanism to control the stock temperature, only air-cooling was considered in this work. Therefore, the type of microstructure expected for all experiments is comprised mainly of ferrite and pearlite fractions. Due to the carbon content of the metal used in these experiments, the austenite phase starts to change to the ferrite phase at approximately 875°C. After the last pass, the operator simply grips the metal until its temperature drops down to 723°C when there is no longer austenite phase, and the microstructure becomes predominantly a mixture of ferrite and pearlite fractions. After this, the rolled metal is put away and given an identification number in order to be machined and prepared for metallographic analysis and mechanical testing.

## 8.4 Metallographic Analyses

The metallographic analysis consisted of preparing the metal surface for examination by polishing and etching in order to reveal the microstructural constituents. After preparation, the sample was analysed using optical microscopy. In this case, the aim was to measure the final ferrite grain size of the rolled metal as well as the volume

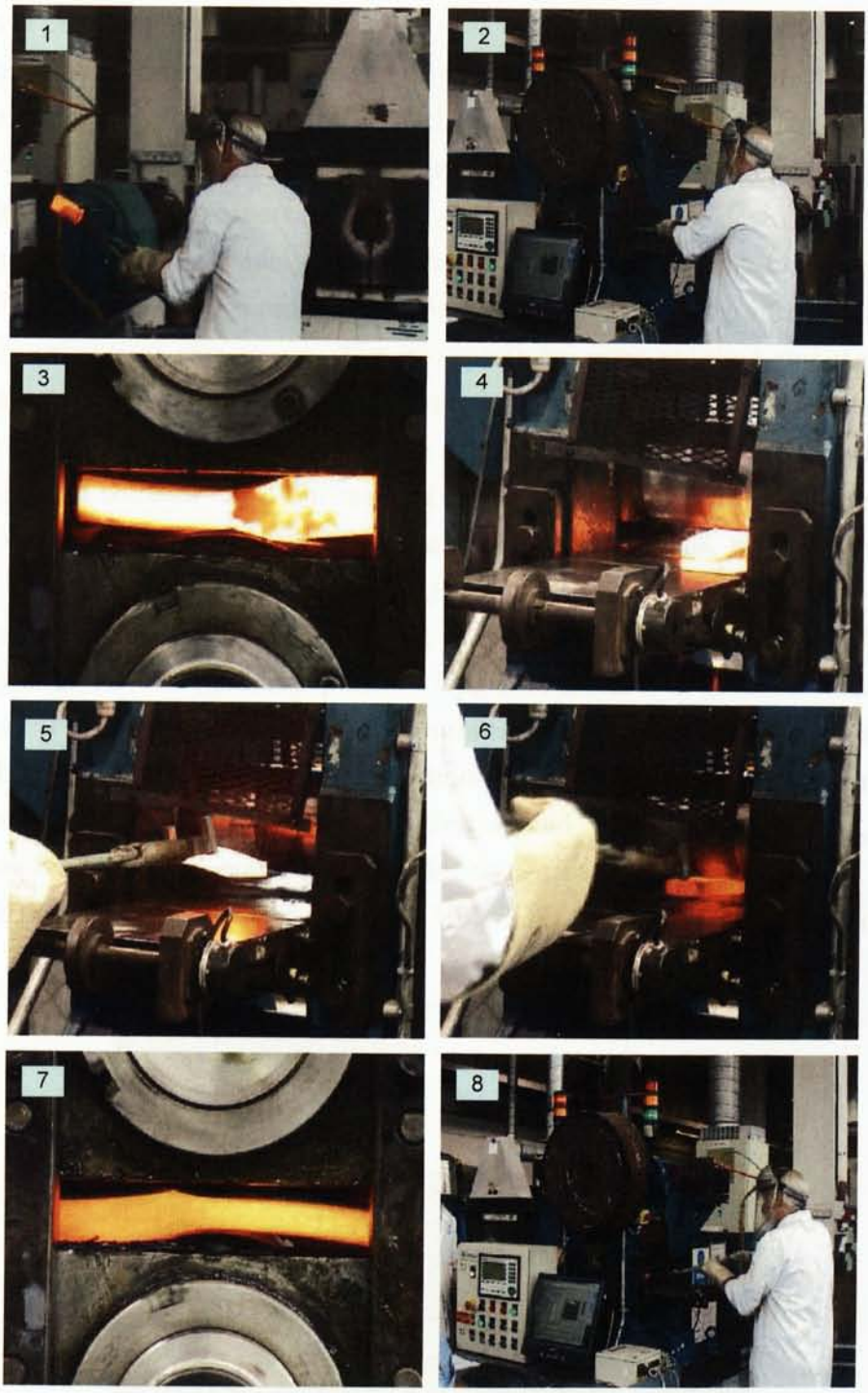


Figure 8.3: A sequence of a typical hot-rolling experiment using the Hille-mill

fraction of pearlite. As already mentioned, this work focused on duplex ferrite-pearlite microstructures produced as a result of air-cooling of the low carbon steel used in hot-rolling experiments. In such a structure, the pearlite colony and the ferrite grain size are the main microstructural features, the latter being the determining aspect that defines the mechanical properties.

To carry-out such an analysis, two small specimens were cut from each rolled stock. Figure 8.4 shows examples of specimens used for metallographic analysis and the 'Polyvar' optical microscope. The two specimens were polished and etched with 5% Nital in such a way that one showed the longitudinal surface of the rolled metal and the other one the transversal surface. In this regard, although it is obvious that the grains and colonies are 3-dimensional features of the metallurgical structure, it is conventional to report sizes measured on the planar sections, with no attempt to convert them to sizes of the 3-dimensional grains [31].

Once the microstructure was revealed, the method of measurement was based on counting numbers of boundaries per unit length or number of grains or colonies per unit area. This method is covered by international standards such as the standard ASTM E112 entitled "Standard Test Methods for Determining Average Grain Size", published by the American Standard for Testing and Materials [4].

Figure 8.5 shows an example of the ferrite-pearlite structure in one of the hot-rolling experiments carried-out using the Hille-mill. On a photomicrograph, a com-

(a) (b)

Figure 8.4: (a) Polyvar optical microscope in the Digital Laboratory located in the Engineering Materials Department; (b) etched specimens for microstructure analysis

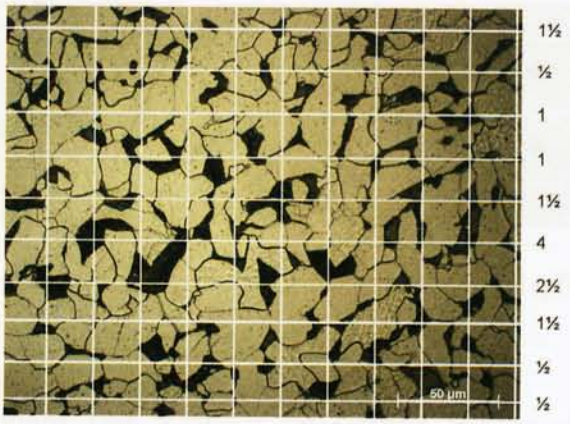


Figure 8.5: Method of point counting using a grid of points to determine pearlite colonies

plete grid of points was drawn as illustrated in Figure 8.5. The grid step size was chosen so as to allow the space of traverses to be sufficiently large for no two adjacent points to fall in the same pearlite colony. Points were registered as 'in pearlite' (counts 1), 'in ferrite' (counts 0), and 'at boundary' (counts $\frac{1}{2}$) to obtain the number of points in pearlite on each traverse.

Next, the same micrograph was used to count the number of boundaries per unit length along the same traverse lines used for counting pearlite colonies. Figure 8.6 shows the method of counting the number of ferrite and pearlite boundaries. As shown in this figure, the method required separate counts of the number of ferrite/pearlite boundaries and the number of ferrite/ferrite boundaries to be made along each of the traverses. Usually, a total of 100 testing lines (traverses) were used on photomicrographs taken from different areas of the specimen surface. A typical example of the procedure used to measure the ferrite grain size and the volume fraction of pearlite is shown in Appendix B.

## 8.5 Mechanical Tests

Several groups have developed standard methods for conducting the tension test. In the United States, standards published by the American Standards for Testing and Materials (ASTM) are commonly used to define tension test procedures and parameters. Indeed, the most common methods for tension testing of metallic materials is

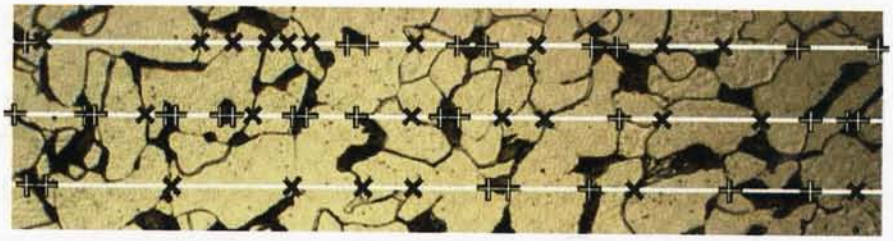

Figure 8.6: Method of counting ferrite/pearlite (+) and ferrite/ferrite (×) boundaries

the ASTM E8 "Standard Test Methods for Tension Testing of Metallic Materials" [5]. Standard methods for conducting the tension test are also available from other organisations, such as the Japanese Industrial Standards (JIS), the Deutche Institut fur Normung (DIN), and the International Organisation for Standardisation (ISO), but in general these are based on the ASTM E8 standard. The procedure for a typical tension test is shown in Appendix B.

### *8.5.1 The Test Specimen*

The test specimen is a small portion of the rolled metal, with dimensions specified by standard, and machined for submission to the tension test. The test specimen geometry is also standardised to allow for setting general specifications and nomenclatures for all tests[1]. Figure 8.7 shows the standard round tension test specimens used in this work [33].

Figure 8.7: Test specimens for tensile tests

[1]See Table B-3 of Appendix B for the specimen nomenclature, geometry, and dimensions.

### *8.5.2 Test Set-up*

The set-up of a tensile test involves the installation of the test specimen in the load frame of the testing machine. Other aspects of the test set-up include proper gripping and alignment of the test specimen, and the installation of an extensometer for measuring yield behaviour. The extensometer is attached to the test specimen so as to sense any small strain and magnify it into a meaningful signal for data processing. Figure 8.8 shows the tension test set-up of one experiment carried-out in the Thermo-mechanical Processing Laboratory of the Materials Engineering Department, at the University of Sheffield.

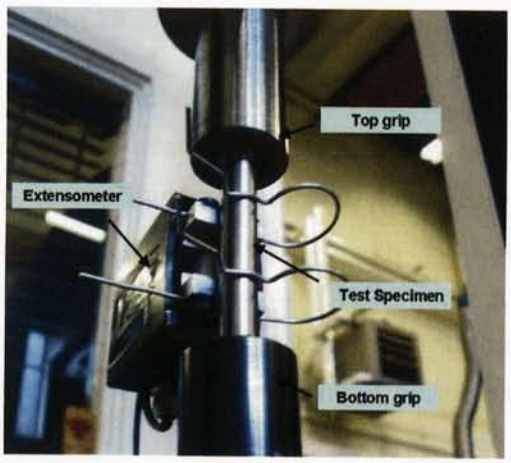


Figure 8.8: Tension test set-up

After the test specimen is adequately measured and prepared, and the test set-up established, conducting the test is fairly routine. The test specimen is installed in the grips, the extensometer fastened for measurement and data recording. The DAQ system has to be checked also. The test parameters used to set-up the testing machine are shown in Table B.2 of Appendix B. After the test, the DAQ system saves the datafile containing the amount of elongation and the load applied during the time of the experiment.

### *8.5.3 Variability of Tensile Properties*

Variability due to of the nonhomogenous nature of metallic materials is always present even when the test is performed successfully. Other material factors may be due to

specimen preparations such as the surface finish, the dimensional accuracy, the fillets at the ends of the reduction area, the taper in the gage length, the thread quality, etc. Additionally, the instrumental factors that can affect the test results are: the stiffness, the damping capacity, the natural frequency, and the mass of the moving parts of the testing machine; the accuracy of the force indication and the use of forces within the verified range of the machine; the rate of the force application, the alignment of the test specimen with the applied force, the verticality of the grips, the grip pressure, the nature of the force control used, the appropriateness and calibration of the extensometers, the heat dissipation, etc. [5].

## 8.6 Experimental Results

This section presents typical results from hot-rolling experiments carried-out using the Hille-mill. The aim was to evaluate experimentally the rolling schedules given by SISSCOR when considering different deformation conditions, and to compare the mechanical properties of the rolled metal with the desired design in order to conclude whether a *right-first-time* production was achieved. Also, it is worth remembering that during the experiments, the adaptive Fuzzy Model-based Predictive Control scheme was used to guarantee the optimal control performance during the experiments[2].

### *8.6.1 Rolling Experiment 1*

The first metal design consisted in calculating the optimal rolling schedule to achieve a C-Mn steel alloy with the following mechanical properties: 460 MPa and 300 MPa of TS and YS respectively, with an ITT of -95°C. For this experiment, all properties received the same degree of importance in the optimality criterion; therefore, each priority factor was set to one (i.e. $\beta = [\ 1 \quad 1 \quad 1\ ]$). The initial conditions included an initial deformation temperature of 1050°C, and an initial austenite grain size of 220 $\mu$m. As mentioned earlier, the stock initial dimensions were 150 mm long, 50 mm wide, and 25.4 mm thick. The inter-pass time was set to 55 seconds.

As far as the stock physical constraints were concerned, these were established bearing in mind the limitations of the metal due to its chemical composition and

[2]See Chapter 7.

the effect of air cooling on the final microstructure. In this case, the solution given by MODULE 1 should include a ferrite grain size between 8 $\mu$m and 30 $\mu$m, with a pearlite fraction no larger that 25%. On the other hand, although the Hille-mill can be operated within a wide range of working regimes, the mill constraints were set assuming different scenarios for 'safe' working conditions. For this experiment, the assumed scenario required a rolling speed between 10 rpm and 40 rpm, an amount of deformation per pass between 15% and 35%, and producing a rolling torque no higher than 3000 kNmm.

For MODULE 1, a random initial population with a uniform distribution was used with 20 individuals. The GA stopping criteria were defined in such a way that the process completed 50 generations or the cost function value was below $10^{-6}$. In the case of MODULE 2, the GA-based sequence was allowed to use a random initial population with a uniform distribution with 50 individuals representing values for the strain and the strain rate; each individual received a fitness score which was scaled in order to rank the population, so that the rank of the most fit individual was 1, the next most fit was 2, and so on in order to remove the effect of the spread of the raw scores. The GA should stop its search when either the fitness value was less or equal to $10^{-3}$, or 300 generations were completed. The scaling factor modulation[3] was set to $\eta = 0.12$, and the fuzzy inverse model was designed to consider air cooling during transformation.

With this initial information, SISSCOR gave the rolling schedule shown in Table 8.1. It is worth noting that the output of MODULE 1 included a required ferrite grain size of 13 $\mu$m with a pearlite fraction of 5.17%. Based upon this, MODULE 2 computed the best rolling parameters leading to a two-pass rolling schedule where the critical parameters were within the feasible range defined by the selected constraints.

As shown in Table 8.1, the predicted microstructure and properties of the rolled metal revealed that after phase transformation, the microstructure included ferrite grains with an average size of 13.86 $\mu$m and with a 6% of pearlite fraction, which was very close to the requirements. Using the property models, the predicted TS, YS, and ITT were 448.65 MPa, 319.31 MPa, and -94.96°C respectively.

Figure 8.9 shows a simulation of the evolution of the microstructure as well as the stock temperature through time when using the obtained rolling schedule. In

[3]See Equation (5.17).

Table 8.1: Rolling schedule and microstructure parameters for sample 1

| Results of Module 1 | | |
|---|---|---|
| Optimal Ferrite Grain Size ($\mu$m) | | 13 |
| Optimal Pearlite Fraction (%) | | 5.17 |
| **Results of Module 2** | | |
| | Rolling Pass No. | |
| | 1 | 2 |
| Temperature (°C) | 1050 | 901 |
| Strain | 0.399 | 0.305 |
| Strain Rate ($s^{-1}$) | 5.12 | 5.07 |
| Rolling Speed (rpm) | 40.00 | 38.00 |
| Reduction (%) | 29.3 | 23.3 |
| Gap Position (mm) | 17.69 | 13.36 |
| Exit Thickness (mm) | 17.96 | 13.78 |
| Torque (kNmm) | 2350 | 1836 |
| Force (kN) | 85 | 123 |
| Grain Target ($\mu$m) | 52 | 23 |
| Recrystallised Grain ($\mu$m) | 51.90 | 23.10 |
| Austenite Grain ($\mu$m) | 52.03 | 23.48 |
| Fraction Recrystallised (%) | 100 | 100 |
| **Predicted Microstructure and Properties at Room Temperature** | | |
| Ferrite Grain Size ($\mu$m) | | 13.86 |
| Pearlite Fraction (%) | | 6 |
| Tensile Strength (MPa) | | 448.65 |
| Yield Strength (MPa) | | 319.31 |
| Imp. Trans. Temp. (°C) | | -94.96 |
| Air Cooling Rate (°K/s) | | 1.63 |

this figure, it can be seen that the parameters given by SISSCOR led to an adequate control of the microstructure events at each rolling pass. For instance, the amount of strain applied in the first pass was enough to refine the initial austenite grain size from 220 $\mu$m to a recrystallised grain size of 51.90 $\mu$m, which eventually rose to 52.03 $\mu$m. For the second pass, the deformation profile achieved the desired target which led to a final austenite grain size of 23.48 $\mu$m. The temperature differences across the

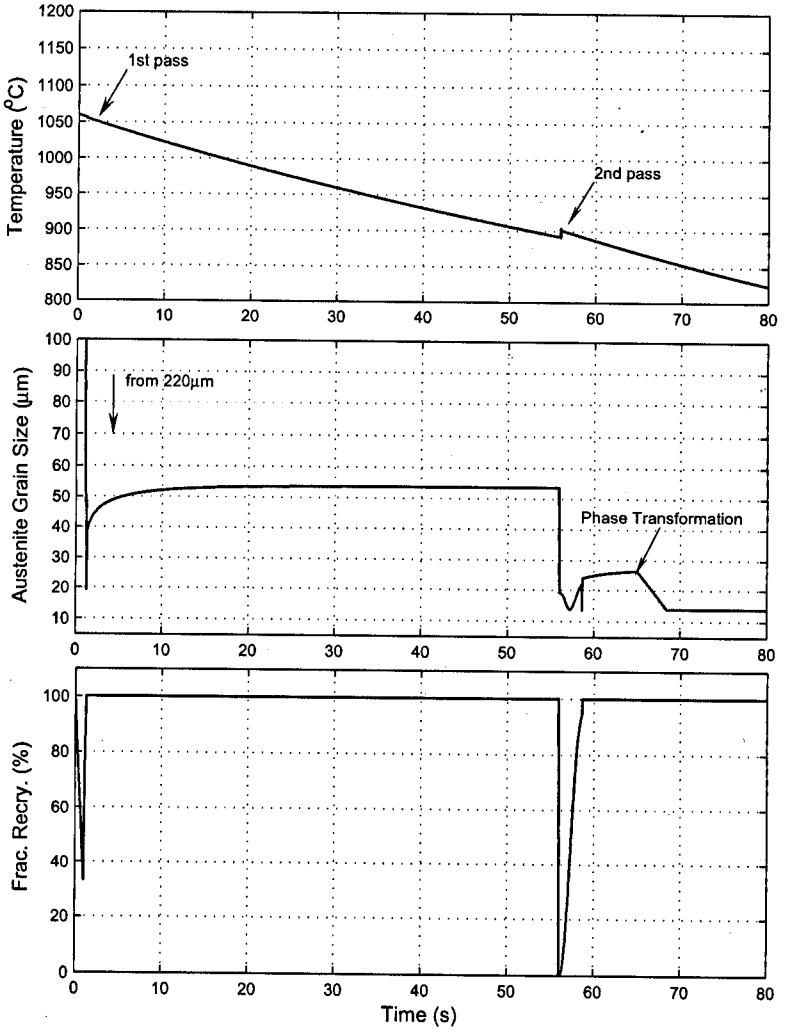


Figure 8.9: Simulation of the microstructure evolution during experiment 1

metal made the microstructure include some but negligible variations. Prior to phase transformation, no accumulated strain was found as a result of the full recrystallisation achieved during rolling.

Figure 8.10 depicts the main variables recorded by the DAQ system during this real-time experiment. Following the rolling schedule, the first pass was carried-out when the stock temperature was 1051°C, with a rolling speed of 40 rpm (forward direction), and a gap between work rolls of 17.69 mm. It is worth noting that this is not the exit thickness of the stock. According to Table 8.1, the exit thickness after the first pass was 17.96 mm, this means that a compensation of 0.27 mm due to the

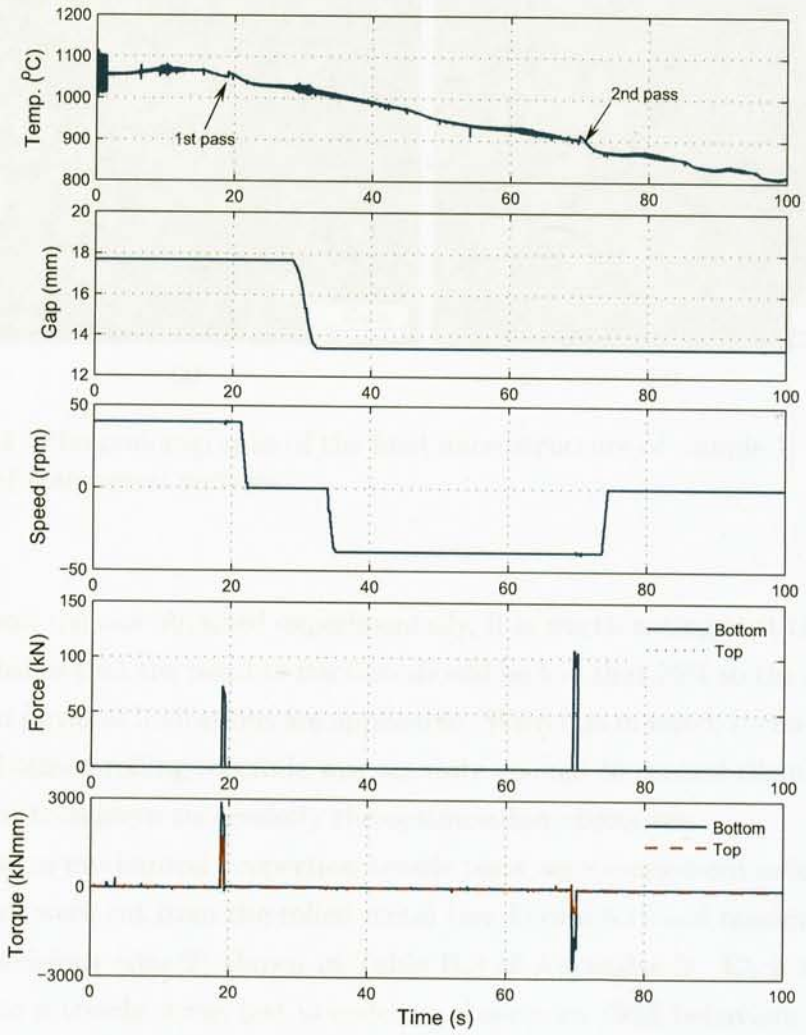


Figure 8.10: Main variables during the rolling experiment 1

mill spring was taken into account.

A metallographic analysis of the rolled metal revealed that, by using the obtained rolling schedule, the required microstructural parameters were achieved successfully. Figure 8.11 shows photomicrographs of the final state of the microstructure at room temperature. As shown in this figure, the duplex microstructure was comprised predominantly of ferrite grains and pearlite fractions (dark areas). By using the methodology for quantifying the microstructure described in Appendix B, a mean ferrite grain size of 12.67 $\mu$m with a pearlite fraction of 20.13% was achieved.

Although there is a large mismatch between the required percentage of pearlite

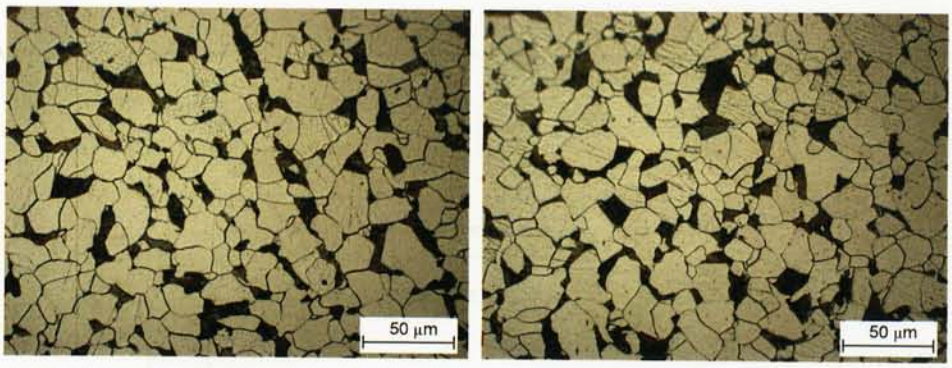


(a) (b)

Figure 8.11: Photomicrographs of the final microstructure of sample 1; (a) longitudinal and (b) transversal sections

fractions and the one obtained experimentally, it is worth noting that the desired design establishes that the pearlite fraction should be less that 25% so that the property models and physical limitations are applicable. With this in mind, it can be concluded that the obtained rolling schedule was accurate enough to control the microstructure events so as to achieve successfully the optimisation objectives.

In terms of mechanical properties, tensile tests were carried-out using three specimens which were cut from the rolled metal (see Figure 8.7) and machined according to the dimensions (size 2) shown in Table B.3 of Appendix B. Each specimen was subjected to a tensile stress test in order to observe its yield behaviour and evaluate its mechanical properties. Figure 8.12 shows the results from such a test. The plots show a linear elastic behaviour of the metal at the beginning of the test until a point in which the stress is too high that the metal started to deform. That point, as given by the 0.2% proof stress, is the lower yield stress, or the yield strength. In this case, the mean YS was 312.33 MPa.

Once in the plastic range, the load change rate became much slower than the elongation change rate producing a very slow stress increment. When the applied strain reached 0.023, the extensometer was removed and further load was applied to the specimen at a faster speed until fracture. The maximum stress developed in the specimen just before fracture was taken as the tensile strength. In this case, the mean TS was 474 MPa.

Table 8.2 summarises the results of this experiment. As already discussed, in

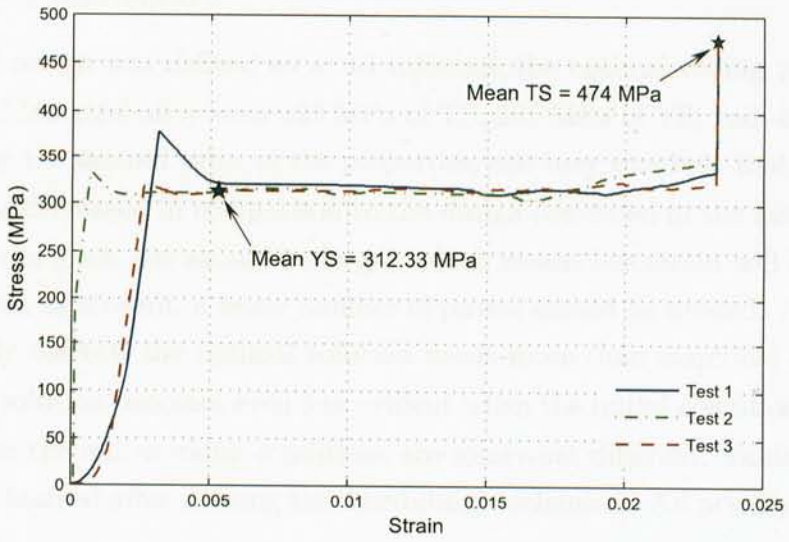


Figure 8.12: Engineering stress-strain curve for sample 1

terms of the microstructure, the desired parameters were successfully achieved. On the other hand, in terms of the mechanical properties, it is worth mentioning that only the tensile and yield strengths were tested. Bearing in mind that an error of as much as $\pm 10\%$ is usually accepted in metal design, the results of the tensile tests can be also considered as acceptable.

Table 8.2: Final microstructure and mechanical properties of sample 1

| | Desired | Final | |
|---|---|---|---|
| | | Predicted | Experiment |
| Ferrite Grain Size ($\mu$m) | 13 | 13.86 | 12.67 |
| Pearlite Fraction (%) | $< 25$ | 6 | 20.13 |
| Tensile Strength (MPa) | 460 | 448.65 | 474 |
| Yield Strength (MPa) | 300 | 319.31 | 312 |
| Imp. Trans. Temp. (°C) | -95 | -94.96 | — |

### *8.6.2 Rolling Experiment 2*

The second design was defined so as to calculate the optimal rolling parameters to produce a C-Mn steel alloy with 420 MPa of TS, 286 MPa of YS, and -60°C for ITT. As shown by the desired value of the properties, one may conclude that, because the strength was decreased in comparison to the design presented in the last section, the required ferrite grain size should be larger, which means less strain will be applied to the stock and, as a result, a lesser number of passes should be needed. Although this is technically correct, the optimal solution needs more than empirical assumptions. In fact, the solution becomes even less evident when the initial conditions have small differences or the mill working conditions are somewhat different. Table 8.3 presents the results obtained after running the scheduling mechanism. All priority factors were also set to 1.

As expected, MODULE 1 provided a larger requirement for the ferrite grain size, i.e. 15 $\mu$m, with 20% pearlite fraction. However, in order to achieve such a microstructure, MODULE 2 gave a completely different schedule for the experiment, which consisted of three rolling passes at a high speed but with smaller reductions per pass. The initial conditions for the experiment were the same as in the previous design, with an initial temperature of 1050°C, and an austenite grain size of 220 $\mu$m. Therefore, the differences in the rolling schedule are mainly due to the mill working conditions. In this experiment the Hille-mill working range was set in such a way that the electric motor worked above the rated speed, which is between 30 rpm and 60 rpm. For this reason, the capability of the motor to deliver electromagnetic torque was diminished, so that the constraints for the amount of reduction and rolling torque per pass had to be narrowed, the percentage of reduction per pass being between 15% and 30%, hence producing a rolling torque of as much as 2500 kNmm.

The simulation results shown in Figure 8.13 show the evolution of the microstructure when applying the optimised rolling schedule. Note that, because of the selected constraints, the process required small reductions per pass, but more rolling passes in order to achieve the grain targets. This can be clearly seen in the first pass, where the deformation profile led to a recrystallised austenite grain size of 103 $\mu$m, which is two times bigger than that in the previous design for the first pass. Another important aspect was that, although the time for full recrystallisation for the first time was slow, the parameters given by the scheduling mechanism eventually led to a proper control

Table 8.3: Rolling schedule and microstructure parameters for sample 2

| Results of Module 1 | | | |
|---|---|---|---|
| Optimal Ferrite Grain Size ($\mu$m) | | | 15 |
| Optimal Pearlite Fraction (%) | | | 20 |
| **Results of Module 2** | | | |
| | Rolling Pass No. | | |
| | 1 | 2 | 3 |
| Temperature (°C) | 1050 | 982 | 917 |
| Strain | 0.199 | 0.270 | 0.280 |
| Strain Rate ($s^{-1}$) | 5.215 | 5.64 | 5.97 |
| Rolling Speed (rpm) | 60.00 | 50.00 | 46.00 |
| Reduction (%) | 15.8 | 20.85 | 21.69 |
| Gap Position (mm) | 21.34 | 16.68 | 12.87 |
| Exit Thickness (mm) | 21.37 | 16.91 | 13.24 |
| Torque (kNmm) | 1270 | 2186 | 1709 |
| Force (kN) | 14 | 97 | 89 |
| Grain Target ($\mu$m) | 103 | 42 | 21 |
| Recrystallised Grain ($\mu$m) | 103 | 41.6 | 21.8 |
| Austenite Grain ($\mu$m) | 61.1 | 42.45 | 26.3 |
| Fraction Recrystallised (%) | 100 | 100 | 100 |
| **Predicted Microstructure and Properties at Room Temperature** | | | |
| Ferrite Grain Size ($\mu$m) | | | 14.29 |
| Pearlite Fraction (%) | | | 20 |
| Tensile Strength (MPa) | | | 421.11 |
| Yield Strength (MPa) | | | 286.14 |
| Imp. Trans. Temp. (°C) | | | -59 |
| Air Cooling Rate (°K/s) | | | 1.75 |

of the microstructural changes.

Prior to phase transformation, the mean austenite grain size was 26.3 $\mu$m with no accumulated strain. When the austenite transformed to ferrite and then to a ferrite-pearlite structure, the predicted microstructure was comprised of ferrite grains with an average size of 14.29 $\mu$m and 20% of pearlite fraction, which was very close to the requirement. However, it is worth mentioning that, although the rolling sched-

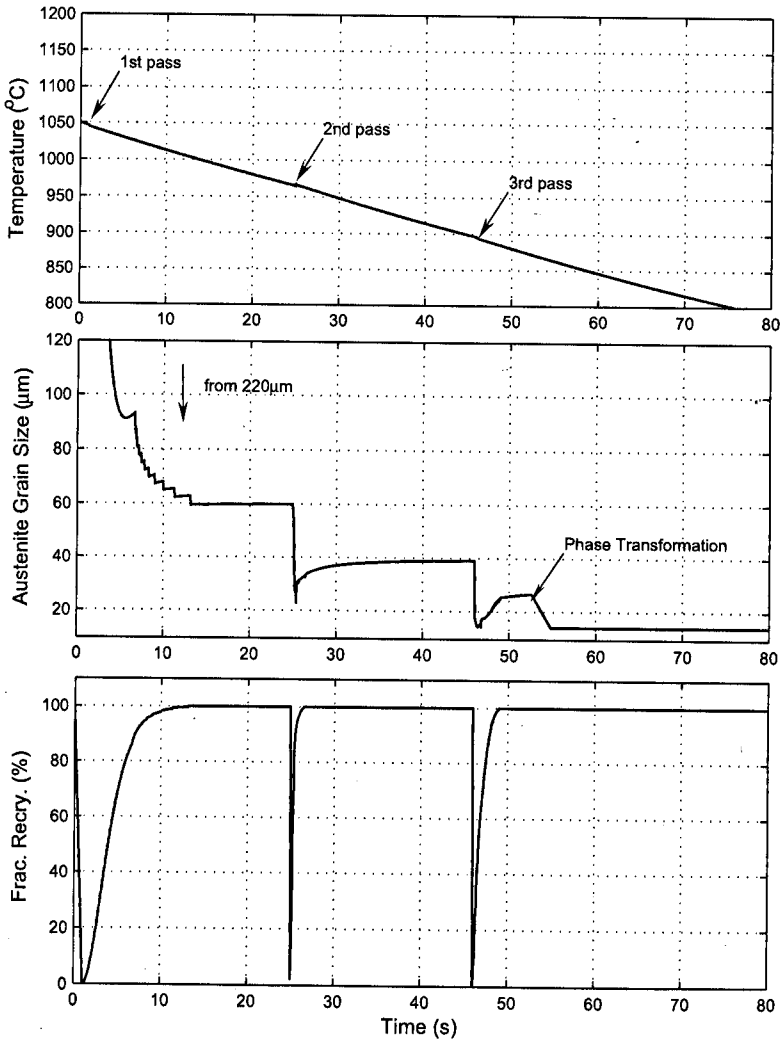


Figure 8.13: Simulation of the microstructure evolution during experiment 2

ule for this experiment worked adequately, it was observed that if reductions smaller than 15% are used, there will not be enough energy in the metal to reach full recrystallisation, so that instead of refining the austenite grain, it may result in grain coalescence. This knowledge is implicitly embedded in the optimality criterion of MODULE 2, which states that, in order for the deformation profile to be optimal, the metal has to complete full recrystallisation before the next pass (i.e. $X \approx 1$ in Equation (5.13)). The fact that the rolling parameters for the first pass are near the constraint boundaries shows that the decision variables were close to the unfeasibility region, making the solution less obvious.

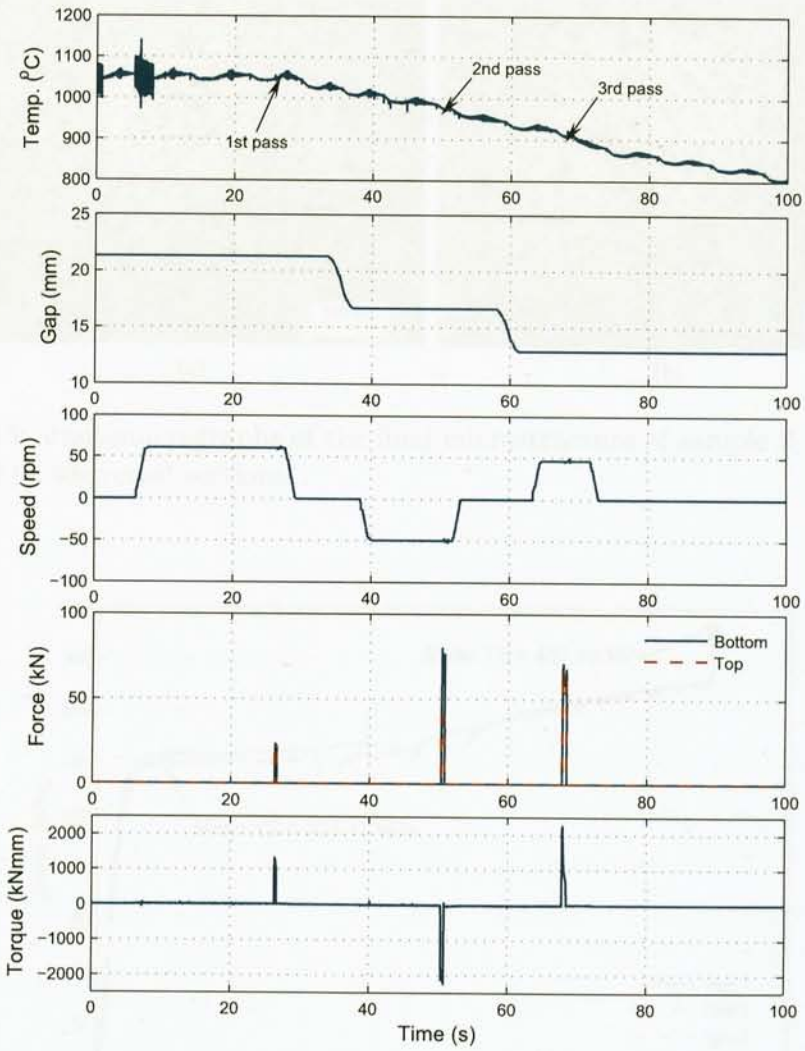


Figure 8.14: Main variables during the rolling experiment 2

Figure 8.14 shows the Hille-mill performance for this experiment. It can be seen that no constraint violation occurred during all passes. In terms of the control performance, both the speed control and regulation were acceptable despite the fact that the system was operated above the rated speed. No overshoot was observed in any case, and a very fast transient response was observed.

Figures 8.15 and 8.16 show the final microstructure and the results from the mechanical tests. After quantification of the metal surface using 10 different micrographs, the final ferrite grain size was 14.72 $\mu$m, whereas the pearlite fraction was 19.22%,

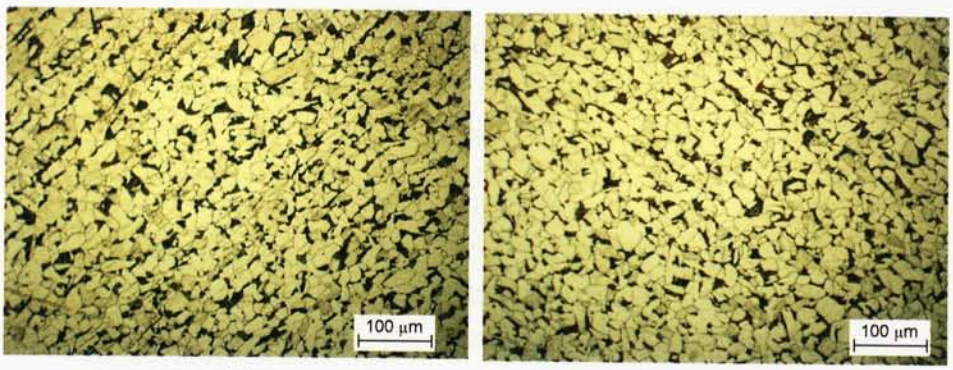


Figure 8.15: Photomicrographs of the final microstructure of sample 2; (a) longitudinal and (b) transversal sections

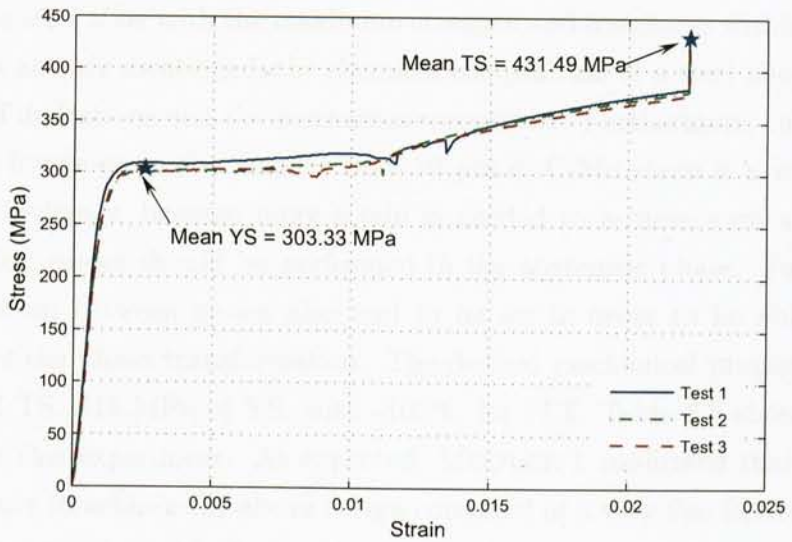


Figure 8.16: Engineering stress-strain curve for sample 2

which is considered to be very close to the optimal microstructure. On the other hand, the yield behaviour of the metal showed that the average starting point of deformation was 303.33 MPa. Similarly, the mean stress of fracture was 431.49 MPa that is only 11.49 MPa more than the set point. Table 8.4 summarises the results of this rolling experiment.

Table 8.4: Final microstructure and mechanical properties of sample 2

| | DESIRED | FINAL | |
|---|---|---|---|
| | | Predicted | Experiment |
| Ferrite Grain Size ($\mu$m) | 15 | 14.29 | 14.72 |
| Pearlite Fraction (%) | $< 25$ | 20 | 19.22 |
| Tensile Strength (MPa) | 420 | 421.11 | 431.49 |
| Yield Strength (MPa) | 286 | 268.14 | 303.33 |
| Imp. Trans. Temp. (°C) | -60 | -59.6 | — |

### *8.6.3 Rolling Experiment 3*

The main aim of the next design was to achieve a very small ferrite grain size in order to produce a steel alloy with the maximum strength and toughness within the range of interest. As already mentioned, the chemical composition of a steel alloy defines also the physical limitations and the mechanical properties. Furthermore, the difficulty of achieving a ferrite grain size smaller than 10 $\mu$m in C-Mn steels is a well publicised fact [70]. Obviously, because more strain is needed to achieve such a small grain, several rolling passes should be performed in the austenitic phase. Furthermore, a quick transition between passes also had to be set in order to be able to roll the metal before the phase transformation. The desired mechanical properties included 463 MPa of TS, 344 MPa of YS, with -100°C for ITT. Table 8.5 shows the rolling schedule for this experiment. As expected, MODULE 1 confirmed that the optimal microstructure to achieve the above design consisted of a very fine ferrite grain. Note that four passes were required to achieve such targets.

The initial conditions for this experiment were different to the previous ones. In this case the starting rolling temperature was 1150°C, which produced an initial austenite grain size of 260 $\mu$m. The mill working conditions were set in such a way that the rolling speed was between 10 rpm and 30 rpm, a percentage of reduction per pass between 10% and 40% producing a load no higher than 3000 kNmm. The inter-pass time was 15 seconds. The refinement of the austenite grain using the obtained schedule can be seen in Figure 8.17. The evolution of the microstructure was very similar to the ones already described. However, the amount of deformation applied to the metal during rolling led to a faster cooling rate which resulted in a smaller

Table 8.5: Rolling schedule and microstructure parameters for sample 3

| Results of Module 1 | | | | |
|---|---|---|---|---|
| Optimal Ferrite Grain Size ($\mu$m) | | | | 10 |
| Optimal Pearlite Fraction (%) | | | | 19 |
| **Results of Module 2** | | | | |
| | Rolling Pass No. | | | |
| | 1 | 2 | 3 | 4 |
| Temperature (°C) | 1150 | 1060 | 975 | 893 |
| Strain | 0.399 | 0.314 | 0.352 | 0.433 |
| Strain Rate ($s^{-1}$) | 2.239 | 1.840 | 4.868 | 5.154 |
| Rolling Speed (rpm) | 17.45 | 13.83 | 29.93 | 24.11 |
| Reduction (%) | 29.21 | 23.82 | 26.28 | 31.32 |
| Gap Position (mm) | 17.74 | 13.41 | 9.72 | 6.38 |
| Exit Thickness (mm) | 17.97 | 13.69 | 10.09 | 6.93 |
| Torque (kNmm) | 1497 | 1545 | 1808 | 2773 |
| Force (kN) | 22 | 42 | 95 | 181 |
| Grain Target ($\mu$m) | 52 | 26 | 18 | 12 |
| Recrystallised Grain ($\mu$m) | 52 | 26.23 | 18.42 | 11.54 |
| Austenite Grain ($\mu$m) | 65.57 | 45.85 | 31.18 | 21.81 |
| Fraction Recrystallised (%) | 100 | 100 | 100 | 100 |
| **Predicted Microstructure and Properties at Room Temperature** | | | | |
| Ferrite Grain Size ($\mu$m) | | | | 11.17 |
| Pearlite Fraction (%) | | | | 19.81 |
| Tensile Strength (MPa) | | | | 462.5 |
| Yield Strength (MPa) | | | | 344.1 |
| Imp. Trans. Temp. (°C) | | | | -99 |
| Air Cooling Rate (°K/s) | | | | 3.1799 |

ferrite grain size of 11.17 $\mu$m after the phase transformation, which is very close to the optimal microstructure.

An interesting aspect of this particular experiment was related to the good accuracy of the developed scheduling mechanism. Because of the fact that hot-rolling is a thermally-activated process, in order to ensure the success of the rolling experiment, careful monitoring of the stock temperature was of sum importance. However, the

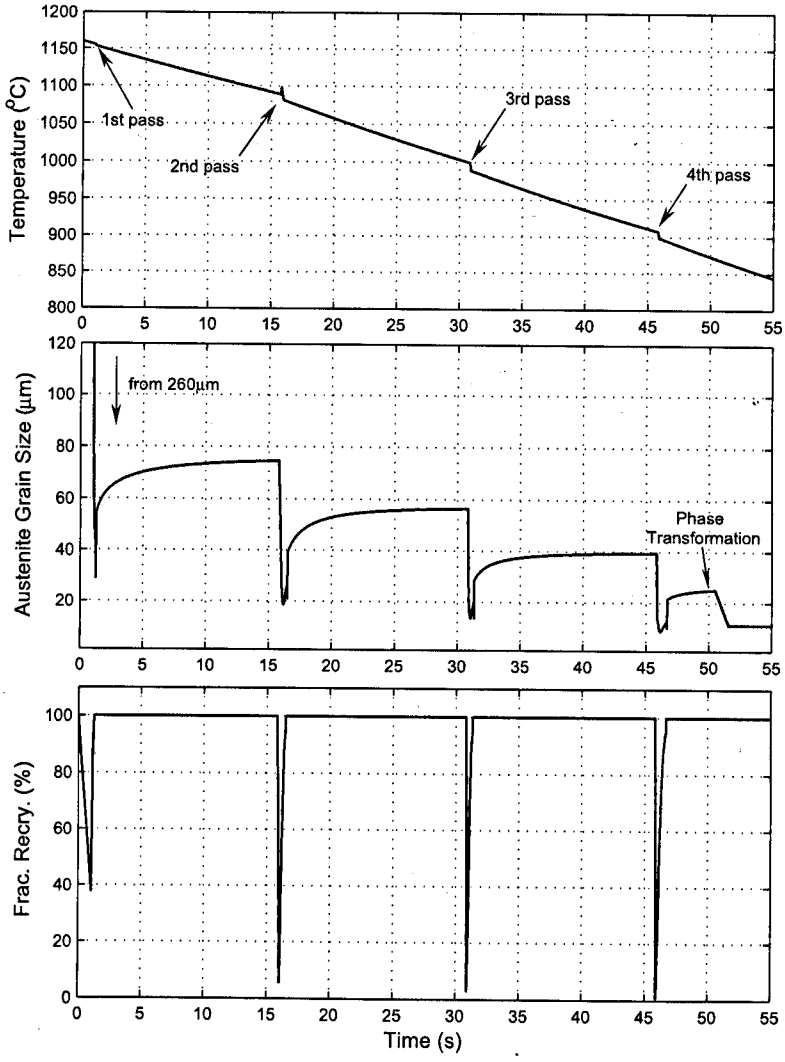


Figure 8.17: Simulation of the microstructure evolution during experiment 3

noisy nature of the measurements was a constant problem that did not allow for more accurate readings of the temperature so that an error range of ±10°C was allowed to mark the beginning of each rolling pass. Yet, in some experiments this was not the worst scenario because, as shown in Figure 8.18, the thermocouple broke as a result of various reasons, such as excessive twist of the wire when the stock was being handled by the operator, the friction between the stock surface and the wire, or even defects in the wire.

Temperature monitoring is especially important in industry even when sophisti-

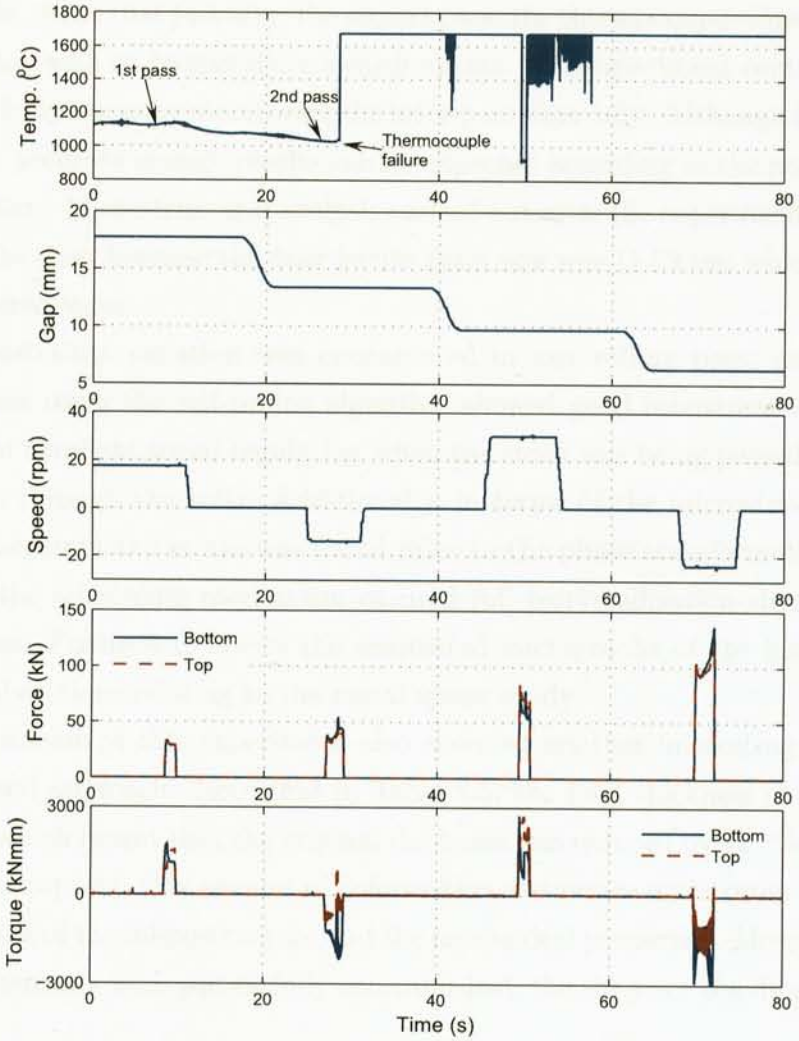


Figure 8.18: Main variables during the rolling experiment 3

cated mechanisms of real-time measurement are used, which include state-of-the-art pyrometers. Nevertheless, one of the main advantages of the model-based designs is that the whole process becomes more fault-tolerant because one can predict the system's behaviour. In this case, since the inter-pass time was known beforehand, the stock temperature can be estimated. Therefore, the rolling experiment can be successful even with no temperature readings by monitoring the holding times between each rolling pass instead.

Figure 8.18, also shows the real-time performance of the rolling mill during this

experiment. Note that just after the second pass, the thermocouple wire broke, leaving the operator with no temperature measurements. The experiment continued with the third and fourth pass by monitoring the inter-pass time only. Although this was not an ideal case, accurate enough results can be expected according to the proposed model-based system. Microstructural analysis carried-out after the experiment revealed that this was the case, because the final ferrite grain size was 11.02 $\mu$m which is very close to the desired value.

No constraints violation was encountered in any rolling pass, and the control performance using the self-tuning algorithm showed good robustness against disturbances and excellent speed regulation when the stock was being passed forwards and backwards through the rolls. Additionally, in terms of the microstructure development, no accumulated strain was found prior to the phase transformation due to the fact that the scheduling mechanism ensured full recrystallisation shortly after each rolling pass. Figure 8.19 shows the associated micrographs of the longitudinal and transversal sections relating to the metal under study.

The outcome of this experiment also revealed another interesting aspect about the proposed approach. Note that in Table 8.5, the final thickness of the stock was 6.93 mm, which meant that the original thickness was reduced by 72.7%. From a metallurgical viewpoint, this amount of deformation was necessary in order to achieve the requirements of the microstructure and the mechanical properties. However, although such requirements were successfully accomplished, the shape or the dimensions of the

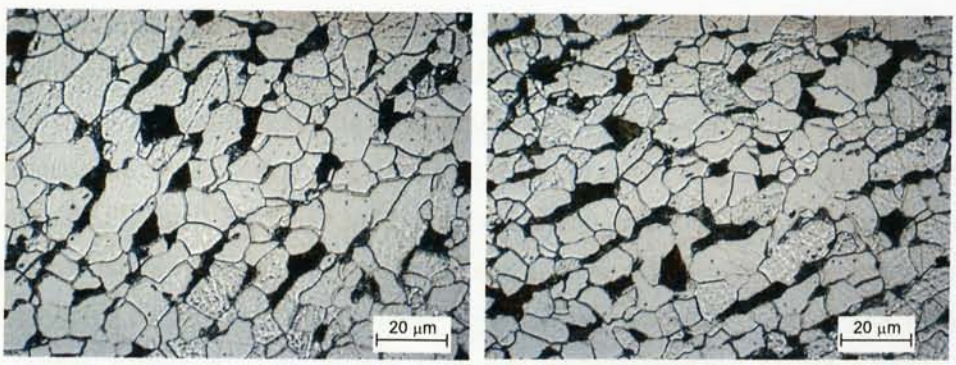


(a) (b)

Figure 8.19: Photomicrographs of the final microstructure of sample 3; (a) longitudinal and (b) transversal sections

final product may not be suitable for a particular application. This fact arose as a result of the often impossible task of machining specimens from the rolled metal in order to test its yield and tensile properties. Notice that the standard dimensions for the specimens subjected to tensile tests [4] require a minimum thickness of 9.5 mm for the grip sections. This inspired the idea of extending the optimality criteria of MODULE 2 by including a **'shape objective'** apart from the microstructure objectives considered. Although this new objective will expand the scheduling capabilities of the proposed approach, the trade-off between obtaining the desired microstructure and the final shape implies a decision to be made by the designer with a full appreciation of both the advantages and disadvantages of a particular application. Further directions relating to this aspect are included in Chapter 9.

Hitherto, only three rolling experiments have been presented showing the general trend in the results of this research work considering different scenarios of metal design and working conditions. However, up to 23 different rolling experiments are reported in this thesis. The next section presents a brief summary of all experiments.

### *8.6.4 A Summary of Results*

Figure 8.20 shows a comparison between the optimal and the final microstructure (i.e. ferrite grain size) obtained after microstructural analysis carried-out on the 23 rolled samples. The optimal values were calculated by SISSCOR. Note that there is a good match between the optimal design and the final product as shown by the $\pm 10\%$ confidence band described by the discontinuous lines. The RMSE of the resulting data was calculated in order to have a quantitative measure of the variations of the experimental data with respect to the optimal value, which resulted in 0.767 $\mu$m.

Similarly, the results from the mechanical test carried-out using 10 rolled samples showed an acceptable accuracy of the developed approach. Figures 8.21 and 8.22 show the results of TS and YS respectively, comparing the user-defined requirements against the characteristics of the final product. Here, it is worth recalling the important role of the priority factors which are used to establish priorities among the properties in the overall criterion. This means that the property with a higher priority factor should be better achieved. For instance, in Figure 8.21, although all data points are within the bands, the one which is further away from the set-point corresponds to the

[4] See Table B.3 in Appendix B.

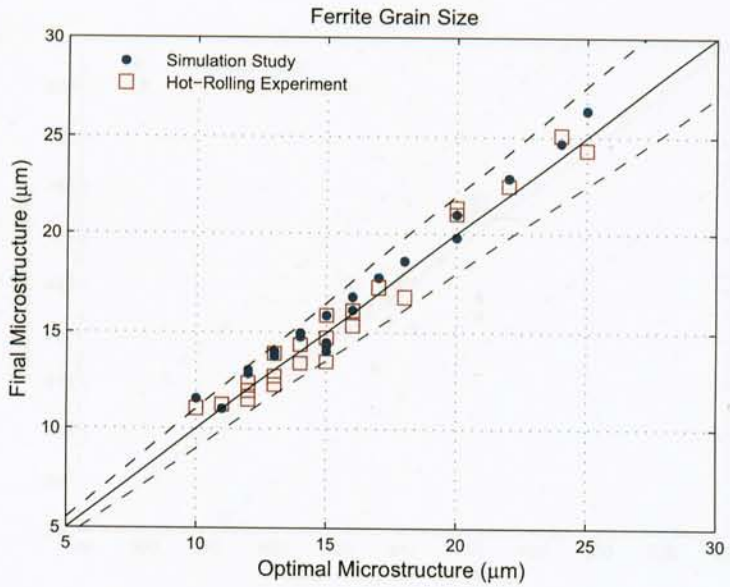


Figure 8.20: Desired vs. Final ferrite grain size

experiment number 15 (see Table 8.6) where the priority factor for TS was set to 2, whereas for YS it was 10. The same can be said in the case of experiment 14, where the priority factor for the TS and YS were set to 10 and 2 respectively. The plots for this example can be seen in Figure 8.22 where one predicted value is out of the band. The RMSE for TS was 12.5 MPa for the predicted data and 15.81 MPa for the experimental data. Similar values for YS were calculated, being 13.23 MPa and 10.40 MPa for the predicted and experimental data respectively.

Figure 8.23 shows the results of the final ITT against the user requirement. Unlike the previous results, no testing procedure was performed to evaluate the impact transition temperature in any rolled sample. As shown in the figure, there are two data points outside the acceptable range. These points correspond to experiments 1 and 21 where the priority factor established ITT as the property with the least degree of importance in the overall design. The RMSE for the predicted values was 3.9°C.

Finally, Tables 8.6 to 8.8 show a summary of the metal designs, the microstructure characteristics, and the rolling schedules for all the experiments carried-out in this research work.

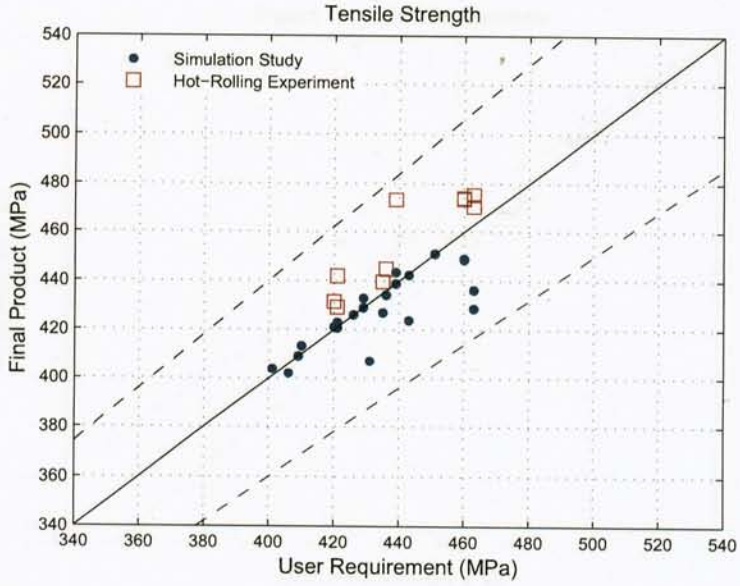


Figure 8.21: Desired vs. Final tensile strength

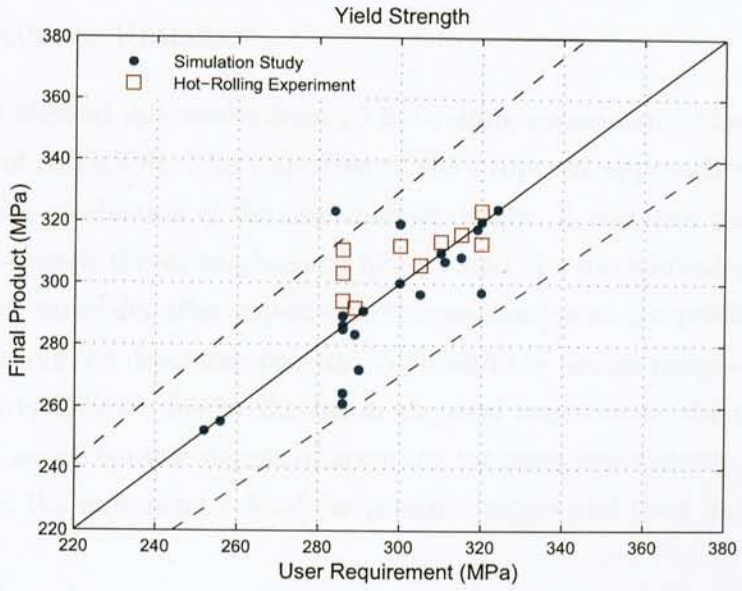


Figure 8.22: Desired vs. Final yield strength

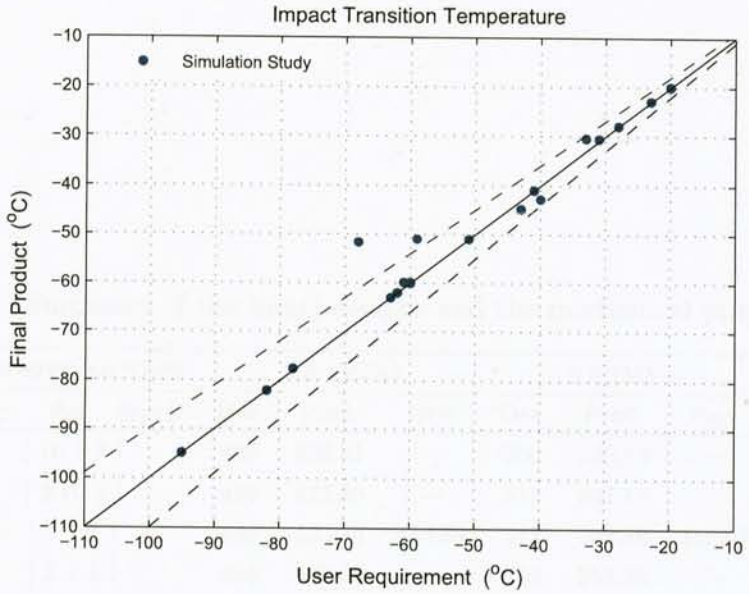


Figure 8.23: Desired vs. Final impact transition temperature

## 8.7 Concluding Remarks

This chapter showed the results from 23 hot-rolling experiments aimed at evaluating the efficacy of SISSCOR. The objective of the proposed approach was to achieve a *right-first-time* production of the user-defined design. It was seen that modelling the correlation between thermomechanical history and the mechanical properties of the final product, especially after experimental confirmation of the predictions, was very important during the designing process. Although the design range of this particular alloy was fairly limited due to the metal physical constraints, the experimental results showed an acceptable degree of accuracy for most experiments. The study also demonstrated the important role of the priority factors and their impact on the final product.

The number of experiments carried-out in this research allows one to evaluate the acceptable efficiency of the proposed scheduling approach, which aims at providing a systematic mechanism to produce metals with higher requirements and superior quality standards.

Table 8.6: Summary of the metal designs and the mechanical properties results

| Exp. | Priority factors | TS (MPa) | | | YS (MPa) | | | ITT (°C) | |
|---|---|---|---|---|---|---|---|---|---|
| No. | [$\beta_{TS}$ $\beta_{YS}$ $\beta_{ITT}$] | Des. | Pred. | Exp. | Des. | Pred. | Exp. | Des. | Pred. |
| 1 | [ 10 5 1 ] | 429 | 428.91 | — | 300 | 300.12 | — | -68 | -51.63 |
| 2 | [ 3 10 1 ] | 429 | 432.83 | — | 311 | 307.14 | — | -61 | -59.84 |
| 3 | [ 1 1 1 ] | 436 | 434.19 | 444.83 | 315 | 308.58 | 316.07 | -51 | -50.98 |
| 4 | [ 1 1 1 ] | 406 | 402.04 | — | 252 | 252.26 | — | -63 | -63.00 |
| 5 | [ 10 1 1 ] | 463 | 428.64 | 475.33 | 289 | 283.48 | 292.00 | -20 | -20.00 |
| 6 | [ 1 10 1 ] | 443 | 423.81 | — | 291 | 290.99 | — | -62 | -61.99 |
| 7 | [ 1 1 1 ] | 443 | 442.33 | — | 324 | 324.15 | — | -82 | -82.08 |
| 8 | [ 1 1 1 ] | 421 | 422.88 | 429.18 | 286 | 289.32 | 311.00 | -40 | -42.78 |
| 9 | [ 1 1 1 ] | 460 | 449.05 | 473.59 | 320 | 320.02 | 323.73 | -60 | -59.99 |
| 10 | [ 1 1 1 ] | 435 | 426.92 | 439.65 | 305 | 293.56 | 305.97 | -43 | -44.74 |
| 11 | [ 1 1 1 ] | 463 | 436.24 | 470.33 | 320 | 297.07 | 313.00 | -28 | -28.00 |
| 12 | [ 1 1 1 ] | 420 | 421.11 | 431.49 | 286 | 286.14 | 303.33 | -60 | -59.90 |
| 13 | [ 1 1 1 ] | 410 | 413.24 | — | 290 | 272.06 | — | -33 | -30.51 |
| 14 | [ 10 2 0 ] | 451 | 450.99 | — | 284 | 323.49 | — | — | — |
| 15 | [ 2 10 0 ] | 439 | 443.45 | 473.33 | 310 | 310.00 | 313.67 | — | — |
| 16 | [ 10 0 0 ] | 426 | 426.00 | — | — | — | — | — | — |
| 17 | [ 1 1 1 ] | 460 | 448.65 | 474.00 | 300 | 319.31 | 312.33 | -95 | -94.96 |
| 18 | [ 1 1 0 ] | 443 | 423.81 | — | 291 | 290.98 | — | — | — |
| 19 | [ 1 1 1 ] | 409 | 409.04 | — | 286 | 264.53 | — | -31 | -30.59 |
| 20 | [ 1 1 1 ] | 439 | 438.76 | — | 319 | 317.75 | — | -78 | -77.56 |
| 21 | [ 1 1 0.1 ] | 421 | 420.56 | 441.93 | 286 | 285.17 | 294.33 | -59 | -50.99 |
| 22 | [ 1 1 1 ] | 431 | 407.14 | — | 286 | 261.13 | — | -23 | -22.89 |
| 23 | [ 1 1 1 ] | 401 | 403.84 | — | 256 | 255.22 | — | -41 | -40.98 |

Table 8.7: Summary of the microstructure results

| Experiment Number | Ferrite Grain Size ($\mu$m) | | |
|---|---|---|---|
| | Required | Predicted | Experiment |
| 1 | 13 | 14.00 | 13.88 |
| 2 | 12 | 13.00 | 12.31 |
| 3 | 12 | 13.00 | 11.92 |
| 4 | 25 | 26.30 | 24.36 |
| 5 | 20 | 19.80 | 21.37 |
| 6 | 15 | 14.00 | 15.89 |
| 7 | 10 | 11.50 | 11.02 |
| 8 | 16 | 16.82 | 15.35 |
| 9 | 13 | 13.71 | 12.23 |
| 10 | 14 | 14.96 | 13.36 |
| 11 | 17 | 17.77 | 14.37 |
| 12 | 15 | 14.29 | 14.72 |
| 13 | 18 | 18.60 | 16.82 |
| 14 | 12 | 12.80 | 11.48 |
| 15 | 15 | 15.88 | 14.71 |
| 16 | 14 | 14.77 | 14.35 |
| 17 | 13 | 13.86 | 12.67 |
| 18 | 15 | 14.47 | 13.44 |
| 19 | 20 | 20.99 | 21.02 |
| 20 | 11 | 10.99 | 11.20 |
| 21 | 16 | 16.14 | 16.13 |
| 22 | 22 | 22.91 | 22.50 |
| 23 | 24 | 24.69 | 25.10 |

Table 8.8: Summary of the rolling schedules

| Experiment Number | Inter-pass time | Mill Constraints | | | Rolling Schedule | | | | |
|---|---|---|---|---|---|---|---|---|---|
| | | Speed | Red. | Torque | Pass | Temp. | Speed | Red. | Gap |
| | (s) | (rpm) | (%) | (kNmm) | No. | (°C) | (rpm) | (%) | (mm) |
| 1 | 35 | 10,30 | 10,40 | 5000 | 1 | 1000 | 30 | 29 | 17.98 |
| | | | | | 2 | 911 | 30 | 19 | 14.61 |
| 2 | 55 | 10,30 | 10,40 | 5000 | 1 | 1000 | 30 | 29 | 17.98 |
| | | | | | 2 | 873 | 30 | 25 | 13.48 |
| 3 | 45 | 10,30 | 10,40 | 5000 | 1 | 980 | 10 | 29 | 17.99 |
| | | | | | 2 | 884 | 20 | 21 | 14.36 |
| 4 | — | 10,30 | 10,40 | 5000 | 1 | 1100 | 30 | 15 | 21.31 |
| 5 | — | 10,30 | 10,40 | 5000 | 1 | 1100 | 30 | 27 | 18.34 |
| 6 | 20 | 10,30 | 10,40 | 5000 | 1 | 1100 | 30 | 29 | 17.73 |
| | | | | | 2 | 992 | 20 | 24 | 13.35 |
| 7 | 15 | 10,30 | 10,40 | 5000 | 1 | 1150 | 17 | 29 | 17.74 |
| | | | | | 2 | 1060 | 14 | 24 | 13.41 |
| | | | | | 3 | 975 | 30 | 26 | 9.72 |
| | | | | | 4 | 893 | 24 | 31 | 6.38 |
| 8 | 20 | 10,40 | 15,40 | 3000 | 1 | 1100 | 40 | 29 | 17.70 |
| | | | | | 2 | 1023 | 40 | 22 | 13.71 |
| 9 | 20 | 10,40 | 10,40 | 3000 | 1 | 1100 | 32 | 29 | 17.72 |
| | | | | | 2 | 1023 | 32 | 25 | 13.28 |
| | | | | | 3 | 984 | 35 | 28 | 9.37 |
| 10 | 35 | 30,60 | 15,25 | 3000 | 1 | 1050 | 60 | 16 | 21.34 |
| | | | | | 2 | 995 | 54 | 21 | 16.72 |
| | | | | | 3 | 939 | 48 | 21 | 13.14 |
| 11 | — | 10,60 | 10,40 | 5000 | 1 | 1050 | 22 | 36 | 15.81 |
| 12 | 20 | 30,60 | 10,30 | 3000 | 1 | 1050 | 60 | 16 | 21.35 |
| | | | | | 2 | 982 | 50 | 21 | 16.69 |
| | | | | | 3 | 917 | 46 | 22 | 12.88 |
| 13 | 20 | 30,60 | 10,40 | 1500 | 1 | 1050 | 34 | 16 | 21.15 |
| | | | | | 2 | 995 | 36 | 19 | 17.04 |
| 14 | 20 | 10,40 | 15,40 | 3000 | 1 | 1050 | 40 | 16 | 21.18 |
| | | | | | 2 | 995 | 36 | 37 | 12.94 |
| | | | | | 3 | 926 | 30 | 35 | 8.19 |
| 15 | 20 | 10,40 | 10,30 | 3000 | 1 | 1050 | 40 | 29 | 17.69 |
| | | | | | 2 | 985 | 40 | 25 | 13.19 |
| 16 | 30 | 10,40 | 10,40 | 3000 | 1 | 1050 | 10 | 29 | 17.66 |
| | | | | | 2 | 958 | 40 | 25 | 13.08 |
| 17 | 55 | 10,40 | 10,40 | 3000 | 1 | 1050 | 40 | 29 | 17.69 |
| | | | | | 2 | 902 | 39 | 23 | 13.36 |
| 18 | 12 | 10,40 | 10,40 | 3000 | 1 | 1050 | 39 | 29 | 17.68 |
| | | | | | 2 | 1009 | 40 | 25 | 13.14 |
| | | | | | 3 | 963 | 34 | 29 | 9.06 |
| 19 | 15 | 10,60 | 10,40 | 1000 | 1 | 1100 | 53 | 16 | 21.32 |
| | | | | | 2 | 1049 | 24 | 14 | 18.13 |
| 20 | 12 | 10,60 | 10,40 | 3000 | 1 | 1150 | 20 | 29 | 17.74 |
| | | | | | 2 | 1093 | 46 | 23 | 13.62 |
| | | | | | 3 | 1033 | 11 | 25 | 9.99 |
| | | | | | 4 | 969 | 23 | 27 | 7.13 |
| | | | | | 5 | 903 | 18 | 31 | 4.72 |
| 21 | 12 | 10,60 | 10,40 | 3000 | 1 | 1150 | 10 | 29 | 17.75 |
| | | | | | 2 | 1093 | 39 | 23 | 13.57 |
| | | | | | 3 | 1033 | 17 | 28 | 9.62 |
| 22 | — | 10,30 | 15,40 | 3000 | 1 | 1100 | 10 | 20 | 20.07 |
| 23 | — | 20,40 | 15,40 | 3000 | 1 | 1100 | 20 | 17 | 21.01 |

# Chapter 9

# Conclusions and Further Work

## 9.1 Final Conclusions and Future Work

The need for model-based approaches is entirely justified in order to accomplish the concept of *right-first-time* production of steel alloys. The approach proposed in this work showed that by employing systematic design procedures of modelling and optimisation, metals can be designed efficiently, producing mechanical properties with a good degree of accuracy. In particular, the approach associated with this work has focused on the integration of systems engineering paradigms for hybrid modelling and optimisation of the mechanical properties and microstructures of steels without any loss of generality. The aim is to integrate knowledge of the alloy being processed and the rolling mill by combining physically-based models and those models derived from data and knowledge such as Neural-Fuzzy systems, to calculate the optimal rolling schedules.

Unlike current methods, this work showed how one can use searching mechanisms to find the optimal rolling schedule for a faster design of steel alloys while ensuring feasibility (in the pragmatic sense) and repeatability of the solutions. The success of the proposed scheduling mechanism is due to the knowledge integration of the different processing stages (i.e. heat treatment, hot-rolling, and cooling) together with the rolling mill characteristics (e.g. structural stiffness, constraints) within a comprehensive hybrid model. Such a hybrid structure was then exploited within a systematic GA-based multi-objective optimisation designed to 'reverse-engineer' the model and to find the 'optimal' process parameters.

The scheduling mechanism is comprised of two main modules or searching engines:

- Module 1: the optimal search is focused on finding the best microstructural

parameters required to achieve the desired mechanical properties including TS, YS, and ITT, the latter being a measure of the metal toughness.

- MODULE 2: by using information relating to the optimal microstructural parameters, this module calculates feasible rolling parameters per pass in order to synthesise the rolling schedule.

Each module uses three basic elements for defining and approaching the optimisation problem:

1. The **Process Model** which relates the mechanical properties, with the critical microstructural and the processing parameters;

2. The **Optimality Criteria** which are related to achieving a set of property and microstructural objectives; and

3. The **Process Constraints** which include the limitations of the forming process and the hot-workability of the stock, as well as the rolling mill constraints.

The developed mechanism was evaluated by conducting a series of up to 23 hot-rolling experiments using a laboratory-scale hot-rolling mill, known as the"Hille-mill", which is located at the Sheffield University. Additionally, comprehensive metallographic analyses and laboratory tests were carried-out using the rolled metal. It is worth mentioning that, the procedures used to perform such analyses and tests were in accordance with international standards such as the ASTM E8 "Standard Test Methods for Tension Testing of Metallic Materials", and the ASTM E112 "Standard Test Methods for Determining Average Grain Size", published by the American Standard for Testing and Materials.

The results obtained from the hot-rolling experiments showed that, when there is sufficient information from the material being processed (in the form of data), intelligent systems-based paradigms can be effectively used to synthesise and optimise the metal microstructure and its processing route within practical limits in order to satisfy the desired requirements. As demonstrated by the metallographic analyses and mechanical tests, a *right-first-time* production was achieved (considering a $\pm 10\%$ error) for all experiments in terms of the requirements associated with the ferrite grain size, the volume fraction of pearlite, the TS, and YS. It is worth mentioning

that no experimental validation of ITT was carried-out. The presented results not only provide a *proof-of-concept* for the proposed GA-based optimisation mechanism, but more importantly, this research work should provide the motivation to extend the use of intelligent systems to solve multi-objective metallurgical problems.

Although the C-Mn steel alloy with only 3 mechanical properties was considered in this study, no special assumptions were made to preclude the use of this methodology for other alloys or properties. Results in such a case, however, will strongly depend on the mathematical models used to correlate the microstructure with such properties, as well as the metal processing.

The developed MATLAB®-based software Sheffield Integrated System for SChedluling and Optimisation in Rolling (SISSCOR), which implements the systematic methodology to calculate the optimal rolling parameters, provides a framework to integrate knowledge of the Hille-mill and the microstructural changes taking place in the stock during deformation. Such methodology, which was described in Chapters 4 and 5, showed a strong dependence on the quantitative knowledge and consistency of the physically-based models to predict the metal behaviour.

SISSCOR is used as a computational tool to help in the design of steel alloys and observe the mill performance via simulations. SISSCOR allows the user for interacting with the whole process by means of a comprehensive simulation and optimisation platform. In fact, all real-time experiments reported in this thesis were designed using this GUI. As a result, the time spent designing the experiments were considerably reduced and with a very easy control and storage of the processed information, which was subsequently used in the laboratory.

The models described in this study are still the subject of continuous developments and improvements. Indeed, existing models can be enhanced by adding knowledge extracted from incremental data. It was shown that, as new data emerge, new discoveries and methodologies can be used to complement the current knowledge and trends. This work showed that Intelligent Systems-based paradigms can be used as an 'updating' mechanism so as to cope with issues of long term maintenance relating to the conventional models. In addition, these models proved to be easily incorporated within current control schemes for scheduling and optimisation. For instance, the developed Neural-Fuzzy model was capable of identifying the sources of deviation in TS of the C-Mn steel alloy. The model predictions were more accurate than those given by conventional models found in the current literature. The results not only

indicate that some chemical elements such as silicon and manganese add nonlinear characteristics to the model, but also confirm the well known Hall-Petch equation, which establishes the linear nature of TS with respect to the ferrite grain size and the carbon content.

The successful implementation of the TS Neural-Fuzzy model within the optimisation mechanism provides the framework to develop similar models to estimate YS and ITT in order to improve the accuracy of the solutions. Furthermore, other important metal properties such as ductility, hardness, and fatigue resistance, may be included to expand the user capabilities in the design. However, the development and validation of such models may be constrained by the lack of reliable experimental data from which the knowledge is extracted.

Further work relating to the Fuzzy Inverse Transformation Model presented in Section 5.5.2 is also required in order to eliminate the need for refinement of the rolling schedule. Because of the fact that the scheduling mechanism of MODULE 2 does not compensate for the austenite grain growth in the last rolling pass, the final ferrite grain size usually has an error of $\pm 3$ $\mu$m. As a result, a refinement of the overall solution is required. For some metal requirements, this renders the scheduling mechanism too sequential, because one or two additional runs have to be performed before obtaining the optimal solution. One can solve the above problem by extending the Fuzzy Inverse Transformation Model so as to include the growth of the austenitic grain, hence a more accurate initial austenite grain target can be set for the first run.

In the light of the above considerations, the formulation of the microstructure and schedule optimisation problem required the consideration of multiple objectives which are often competing. It was shown that, although the weighted sum approach described in Chapter 4 produced solutions that worked well in experiments, the solutions provided may not describe as well the concept of an optimal microstructure since some important assumptions (e.g. the priority factors in MODULE 1) needed to be decided *a priori*. When multiple competing objectives exist, the optimal solution is not a single point but an entire set of non-dominated points, which is commonly referred to as the *Pareto* set. The designer must then resort to tradeoffs between the objectives to determine the best solution. It is worth noting at this stage that, the tradeoffs may become more problematic as the number of objectives increases. For instance, the need for a more sophisticated strategy to solve the multi-objective optimisation problem becomes more relevant if the cost function described by Equation

(5.13) is extended to include a 'shape objective'. As described in Chapter 8, this is necessary to ensure that the final product will satisfy not only the specified properties, but also the shape and the dimensions required for a certain application.

Future work in this direction includes the use of evolutionary algorithms for multi-objective optimisation problems such as the Strength Pareto Evolutionary Algorithm (SPEA) or the Nondominated Sorting Genetic Algorithm II (NSGA-II). As far as the latter is concerned, for each solution one has to determine how many solutions dominate it and the set of solutions which it dominates. The NSGA-II estimates the density of solutions surrounding a particular solution in the population by computing the average distance of two points on either side of this point using all the objectives of the problem.

Although the parameters selected by the algorithm[1] to minimise the cost functions led to acceptable results, choosing the optimal GA parameters for a specific metal design may require a parametric study to see the effect of changing the value of each parameter on the final design. Additionally, a statistical analysis of the results should be carried-out to examine the effect that the initial assumptions (e.g. inter-pass times, initial temperature, and initial microstructure) have on the final rolling schedule. This will be very useful because the results from such an analysis can be used to obtain a suitable set of relevant descriptive optimal schedules. In particular, it would be very interesting to compare current results with the statistical results obtained from other methodologies. This will provide a good perspective on the similarities or differences in order to extend the proposed methodology to cover other experimental scenarios such as the temperature-controlled rolling or the use of multi-stand hot-rolling mills.

Chapter 7 described the real-time implementation of GPC in the Hille-mill, which led to an improvement in the rolling speed control and regulation. In real-time operation, GPC worked better that the PID controller in terms of the control effort required for the same tasks. Also, improvements in the overall speed response were observed as indicated by the RMSE when the mill was operated under different working conditions. The results clearly demonstrated that the additional features that GPC provides to the Hille-mill, such as the on-line system parameter identification, the observer polynomial, and the pre-defined set-point feature, allow for increasing the robustness and flexibility to the control system.

[1]See steps outlined in Section 4.4.2.

"Intelligence" was added to the control system when a synergy between the GPC algorithm and Fuzzy Logic took place via a TSK Fuzzy process model to calculate the control sequence. Even though the fuzzy model consisted of a number of linear sub-models, the overall input-output mapping was nonlinear. However, to facilitate the implementation of the fuzzy model into the GPC algorithm, a simple method of linearising the fuzzy model about the current operating point by weighting the fuzzy model parameters at each sampling instant was used leading to an excellent control performance in simulations.

However, examining GPC from a computational viewpoint revealed that the computational burden of the control algorithm was big compared to the one showed by conventional controllers. This was inevitably due to the series of matrices manipulations that take place at every sampling instant in addition to the parameter estimation algorithm. Due to the time-consuming nature of this strategy, it was decided to use an adaptive linear model which led to acceptable results and yet optimal performances when rolling experiments were performed. Further work should be carried-out in this regard in order to facilitate the inclusion of the mill constraints within the cost function optimisation for real-time operations.

Future work using the Hille-mill can be also focused on the development of an active fault-tolerant control system. Such a system will consider faults associated with the sensors and/or the actuators used by the mill during real-time operations. An active fault-tolerant control system is comprised of a set of filter-observers which are capable of estimating and isolating faults while preserving the system integrity in terms of performance. Further information about this topic can be found in [80].

## 9.2 Main Contributions of this Research Project

The main achievements of this project can be summarised as follows:

1. Development of a novel GA-based mechanism for the optimisation of the hot-rolling of steel alloys using the Hille-mill. The aim of the optimisation problem was to develop a set-up mechanism to provide optimal rolling schedules (i.e. number of passes, rolling speeds, reductions and deformation temperatures, etc.) by integrating knowledge of both the rolled stock and the rolling mill. The proposed scheduling platform uses hybrid modelling, combining physically-based equations and Neural-Fuzzy models that describe the structure-property

relationships of the rolled metal. This methodology is based on the evolutionary optimisation of a set of cost functions to allow the setting-up of multiple optimisation objectives in order to achieve a *right-first-time* production of steel alloys.

2. Modelling of the mechanical properties for the C-Mn steel alloy using Neural-Fuzzy Systems-based paradigms. The proposed intelligent model was developed using industrial data that included values for different chemical compositions, microstructures, and mechanical properties such as TS. The predictive capabilities of such a model were compared with traditional lineal models taken from the current literature. The results showed that a better match with the industrial data was achieved by the Neural-Fuzzy model which was later used for the estimation of the microstructure and the properties of the rolled products.

3. Laboratory validation of the approach described in 1 and 2 by carrying-out up to 23 real-time hot-rolling experiments, quantitative and metallographic analyses of microstructure, and mechanical tests on the rolled metal. The results showed that the final product was in a good agreement with the desired design in terms of the microstructure, TS, and YS. This validation exercise also demonstrated the advantages of the proposed methodology over current methods which are generally *ad hoc* and lack adequate capabilities for finding the optimal process parameters.

4. Development of SISSCOR (Sheffield Integrated System for SCheduling and Optimisation in Rolling) which is a MATLAB®-based graphical user interface to be used as a computing tool for experiment design, system integration, and process simulation. SISSCOR was implemented in the Hille-mill computer interface in order to set-up the optimal rolling schedule and carry-out the process.

5. Development of a realistic simulation platform for the study and analyses of the dynamics of the Hille-mill, using real critical system parameters such as the inertia of the different rotational parts, the friction coefficients, and the stiffness; this included the modelling of the mill, the electric drive, the gap mechanism, and the speed control system. The simulation results showed a good match with experimental data both in open- and closed-loop demonstrating the reliability

of the developed model simulation platform, and as a result, the integrity of the control designs.

6. Implementation of an adaptive Model-based Predictive Controller in the speed control system of the Hille-mill, which substituted the original fixed PID controller. The performance of this self-adaptive controller was evaluated via simulations and real-time experiments under different working regimes. From such experiments the model-based controller proved to perform better than the conventional one by showing good robustness and disturbance rejection in a wider range of operating conditions. It was also observed that by using this predictive controller, a better control and regulation of the rolling speed were achieved, while reducing the control effort and the noise interference.

# References


[1] M. F. Abbod, C. M. Sellars, D. A. Linkens, Q. Zhu, and M. Mahfouf. Physically based and nero-fuzzy hybrid modelling of thermomechanical processing of aluminium alloys. *Materials Science and Engineering A*, 333:380–97, 2002.

[2] D. Aliya and S. Lampman. *Properties and Selection*, volume 1, chapter Physical Metallurgy Concepts in Interpretation of Microstructures. Materials Park, OH. ASM International, 1990.

[3] J. C. Alvarez. Thick unevenness compensation in a hot rolling mill having automatic gage control. *IEEE Transactions on Industry Applications*, 38, 2002.

[4] ASTM. E112: Standard test methods for determining average grain size. *American Society for Testing and Materials*, 1999.

[5] ASTM. E8: Standard test methods for tension testing of metallic materials. *American Society for Testing and Materials*, 2000.

[6] R. A. Barbosa and R. Ballas. Static recrystallisation of type 316L stainless steel under hot working conditions. *Materials Science Forum*, 113:461–66, 1993.

[7] J. H. Beynon and C. M. Sellars. Modelling microstructure and its effects during multipass hot rolling. *ISIJ International*, 32:359–67, 1992.

[8] G. J. Bierman. *Factorization Methods for Discrete Sequential Estimation.* New York Academic, 1977.

[9] B. L. Bramfitt. *Metallography and Microstructures*, volume 9, chapter Effects of Composition, Processing, and Structure on Porperties of Iron ans Steels. Materials Park, OH. ASM International, 1990.

[10] S. Chandra and U. S. Dixit. A rigid-plastic finite element analysis of temper rolling process. *Journal of Materials Processing Technology*, 152:9–16, 2004.

[11] M. Y. Chen and D. A. Linkens. A systematic neuro-fuzzy modeling framework with application to material property prediction. *Transactions on Systems, Man and Cybernetics - Part B: Cybernetics*, 31(5):781–90, 2001.

[12] S. L. Chiu. Fuzzy model identification based on cluster estimation. *Journal of Intelligent and Fuzzy Systems*, 2(3), 1994.

[13] S. I. Choi, A. Rossiter, and P. Fleming. A chance-constrained robust MPC and application to hot-rolling mills. In *International Control Conference*. IFAC, 2006.

[14] D. W. Clarke, C. Mohtadi, and P. S. Tuffs. Generalized predictive control - Part I: The basic algorithm. *Automatica*, 23:137–48, 1987.

[15] D. W. Clarke, C. Mohtadi, and P. S. Tuffs. Generalized predictive control - Part II: Extensions and interpretations. *Automatica*, 23:149–60, 1987.

[16] R. Dhaouadi, K. Kubo, and M. Tobise. Two-degree-of-freedom robust speed controller for high-performance rolling mill drives. *IEEE Transactions on Industry Applications*, 29, 1993.

[17] G. Dieter. *Mechanical Metallurgy*. McGraw Hill, 1988.

[18] U. S. Dixit and P. M. Dixit. Application of fuzzy set theory in the scheduling of a tandem cold-rolling mill. *Transactions of ASME*, 122:494–500, 2000.

[19] E. El-kholy, S. Shokralla, A. H. Morsi, and S. A. El-Absawy. Improved performance of rolling mill drives using a hybrid fuzzy-PI controller. In *International Conference on Power Electronics and Drive Systems*. IEEE, 2003.

[20] A. E. Fitzgerald. *Electric Machinery*. McGraw Hill, 1992.

[21] M. A. Gama and M. Mahfouf. Speed control of an experimental hot-rolling mill using generalised predictive control. In *International Control Conference*. IFAC, 2006.

[22] M. A. Gama, M. Mahfouf, and Y. Y. Yang. Modelling and simulation of an experimental ac induction motor drive and rolling mill system. In *Colloquium*

*of the Institute for Microstructural and Mechanical Process Engineering: The University of Sheffield.* IMMPETUS, 2005.

[23] D. F. Garcia. A novel real-time fuzzy-based diagnostic system of roll eccentricity influence. *IEEE Transactions on Industry Applications*, 34, 1998.

[24] S. S. Garimella and K. Srinivasan. Application of iterative learning control to coil-to-coil control in rolling. *IEEE Transactions on Control Systems Technology*, 6:281–93, 1998.

[25] V. B. Ginzburg. *Flat Rolling Fundamentals.* Marcel Dekker, 2000.

[26] T. Gladman, D. Dulieu, and I. D. McIvor. Structure-property relationships in high-strength microalloyed steels. In *Microalloying 75.* American Society for Metals, 1977.

[27] D. E. Goldberg. *Genetic Algorithms in Search, Optimisation, and Machine Learning.* Addison Wesley, 1989.

[28] R. E. Haber, C. R. Peres, A. Alique, S. Ros, C. Gonzalez, and J. R. Alique. Toward intelligent machining: Hierarchical fuzzy control for the end milling process. *IEEE Transactions on Control Systems Technology*, 6:188–99, 1998.

[29] T. Hesketh. Controller design for hot strip finishing mills. *IEEE Transactions on Control Systems Technology*, 6, 1998.

[30] R. A. Higgins. *Engineering Metallurgy: Applied Physical Metallurgy.* Edward Arnold, Hodder and Stoughton, 1993.

[31] R. L. Higginson and C. M. Sellars. *Worked Examples in Quantitative Metallography.* London Maney, 2003.

[32] P. D. Hodgson and R. K. Gibbs. A mathematical model to predict the mechanical properties of hot-rolled C-Mn and microalloyed steels. *ISIJ International*, 32:1329–38, 1992.

[33] J. Holt. Uniaxial tension testing. *ASM International Handbook*, 8, 1990.

[34] R. Honeycombe. *Steels, Microstructure and Properties.* Butterworth - Heinemann, 1995.

[35] R. Honeycombe and F. B. Pickering. Ferrite and bainite in alloy steels. *Metallurgy Transactions*, 3:1099–1112, 1972.

[36] M. Ibrahim. *Hybrid Modelling and Sequence Control for a Laboratory-scale Rolling Mill.* PhD thesis, Department of Automatic Control and Systems Engineering, The University of Sheffield, 2002.

[37] J. S. R. Jang. ANFIS: Adaptive-networks-based fuzzy inference system. *IEEE Transactions on Systems, Man and Cybernetics*, 23(3), 1993.

[38] J. S. R. Jang and C. T. Sun. *Neuro-Fuzzy and Soft Computing - A Computational Approach to Learning and Machine Intelligence.* Prentice Hall, 1997.

[39] E. John and I. Postlethwaite. Improvements in product quality in tandem cold rolling using robust multivariable control. *IEEE Transactions on Control Systems Technology*, 6, 1998.

[40] D. Kalyanmoy. *Multiobjetive Optimisation using Evolutionary Algorithms.* Wiley, 2001.

[41] S. Kandiah. *Fuzzy Model Based Predictive Control of Chemical Processes.* PhD thesis, Department of Automatic Control and Systems Engineering, The University of Sheffield, 1996.

[42] P. C. Krause. *Analysis of Electrical Machinery.* IEEE Press / Wiley Interscience, 2002.

[43] G. Krauss. *Steels: Heat Treatment and Processing Principles.* ASM International, 1990.

[44] G. Krauss. *Metallography and Microstructures*, volume 9, chapter Microstructures, Processing, and Properties of Steels. Materials Park, OH. ASM International, 2004.

[45] A. Kugi. Active compensation of roll eccentricity in rolling mills. *IEEE Transactions on Industry Applications*, 36, 2000.

[46] A. Kugi. Nonlinear control in rolling mills: A new perspective. *IEEE Transactions on Industry Applications*, 37, 2001.

[47] A. J. Kulkarni, K. Krishnamurthy, S. P. Deshmukh, and R. S. Mishra. Microstructural optimization of alloys using genetic algorithms. *Materials Science and Engineering A*, 372:213–20, 2004.

[48] R. K. Kumar. An on-line parallel controller for the runout table of hot strip mills. *IEEE Transactions on Control Systems Technology*, 9, 2001.

[49] K. J. Kurzydlowski and B. Ralph. *The Quantitative Description of the Microstructure of Materials.* CRC Press, Inc., 1995.

[50] J. Larkiola, P. Myllykoski, A. S. Korhonen, and L. Cser. The role of neural networks in the optimisation of rolling processes. *Journal of Materials Processing Technologys*, 80-81:16–23, 1998.

[51] S. Latzel. Advanced automation concept of runout table strip cooling for hot strip and plate mills. *IEEE Transactions on Industry Applications*, 37, 2001.

[52] J. G. Lenard, M. Pietrzyk, and L. Cser. *Mathematical and Physical Simulation of the Properties of Hot Rolled Products.* Elsevier Science Ltd., 1999.

[53] M. Mahfouf, M. F. Abbod, and D. A. Linkens. Multivariable adaptive fuzzy TSK model-based predictive control using a CARIMA model structure. *Transactions of the Institute of Chemical Engineers, Chemical Engineering Research and Design*, 78:590–96, 2000.

[54] M. Mahfouf, S. Kandiah, and D. A. Linkens. Fuzzy model-based predicitive control using an ARX structure with feedforward. *Fuzzy Sets and Systems*, 125:39–59, 2002.

[55] M. Mahfouf and D. A. Linkens. *Generalised Predictive Control (GPC) and Bioengineering.* Tylor and Francis, 1998.

[56] M. Mahfouf, Y. Y Yang, M. A. Gama, and D. A. Linkens. Roll speed and roll gap control with neural network compensation. *ISIJ International*, 45(6):841–50, 2005.

[57] M. Mahfouf, Y. Y Yang, and D. A. Linkens. Roll speed and roll gap modelling - A case of study for an experimental rolling mill. In *Symposium on Automation in Mining, Mineral and Metal Processing*. IFAC, 2004.

[58] P. A. Manohar, S. S. Shivathaya, and M. Ferry. Design of an expert system for the optimization of steel compositions and process route. *Expert Systems with Applications*, 17:129–34, 1999.

[59] S. Moaveni. *Finite Element Analysis*. Prentice-Hall International, 1999.

[60] C. M. Ong. *Dynamic Simulation of Electric Machinery*. Prentice Hall, 1998.

[61] E. Orowan and K. J. Pascoe. A simple method for calculating roll pressure and power consumption in flat hot rolling. *Journal of the Iron and Steel Institute*, 34:124–26.

[62] K. Passino. *Fuzzy Control*. Addison-Wesley, 1998.

[63] L. M. Pedersen. Multivariable controller design for a hot rolling mill. *IEEE Transactions on Control Systems Technology*, 6, 1998.

[64] F. B. Pickering. *Physical Metallurgy and the Design of Steels*. Applied Science Publishers LTD, 1978.

[65] J. V. Ringwood. Shape control systems for sendzimir steel mills. *IEEE Transactions on Control Systems Technology*, 8:70–86, 2000.

[66] W. L. Roberts, A. Sandberg, T. Siwecki, and T. Welefors. Prediction of microstructure development during recrystallization hot rolling of Ti-V steels. In *HSLA Steels, Technology and Applications*. ASM, 1983.

[67] D. Sbarbaro-Hofer, D. Neumerkel, and K. Hunt. Neural control of a steel rolling mill. In *International Symposium on Intelligent Control*. IEEE, 1992.

[68] C. M. Sellars. The physical metallurgy of hot working. In *Hot Working and Forming Processes.* Metals Society, 1980.

[69] C. M. Sellars. Modelling microstructural development during hot rolling. *Materials Science and Technology*, 6:1072–81, 1990.

[70] C. M. Sellars. Private communication, 2007.

[71] C. M. Sellars and J. A. Whiteman. Recrystallization and grain growth in hot-rolling. *Metal Science*, 13:187–94, 1979.

[72] R. B. Sims. The calculation of roll force and torque in hot rolling. *Proceedings of the Institution of Mechanical Engineers*, 168:191–200.

[73] J. S. Son, D. M. Lee, I. S. Kim, and S. G. Choi. A study on on-line learning neural network for prediction for rolling force in hot-rolling mill. *Journal of Materials Processing Technology*, 164-165:1612–17, 2005.

[74] Z. Sterjovski, D. Nolan, K. R. Carpenter, D. P. Dunne, and J. Norrish. Artificial neural networks for modelling the mechanical properties of steel in various applications. *Journal of Materials Processing Technology*, 170:536–44, 2005.

[75] M. Sugeno and T. Yasukawa. A fuzzy-logic-based approach to qualitative modeling. *IEEE Trans. Fuzzy Syst.*, 1:7–29, 1993.

[76] T. Takagi and M. Sugeno. Fuzzy identification of systems and its application to modeling and control. *IEEE Trans. Syst. Man and Cybern.*, SMC-3:28–44, 1985.

[77] Control Techniques. *AC & DC Drives, Servos and Motors.* Control Techniques LTD, 2002.

[78] Control Techniques. *Unidrive-User's guide.* Control Techniques LTD, 2003.

[79] T. Tezuka. Application of a new automatic gauge control system for the tandem cold mill. *IEEE Transactions on Industry Applications*, 38, 2002.

[80] D. Theilliol, M. Mahfouf, D. Sauter, and M. A. Gama. Actuator fault detection isolation method and state estimator design for hot-rolling mill monitoring. In *Symposium on Fault Detection Supervision and Safety for Technical Processes — SAFEPROCESS.* IFAC, 2006.

[81] A. Trzynadlowski. *Control of Induction Motors.* Academic Press, 2001.

[82] P. S. Tuffs and D. W Clarke. Self tuning control of offset: A unified approach. In *Conference on Decision and Control*, volume 3, pages 991–96, 1985.

[83] P. Vas. *Sensorless Vector and Direct Torque Control.* Oxford University Press, 1998.

[84] S. Venugopal, E. A. Medina, J. C. Malas, S. Medeiros, and W. G. Frazier. Optimization of microstructure during deformation processing using control theory principles. *Scripta Materialia*, 36:347–53, 1997.

[85] H. Yada. Prediction of microstructural changes and mechanical properties in hot strip rolling. In *Accelerated Cooling of Rolled Steel.* ASM, 1987.

[86] Y. Y. Yang, D. A. Linkens, J. Talamantes-Silva, and I. C. Howard. Roll force and torque prediction using neural network and finite element modelling. *ISIJ International*, 43(12), 2003.

[87] L. Yao, I. Postlethwaite, W. Browne, D. Gu, M. Mar, and S. E. Lowes. Design, implementation and testing of an intelligent knowledge-based system for the supervisory control of a hot rolling mill. *Journal of Process Control*, 15:615–28, 2005.

[88] Q. Zhang and M. Mahfouf. Fuzzy predictive modelling using hierarchical clustering and multi-objective optimization for mechanical properties of alloy steels. In *Symposium on Automation in Mining, Mineral and Metal Processing.* IFAC, 2007.

# Appendix A

# The Torque Control System of the Hille-mill

## A.1 The Induction Motor Model

The main electric drive comprises a balanced three-phase voltage source, a rectifier bridge, a voltage source inverter and an 18.5 kW, 400 V, 50 Hz induction motor. The drive has the capability to reach twice the motor rated speed by means of controlling the angular frequency. Figure A.1 presents the electric diagram of the internal connections of the motor.

The motor model was first introduced by R. H. Park when he formulated an approach in which all variables (voltages, currents, and flux linkages) were associated to fictitious axes rotating at the rotor angular velocity. In other words, he transformed or referred the stator variables to a fictitious frame of reference using trigonometric operations. The Park's transformation has the unique property of eliminating all time-varying inductances from the voltage equations [42]. Therefore, it can be shown that the voltage equations of the induction machine in the fictitious $qd$-reference frame can be expressed using the following equations:

$$\mathrm{v}_s^{qd} = \mathrm{r}_s \mathrm{i}_s^{qd} + \omega \psi_s^{dq} + \frac{d}{dt}\psi_s^{qd}, \tag{A.1}$$

$$0 = \mathrm{r}_r \mathrm{i}_r^{qd} + (\omega - \omega_m)\, \psi_r^{dq} + \frac{d}{dt}\psi_r^{qd}, \tag{A.2}$$

where

$$\psi_s^{dq} = \begin{bmatrix} \psi_s^d & -\psi_s^q \end{bmatrix}^T, \tag{A.3}$$

$$\psi_r^{dq} = \begin{bmatrix} \psi_r^d & -\psi_r^q \end{bmatrix}^T. \tag{A.4}$$

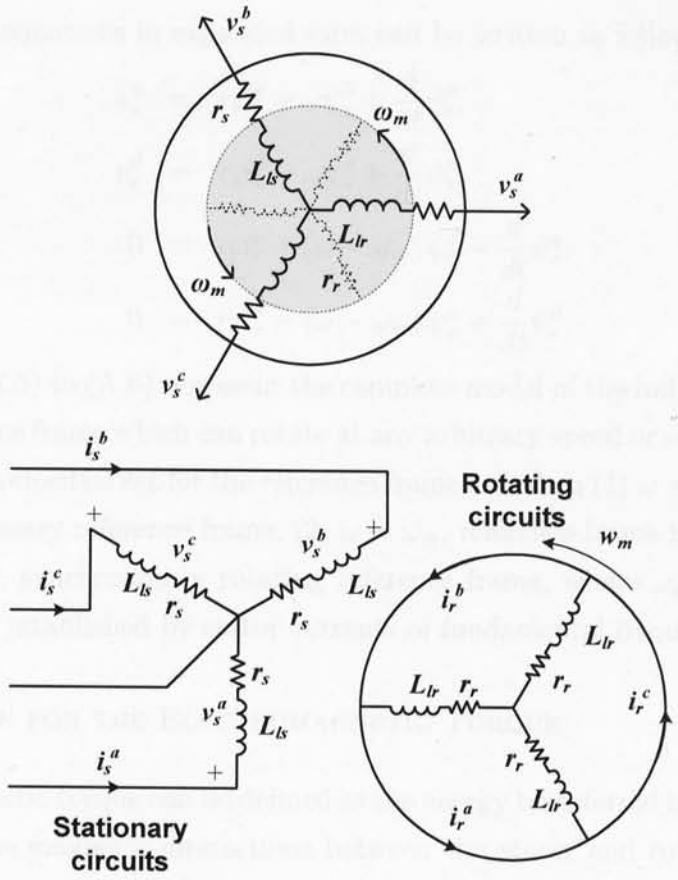


Figure A.1: Electrical connections of the 3-phase induction motor

In the above formulation, v, i and $\psi$ are the voltage, the electric current, and the flux linkages respectively in vector form containing their $qd$-components; r is a diagonal matrix representing the winding resistance. In the above equations the subscripts $s$ and $r$ denote variables associated to stator and rotor windings respectively; $\omega$ represents the angular velocity of the $qd$-reference frame, whereas $\omega_m$ is the motor angular speed.

The voltage equations in expanded form can be written as follows:

$$v_s^q = r_s i_s^q + \omega\psi_s^d + \frac{d}{dt}\psi_s^q, \tag{A.5}$$

$$v_s^d = r_s i_s^d - \omega\psi_s^q + \frac{d}{dt}\psi_s^d, \tag{A.6}$$

$$0 = r_r i_r^q + (\omega - \omega_m)\,\psi_r^d + \frac{d}{dt}\psi_r^q, \tag{A.7}$$

$$0 = r_r i_r^d - (\omega - \omega_m)\,\psi_r^q + \frac{d}{dt}\psi_r^d. \tag{A.8}$$

Equations (A.5) to (A.8) represent the complete model of the induction motor in a fictitious reference frame which can rotate at any arbitrary speed or remain stationary. The most usual velocities set for the reference frame are when (1) $\omega = 0$, in which case it is called stationary reference frame; (2) $\omega = \omega_m$, reference frame fixed in the rotor; and (3) $\omega = \omega_e$, synchronously rotating reference frame, where $\omega_e$ is the electrical angular velocity established by stator currents of fundamental frequency [60].

## A.2 Equation for the Electromagnetic Torque

The electromagnetic torque can be defined as the energy transferred to the motor shaft as a result of the magnetic interactions between the stator and rotor flux linkages. These transactions of energy take place in the air gap and produce a tangential force in the motor shaft to compensate for any mechanical force. There are different expressions for the electromagnetic torque; however, because of the fact that some of the motor inductances are time-varying, the electromagnetic torque equation has also to be transformed in terms of the *qd*-components of the fictitious reference frame [81]. In this work, the electromagnetic torque is determined by the following equation:

$$T_{EM} = \left(\frac{3}{2}\right)\left(\frac{P}{2}\right)\left(\psi_s^d i_s^q - \psi_s^q i_s^d\right), \tag{A.9}$$

where $P$ is the number of poles. As mentioned in Chapter 6, the electromagnetic torque is the input to the mechanical system of the Hille-mill.

Table A.1 shows the critical parameter of the induction motor associated with the Hille-mill as provided by the motor's manufacturer.

## A.3 Field Oriented Control

The aim of this section is to describe the torque control system used by the Hille-mill. According to the drive manufacturer, there are two main control methodologies

Table A.1: Critical parameters of the induction motor

| PARAMETER | VALUE | UNITS |
|---|---|---|
| Stator resistance, $r_s$ | 0.1625 | $\Omega$ |
| Rotor resistance, $r_r$ | 0.1536 | $\Omega$ |
| Stator inductance, $L_{ls}$ | $1.30 \times 10^{-3}$ | H |
| Rotor inductance, $L_{lr}$ | $2.41 \times 10^{-3}$ | H |
| Mutual inductance, $L_M$ | $64.19 \times 10^{-3}$ | H |
| Num. of poles, $P$ | 4 | |

that can be used by the induction motor to improve its performance under different applications [78][77]:

- Scalar (Volts/Hertz) control; and
- Vector control.

Vector control provides the motor with linear voltage characteristics from 0 Hz to the motor rated frequency, and then constant voltage above the motor rated frequency. Further, this methodology leads to a very good performance at low and high speeds [83]. In the current drive, the well known FOC was implemented to carry-out the torque control. In essence, the objective of FOC is to provide the motor with adjustable torque. The principles of field orientation can be summarised as follows:

1. Given the references values, $T_{REF}$ and $|\psi_r|_{REF}$, of the developed torque and rotor flux, the corresponding reference components, $i_s^q*$ and $i_s^d*$, of the stator current vector in the rotor reference frame are found.

2. The angular position of the rotor flux $\theta_e$ is determined and used by the Park's transformation to obtain the reference stator currents, $i_s^a*$, $i_s^b*$ and $i_s^c*$, for the current-controlled inverter feeding the motor.

By this way, the rotor flux and the electromagnetic torque can be separately controlled using the $d$-axis stator current and $q$-axis current respectively. The stator $q$-axis current reference is calculated from the torque reference $T_{REF}$ with the following equation:

$$i_s^q* = \left(\frac{2}{3}\right)\left(\frac{2}{P}\right)\left(\frac{L_{lr}}{L_M}\right)\frac{T_{REF}}{|\psi_r|_{est}} \tag{A.10}$$

and the estimated rotor flux linkage $|\psi_r|_{est}$ is determined by:

$$|\psi_r|_{est} = \frac{L_M i_s^d}{1 + \tau_{rs}}, \tag{A.11}$$

where $\tau_{rs}$ is the rotor time constant. The rotor flux position $\theta_e$ required for the variable transformation is generated from the motor speed $\omega_m$ and the slip frequency $\omega_{sl}$:

$$\theta_e = \int (\omega_r + \omega_{sl})\, dt, \tag{A.12}$$

where the slip frequency is calculated from the stator reference current $i_s^q*$ and the motor parameters using the following expression:

$$\omega_{sl} = \left(\frac{L_M}{|\psi_r|_{est}}\right)\left(\frac{r_r}{L_{lr}}\right) i_s^q * . \tag{A.13}$$

The stator $d$-axis current reference $i_s^d*$ is obtained from the rotor flux reference input $|\psi_r|_{REF}$ by the following expression:

$$i_s^d* = \frac{|\psi_r|*}{L_M}. \tag{A.14}$$

Figure A.2 shows the control scheme associated with FOC. As shown in this figure, the $i_s^q*$ and $i_s^d*$ current references are transformed into $abc$-current references $i_s^a*$, $i_s^b*$ and $i_s^c*$, for the current regulators. Such regulators process the measured and the reference currents to produce the inverter gating signals for the electronic devices to produce balanced PWM voltages to be applied to the stator motor.

The start-up performance of the induction motor using FOC is depicted in Figure A.3. The torque command is initially set at 200 Nm and then stepped to -200 Nm. No rolling torque (load) was applied in this simulation. It can be seen the nearly instantaneous torque response characteristics of the drive which leads to faster control of the frequency to solve the speed control problem. However, this good performance is compromised due to the high harmonic content of the electric current which results in a noise-contaminated torque signal.

The use of FOC is special useful in this application because it is desirable to make the drive act as a torque transducer wherein the electromagnetic torque can nearly instantaneously be made equal to a torque command. Therefore, the speed control problem is dramatically simplified because the electrical dynamics of the drive become irrelevant.

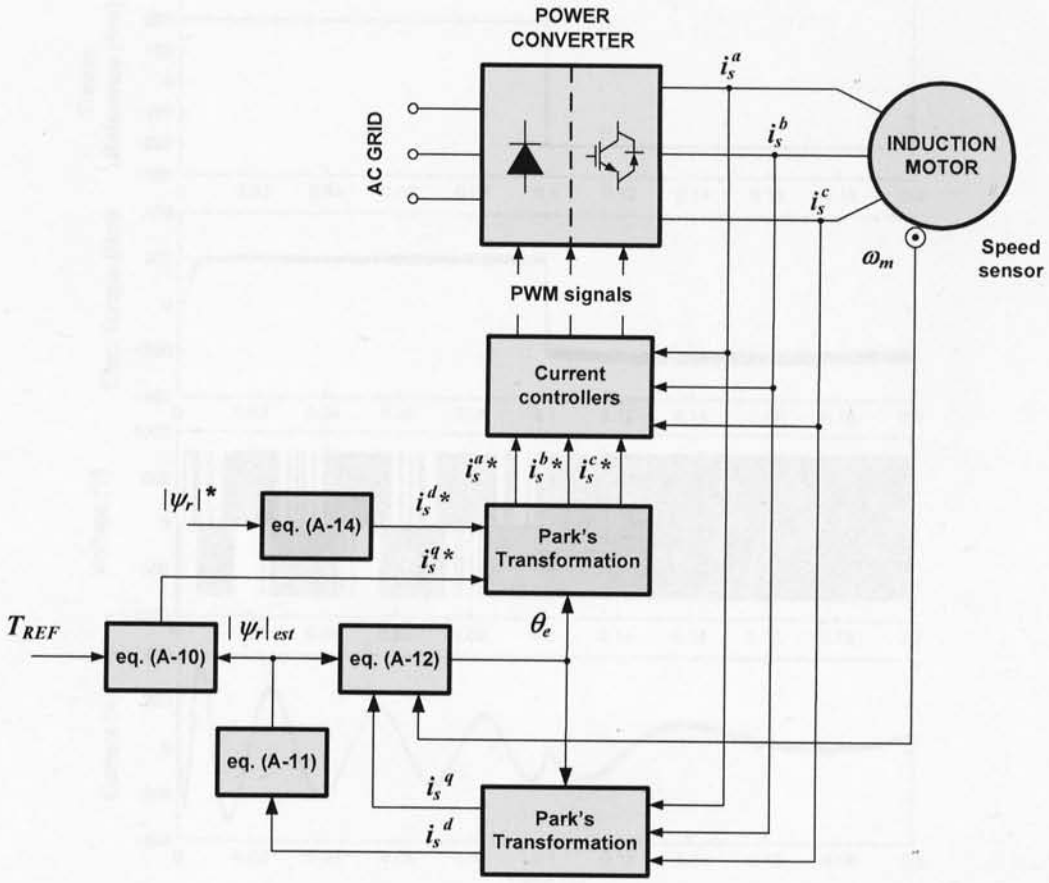


Figure A.2: A block diagram of FOC used for simulations

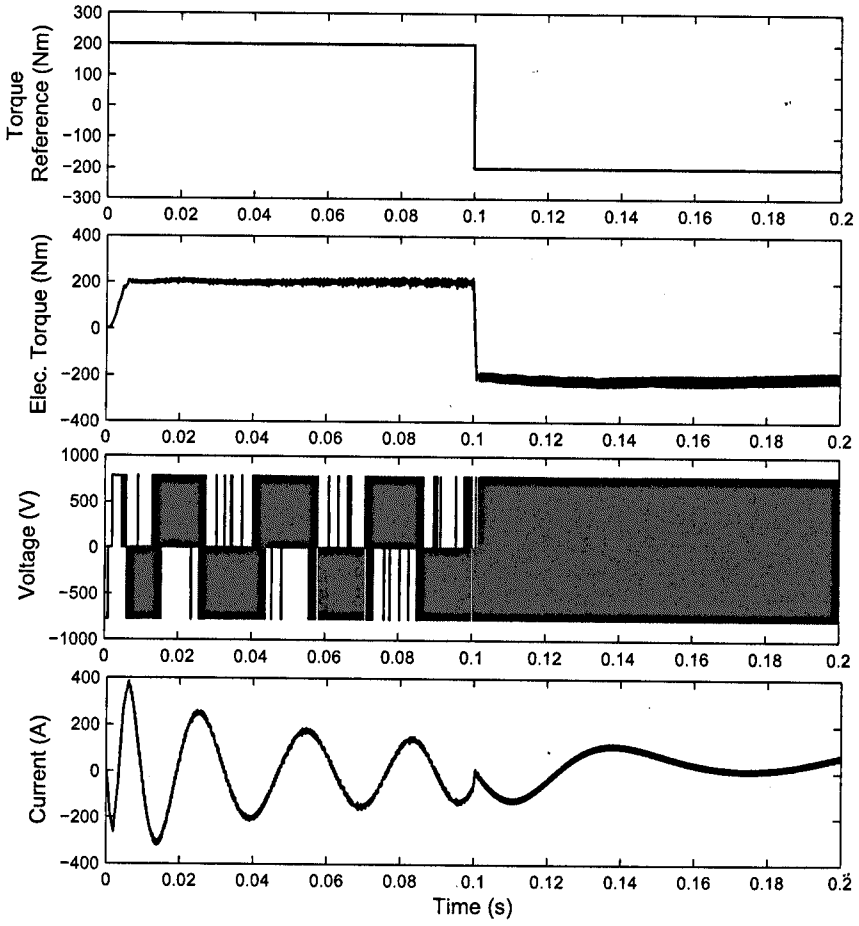


Figure A.3: Drive performance during changes in the torque reference

# Appendix B

# Methodology for Metallographic Analysis and Mechanical Testing

## B.1 Measurement of the Ferrite Grain Size and Volume Fraction of Pearlite

Figure B.1 shows an example of the ferrite-pearlite structure in one of the hot-rolling experiments carried-out using the Hille-mill. On a photomicrograph a complete grid of points is drawn. The grid step size is chosen so as to allow the space of traverses to be sufficiently large for no two adjacent points to fall in the same pearlite colony. Points are registered as 'in pearlite' (counts 1), 'in ferrite' (counts 0), and 'at boundary' (counts $\frac{1}{2}$) to obtain the number of points in pearlite on each traverse. An example is shown in Figure B.1.

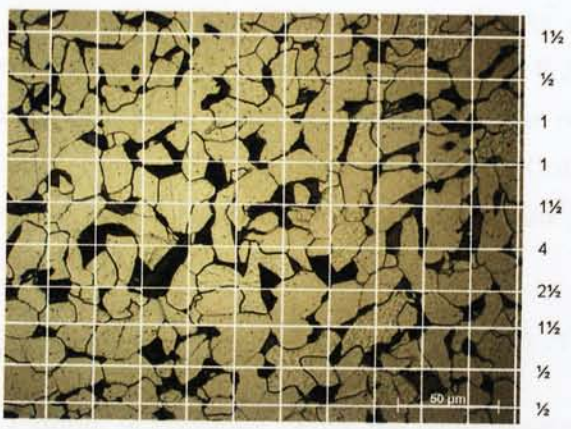


Figure B.1: Method of point counting using a grid of points to determine pearlite colonies

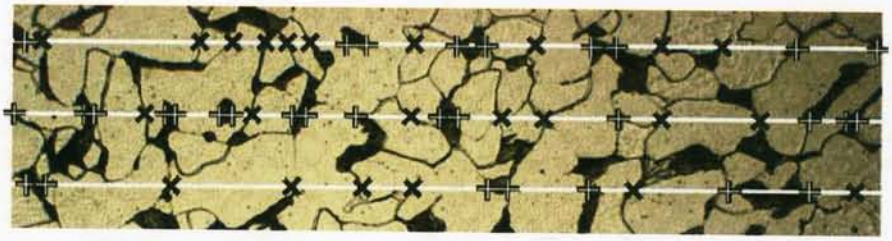

Figure B.2: Method of counting ferrite/pearlite (+) and ferrite/ferrite (×) boundaries

Next, the same micrograph is used to count the number of boundaries per unit length along the same traverse lines used for counting pearlite colonies. Figure B.2 shows the method of counting the number of ferrite and pearlite boundaries. As shown in this figure, the method requires separate counts of the number of ferrite/pearlite boundaries and the number of ferrite/ferrite boundaries to be made along each of the traverses. Each pearlite colony has two boundaries, so the number of colonies on each traverse is half the number of boundaries. The pearlite point fraction ($P_{p(i)}$) of each traverse is obtained by dividing the number of points in pearlite ($P_{pear(i)}$) by the number of total points of the traverse. Hence the number of pearlite colonies per unit length on each traverse is calculated by the following formula:

$$N_{p(i)} = \frac{n_{p(i)}}{2P_{p(i)}L}, \tag{B.1}$$

where $n_{p(i)}$ is the number of ferrite/pearlite boundaries, $L$ is the length of each traverse considering the magnification of the micrograph. As an example, consider the micrograph shown in Figure B.1. Using 10 traverses of 0.255 mm long with 11 points each, the counting procedure described above led to the results shown in Table B.1. Taking the mean of $\bar{P}_p$ , calculated from the total in Column 3 and the total of Column 4, one can calculate the mean of pearlite colonies per unit length ($\bar{N}_p$) similarly as in Equation (B.1), as follows:

$$\bar{N}_p = \frac{n_p}{2\bar{P}_p LM} = \frac{98}{2 \times 0.1318 \times 0.255 \times 10} = 145.77\,\mathrm{mm}^{-1}, \tag{B.2}$$

where $M$ is the total number of traverses. Thus the mean pearlite colony size ($\bar{L}_p$) is obtained using the following formula:

$$\bar{L}_p = \frac{1}{\bar{N}_p} = \frac{1}{145.77} = 0.00686\,\mathrm{mm} = 6.86\,\mu\mathrm{m}. \tag{B.3}$$

Table B.1: Results of point counting and counting boundaries

| Column 1 | Column 2 | Column 3 | Column 4 | Column 5 | Column 6 | Column 7 |
|---|---|---|---|---|---|---|
| Traverse number $(i)$ | No. of points in pearlite $P_{pear(i)}$ | Point fraction $P_{p(i)}$ | No. of pearlite boundaries $n_{p(i)}$ | No. per length, $mm^{-1}$ $N_{p(i)}$ | No. of ferrite boundaries $n_{\alpha(i)}$ | No. per length, $mm^{-1}$ $N_{\alpha(i)}$ |
| 1 | 1.5 | 0.136 | 9 | 129.4 | 10 | 65.8 |
| 2 | 0.5 | 0.045 | 13 | 690.2 | 7 | 61.6 |
| 3 | 1.0 | 0.091 | 7 | 151.0 | 6 | 41.0 |
| 4 | 1.0 | 0.091 | 11 | 237.3 | 6 | 49.6 |
| 5 | 1.5 | 0.136 | 13 | 186.9 | 9 | 70.4 |
| 6 | 4.0 | 0.364 | 13 | 70.1 | 9 | 95.5 |
| 7 | 2.5 | 0.227 | 11 | 94.9 | 9 | 73.6 |
| 8 | 1.5 | 0.136 | 7 | 100.7 | 8 | 52.2 |
| 9 | 0.5 | 0.045 | 7 | 302.0 | 10 | 55.5 |
| 10 | 0.5 | 0.045 | 4 | 172.5 | 9 | 45.2 |
| Total | 14.5 | 1.318 | 98 | 2134.9 | 83 | 610.41 |

Similarly, the ferrite grain size is obtained from the number of ferrite grain boundaries and the number of pearlite colony boundaries on each traverse, and the line fraction occupied by ferrite, i.e. $1 - P_{p(i)}$, as follows:

$$N_{\alpha(i)} = \frac{\left(n_{\alpha(i)} + \frac{1}{2} n_{p(i)}\right)}{\left(1 - P_{p(i)}\right) L}, \tag{B.4}$$

where $n_{\alpha(i)}$ is the number of ferrite/ferrite boundaries. Taking the mean value of $\bar{P}_p$ and the totals from Column 4 and 6 of Table B.1, the mean of ferrite grains per unit length ($\bar{N}_\alpha$) is calculated as follows:

$$\bar{N}_\alpha = \frac{\left(n_\alpha + \frac{1}{2} n_p\right)}{\left(1 - \bar{P}_p\right) LM} = \frac{\left(83 + \frac{98}{2}\right)}{(1 - 0.1318) \times 0.255 \times 10} = 59.62\,\text{mm}^{-1}. \tag{B.5}$$

Thus the mean ferrite grain size ($\bar{L}_\alpha$) is calculated by the following expression:

$$\bar{L}_\alpha = \frac{1}{\bar{N}_\alpha} = \frac{1}{59.62} = 0.01677\,\text{mm} = 16.77\,\mu\text{m}. \tag{B.6}$$

The procedure shown above was used to measure the mean ferrite grain size of all hot-rolling experiments reported in this thesis. Usually a total of 100 testing lines (traverses) were used on photomicrographs taken from different areas of the polished and etched specimen surface.

## B.2 General Test Method for Tension Testing of Metallic Materials

A flow diagram of the steps involved in the tension tests conducted in accordance with ASTM E8 is shown in Figure B.3. In general, the test consisted of three distinct parts, (1) Test-specimen preparation, geometry, and material condition; (2) Test set-up and equipment; and (3) Test [33].

Table B.2 shows the test parameters used in this work to set-up the testing machine.

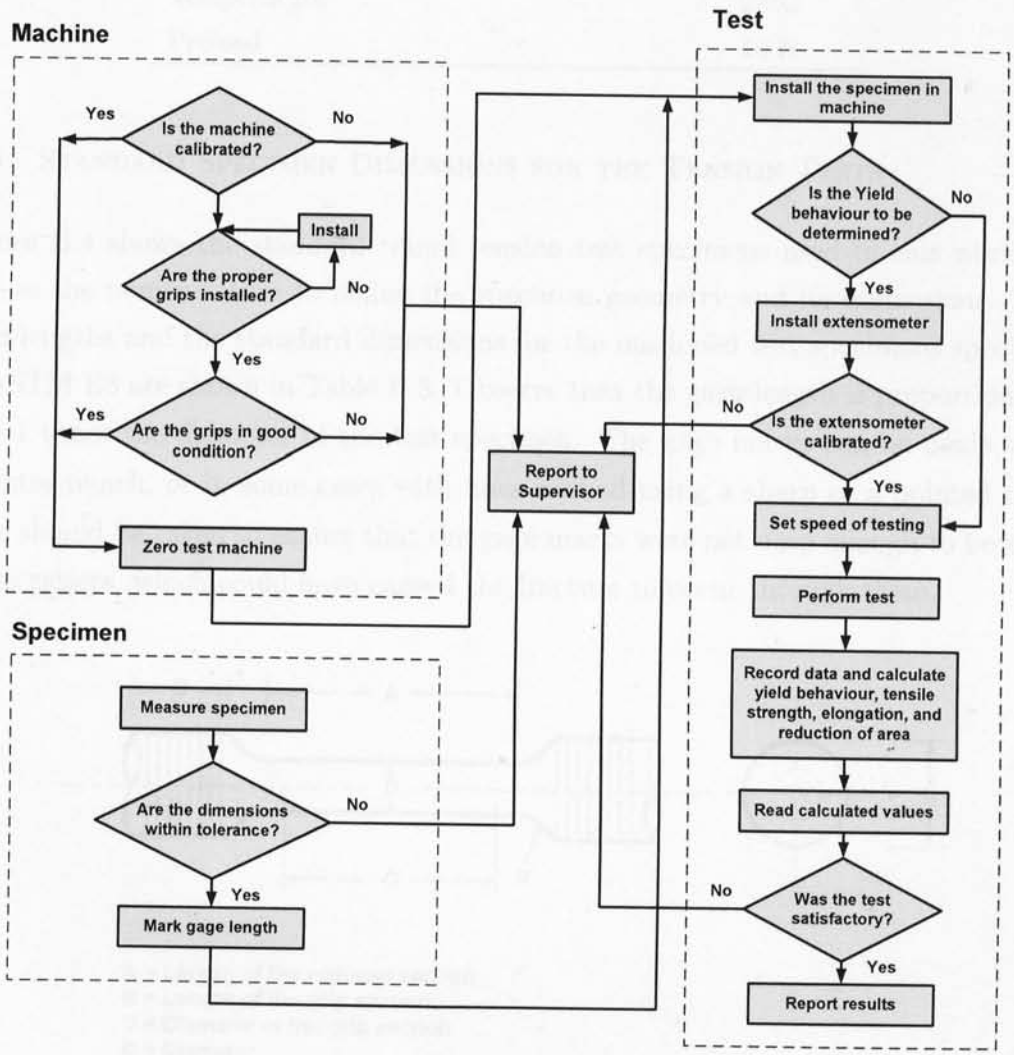


Figure B.3: A general flow chart of a standard tension test

Table B.2: Main parameters for the tensile testing machine

| PARAMETER | VALUE |
|---|---|
| Speed of testing for the yield behaviour | 0.5 mm/min |
| Speed of testing for the tensile strength | 10.0 mm/min |
| Diameter of the test specimen | See Table B.3 |
| Gage length | See Table B.3 |
| Load range | 50 kN |
| Extension range | 1 mm |
| Temperature | 22°C |
| Preload | 10 N |

## B.3 Standard Specimen Dimensions for the Tension Tests

Figure B.4 shows the standard round tension test specimens used in this work, as well as the nomenclature to define the specimen geometry and its dimensions. The gage lengths and the standard dimensions for the machined test specimens specified in ASTM E8 are shown in Table B.3. Observe that the gage length is proportionally 5 to 1 times the diameter of the test specimen. The gage marks can be made with a centre punch, or in some cases with lines scribed using a sharp or a pointed tool. Care should be taken to ensure that the gage marks were not deep enough to become stress raisers, which could have caused the fracture to occur through them.

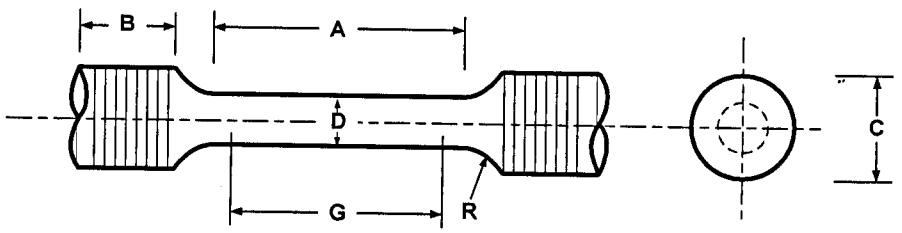


**A = Length of the reduced section**
**B = Length of the grip section**
**C = Diameter of the grip section**
**D = Diameter**
**G = Gage length**
**R = Radius of fillet**

Figure B.4: Standard round tension test specimen

Table B.3: Standard dimensions for the round tension test specimen used in this work

| DESCRIPTION | NOMENCLATURE (see Figure B.4) | SIZE 1 mm (in) | SIZE 2 mm (in) |
|---|---|---|---|
| Length of the reduced section | A | 54 (2.126) | 36 (1.4173) |
| Length of the grip section | B | 12 (0.472) | 12 (0.472) |
| Diameter of the grip section | C | 12.7 (0.5) | 9.5 (0.375) |
| Diameter | D | 9 (0.354) | 6 (0.236) |
| Gage length | G | 45 (1.968) | 30 (1.378) |
| Radius of fillet | R | 8 (0.314) | 6 (0.236) |

The general trend for the tensile test specimen used in this work was the following:

1. The reduced section had a gradual taper from the ends toward the centre, with the ends no more than 1% larger in diameter than the centre.

2. The length of the reduced section was long enough to accommodate an extensometer. Reference marks for the measurement of elongation were spaced at the indicated gage length.

3. The gage length was 5 times the diameter of the specimen.

4. The ends were in form to fit the holders of the testing machine in such a way that the load was axial; in this case, threaded ends were used to fit the testing machine.

5. The reduced section of the specimen was free of cold work, notches, chatter marks, grooves, gouges, burrs, rough surfaces or edges, overheating, or any other condition which may have deleteriously affected the properties to be measured.